SYNTHESIS OF DISPERSIBLE NANOSTRUCTURES USING ANTI-SINTERING CAST MATERIALS

by

DEAN CHARLES FLETCHER

A thesis submitted to the University of Birmingham for the degree of

DOCTOR OF PHILOSOPHY

School of Chemistry

College of Engineering and Physical Sciences

University of Birmingham

February 2018

Word Count: 27,500

ABSTRACT

At the elevated temperatures required for metal carbide synthesis, atomic diffusion across particle boundaries can occur, resulting in the fusion of smaller particles into larger ones. This process is termed sintering. By providing a physical barrier for the inhibition of sintering, in the form of easily removable alkaline earth metal oxide “cast materials”, this thesis shows that Prussian blue nanoparticles can undergo thermal decomposition to produce discrete Fe_3C nanoparticles.

The overarching aim of this work is to push the boundaries of metal carbide synthesis by forming the basis of a technique that can eventually be applied to the synthesis of a wide range of discrete metal carbide nanostructures.

A combination of energy dispersive X-ray analysis and electron tomography provides evidence of efficient dispersal of Fe_3C nanoparticles throughout various cast materials and ample evidence of <100 nm Fe_3C particle diameters. Scanning electron microscopy provides evidence of the ability to disperse these particles over a catalyst support, and superconducting quantum interference device measurements show superparamagnetic behaviour for the Fe_3C particles. The technique is then extended to larger size regimes in the biotemplating of carbonised microcoils using the algae species spirulina.

ACKNOWLEDGEMENTS

I've met many great people throughout the course of my PhD, far too many to list here, so I would like to start by thanking anybody that I've missed out. Many of which have had a positive influence, either through words of motivation or general support and advice.

To start, I would like to thank my supervisor Dr. Zoe Schnepp. Thank you for giving me the chance to work in your group and for all of the support and great opportunities you've subsequently provided me with. I feel especially fortunate to have been given the chance to work on experiments at places like the Diamond Light Source and Brookhaven National Labs.

Outside of the School of Chemistry, I would like to thank Alexander Kulak at the University of Leeds for helping with a large amount of the SEM analysis found in this thesis. His help has been hugely appreciated. I would also like to thank Dr. Elizabeth Blackburn from the department of physics here at the University of Birmingham for all of her help in collecting SQUID measurements. My thanks also go out to Dr. Huolin Xin at Brookhaven National Laboratories for facilitating our scanning transmission electron microscopy experiments.

There are many great people that I've met in my time here in Birmingham that I'd like to thank, including all of my colleagues on floor 5. In particular, I would like to thank my partner Beth for her unwavering support throughout the writing process, hopefully I can pay you back in a years' time. I would also like to thank my buddy George for helping make my PhD years a lot of fun. Those broad Street adventures were a highlight. The same goes to Ben for putting up with me for a year and for all of those trips to Nando's. It's just a pity he's not very good at FIFA.

Finally, I would like to thank my family for supporting me throughout this entire experience.

TABLE OF CONTENTS

LIST OF FIGURES

LIST OF TABLES

LIST OF EQUATIONS

LIST OF ABBREVIATIONS

1. AC – Alternating Current
2. CPB – Commercial Prussian blue
3. CTAB – Cetrimonium Bromide
4. CTEM – Conventional Transmission Electron Microscopy
5. DLS – Dynamic Light Scattering
6. EDTA – Ethylenediaminetetraacetic Acid
7. EDX – Energy Dispersive X-Ray Analysis
8. EtOH - Ethanol
9. FAAS – Flame Atomic Absorption Spectroscopy
10. HAADF – High Annular Angle Dark Field
11. IR – Infra – Red
12. MeOH – Methanol
13. PB – Prussian blue
14. PVP – Polyvinylpyrrolidone
15. PXRD – Powder X-Ray Diffraction
16. SEM – Scanning Electron Microscopy
17. SQUID – Superconducting Quantum Interference Device
18. STEM – Scanning Transmission Electron Microscopy
19. TEMPO – 2,2,6,6-Tetramethylpiperidinyloxy
20. NFC – Nano Fibrillated Cellulose
21. HPC – Hydroxypropyl Cellulose

CHAPTER 1

INTRODUCTION

1.1 GENERAL INTRODUCTION

In popular culture nanotechnology is commonly portrayed as a science of the future which will one day herald a new generation of advanced consumer goods, including nano-electronics and medical technologies, as well as a myriad of other potential possibilities. Yet, engineering on the nanoscale is not merely the science of the future, it has already become a part of our everyday lives. We have already begun to see sub 100 nm features etched onto silicon substrates in the mass manufacture of computer chips, with this kind of technology a key foundation of the modern world. In fact, "The Project on Emerging Nanotechnologies" commissioned in part by the United States government think tank, the Wilson Centre, currently identifies 1628 consumer products as containing nanoscale materials. Vance *et al.*[1] have published a study detailing this inventory and the types of nanomaterials found in it. The two largest categories that these consumer products fall into are nanomaterials suspended in fluids such as sun screens that contain nano-particulate ZnO, and solid materials with surface bound nanoparticles, tennis balls coated in nanocomposite rubbers for example. Yet these applications only scratch the surface of what may one day become possible. Many of the current technologies that utilise nanomaterials do so in the form of structurally simple, passive nanostructures. Yet as technology advances it is possible to envision the fabrication of fully functional nano-devices. It is evident therefore that new synthesis techniques, capable of producing nanostructures with high levels of structural fidelity are going to become highly sought after.

The importance of nanomaterials, *i.e.* materials with at least one sub 100 nm dimension, in future applications and technologies has also been highlighted in the scientific community. In

light of the huge potential presented by nanoscale materials, the International Council for Science (ICSU) held a workshop in Paris in February 2012 with aim of creating a system for defining and describing nanoscale materials. Through these discussions, three of the major conclusions that were drawn included: nanoscale materials have structures, properties and interactions that can differ significantly from their macroscopic counterparts; nanoscale materials are of interest to a wide range of scientific disciplines; large amounts of data will need to be collected on nanomaterials as their use spreads across many different applications and technologies. Thus, it seems that there is a consensus that we are only just beginning to scratch the surface with our current use of nanomaterials.

1.2 CHEMICAL PROPERTIES OF NANOMATERIALS

One of the most important features of many nanoscale materials is the fascinating way in which their behaviours can differ relative to macroscopic forms of the same material. Reactivities can be greatly increased, melting points can be greatly reduced and the ways in which a material interacts with light can differ.

1.2.1 REACTIVITY

From a chemical standpoint, the behaviour of nanoscale materials is very interesting. At such small length scales the surface area to volume ratio starts to become a much more significant factor in a material's reactivity. For a spherical particle, the surface area to volume ratio is 3/r (Eq. 1.1). Therefore, as the radius of a spherical particle decreases, a larger percentage of the constituent atoms can be found at the surface than in the bulk. This is important as atoms at a surface will not be in their preferred bonding environment and so form "dangling bonds".

Consequently, these surface atoms are more reactive than their bulk counterparts, meaning smaller particles have higher surface energies. Generally, these higher surface energies then mean much higher reactivities per unit of mass relative to larger particles.

Surface area of a sphere = $4\pi r^2$

Volume of a Sphere = $4/3\ (\pi r^3)$

Surface to volume ratio = $4\pi r^2/\{4/3\ (\pi r^3)\} = 3/r$

Equation 1.1 Surface area to volume ratio of a sphere.

The high surface reactivity and large surface areas that are characteristic of nanomaterials also make them desirable in catalysis applications. Driving up a materials catalytic activity while reducing the mass of catalyst required is extremely important from an economical viewpoint, especially for reactions that require expensive catalyst materials such as noble metals. It is also possible to increase the activities of some traditionally less active catalysts when synthesising them on the nanoscale, opening the way to cheaper, more sustainable catalysts for many applications.

1.2.2 MELTING POINTS

Atomic diffusion also becomes much more favourable with so few atoms in the bulk of the particle. In many cases this results in melting points that can be drastically reduced compared to macroscale particles of the same material[2 3]. Similarly, magnetic permeability can be much higher. Ferromagnetic particles of sufficiently small size, usually <50 nm can be observed to

have just one magnetic domain, meaning they can display superparamagnetism[4]. That is, all of the single magnetic moment particles can align in either a parallel or antiparallel fashion under a magnetic field to give one large magnetic moment equal to the sum of the moments of each particle. A major application for ferromagnetic nanoparticles is in ferrofluids where the particles are usually coated in a surfactant and then immersed in a carrier fluid to form a colloidal magnetic liquid in which the rheological properties can be manipulated by an external magnetic field.

1.2.3 QUANTUM EFFECTS

Quantum effects are another interesting property that can be exploited in nanomaterials. For structures where the nanoscale dimensions approach the size of the wavelength of an electron, determined by the de Broglie equation (Eq. 1.2), usually approximately 1-5 nm, the energy levels within the particle become quantized leading to some people referring to them as "artificial atoms"[5]. These so called "zero dimensional (0D)" particles in which each dimension is within this size range are usually referred to as quantum dots. The energy gap between the quantized levels in a quantum dot is proportional to the size of the particle and can therefore be tuned, with the wavelength of fluorescence from an excited quantum dot becoming shorter as the radius of the particle becomes smaller. This makes quantum dots of particular interest in solar energy applications, where the absorption energy of the particles can be tuned with a high level of efficiency. They are also becoming a popular prospective material in the fabrication of ultra-high definition displays[6].

$\lambda = h/p$

$p = mv$

$v = \sqrt{}(2K.E./m)$

λ = wavelength, h = planks constant, p = momentum of electron, m = mass, v = velocity, K.E. = kinetic energy

Equation 1.2 Equation for determining the De Broglie wavelength of an electron.

1.3 NANOMATERIAL SYNTHESIS

Due to the large range of potential nanomaterial applications many synthesis techniques have been developed. These approaches, which range from coprecipitation, to the use of microemulsions, to sol gel chemistry and more, are capable of producing a variety of crystalline phases and morphologies. Nanoparticulate ceramics, metal nanoparticles, and porous silicas are just three of the most commonly seen types of nanomaterial. The sheer depth of work done relating to these fields is demonstrated in a 2004 review produced by B. L. Cushing *et al.* [7]. A 2013 review by Yin *et al.*[8] is another good resource on the subject, covering more recent methods of producing functional nanomaterials including quantum dots.

1.3.1 COPRECIPITATION

Coprecipitation is one of the simplest approaches in the field of nanomaterial synthesis. It involves the precipitation of a product with low solubility from a supersaturated solution.

Chemical reactions leading to precipitation can be thought of as an equilibrium reaction in which ions associate and dissociate with a solubility constant expressed as K_{sp} (Eq. 1.3). Thus, concentration and temperature are very important factors in coprecipitation reactions.

$$xA^{y+}_{(aq)} + yB^{x-}_{(aq)} \rightleftarrows A_xB_{y(s)}$$

$$K_{sp} = (a_A)^x(a_B)^y$$

a_A = activity of cation A

a_B = activity of anion B

Equation 1.3 Relationship leading to the solubility product constant.

The term supersaturation refers the ratio of the activity product of a solution to the equilibrium solubility product (Eq. 1.4). This effectively relates to the fact that in a coprecipitation reaction, two highly soluble reagents are combined in solution to form a product with a much lower solubility, meaning the original reagents are oversaturated with respect to the product. Supersaturation is a measure of this oversaturation. If superstation is high, then it acts as a large driving force behind the reaction. If the supersaturation is low, the driving force behind the reaction is lowered.

The process of coprecipitation can be broken down into several steps, each of which have an influence over the morphology of the product. The first of these steps is nucleation, in which a species acts as a seed for the growth of larger particles. Nucleation can be categorised in two different forms. Heterogeneous nucleation involves the presence of some secondary material that acts as a seed for further growth. Practically, this is usually caused by

imperfections in the surface of the reaction vessel, meaning the choice of vessel can have an influence on nucleation rate. Dust particles are another primary cause of heterogenous nucleation. Homogeneous nucleation on the other hand requires ions within a given reaction mixture coming into the correct arrangement for the formation of a crystal. The probability of this occurring is directly related to the activity of the ions in solution, meaning charge, ionic radius, concentration and temperature all play important roles.

$S = (a_A)^x(a_B)^y / K_{sp}$

S = Supersaturation

a_A = activity of cation A

a_B = activity of anion B

Equation 1.4 Supersaturation given by the ratio of the activity product of a solution to the equilibrium solubility product.

The second step is growth. Here, temperature and concentration gradients within solutions both play major roles as growth rate is primarily determined by the diffusion rate of ions within the solution. This effect is then quickly followed by Ostwald Ripening, a process in which larger particles grow at the expense of smaller particles. The effect is thermodynamically driven with the minimisation of the percentage of atoms at the surface of particles the key driving force.

Finally, particle growth is terminated and the particles are stabilised. This can be achieved through the use of capping ligands such as surfactants which bind themselves to particle surfaces. These molecules then provide steric repulsion between particles. Electrostatic repulsion can also terminate growth. For example, the chemisorption of hydroxyl groups to a particle surface will endow it with a negatively charged shell, creating interparticle repulsion.

Although a simple technique, coprecipitation reactions are capable of producing complex materials. It is possible, for example, to produce nanoparticulate magnetic iron oxides. Carbon nanotubes have been decorated with Fe_3O_4 nanocrystals in order to tune microwave absorption capacities by allowing the composite to exploit the absorption bandwidth of the two materials in synergy[9]. Fe_3O_4 nanoparticles for Cr^{6+}/Pb^{2+} adsorption have also been synthesised, with the magnetic properties of Fe_3O_4 providing a means of extraction from water[10]. Fe_3O_4-Graphene oxide composites are another example, with graphene oxide acting as a high surface area support for the magnetic nanoparticles[11]. In these cases, the carbon surface provides nucleation points for the heterogeneous growth of the coprecipitated phase. Thus, in many cases the carbon surfaces need to be pre-treated in order to provide metal binding sites for nucleating growth. Acid treatments that provide carboxylate functionalities are popular.

Traditionally important catalysts like Pd nanoparticles can also be functionalised by synthesising them via coprecipitation routes, Pd/Fe_2O_3 composites in which Pd nanoparticles are grown on Fe_2O_3 surfaces are a nice example of this[12]. In this case the magnetic properties of maghemite allow for easy recycling of the Pd catalyst particles. Moving away from inorganic

ceramics, coprecipitation has even been used to produced organic polymeric nanoparticles for drug encapsulation and release[13].

1.3.2 SOL GEL SYNTHESIS

Though widely used for many purposes, sol gel processing has become commonplace in nanomaterial synthesis[14]. A comprehensive review of sol gel processing in ceramic nanomaterial synthesis has been produced by A. Danks *et al.*[15] to illustrate this point.

Sol gel reactions traditionally involve the hydrolysis and condensation of alkoxides to form a network in a continuous liquid phase, linked by metalloxane bonds. This extended network or "gel" is then aged and dried to remove any solvents, dehydrated to remove any surface bound hydroxyl groups, then calcined leading to decomposition of organics and densification of the product to give a ceramic. However, the range of elements that form stable alkoxides is somewhat limited. As a work around, alternative sol gel processes have been developed which enable the use of aqueous metal cations as starting materials. This generally involves the use of polymers or small molecules that are polymerised during the process. So, rather than the formation of a gel via metalloxane bonds, a gel is formed through the covalent bonds present in the organic polymer. The Pechini synthesis[16] is a famous example in which citrate and ethylene glycol undergo transesterification, with the citrate acting as a metal chelating agent.

An increasingly popular sol gel processing option is to use biopolymers capable of metal binding in the formulation of the gel[17]. The biopolymer can help inhibit sintering of nanoparticles and act as a carbon source, while at the same time provide a use for negative value waste products such as gelatin from the meat industry. A prominent example of the use

of gelatin in such processes is in the synthesis of iron carbides and nitrides. Schnepp *et al.* have produced a one pot synthesis capable of producing Fe_3C and Fe_3N inside a carbon support with hierarchical porosity[18, 19].

Sol gel processing is also useful in the synthesis of metal oxide nanoparticles and can even produce complex multiphase products. ZnO for example, can be synthesised as a kind of composite with magnetic Fe_3O_4 nanoparticles in which the magnetic particle is coated in photocatalyst particles[20]. This not only provides a means of extracting the catalyst from a liquid, it also enhances the activity of the catalyst in phenol degradation to give an efficiency of 82.3% compared to 52% for ZnO alone.

It is important to note that while sol gel processing can provide useful and, in many cases, relatively simple synthesis routes to a variety of nanostructures, many approaches still utilise hard templates. The removal these templates, which can be composed of materials such as carbon or SiO_2 is not always trivial and can require treatment with chemicals such as concentrated NaOH or hydrofluoric acid.

1.3.3 MICROEMULSIONS

Through the combination of specific oils (i.e. water insoluble liquids), surfactants, water and in many cases alcohol/amine based cosurfactants, it is possible to form isotropic mixtures. In many cases the surfactant forms a monolayer at the water-oil interface (Fig. 1.1), with the hydrophobic functionalities at one end of the surfactant molecule dissolved in the oil and the hydrophilic functionalities at the other end dissolved in the water. In such an arrangement, aqueous droplets surrounded by a shell of surfactant molecules form, in which hydrophilic

surfactant heads are packed closely together. Thus, the function of the polar cosurfactant is to act as an electrostatic spacer via ion dipole interactions, minimising repulsion between the tightly packed hydrophilic groups.

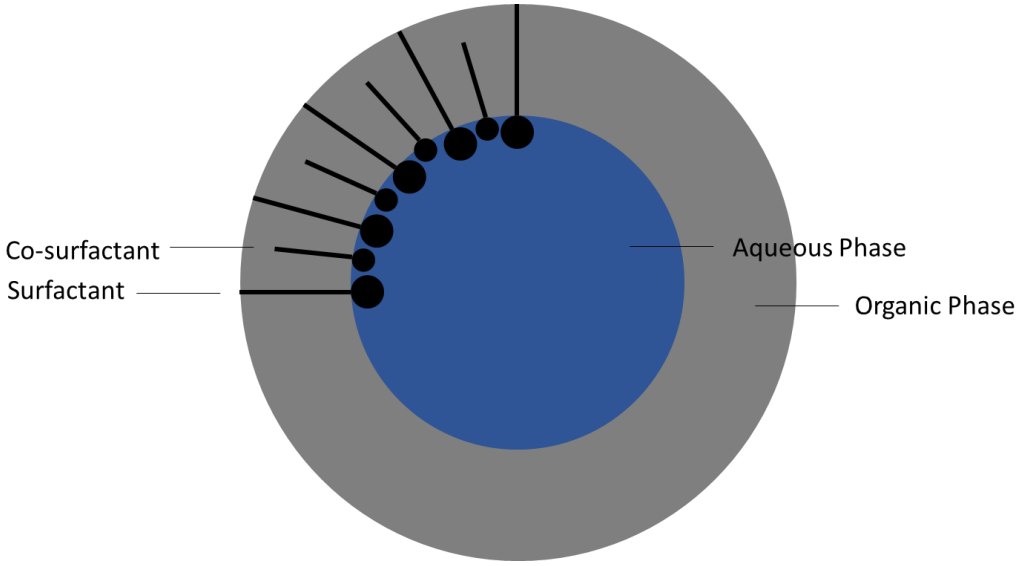

Figure 1.1 Schematic illustrating how amphiphilic surfactant molecules can form a monolayer around an aqueous droplet, with their hydrophobic heads stabilised by polarisable co-surfactants.

Such systems are useful in nanoparticle synthesis as it is possible to trap reactants within the core of the aqueous micelles. Approximately one in every thousand collisions between micelles results in the formation of a short-lived dimer. During the lifetime of the dimer the contents of the micelles are mixed meaning a chemical reaction can occur. Furthermore, the degree to which the microemulsion is agitated and the concentration of surfactant have a direct effect on the size of the micelles and thus the size of the pools of aqueous reactants. In fact, it is now also possible to create nanoscale micelles[21]. Control over micelle size and thus

the dimer can help endow some control over particle size, although this is by no means a simple relationship

The use of microemulsions is very popular in metal nanoparticle synthesis[22]. Generally aqueous metal cations are reduced within a water micelle. Seip *et al.* have used this approach to synthesize Fe nanoparticles[23]. By using CTAB as a surfactant and butanol as a cosurfactant the authors created aqueous micelles with dissolved Fe^{II}, in octane. Hydrazine was then added to the reaction mixture, reducing Fe^{II} to Fe^{0} within the confines of the micelle. They were then able to add Au^{II} which was reduced to Au^{0}, giving the particles an Au coating, allowing them to self-assemble at a thiol functionalised surface. A similar approach can be used to synthesise Pt nanoparticles. This time H_2PtCl_6 is reduced with hydrazine within the confines of an aqueous micelle suspended in *n*-heptane, using $C_{12}H_{25}(OCH_2CH_2)_4OH$ (Brij 30) as a surfactant[24].

Bis(N-octylethylenediamine)metal(II) complexes are an important reagent in microemulsion routes to metal nanoparticles. Here, the alkylethylenediamine ligand acts as a surfactant, stabilising the water in oil microemulsion, whilst also acting as the metal cation source. $Zn(oct\text{-}en)_2Cl_2$ has been used in a water in benzene microemulsion for example[25]. Likewise, Pd nanoparticles have been produced by using the Pd analogue of this complex in a water/chloroform microemulsion, using $NaBH_4$ as a reducing agent[26].

1.3.4 HYDROTHERMAL/SOLVOTHERMAL SYNTHESIS

Solvothermal syntheses employ the use of a sealed vessel known as an autoclave in which high solvent temperatures can be used to auto-generate high pressures. Through the use of this technique it is possible to alter the density and dielectric constant of many solvents,

including water (hydrothermal synthesis). This is extremely useful for reactions that employ chemicals that are insoluble under normal conditions. The elevated temperatures and pressures can also result in increased reactivities. The high pressures employed mean it is even possible to synthesise many products that are unstable at or near their melting points. More specifically, it is possible to synthesise crystalline phases that are not necessarily the most thermodynamically stable possible product. The approach is therefore notable in its ability to produce materials at greatly reduced temperatures, which is quite an advantage in nanomaterial synthesis.

Metal oxide nanoparticles are particularly prevalent nanomaterials produced by hydrothermal reactions. The size of these particles is directly related to the hydrolysis rate and solubility of the metal oxide. Thus, fine control can be achieved by controlling the temperature and pressure within the autoclave. A wide range of examples of such syntheses have been covered in a review by Hayashi *et al.*[27].

Particle size control can even be taken to the extremes of carbon dot synthesis. With biomedical applications in mind, nitrogen doped carbon dots measuring just 7 nm in diameter have been produced for Fe^{3+} sensing, through the hydrothermal reduction of a fruit extract[28]. Ordinarily the dots fluoresce at 411 nm when exposed to radiation with a wavelength of 310 nm, whereas fluorescence is shut off in the presence of Fe^{3+}. This kind of effect can only be achieved at <10 nm particle diameters, illustrating just how useful this kind of size control can be.

Interestingly, cutting edge research is now allowing for morphological control that moves past the control of simple particle size, to control over shape and structure. A recent high-profile

example is the synthesis of Fe_3O_4/C composite nanorings for microwave absorption[29]. The authors first produced elliptical sheets of iron glycolate. They then functionalised the elliptical sheets with polyvinylpyrrolidone (PVP) which preferentially binds to the high energy surfaces at the side faces and edges of the sheets, protecting them in the latter reduction steps. Hydrothermal reduction was then performed in the presence of glucose, which acts as both a reducing agent and carbon source for carbon shell growth. In these reducing conditions some Fe^{3+} cations are reduced to Fe^{2+} resulting in the precipitation of Fe_3O_4 crystals. These crystals then undergo Ostwald ripening, while the protected iron glycolate surfaces remain structurally intact, resulting in the formation of Fe_3O_4 nanorings. Furthermore, by controlling the molar ratio of glucose to precursor the authors were able to alter the carbon content of the rings, demonstrating knock on effects on their microwave absorption properties.

It is important to point out that the limitations of the finite volume of an autoclave have also been addressed with the invention of hydrothermal flow systems, allowing for large batch and continuous flow production of nanomaterials[30].

1.4 CONTROLLING MORPHOLOGY

Control over the morphology of nanomaterials is of the utmost importance as we start to look towards more advanced applications.

An area that has already gained a significant amount of focus has been the creation of porous ceramics such as cellular ceramics[31]. These materials have porosities greater than 60 vol% giving them impressive strength to weight ratios, making them ideal materials for lightweight load bearing structures. The ability to control pore size and structure in these materials has

also opened up routes to materials suitable for biomedical devices and liquid/gas filtration systems. Macro-porous ceramics have also garnered a lot of attention[32] with applications such as catalysis and refractory insulation in mind.

Ordered porosity is a strong theme in nanomaterials research. The high surface areas and physiochemical properties of mesoporous carbons make them invaluable materials in electrode, gas storage and catalyst support technologies. Coupled with the abundance of carbon, these properties justify the vast amount of research that has been done in this field.

Taking the idea of morphological control even further, it would be highly desirable to develop simple industrially scalable routes to complex micro and nanostructures. Nanoparticles[33], wires[34] [35] whiskers[36] and rods[37] are just a small selection of the possibilities. Doing so would open up routes to highly specialised applications.

It is unfortunate then, that controlling the morphology of nanoscale structures, particularly those composed of ceramic materials, is not simple proposition. The crux of the problem relates to the high temperatures required during synthesis. For example, it is not uncommon for transition metal carbide syntheses to require temperatures in excess of 1000 °C [38]. At these temperatures sintering occurs. In fact, sintering is a key step in the industrial fabrication of a ceramic in which individual particles fuse together to produce a strong, hard, dense material. However, problems arise when trying to exert fine control over the morphology of said materials, particularly at the micro and nano scales, as the fusing of particles will result in the loss of structural information and the formation of agglomerates, as well of shrinkages of anywhere between 10-40%.

Below are some of the most common-place approaches currently in use that allow control over morphology on the nanoscale.

1.4.1 SOFT TEMPLATING

Soft templating, also termed “endotemplating”, particularly in the synthesis of porous materials, utilises self-organising molecular systems such as surfactants or block copolymers that form micelles or other supramolecular aggregates. These aggregates then act as a template around which structures can be built up. These “soft templates” can then be removed to leave voids in a solid, creating a porous network[39]. Thus, the nature of the chosen template material grants a degree of tunability over pore size. This control can be further supplemented by the use of a swelling agent.

However, the technique suffers from some significant drawbacks, a key one being that the templated material must be more thermally stable than the soft template polymers, as the soft template is usually removed by heat treatment at the end of the process. This is further complicated by the fact that the template molecules must be thermally stable enough to resist micelle collapse. There must also be a favourable interaction at the interface between the soft template and the templated material in order for the template aggregates to be incorporated into the solid. This means that the choice of template can be limited by the choice of solid.

Soft templating is a common synthetic method used in the creation of zeolitic materials[40]. However, in this case it is not uncommon for the shape of the template, commonly a metal complex, to have no direct link to the shape of the void in the product material. In cases such

as this the template is commonly referred to as a structure directing agent rather than a soft template[41]. For a direct link, it is necessary to move to slightly larger size regimes. As mentioned previously surfactants can also provide this link. For example, at high temperatures, methyltrioxorhenium(VII) forms an organometallic polymeric structure in aqueous solutions, with the rate of aggregation having a strong link to pH. This structure is graphitic in appearance leading to electrical conductivity. Removal of the template yields a nanostructured crystalline ReO_2 phase[42].

1.4.2 HARD TEMPLATING

Hard templating, otherwise known as "exotemplating", involves the use of a rigid structure in which voids can be filled with a precursor to the desired material. The template is then removed to leave a "negative replica"[43]. This raises interesting possibilities. For example, if a hard template with a continuous pore network is used, an intricately structured, extended solid can be "cast". On the other hand, if a template with a non-continuous network is used, then discrete smaller particles can be formed[44].

Colloidal crystal templating is an important example within the hard templating remit, particularly in the synthesis of inverse opals. Uniform, spherical, colloidal particles that assemble themselves into an extended array that resembles the crystalline nature of natural opals, form the template. A fluid that can later be transformed into a solid is then used to penetrate the structure. Removal of the template leaves a highly accurate three-dimensional

skeleton that can act as a photonic crystal[43]. The technique is therefore very useful in the synthesis of materials with functional optical properties.

Activated carbons are another particularly useful hard template. By infilling the pores with a metal salt, then calcining the template, it is possible to remove the template to leave metal oxide particles with diameters similar to those of the template pores[44]. Alumina into which nanochannels have been etched has also been used as a hard template for infilling to produce many structures, including bismuth nanowire arrays[45]. Carbon nanotubes have even been shown to be effective hard templates. By exploiting capillary forces, Ugarte *et al.* were able to selectively fill carbon nanotubes with diameters <4 nm with molten silver nitrate. By decomposing the silver nitrate with an electron beam in an in situ SEM experiment the team were able to form silver nanobead chains[46], using the nanotubes as "nanosized test tubes".

1.4.3 BIOTEMPLATING

Biotemplating exploits the tendency of smaller basic building blocks such as transition metal ions to self-assemble at the surface of natural organic templates. These templates are commonly rich in polysaccharides that have a high affinity for metal cations. The extent to which these properties can be exploited is demonstrated in a review authored by Sotiropoulou *et al*.[47]

The technique incorporates a broad range of strategies that can be characterised into the three main groups summarised in Fig. 1.2. Negative biotemplate replicas can be formed via coating strategies such as atomic layer deposition and electroless deposition. Hollow replicas on the other hand, can be formed by the infilling of a template with a sol, followed by a sol gel

synthesis. Finally, a positive replica can be formed through thermal conversions such as combustion and carbothermal reduction. Ordinarily, in the final step, the template is then removed by calcination or chemical etching, to leave behind a free standing inorganic structural replica. This process is an example of a bottom up fabrication technique.

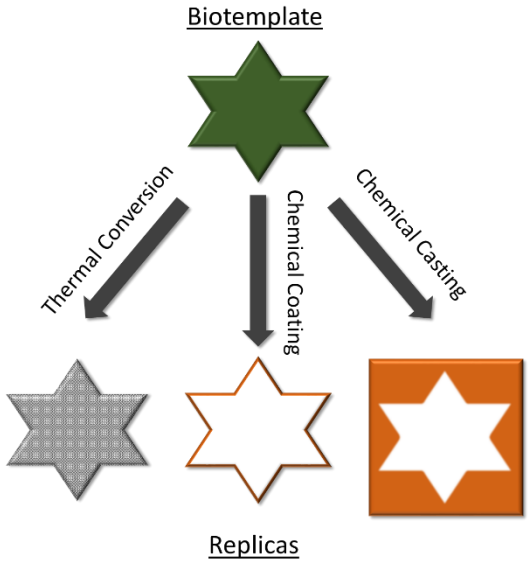

Figure 1.2 Schematic illustrating the three major biotemplating strategies: chemical casting in which a hollow copy of the template is formed; chemical coating in which a negative of the template is formed; and thermal conversion in which a positive replica is formed, usually through calcination.

One of the chief advantages to this technique is that through millions of years of natural selection, nature has amassed a wide assortment of small structures with unique morphologies and topologies, capable of an eclectic variety of functions. Mimicking these properties is therefore an attractive proposition for materials chemists.

The left handed helical microstructure of the microalgae spirulina has found numerous uses as a template, since structures with this level of complexity are very time intensive and costly to produce using traditional top down fabrication methods. The cellulosic algal cell walls

provide a source of carbon for metal reduction as well as a potential support for metal nanocrystals, making spirulina a particularly attractive template for battery electrode materials[48], [49].

The chiral helical structure of spirulina is also useful in the synthesis of functional optical materials. By manipulating the helical pitch of the spirulina microcoils through culturing conditions, Kamata *et al.* were able to create a variety of templates for Cu coating. By dispersing the resulting Cu microcoils in a silicon sheet for use in transmission and reflectance spectroscopies, the team discovered that the metal microstructures displayed resonance frequencies specific to their coil structure. Thus, the team demonstrated the possibility of manipulating a biotemplate to produce a tangible response in a function directly related to its structure[50].

Similarly, many varieties of insect wing contain periodically repeating micro/nano-structures that form photonic crystals capable of scattering light in interesting ways. The wings of the Australian Green Grocer Cicada "*Cyclochila Australasiae*" for example are covered in a hexagonal array of 110 nm wide, 200 nm tall, chitinous pillars. By using nanoimprint lithography G. Kostaovski *et al.* were able to use these wings as a template to create nanoimprinted optical fibres for use in surface enhanced raman spectroscopy (SERS) sensing[51].

1.4.4 NANOCASTING

The conventional interpretation of the term nanocasting would refer to a process involving the use of a nanoscale mould, in which the empty space is infilled with a substance that can

be hardened through a chemical transformation. Removal of said mould would then yield a negative replica. The “mould” or “template” in this case can be either a hard template or a soft template.

One of the more famous examples of this technique is the replication of the hydrophobic surface of a lotus leaf. Here, Sun *et al.*[52] coated the surface of a lotus leaf with polydimethylsiloxane (PDMS). Once hardened, removal of the lotus leaf left a negative PMDS replica. The surface of the negative was given an anti-stick coating then infilled with more PDMS. Removal of this new PDMS coating gave a positive replica of the original lotus leaf. A comprehensive review of this kind of nanocasting, with a major focus on the use of hard templates to produce porous materials, has been compiled by Schüth *et al.*[53].

The results chapters in this thesis will refer to a variation on the nanocasting concept. In this variation, soluble Prussian blue nanoparticles with the formula $KFe[Fe(CN_6)]$ will be used as “templates” for the formation of Fe_3C nanoparticles via thermal decomposition. The use of Prussian blue affords several advantages, a major one being that the Prussian blue particles can be used as a source of both Fe and C, eliminating the need for secondary active reagents. Soluble Prussian blue nanoparticles are also easily synthesised by coprecipitation, a point that not only makes synthesis simple but also raises the potential for particle size control through the incorporation of a surfactant[54].

More importantly, the nanocasting aspect refers to the use of a secondary material, a “nanocast”, that is used to immobilise the template particles during the calcination process. In doing so, the sintering of template particles is inhibited, and the formation of large agglomerates is avoided. The general approach in this regard is to pack cast particles around

the template particles, creating a physical barrier between template particles during heat treatments. The general scheme for such a reaction is depicted in Fig. 1.3.

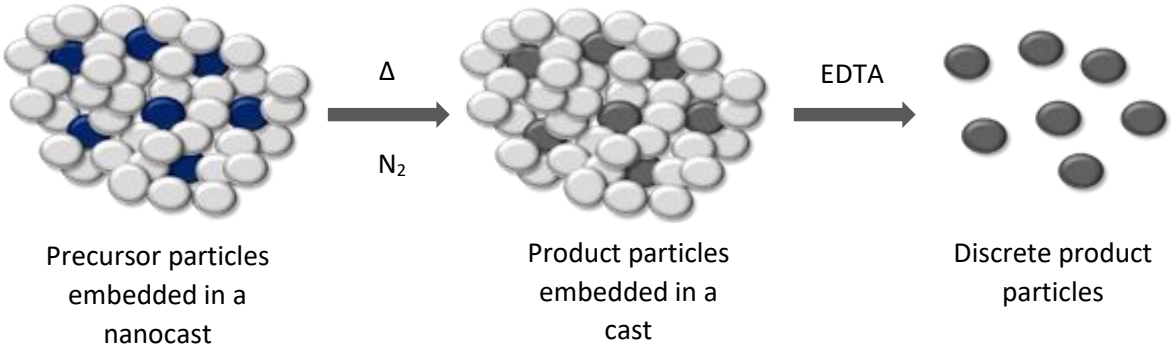

Figure 1.3 Schematic illustrating our nanocasting concept.

Similar anti-sintering effects can be achieved through techniques such as sol gel processing, in which the sol, possibly a biopolymer, immobilises nanoparticles as they form[18]. However, in processes that result in the reduction of an organic precursor, large amounts of amorphous carbon are produced. While this may be useful in applications that can utilise nanoparticles embedded in a mesoporous carbon support, when discrete, dispersible particles are required this is a significant issue. With this issue at the forefront of our thinking, a key feature in our new variation on the nanocasting concept is that the cast will be readily removable, meaning that the discrete product nanoparticles can in fact be isolated.

1.5 CHEMICAL METHODS FOR TEMPLATING/CASTING

Putting aside the discussion into the various types of templating and casting, it is important to consider the various chemical methods that can be utilised in a templating synthesis. These methods themselves, while having their own individual advantages, can also impose significant limitations on the types of morphologies and chemical phases that can be fabricated.

1.5.1 DEPOSITION

If fine control over the uniformity and thickness of a coating is of paramount importance, then it is hard to beat direct deposition techniques such as atomic layer deposition (ALD). By sequentially exposing a substrate to two chemical vapour "precursors" inside an ALD chamber, sequential chemical reactions can be initiated that result in the controlled deposition of a thin film. By combining this technique with templating, thin films with complex topologies can be produced. For example, by applying ZnO to the surface of egg shell membranes, Lee *et al.*[55] were able to impart some of the original functionalities of the egg shell membranes, such as mechanical stability, to the resulting ZnO film, without compromising the bactericidal efficiency of the film.

To give a simple example of how ALD might be carried out, the formation of a TiO_2 film may involve the exposure of a substrate to a titanium alkoxide vapour such as titanium isopropoxide (TIP), followed by water vapour, in order to initiate hydrolysis at the substrate surface.

A typical ALD process involves three stages: i) a “pulse”, in which one of the chemical precursors is introduced into the ALD chamber; ii) exposure i.e. a set period of time in which substrate is exposed to the precursor; and iii) a purge, in which the chamber is purged of precursor. Thus, parameters such as injection and exposure times can be varied to give different growth rates and surface uniformity. Temperature is another variable, however mild temperatures are commonplace, meaning the use of precursors with low thermal stabilities is often feasible.

Unfortunately, the technique also has significant draw-backs, namely the speed at which a coating can be applied. Although the sequential application of atomic scale layers onto a substrate can produce exceptionally uniform coatings, it also severely limits the speed at which a coating can be produced, with 300 nm per hour representing the higher end of the scale. The requirement for volatile precursors that are not likely to decompose during the process also imposes practical limits on the range of suitable reactants.

1.5.2 SOL GEL CHEMISTRY AND INFILLING

Sol gel chemistry involves the use of a sol in which particles, be they crystalline or amorphous, form a colloidal suspension in a solvent. Gelation of the sol is then initiated by increasing the volume fraction of the solid by removing fluid through sedimentation, centrifugation or drying, allowing for the formation of a continuous three-dimensional network of agglomerated particles. Alternatively, a polymer sol can be used in which the network develops through either the formation of covalent bonds, or through intermolecular bonding

interactions such as hydrogen bonding. Through further drying of the gels, a solid, porous, structural template is formed.

Alkoxides such as tetraethylorthosilicate (TEOS) are some of the most favoured sol gel precursors due to their ability to rapidly hydrolyse in the presence of water, to give a monomeric species analogous to $Si(OH)_4$. In the case of $Si(OH)_4$, a large continuous network of siloxane bonds will form through condensation reactions, resulting in a SiO_2 gel that can be dried to give a porous solid. A key strength of this approach is that the condensation step is favourable in both acidic and basic conditions.

Thus, by infilling a microporous hard template with a sol and then drying it, it is possible to produce a reverse replica of the template. However, if the gel is dried by the evaporation of the solvent, then an important factor that must be considered is the amount of capillary force the gel network will undergo[56]. If capillary forces are reduced, potentially by drying via sublimation, slight shrinkage effects may still occur, but a porous aerogel may be formed. However, drying by evaporation can cause total collapse of the gel network, producing a dense xerogel. In either case this will have a significant effect on the fidelity of the templated replica.

A novel approach at overcoming these shrinkage issues was demonstrated by Shin *et al.*[57] in a paper published in 2001. In their work, the authors managed to reproduce the cellular structures found in wood tissue as a part of a hierarchical porous ceramic material. They achieved this by utilising TEOS in a sol gel infilling process in conjunction with the surfactant - cetyltrimethylammonium chloride (CTAC). In doing so, surfactant micellar structures were incorporated into the mineralised silica network, resulting in the formation of organised channels during calcination. These channels provided a pathway for decomposition products

to escape without straining the overall structure of the material. A similar synthesis carried out in the absence of the surfactant resulted in the total collapse of the desired cellular structures.

1.5.3 ELECTROLESS DEPOSITION

Achieving thin coatings with a constant thickness can prove extremely difficult, particularly when the substrate has a complex topology. When a Ni, Co, Pd, Cu or Au coating is required, an appealing approach to this problem can be the utilisation of redox chemistry through the use of electroless deposition. In brief, the technique involves the immersion of a template in a metal ion solution, thus exposing the entire surface, including any complex features, to a constant ion concentration. A mild reducing agent such as formaldehyde is then used to reduce the complexed metal ions to give an even metallic coating. To contrast this with electrodeposition; there is no need for an external current; instead of an anode a metal salt is used as the metal ion source; the substrate surface acts as the cathode and the reducing agent, commonly formaldehyde, supplies the electrons.

In some cases a small amount of Pd can be deposited at the surface as a pre-treatment step. This coating is commonly achieved via one of two routes; either the substrate surface is sensitised by the adsorption of acidic Sn(II)/(IV), $AgNO_3$ or $AuCl_3$, then exposed to Pd(II) (Fig. 1.4), or the substrate is exposed to a mixed colloid of Pd, stabilised by a layer of Sn(II)/(IV) which is later removed by KF, HF, HCl or NaOH during an “activation step”.

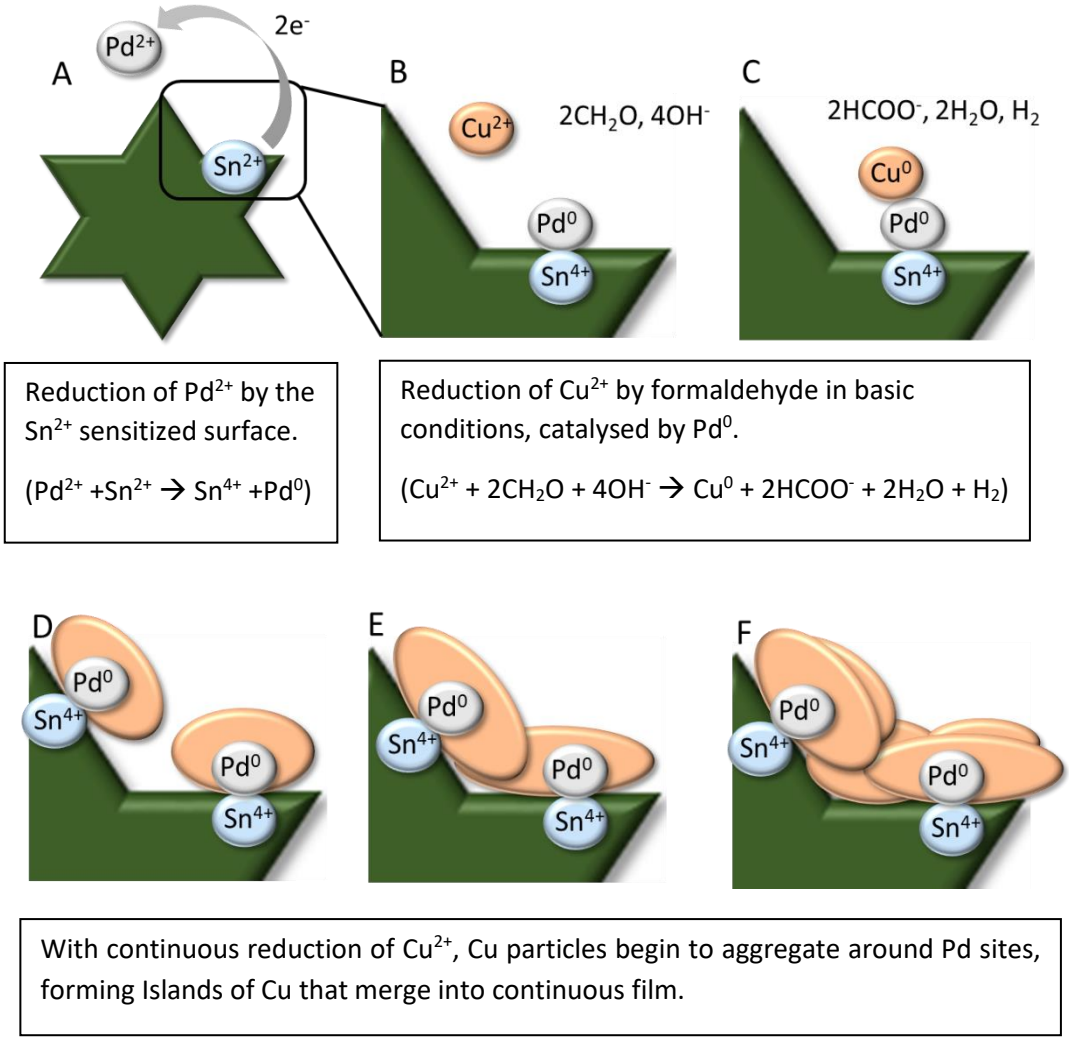

Figure 1.4 Schematic illustrating a general electroless deposition process. A) Template with a surface sensitised by acidic Sn(II)/IV), B) surface coated with a catalytic amount of Pd C) Cu particles begin to aggregate around Pd sites with formaldehyde acting as a reducing agent, D) formation of Cu clusters, E) Islands of Cu begin to form a continuous film, F) Thickening of continuous Cu film.

From the description above it is also evident that electroless deposition can be carried out in relatively mild conditions. Thus, not only can even metallic coatings be achieved, the risk of destroying or degrading the template itself in the process can also be minimised. An

impressive level of control over the morphology of the product material is therefore possible. This has led to an exciting amount of interest in combing electroless deposition and nanomaterial templating. For example, synthesis of potential microdevice components such as metallic microrods[58] and micro springs[59] has been achieved through this method.

1.5.4 COMBUSTION/CARBOTHERMAL REDUCTION

It is possible to reduce many organic templates to pure amorphous carbon simply by heating them to several hundred degrees Celsius in an inert atmosphere[60]. Fascinatingly, many of these templates will retain their initial structures given the appropriate heating conditions. For example, Wool *et al.*[61] have shown that if chicken feathers are given a prolonged heat treatment below the melting point of their protein matrix, then enough protein crosslinking can be induced for the fibrous structure to remain intact upon further heating. Additionally, inducing various level of crosslinking through similar heat treatments was found to significantly affect the thermal stability of the products as well as the physical properties of the chicken feathers themselves. Thus, the combustion of templates using specific heating protocols can provide a means of producing materials with tailored characteristics.

Carbon replicas produced through combustion can also be valuable as templates in and of themselves, particularly if they happen to be porous. Work by Kaskel *et al.*[62] in which a carbide-derived carbon with the hierarchical porosity of wood is produced provides a good illustration of this point. The authors achieved this result by creating a pyrolyzed wood monolith and transforming it with SiC, by first filling it with polycarbosilane, then pyrolyzing it for a second time.

At high temperatures carbon can also be employed as a strong reducing agent, meaning that if a carbon-based template is first soaked in an aqueous metal salt, it becomes possible to reduce the metal and carbonize the template simultaneously. This is illustrated nicely in the synthesis of a "magnetic leaf" by Schnepp *et al*.[63] The authors here were able to produce a Fe_3C/C composite leaf with impressive magnetic properties, by first soaking a leaf skeleton in an $Fe(NO)_3$ solution, then calcining it in a N_2 atmosphere.

1.6 CONCLUSIONS

This introduction has hopefully emphasised the sheer depth and breadth, as well as the importance, of nanomaterial research, highlighting not only the need for the synthesis of new nanoscale materials, but also the need for new processes that allow for the control of nanoscale morphologies. With this information in mind, the following chapters of this thesis will set out to find methods for producing nanoscale materials while exerting morphological control. With iron carbide the major material of interest, high temperature syntheses will be performed, with the inhibition of nanoparticle sintering at the centre of the work.

CHAPTER 2

PRELIMINARY DESIGN OF ANTI-SINTERING CAST CONCEPT FOR THE SYNTHESIS OF IRON CARBIDE NANOPARTICLES

2.1 INTRODUCTION

Ceramics are classically defined as highly crystalline, generally non-metallic, inorganic solids, with either ionic or covalent chemical bonds, depending on their chemical composition. Ceramics that contain both metals and non-metals are typically described as having bonds that are ionic in nature, whereas ceramics containing metalloids and non-metals are usually thought to have bonds that are more covalent in nature. The vast majority of these materials are characterised by being both hard and brittle, as well being highly resistant to abrasion, corrosion and high temperatures.

These properties are so well suited to such a wide range of applications that ceramic materials can be found in countless areas of modern life. The utilisation of their extreme hardness can be seen in military grade body armour[64] in which their brittleness also helps dissipate the impact energy of a projectile. Moreover, their high temperature resistance[65] can be seen in anything from ceramic table-ware, to the brake disks in a car, to the heat proof tiles used for shielding spacecraft during atmospheric re-entry.

The design and discovery of advanced ceramics has also allowed for the utilisation of other finely tuned properties. One example is that of magnetic ceramics[66], which can be found in the magnetic recording read heads of mechanical hard disk drives, as well as multiple forms of random access memory (RAM) used in modern day computing. We also have access to a myriad of electrical properties from ceramics such as semi-conductivity, superconductivity and piezoelectricity, meaning they can be found in a large variety of consumer electronics.

2.1.1 TRANSITION METAL CARBIDES

An important class of ceramic material in which the previously described properties are evident, particularly high melting points, hardness, and brittleness, are the transition metal carbides. Not only are they widely used in applications requiring these more conventional properties, they are also now a major area of interest in the search for new energy storage and conversion technologies[67]. Many carbides and nitrides have electrochemical properties desirable in Na/Li ion battery materials[68]. They also possess high electro-catalytic activities in common energy storage/conversion reactions such as the oxygen reduction reaction[69] and the hydrogen evolution reaction[70].

Structurally, most transition metal monocarbides contain a face centred cubic array of metal atoms with carbon atoms occupying the octahedral interstitial sites. The presence of carbon results in an increase in M-M bond length of approximately 30% relative to the pure metal, yet the nature of the bonds can be difficult to define. Although the combination of a metal and a non-metal would usually signify ionic bonding, the bonding in transition metal carbides cannot be described as purely ionic due to their tendency to slip on the {111} plane[71]. This is a feature not normally seen in ionic materials. The characterisation of the bonding in transition metal carbides is therefore still an active area of research[71].

Data relating to a group of transition metal carbides known as the refractory carbides can be seen in Table 2.1. The high Young's moduli, which measures the ratio of stress to strain for a material, suggests that large stress forces cause little strain i.e. elongation, a property that also results in the materials being brittle. Whereas the high micro-hardness values illustrate just how hard these materials are. However, as impressive as these physical properties are,

they mainly relate to the chemical composition of the materials. In order to start achieving the full technological potential of these materials we also need to start gaining further control over morphology.

Table 2.1 Table showing data relating to the physical properties and applications of refractory carbides[38].

Carbide Phase	**Melting point (°C)**	**Lattice Parameters (Å)**	**Young's modulus x 10^6 (psi)**	**Micro-hardness (kg/mm^2)**	**Colour**
TiC	3067	4.328	39-67	7.4	grey
$ZrC_{0.97}$	3420	4.698	56	6.7	grey
$HfC_{0.99}$	3928	4.64	46-61	6.6	grey
$VC_{0.97}$	2648	4.166	63		grey
$NbC_{0.99}$	3600	4.47	49-74	6.6	lavender
$TaC_{0.99}$	3983	4.456	53-78	6.3	gold
Cr_3C_2	1810	a: 11.47 b: 5.545 c: 2.83	56	10.3	grey
Mo_2C	2600	a: 7.244 b: 6.004 c: 5.199	33	4.9//a, 8.2//c	grey
WC	2776	a: 2.906 c: 2.837	97	5.0//a, 4.2//c	grey

2.1.2 IRON CARBIDES

The iron carbides are very hard and brittle with hardness increasing with carbon content making cementite (Fe_3C). For this reason, iron carbides are inextricably linked to steels, used mainly to harden them, with a wide variety of structures and carbon contents possible. Fig. 2.1 shows the iron-carbon phase diagram, with the key phases listed in Table 2.2. An in depth look at the nature of iron carbides, nitrides and carbonitrides in steels has been assembled by Jack *et al.*[72]

The main phase of interest in this thesis is Fe_3C (cementite). As with other iron carbides such as Fe_5C_2 (Hägg Carbide) and Fe_7C_3 (Eckstrom-Adcock iron carbide) the carbon atoms sit in trigonal prism environments (Fig. 2.2). Nitrogen atoms on the other hand only ever sit in octahedral interstitial sites in iron nitrides. The result of this is that unlike iron nitride which can dissolve large amounts of carbon, cementite cannot dissolve nitrogen.

From a synthetic standpoint, in short, the key requirements for iron carbides almost always include reducing conditions, relatively high temperatures and a carbon source. Thus, these are the key requirements that make up the focus of the synthesis work in thesis.

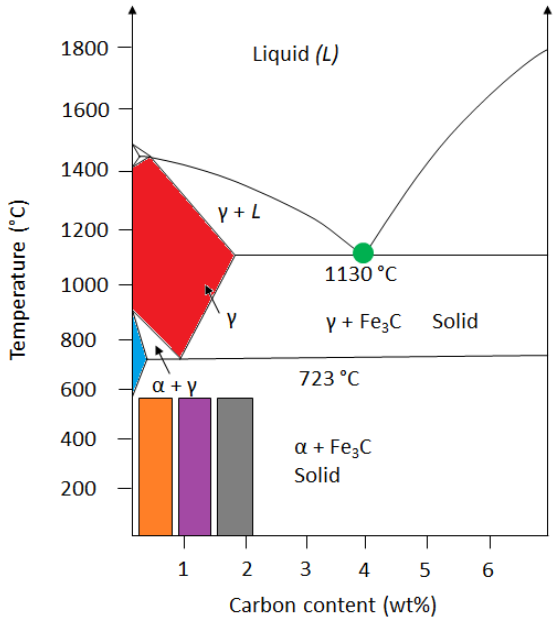

Figure 2.1 The iron-carbon phase diagram Austenite (red), Ferrite (blue), Pearlite (orange), Pearlite and cementite (purple), pearlite and carbides (Hägg/Eckstrom-Adcock) (grey), eutectic point (green).

Table 2.2 The key phases found in the iron-carbon phase diagram[73].

Phase	**Carbon content (%wt.)**	**Temperature Range**	**Crystal Structure**
Ferrite (α)	0-0.022	<912	BCC
Austenite (γ)	0-2.11	727-1495	FCC
Pearlite	0.022-2.11	<727	BCC and Orthorhombic
Cementite	6.69	<1227	Orthorhombic

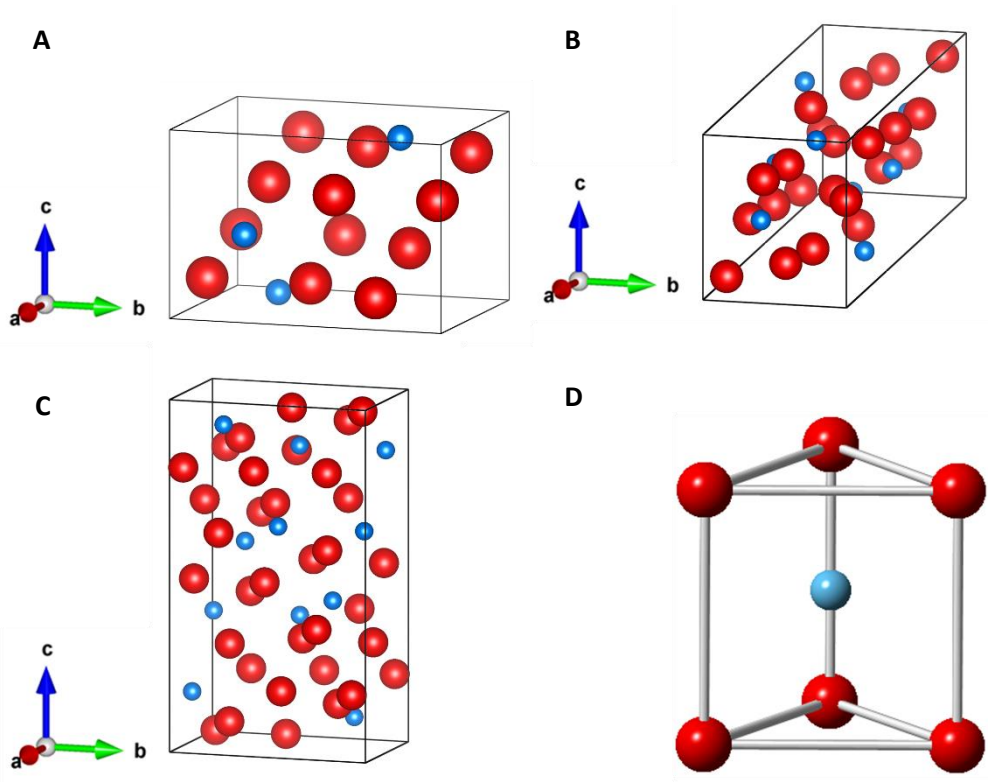

Figure 2.2 A – Unit cell of Fe_3C (Cementite) a = 5.08 Å, b = 6.75 Å, c = 4.52 Å, space group = pnma, **B** – Unit cell of Fe_5C_2 (Hägg Carbide) a = 11.57 Å, b = 4.57 Å, c = 5.06 Å, space group = pnma, **C** – Unit cell of Fe_7C_3 (Eckstrom-Adcock iron carbide) a = 4.54, b = 6.89, c = 11.91, space group = C2/c, **D** - The trigonal prism environment of a carbon atom in the cementite crystal structure, Red = iron, blue = carbon.

2.1.3 CEMENTITE

Cementite's high stoichiometric amount of Fe means that it has a much higher saturation magnetisation than many of the other common iron containing ceramics used in nanoscience, such as Fe_2O_3 and Fe_3O_4. This makes Fe_3C a strong contender for use in ferrofluids and magnetorheological fluids[74]. Additionally, unlike Fe, iron carbides have been shown to be biocompatible[75], opening the way for their use in biomedical applications such as drug delivery[76] and as MRI contrast agents[77]. Fe_3C has also been shown to be an active catalyst in

the oxygen reduction reaction[78], oxygen evolution reaction[79], and Fischer Tropsch reactions[80] [81].

As different as these applications seem, a characteristic that all of these applications share is the need for nanostructured Fe_3C. Catalysts require large surface areas in order to maximise activities; medical applications require size regimes small enough for *in vivo* use and ferrofluids require nanoscale particles with masses low enough for Brownian motion to prevent sedimentation. A large body of work has been accrued with the aim of producing nanostructured Fe_3C, with many techniques utilised with varying degrees of success. A selection of these techniques is detailed below.

2.1.3.1 ARC PLASMA SYNTHESIS

Methods that use arc plasmas and lasers *i.e.* laser ablation, have been explored due to their apparent scalability, making them an attractive proposition for industrial scale up[82]. The achievable particles sizes however, can be a significant limitation, with particle sizes <200 nm very hard to attain. Podgornyi *et al.* for example, have shown that particles of Fe_3C can be produced by introducing Fe atoms into an arc between two graphite electrodes in Ar gas[83]. Yet unfortunately the particles are highly polydisperse with many of the resulting particles appearing to have diameters >1 μm.

2.1.3.2 LASER ABLATION SYNTHESIS

Laser ablation of bulk iron submerged in various organic solvents, in which species react in the plasma plume created by the laser, has been shown to produce a range of magnetic iron based nanoparticles[84]. During this study Fe_3C was produced when using ethanol as the solvent. While this approach produced significantly smaller, higher quality particles than the kind of arc plasma technique previously described, it is important to note that polydispersity was still an issue. Another drawback, common amongst many type of syntheses, is that many of the organic solvents used also resulted in the formation of a carbon matrix around the product nanoparticles. Setting these drawbacks aside, however, the scalability of laser ablation makes these results important when considering transferability from the lab to industry[85].

2.1.3.3 CHEMICAL VAPOUR DEPOSITION

Chemical vapour deposition (CVD) has become a popular approach, as the use of vapour phases can lead to nanoscale particles with high degrees of monodispersity and high purities, with the primary drawback being the time required to perform the process to attain bulk quantities[86]. Lee *et al.*[87] have been able to bypass one of the major yield limiting factors in a type of CVD known as Chemical vapour condensation (CVC). Ordinarily, condensation of particles occurs on the wall of a liquid nitrogen chiller. Lee *et al.* were able to synthesis iron carbide nanoparticles by CVC without a liquid nitrogen chiller by heating a mixture of iron pentacarbonyl and methane at atmospheric pressure. In this process, temperature and pressure played a vital role in not only the composition of the particles, but also particle size and the core shell structure of the particles. At 650 °C the authors were able to passivate the

particles with a layer of Fe_3O_4 using an Ar/O_2 mixed atmosphere, whereas at 800 °C they were able to form a thin carbon shell in conditions that otherwise remained the same.

Work of this kind has even been extended into the nanostructuring of carbon. Iron, amongst other transition metals with sufficient carbon solubility, has been shown to have a high activity in graphite catalysis, particularly in the formation of carbon nanotubes [88, 89]. In fact, the formation of carbon nanotubes, using Fe_3C nanoparticles as a catalyst, has been observed directly via an in situ environmental transmission electron microscopy experiment in which Fe_3C nanoparticles are formed by CVD[90].

2.1.3.4 IONIC LIQUID SYNTHESIS

Another interesting approach is the use of ionic liquids; salts with poorly coordinated ions that also contain an organic component, resulting in them being liquids at <100 °C [91]. Here, the ionic liquids can act as stabilizers, solvents and a carbon source simultaneously. Although the use of ionic liquids in metal and metal oxide nanoparticle syntheses is a fairly well documented field, their use in iron carbide nanoparticle synthesis has only received attention in recent years, with the earliest report coming in 2013. Lartigue *et al.* were able to show that Fe_3C nanoparticles can indeed be synthesised by decomposing iron carbonyl complexes in imidazolium based ionic liquids[92].

Similar results can be achieved through sol gel syntheses that use biopolymer gels such as gelatin as a carbon source, solvent and stabilizer[18]. A key drawback with both ionic liquid and biopolymer based approaches is that although particles sizes of <20 nm are readily accessible,

the amount of amorphous carbon resulting from the need for reducing synthesis conditions means that the particles lack the dispersibility required for many applications.

2.1.3.5 TEMPLATING

Templating of Fe_3C with iron oxide particles produced through more straightforward means such as coprecipitation is another possibility. Schliehe *et al.* have demonstrated this with iron oxide particles with a variety of morphologies. The template particles were calcined alongside urea and agar, both of which act as a carbon source, with the added functions of the former helping control composition and latter helping protect against agglomeration. Post calcination, the Fe_3C particles retained the template morphologies to an extent, although the particles were not perfect replicas[93]. Due to the amount of carbon used in the synthesis a large amount of excess carbon is also present in the product. The authors were however able to remove this carbon through washing with H_2O_2, likely due to the reaction of H_2O_2 and carbon to give water and CO_2.

Taking the idea of using precursor template particles further, Prussian blue nano particles can be used as a template as well as a carbon source for the synthesis of iron carbide, in fact this has been performed multiple times in the literature[94, 95, 96]. Yet steps must still be taken to control morphology as high temperature decomposition of the particles will lead to agglomeration and sintering. Indeed, this is the main focus of this thesis.

2.1.4 PRUSSIAN BLUE

A large portion of this thesis will centre around the decomposition of Prussian blue nanoparticles to give Fe_3C nanoparticles. As Prussian blue itself is not a trivial compound this section will set out to briefly describe the material.

Although Prussian blue is never a truly soluble compound, it can be synthesised in two forms; soluble Prussian blue ($KFe[Fe(CN)_6].xH_2O$ where x = 1-5) (Fig. 2.3a) and insoluble Prussian blue ($Fe_4[Fe(CN)_6]_3.xH_2O$ where x = 14-16) (Fig. 2.3b). In the case of Prussian blue, the term solubility is not used in the normal sense, instead it refers to the ability of the compound to form a colloidal sol in water due to its nanoscale particle size. In terms of crystal structure, both forms of Prussian blue are described as being face centred cubic with the space group *Fm*-3*m*, consisting of low spin Fe^{2+} and high spin Fe^{3+} ions bridged by CN ligands. Thus, each Fe cation finds itself in an octahedral site with Fe^{3+} cations bound to the nitrogen end of the cyanide bridge with Fe^{2+} cations bound to the carbon end.

The insoluble and soluble structures differ in that for insoluble Prussian blue, in order to maintain an electrically neutral structure, a quarter of the iron hexacyanate sites are left vacant. These vacancies mean that Fe^{3+} cations are accessible and free to coordinate water molecules. Thus, the average composition of the Fe^{3+} coordination unit is $FeN_{4.5}O_{1.5}$. The soluble form on the other hand remains electrically neutral without these vacancies, instead incorporating interstitial monovalent cations such as K^+. A transition between these two structures can be observed by cyclic voltammetry in a potassium salt solution[97].

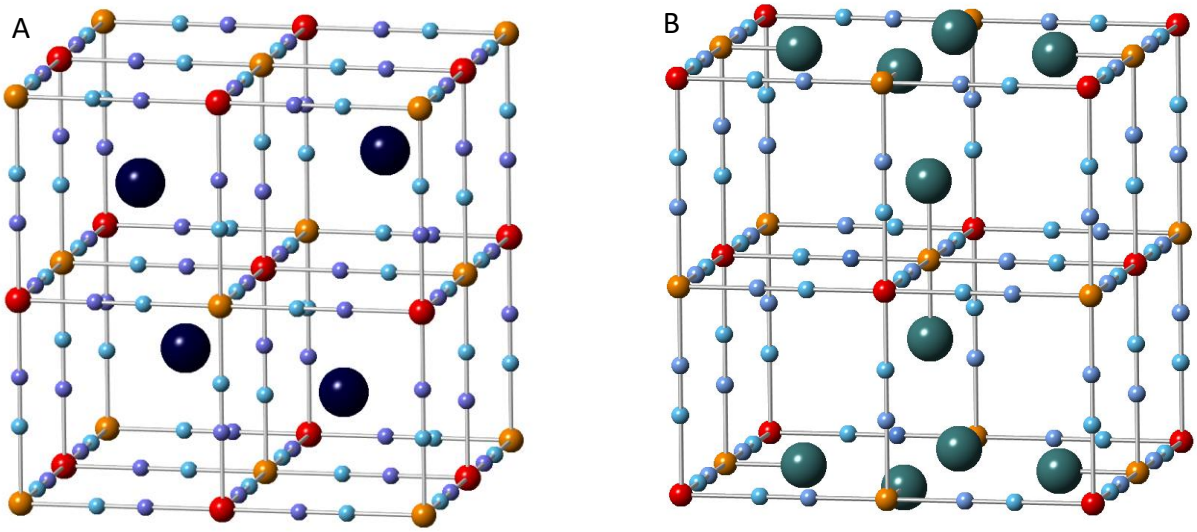

Figure 2.3 A - The crystal structure of Soluble Prussian blue - Orange = Fe^{2+}, Light blue = C, Violet = N, Red = Fe^{3+}, Dark blue = K^{+}, **B** - The crystal structure of Insoluble Prussian blue - Orange = Fe^{2+}, Light blue = C, Light blue = N, Red = Fe^{3+}, Green = H_2O.

The low solubility of both materials results in rapid precipitation and thus the formation of a large number of lattice defects, accounting for the variable hydration states of both compounds. Eqs. 2.1 and 2.2 detail the synthesis routes to both materials. It is important to note that identical products can be synthesised by simply exchanging $FeCl_2$ for $FeCl_3$ and $K_3[Fe(CN)_6]$ for $K_4[Fe(CN)_6$ for both of these reactions.

Potassium ferric (III) hexacyanoferrate (II) (colloidal soluble Prussian blue) $KFe[Fe(CN)_6]$

$FeCl_2 + K_3[Fe(CN)_6] \rightarrow KFe[Fe(CN)_6] + 3\ KCl$

Equation 2.1 Chemical formula detailing the synthesis of soluble Prussian blue

Ferric (III) hexacyanoferrate (II) (insoluble Prussian blue) $Fe_4[Fe(CN)_6]_3$

$4\ FeCl_2 + 3\ K_3[Fe(CN)_6]$----- > $Fe_4[Fe(CN)_6]_3 + 12\ KCl$

Equation 2.2 Chemical formula detailing the synthesis of insoluble Prussian blue.

While both forms of Prussian blue have compositions that are desirable in a precursor to iron carbides and nitrides, the nanoparticulate nature of the soluble form makes it particularly attractive for the purpose of this project *i.e.* as a template in the synthesis of Fe_3C nanoparticles.

2.2 CHAPTER SUMMARY

This chapter will examine the use of Prussian blue nanoparticles as templates in the synthesis of Fe_3C nanoparticles. Not only do the template particles possess the dimensions desirable in the Fe_3C product, they also contain all of the prerequisite elements necessary. Thus, the chapter will first look at the thermal decomposition of Prussian blue, moving into the incorporation of surfactants into this reaction. Anti-sintering cast materials will then be tested for chemical compatibility with this process. Then finally, methods for the removal of cast materials will be examined.

2.3 EXPERIMENTAL

2.3.1 MATERIALS

Table 2.3 List of materials used in chapter 2.

Chemical	Supplier	CAS number
Iron (II) chloride tetrahydrate ($FeCl_2.4H_2O$) 98%	Sigma Aldrich	13478-10-9
Potassium ferricyanide ($K_3Fe(CN)_6$) >99%	Sigma Aldrich	13746-66-2
Polyvinylpyrrolidone $(C_6H_9NO)_n$ >99%	Sigma Aldrich	9003-39-8
Magnesium Oxide (MgO) >99%	Acros Organics	1309-48-4
Calcium Oxide (CaO) >99%	Acros Organics	1305-78-8
Hydrochloric Acid (HCl) 36%	Sigma Aldrich	7647-01-0
Ethylenediaminetetraacetic acid ($C_{10}H_{16}N_2O_8$) >99%	Sigma Aldrich	60-00-4
Ethanol (CH_3CH_2OH) >99%	VWR	64-17-5
Acetone (CH_3COCH_3)>99%	VWR	67-64-1

2.3.2 SYNTHESIS OF SOLUBLE PRUSSIAN BLUE - $KFe[Fe(CN_6)]$

$FeCl_2.4H_2O$ (0.6 g) was added to distilled water (240 cm^3). $K_3[Fe(CN)_6]$ (0.99 g) was added to distilled water (60 cm^3). The $K_3[Fe(CN)_6]$ solution was then added to the $FeCl_2$ solution dropwise with vigorous stirring. The solution was then stirred for a further 30 mins. Acetone (300 cm^3) was then added to induce agglomeration of the Prussian blue particles. The particles were then washed three times with acetone via centrifugation. The final washed solid was then dried overnight at 70 °C.

2.3.3 PRUSSIAN BLUE SYNTHESIS WITH PVP

$FeCl_2.4H_2O$ (0.6 g) and a given mole fraction of polyvinylpyrrolidone were added to distilled water (240 cm^3). $K_3[Fe(CN)_6]$ (0.99 g) was added to of distilled water (60 cm^3). The $K_3[Fe(CN)_6]$ solution was then added to the $FeCl_2$ solution dropwise with vigorous stirring. The solution was then stirred for a further 30 mins. Acetone (300 cm^3) was then added to induce agglomeration of the Prussian blue Particles. The particles were then washed three times with acetone via centrifugation. The final washed solid was then dried overnight at 70 °C.

2.3.4 PRUSSIAN BLUE/CAST DRY MIXING

Prussian blue (1.0 g) was mixed with MgO/CaO at a given mass ratio. The powders were then ground together in a mortar and pestle until a homogeneous mixture was achieved.

2.3.5 PRUSSIAN BLUE FURNACE CALCINATION

The precursor material mixtures were placed in an alumina boat crucible and calcined under N_2 in a tube furnace at 5 °C min^{-1} to a given temperature, usually 800 °C for Fe_3C formation, unless otherwise stated.

2.3.6 PRUSSIAN BLUE MICROWAVE CALCINATION

The precursor material mixtures were placed in a quartz tube and heated with 700 W of microwave power in a modified domestic microwave oven. Full details of the microwave heating procedure can be found in the results and discussion section of chapter 2.

2.3.7 HCL WASHING

The Fe_3C/MgO/CaO mixtures were acid washed with either a 10% molar excess of HCl (0.1 M), relative to MgO/CaO content. These mixtures were then left to stir overnight. The HCl washed samples were then washed with distilled water and EtOH via centrifugation and subsequently left to dry at room temperature for 24 hours.

2.3.8 EDTA WASHING

The Fe_3C/MgO/CaO mixtures were acid washed with either a 7% or a 100% molar excess of EDTA (0.2 M), relative to MgO/CaO content. These mixtures were then left stir overnight. The EDTA washed samples were then washed with distilled water and EtOH via centrifugation and subsequently left to dry at room temperature for 24 hours.

2.3.9 POWDER X-RAY DIFFRACTION

Powder samples were prepared by first grinding them in a mortar and pestle to give homogeneous crystallite sizes and then either placing on a silicon wafer or a sample holder

sourced from Panalytical. In both cases, samples were flattened to give a uniform sample height.

All samples apart from the Prussian blue samples for which particle size was calculated using the Scherrer equation, in chapter 2, were analysed using a Panalytical Empyrean diffractometer in a flat plate reflection geometry. The diffractometer was not equipped with a monochromator, but a nickel filter was used to remove Kβ radiation. Thus, samples were analysed with Kα radiation. A Pixcel-2D position sensitive detector was used to collect data between the 2θ angle range 10-70 °. The majority of this data was simply used for phase identification by comparison with the ICDD PDF-4+ database using the EVA software.

Particles sizes were calculated using data collected on the D2 Phaser diffractometer using Co radiation and a Lynx eye scintillation counter. The Scherrer equation was used to calculate average crystalline domain sizes. Idealised spherical particles with no strain were assumed allowing the use of a shape factor (K) of 0.95. The wavelength (λ) produced by the cobalt source was 1.79 Å. The β term, which corresponds to the contribution from instrumental line broadening, given in radians, was calculated by finding the line of best fit for the full width at half maximum values of diffraction peaks produced by a corundum standard, plotted against 2θ values. θ in this equation is equal to the Bragg diffraction angle. The Scherrer equation is as follows; $\tau = K\lambda/\beta\cos\theta$

2.3.10 INFRA-RED SPECTROSCOPY

Scans were performed using a Perkin Elmer FT-IR spectrometer Spectrum Two for 2 minutes between 1000 cm^{-1} and 4000 cm^{-1}.

2.3.11 TRANSMISSION ELECTRON MICROSCOPY

Samples (≈ 100 mg) were dispersed in EtOH (≈ 1 mL) and sonicated for approximately 15 mins. One drop of the dispersed sample was then applied to a Cu TEM grid with a carbon coating. All TEM images were recorded using a JEOL 2100 TEM with a tungsten filament and a charge coupled device (CCD) detector.

2.3.12 DYNAMIC LIGHT SCATTERING

Measurements were taken at 25 °C using a Malvern Nano-Zetasizer ZS with a fixed scattering angle of 173 °. Samples were prepared by sonicating 0.1 g l^{-1} PVP coated Prussian blue for 1 hour. The samples were then filtered through a 0.2 µm filter to remove any dust or other contaminants. Prior to collecting data each sample was given a 120 second equilibration time. All measurements were made in triplicate and subsequently averaged.

2.3.13 FLAME ATOMIC ABSORPTION SPECTROSCOPY

Samples were analysed on a Perkin Elmer AAnalyst 300 FAAS using acetylene gas and a hollow cathode lamp suitable for magnesium detection (285 nm max absorption wavelength). A

linear calibration was produced by analysing standard solutions prepared at concentrations of 0.2, 0.5, 1.0, 1.5 and 2.0 ppm. Sample solutions were prepared by dissolution in HNO_3. Resulting solutions were then passed through a microfilter (0.2 μm) and diluted with distilled water.

2.4 RESULTS AND DISCUSSION

2.4.1 THE DECOMPOSITION OF PRUSSIAN BLUE

The literature contains reports looking at the decomposition of Prussian blue in both oxidative[98] and inert atmospheres[94]. In the former study, relatively low temperatures of approximately 300 °C were used to give iron oxide decomposition products, whereas the latter gave Fe_3C and Fe^0 at significantly higher temperatures of up to 1000 °C. In this thesis, Prussian blue decomposition under inert conditions will be performed in various experiments in the hope of producing Fe_3C nanoparticles while exerting control over their morphology. For this reason, this section will look at the decomposition profile of Prussian blue under N_2 and establish whether Fe_3C can be reliably produced.

2.4.1.1 FURNACE DECOMPOSITION OF PRUSSIAN BLUE

A study was carried out in which 1 g samples of Prussian blue were decomposed under nitrogen at set temperature intervals ranging from 300 °C to 800 °C, using ramp rates of 5 °C min^{-1} and a hold time of 1 minute.

PXRD performed on the samples (Fig. 2.4) revealed that at 400 °C, while a Prussian blue phase remains, a phase with a diffraction pattern matching that of α-carbon nitride has formed. By 500 °C total decomposition of Prussian blue and the α-carbon nitride-like phase has occurred and the first occurrence of an iron carbide phase is visible (Fe_2C). Fe_2C can be seen to persist at 600 °C, as well as a phase that partially matches the diffraction pattern of iron cyanamide. At 650 °C Fe_2C is still present in the sample, with the appearance of a second carbide phase

(Fe_7C_3) now apparent. The presence of these two phases is in accordance with the results of Aparicio *et al.* who observe both phases by PXRD in a sample prepared under Ar at 670 °C [94].

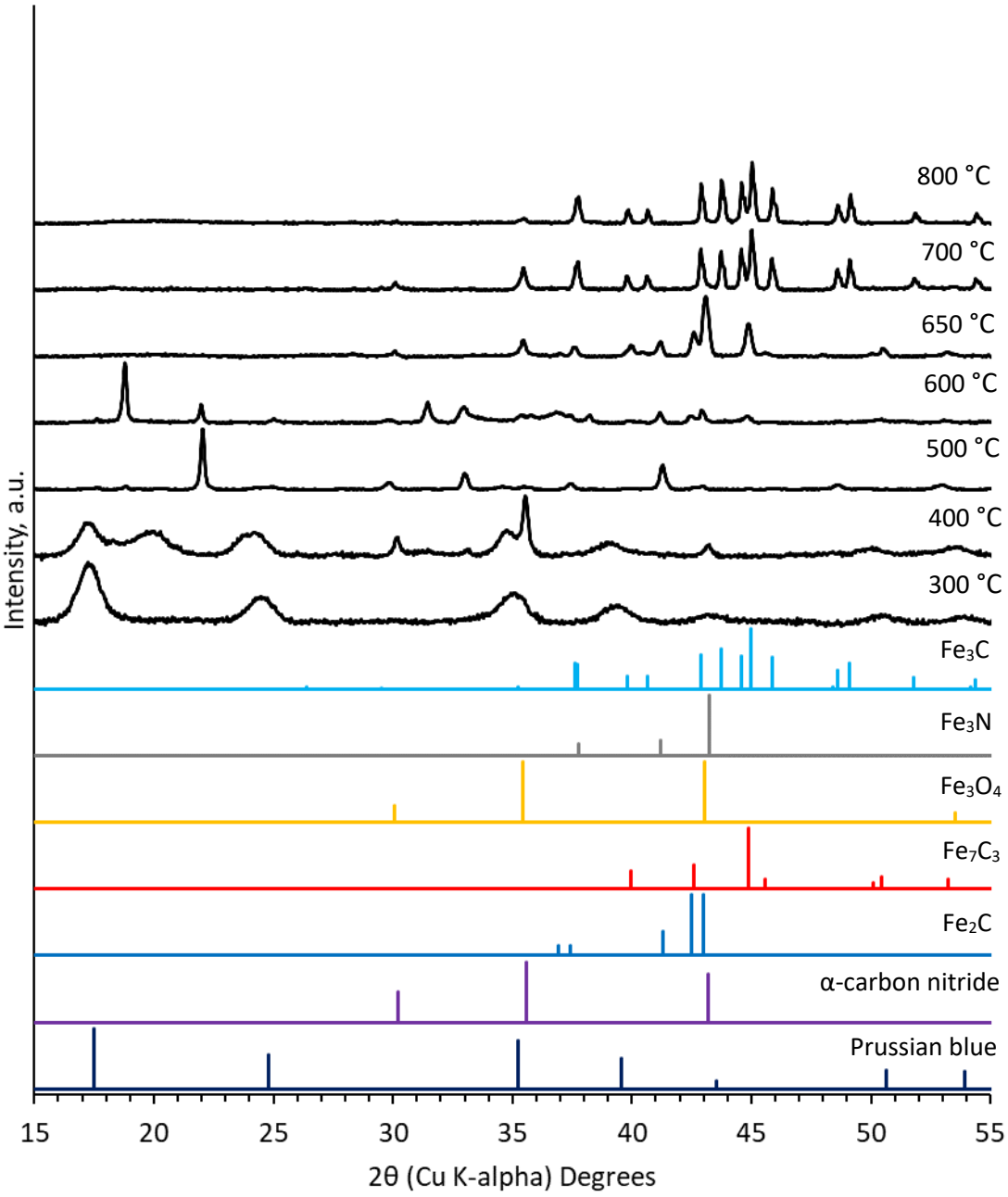

Figure 2.4 PXRD patterns recorded for the decomposition of Prussian blue under a nitrogen atmosphere, in a tube furnace, performed at various temperatures.

Interestingly, the sample prepared at 650 °C also appears to contain Fe_3N and Fe_3O_4 prior to the formation of Fe_3C. The appearance of these phases match observations made by Schnepp *et al.*[99] in which the authors synthesised Fe_3C via a biopolymer sol gel route. In this work, the authors state a mechanism of Fe_3C formation that proceeds through an oxide phase to a nitride phase into a carbide phase. Thus, a similar sequence of phase transitions may be occurring in Prussian blue decomposition.

Fe_3C can then be seen to form at 700 °C, a temperature that is significantly lower than the 1000 °C observed by Aparicio *et al.* Fe_3C persists at 800 °C. Thus, Fe_3C should readily form in the 700-800 °C temperature range. Fig. 2.5 shows TEM images recorded for the sample of Fe_3C prepared at 800 °C. The images help illustrate the extent to which these particles undergo sintering during the calcination process, producing a polydisperse sample. Mitigating these effects is the overarching aim of work appearing later in this thesis. However, the average crystal domain diameters calculated using the PXRD data in Fig. 2.4 and the particles sizes calculated using TEM images in Fig. 2.5, displayed in table 2.4, are still <100 nm. This data demonstrates the potential of Prussian blue as a nanoscale template.

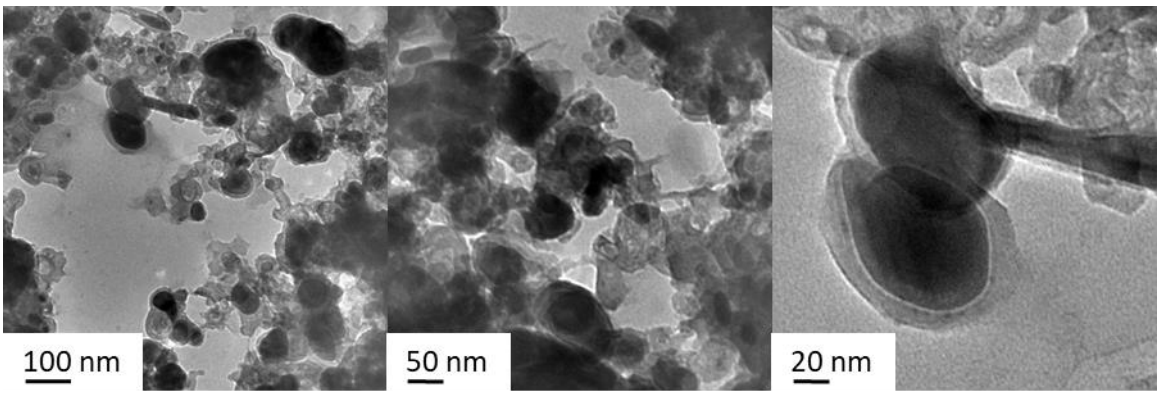

Figure 2.5 TEM images of sintered Fe_3C nanoparticles prepared by calcining Prussian blue at 800 °C under a N_2 atmosphere.

Table 2.4 Particle size data for Fe_3C nanoparticles synthesised by decomposing Prussian blue.

Calcination Temperature °C	2θ values used for Scherrer analysis (Fig. 2.4)	Average crystalline domain size – Scherrer (nm)	Average particle diameter - TEM (nm) (Fig. 2.5)
800	37.965, 40.029, 40.864, 43.104, 43.965, 46.090	46	54
700	37.925, 40.002, 40.822, 43.074, 43.935, 46.053	47	-

2.4.1.2 MICROWAVE DECOMPOSITION OF PRUSSIAN BLUE

As has been stressed, a key objective of this work is to retain the nanoscale dimensions of the Prussian blue precursor particles. Thus, heating the sample as quickly as possible, thereby minimising the time available for the sintering of particles, was a key avenue to explore. Most conventional furnaces are limited to heating rates of 5-10 °C min^{-1} but there are alternatives, one of which is the use of microwave heating. Microwave heating is becoming more commonplace in solid state synthesis[100] due to its rapid heating rates and improved energy efficiency compared to traditional heating techniques. The use of a specialized microwave reactor was prohibited by cost in this work. However, a modified domestic microwave oven was used in order to test the concept.

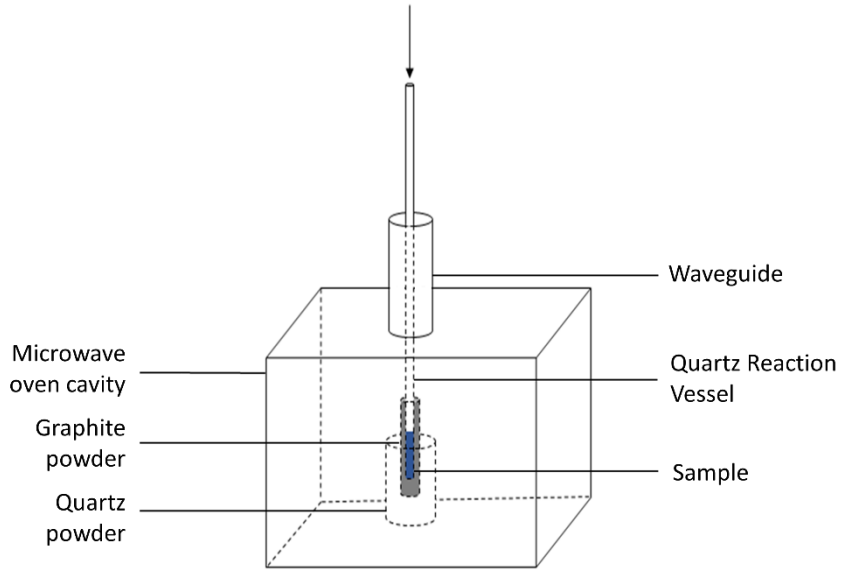

Figure 2.6 Schematic of a modified domestic microwave reactor (700 W).

In our set up (Fig. 2.6), graphite, which is known to couple strongly with microwaves, was used as a heat source to affect the decomposition of the sample. In other words, a graphite containing vessel was placed in the standing wave of a domestic microwave oven into which a quartz sample tube could be placed. A waveguide, which also acted an access point for gas flow was used to flow N_2 over the sample in order to achieve inert reaction conditions. Upon heating of the graphite, heat was rapidly transferred to the sample tube, heating the sample. The major drawback to this approach was the inability to control temperature. However, by applying 700 W of microwave power it was possible to decompose Prussian blue to give an Fe_3C product.

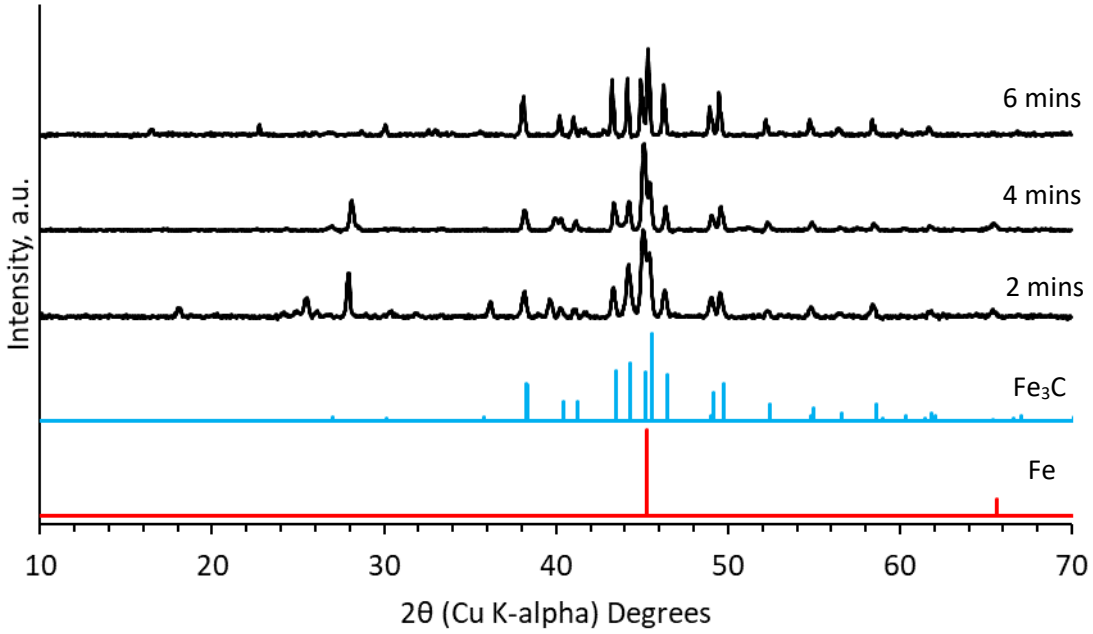

Figure 2.7 PXRD patterns recorded for the decomposition of PB under a nitrogen atmosphere, in a modified microwave oven, performed over various time durations.

Table 2.5 Particle size data for Fe_3C particles synthesised by decomposing Prussian blue in a microwave reactor.

Calcination Time (mins)	2θ values used for Scherrer analysis (Fig. 2.7)	Average crystalline domain size – Scherrer (nm)
2	38.163, 40.261, 41.076, 43.336, 44.200, 46.319	33
4	38.181, 40.299, 41.135, 43.377, 44.239, 46.250	39
6	37.704, 37.780, 40.616, 42.869, 43.727, 45.850	44

While electron microscopy has not been performed on the Fe_3C samples produced by microwave calcination, studies have been performed on a similar system. When conventional furnace calcination was replaced with our microwave heating technique in an Fe/gelatin sol gel synthesis, analysis by TEM showed little difference in particles size when comparing the microwave synthesis to a convention furnace synthesis[101]. Scherrer analysis of the (Fig. 2.7) PXRD data, displayed in table 2.5, suggests average crystalline domain sizes of approximately 40 nm, with the sizes trending upwards as synthesis time is increased. This suggests that a faster synthesis provides less time for sintering and thus greater template size preservation. Furthermore, the speed of the process, which can be carried out in just 2 minutes (Fig. 2.7), provides a significant improvement over a multiple hour furnace calcination process. Thus, this is an area that is ripe for further investigation.

2.4.2 INCLUSION OF A SURFACTANT IN PRUSSIAN BLUE SYNTHESIS.

The potential for controlling the size and morphology of the template particles was and still is an enticing one. The major benefit of this is the possibility of producing a process that can access a range of tunable particles sizes. This could then lead to systematic studies on how particle sizes affect the catalytic and magnetic properties of Fe_3C. The literature contains various studies aimed at finding methods for the controlled synthesis of Prussian blue nanoparticles of various sizes, ranging from the use of microemulisions[102] to the use of simple co-precipitation reactions[103].

Hornok *et al.* have shown that polyvinylpyrrolidione (PVP) can be used to produce Prussian blue particle diameters as low as 20 nm[54], whereas Kong *et al.* have produced similar results

looking at Cu/Ni/Cu containing analogues of Prussian blue[104]. PVP is also attractive from a synthetic standpoint as it is relatively environmentally friendly substance, especially when compared to more commonly used surfactants such as cetyl trimethylammonium bromide (CTAB). Functionalising the surface of the particles with PVP has also proved advantageous in this work when dispersing the particles in solvents other than water, a point that will become more important in work described later in this thesis.

Still, while the use of PVP seemed like a straightforward decision, an important caveat was that having PVP present during the decomposition process must not adversely affect the formation of the Fe_3C product. For example, adding a long chain polymer like PVP means significantly increasing the carbon content of the system, which under an inert atmosphere and high temperatures would likely result in a significantly more reducing atmosphere. The possibility of producing Fe^0 in place of Fe_3C therefore starts to become more likely. It also raised the possibility of producing a carbon matrix, which runs counter to the aim of producing discrete, dispersible particles.

2.4.2.1 FUNCTIONALISING PRUSSIAN BLUE WITH PVP

The next important step was to investigate the decomposition of Prussian blue particles with various PVP loadings. Powder X-ray diffraction (PXRD) analysis was then used to spot any important changes in the composition of the product.

Polyvinylpyrrolidone (40000 g mol^{-1}) was incorporated into the synthesis of Prussian blue at varying PVP : Fe^{2+} molar ratios, in order to see if using the polymer had a measurable effect. All PVP : Fe^{2+} molar ratios are based on the molecular weight of the PVP monomer.

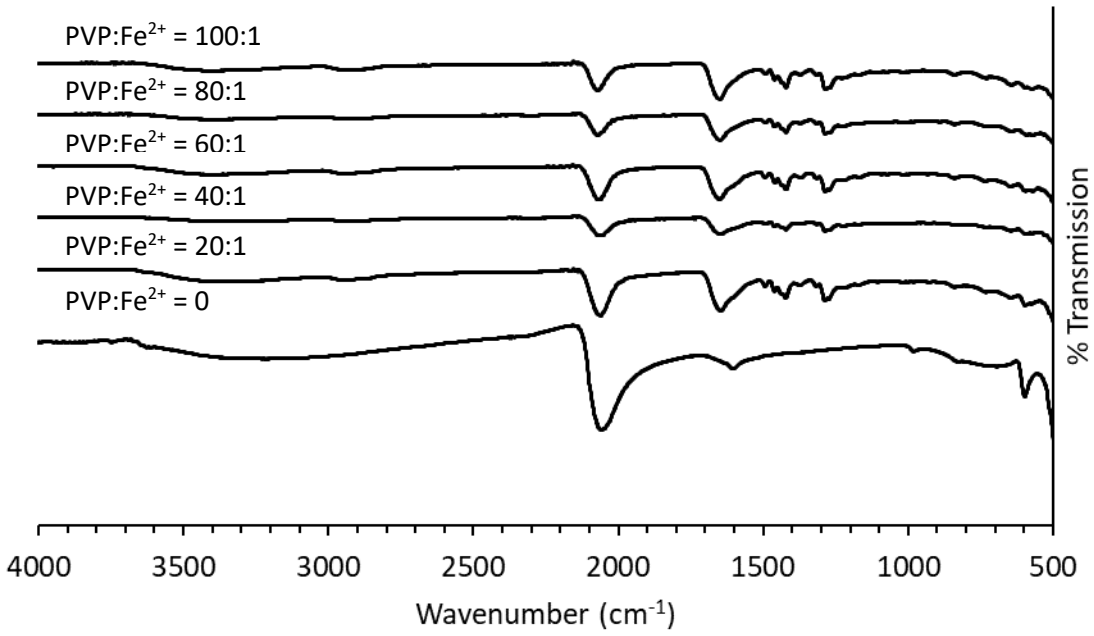

Figure 2.8 IR spectra recorded for Prussian blue with PVP loadings at various PVP : $FeCl_2$ synthesis molar ratios.

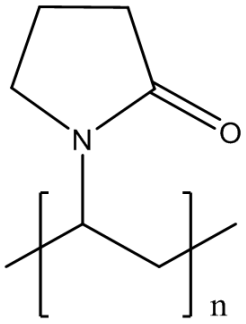

Figure 2.9 The molecular structure of the PVP monomer.

As an initial step, IR spectra were recorded for the samples in order to confirm that the particle surfaces were in fact coated with PVP. Prior to analysis the samples were washed several times with distilled water and ethanol, removing any excess PVP. The relevant IR spectra and the

molecular structure of the PVP monomer can be seen in Figs. 2.8 and 2.9 respectively. Key features can be seen at the CN stretching frequency of approximately 2100 cm^{-1}, which can be attributed to the carbon – nitrogen triple bonds found in Prussian blue, and the carbonyl stretching frequency of 1600 cm^{-1}, which can be attributed to the carbonyl group found in PVP. The presence of a carbonyl stretching motion suggests that PVP is in fact present in the relevant samples. The carbonyl peak also seems to be growing in intensity relative to the CN peak as the quantity of PVP is increased suggesting a higher PVP loading.

PXRD patterns recorded for these samples can be seen in figure 2.10. Scherrer analysis performed on this data, in which instrumental line broadening has been accounted for using a corundum standard, can be seen in Table 2.6. The data suggests that the average crystalline domain size of particles synthesised using PVP : Fe^{2+} molar ratios ranging from 0:1 – 100:1, all fall below 10 nm.

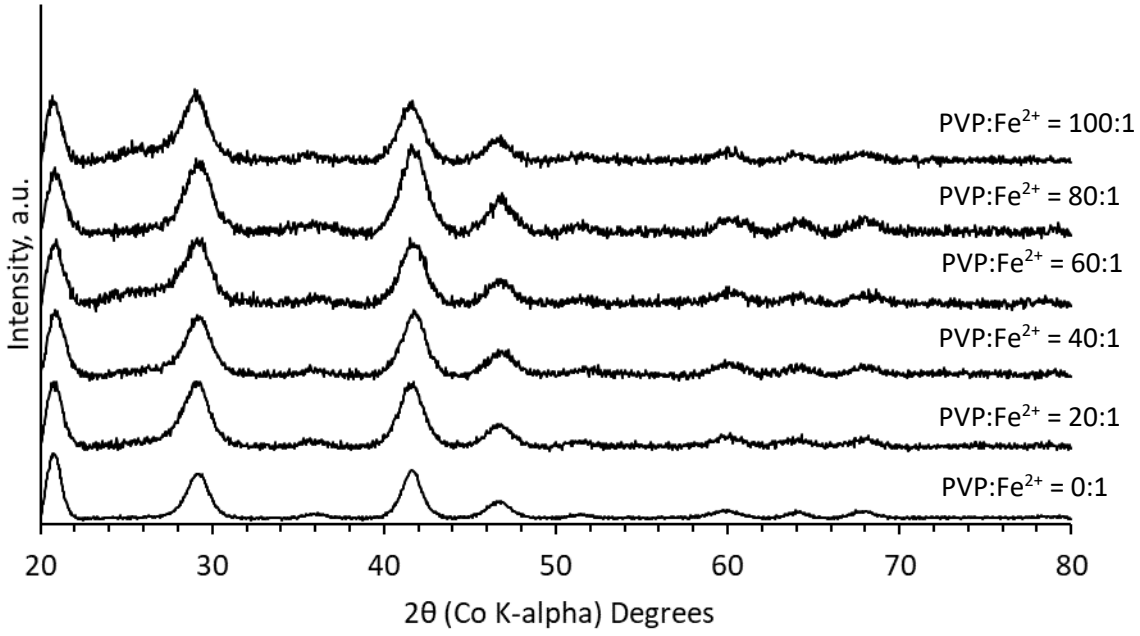

Figure 2.10 PXRD Patterns recorded for PB with various PVP loadings at various $FeCl_2$: PVP synthesis molar ratios.

Table 2.6 Particle size data for Prussian blue with various PVP loadings.

PVP : Fe^{2+} molar ratio - based on monomer mass	2θ values used for Scherrer analysis (Fig. 2.10)	Average crystalline domain size – Scherrer (nm)	Average particle diameter - DLS (nm)	Polydispersity Index - DLS
0:1	29.810, 36.140, 41.627, 46.684	8	70	0.350
20:1	29.107, 35.713, 41.586, 46.668	8	70	0.575
40:1	29.231, 35.844, 41.735, 46.782	7	60	0.602
60:1	29.204, 35.720, 41.770, 46.777	7	60	0.505
80:1	29.003, 35.559, 41.562, 46.643	8	100	0.542
100:1	29.165, 35.965, 41.687, 46.802	9	40	0.370

However, dynamic light scattering data recorded for the samples (table 2.6) suggests that the nanoparticles have agglomerated into highly polydisperse particles. Unfortunately, this also means that the diameter measurements produced using DLS are likely to have a significant margin of error associated with them. DLS can only give a value for the diameter of the particle aggregates not individual crystallites. Likewise, a significant source of error is likely to be the fact that the particles have a varying amount of a long chain polymer (PVP) bound to their surface. DLS measures the hydrodynamic radius of particles in a solvent and thus any structures at the particles surface will be included in the measurement. It is also possible that the presence of PVP affects the diffusion speed of the particles. Again, this would introduce error into any inference of particle size. It is also important to consider the fact that a sphere is the only three-dimensional shape that can be truly described by a single figure. Non-spherical particles therefore introduce another source of error. However, when viewed in

conjunction with the results of the Scherrer analysis it seems the synthesis of particles with diameters of 100 nm or less is likely.

2.4.2.2 DECOMPOSITION OF PVP FUNCTIONALISED PRUSSIAN BLUE IN A FURNACE

Fig. 2.11 shows a selection of PXRD patterns recorded for Prussian blue samples synthesised with PVP : Fe^{2+} molar ratios ranging from 0:1 to 100:1, that have been decomposed under a nitrogen atmosphere at 5 °C min^{-1} to 800 °C and held there for 1 min. The patterns show that in each case Fe_3C was successfully formed.

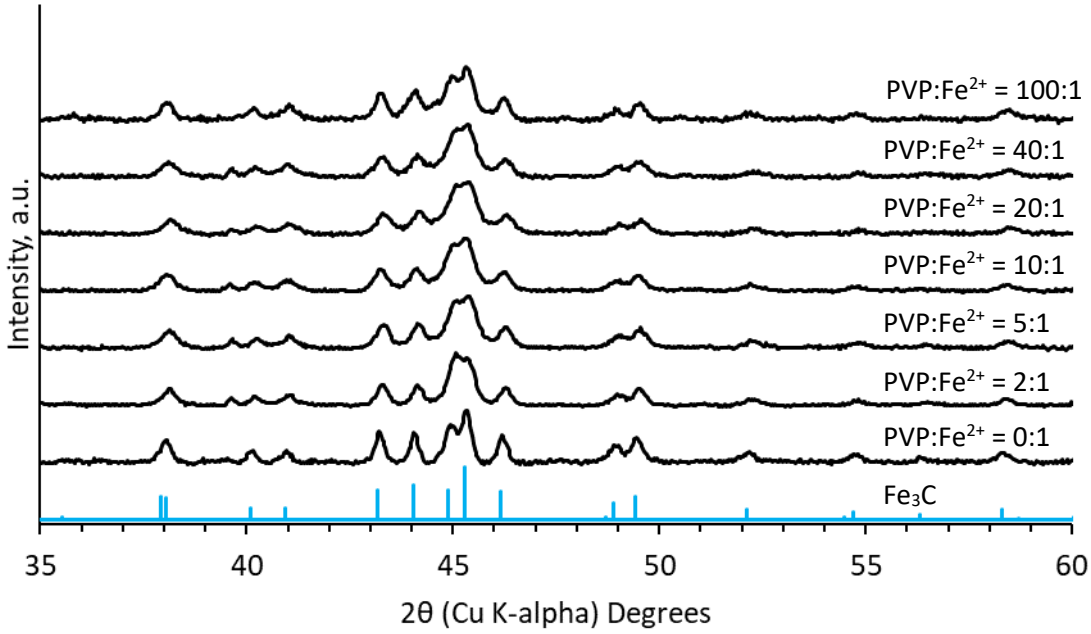

Figure 2.11 PXRD patterns recorded for Fe_3C produced by the decomposition of PB with various PVP loadings in a tube furnace.

The presence of PVP appears to lead to peak broadening relative to plain Prussian blue decomposed under the same conditions. This suggests that calcining Prussian blue particles

with PVP functionalised surfaces either provides smaller Prussian blue template particles or it helps limit sintering, or more likely there is a combination of the two effects occurring.

Table 2.7 Particle size data for Fe_3C particles calcined from Prussian blue with various loading of PVP.

PVP : Fe^{2+} molar ratio - based on monomer mass	**2θ values used for Scherrer analysis (Fig. 2.11)**	**Average Fe_3C crystalline domain size – Scherrer (nm)**	**Corresponding Prussian blue average crystalline domain size - Scherrer (nm) (Table 2.4)**	**Corresponding Prussian blue average particle diameter - DLS (nm) (Table 2.4)**
0:1	38.053, 40.142, 40.964, 43.219, 44.072, 46.198	38	8	70
2:1	38.144, 40.192, 41.063, 43.300, 44.137, 44.275	32	-	
5:1	38.145, 40.259, 41.035, 43.325, 44.161, 46.288	28	-	
10:1	38.085, 40.203, 40.974, 43.260, 44.111, 46.240	25	-	
20:1	38.177, 40.243, 41.045, 43.302, 44.180, 46.299	25	8	70
40:1	38.120, 40.212, 40.990, 43.290, 44.135, 46.277	24	7	60
100:1	38.083, 40.185, 41.029, 43.252, 44.084, 46.230	27	9	40

The crystal domain size data presented in table 2.7 does appear to show a reduction in the average size of Fe_3C crystallites as the Prussian blue PVP loading is increased. However, increasing the loading appears to produce diminishing returns.

Another important feature of the PXRD patterns is the lack of peaks associated with graphitic carbon at 2θ values of approximately 26.4°, 42.8° and 44.6°. It seemed likely therefore, that the extra carbon provided by PVP was being converted into a disordered carbon matrix, something that needed to be avoided if the particles were to be dispersible. Of course, it was also possible that graphite was present in such small quantities that it was not visible above the background noise in the diffraction pattern.

The carbon matrix can be seen in TEM micrographs recorded for the calcined PVP : Fe^{2+} = 10:1 and 20:1 samples (Fig. 2.12A and 2.12B.). They show what appear to be Fe_3C nanoparticles as small as 20 nm, embedded a larger piece of amorphous carbon. The nano-scale dimensions of the particles are in good agreement with the broad appearance of the Fe_3C X-ray diffraction peaks.

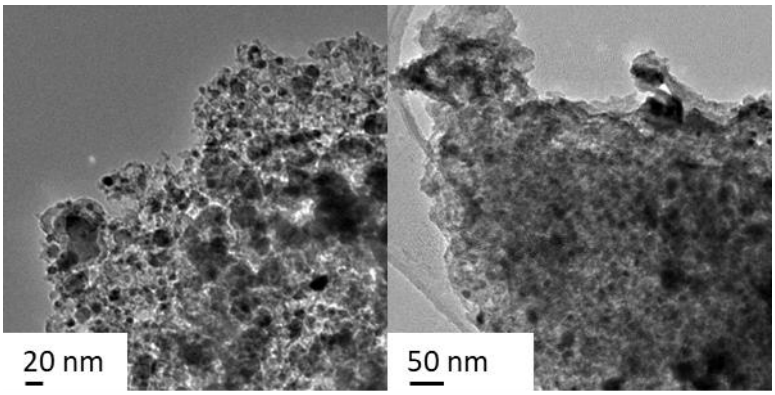

Figure 2.12 TEM micrographs showing Fe_3C nanoparticles embedded in amorphous carbon, produced by decomposing Prussian blue loaded with PVP (40000 g mol^{-1}), at **A** – PVP : Fe^{2+} = 10:1 molar ratio and **B** – PVP : Fe^{2+} = 20:1 molar ratio.

The important point here in relation to the aim of this thesis is that although the abundance of carbon in this system appeared to help prevent sintering during calcination, the fact that the Fe_3C nanoparticles were bound in an extended carbon matrix presented a challenge in the synthesis of discrete particles. This illustrates the need for reducing the carbon content of the precursor material.

Reduction of carbon content was attempted using 2 strategies. The first was to use PVP with an average molecular weight of 10000 g mol^{-1}, rather than the 40000 g mol^{-1} PVP used up to this point. The second strategy was to simply use the minimum amount of PVP possible.

The broad PXRD peaks shown in Fig. 2.11 for the sample of calcined Prussian blue with a PVP : Fe^{2+} molar ratio of 2:1 suggests that low PVP concentrations are still effective at reducing particle size. So, with the two aforementioned strategies in mind, an approximate calculation was carried out in order to calculate how much 10000 g mol^{-1} PVP would be required in order to form a monolayer on a sample of Prussian blue with an average particle size of 20 nm. The area occupied by each polymer chain of PVP was assumed to be the same as the hydrodynamic radii found experimentally by Armstrong *et al.*[105] of 2.16 nm for 10000 g mol^{-1} PVP. The result was a PVP : Fe^{2+} molar ratio of approximately 1:1. Fig. 2.13 shows TEM images of these particles measuring approximately 100-200 nm in diameter, a size that was determined to be suitable for template particles for the purposes of this work. This sample was then calcined to produced phase pure Fe_3C (Fig. 2.14).

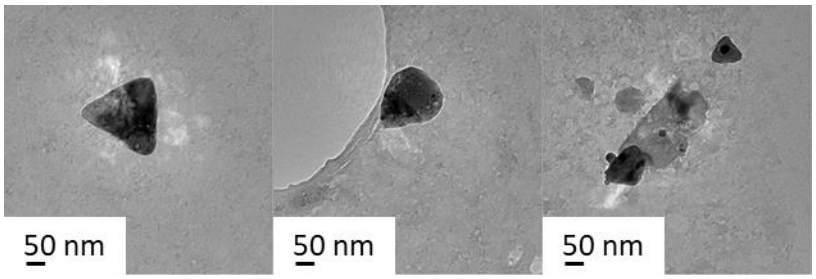

Figure 2.13 TEM images of Prussian blue nanoparticles synthesised using a PVP:Fe^{2+} molar ratio of 1:1.

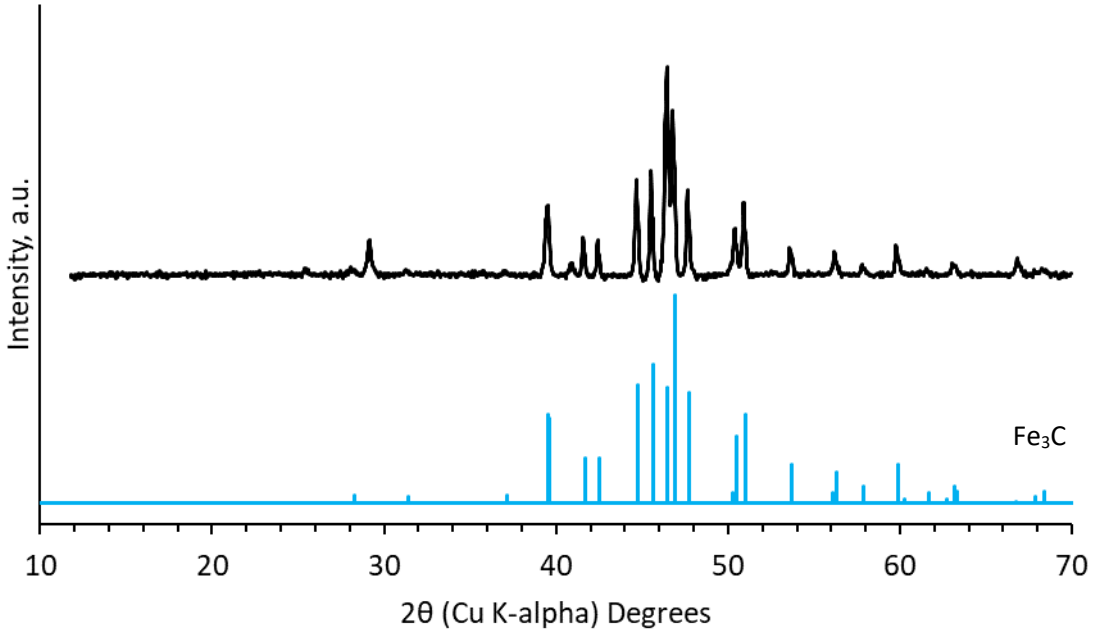

Figure 2.14 PXRD pattern recorded for Fe_3C prepared by calcining a sample of Prussian blue with an approximate monolayer of PVP at 800 °C.

2.4.2.3 DECOMPOSITION OF PVP FUNCTIONALISED PRUSSIAN BLUE IN A MICROWAVE

Following the rapid rate of decomposition of Prussian blue to Fe_3C observed in our modified microwave oven it seemed logical to then perform a similar experiment looking at the decomposition of PVP coated Prussian blue using microwave assisted heating. With the

minimisation of carbon contributed by PVP deemed to be a priority, the work was carried out using low PVP concentrations. The resulting PXRD patterns can be seen in Fig. 2.15. Phase pure Fe_3C was produced in each case with the exception of a PVP : Fe^{2+} molar ratio of 0.5 : 1, in which a significant amount of Fe^0 is present.

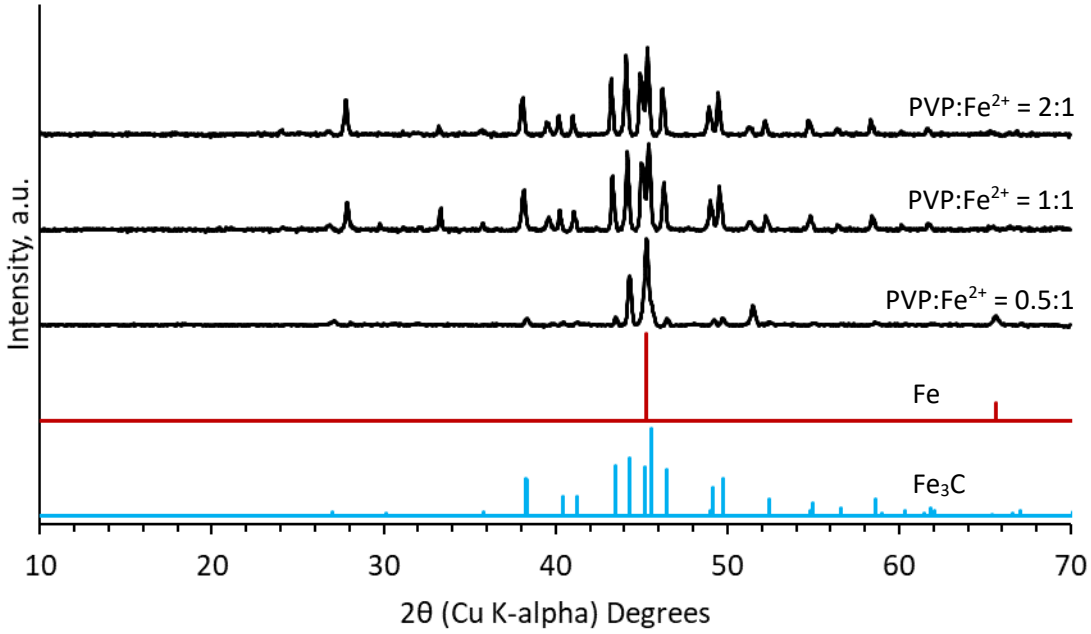

Figure 2.15 PXRD patterns recorded for Fe_3C produced by the decomposition of PB with various PVP loadings in a microwave at 700 W for 4 mins.

2.4.3 IDENTIFYING A COMPATIBLE CAST MATERIAL

While the previous section has shown the surfactant PVP to be chemically compatible with the formation of Fe_3C, this section will now examine the compatibility of potential cast materials. When selecting a material to be used as a potential cast there were several

immediate criteria that the material needed to meet. The first was that the material would need to perform well at its intended function, that is; preventing the sintering of the Prussian blue template particles during their thermal decomposition process. This requirement was deemed to be related more to the morphology of the material and therefore not a major consideration at this early stage. The second requirement was that the material would need to be thermally stable at temperatures of at least 800 °C. The third was that there must be a means of removing the material with relative ease after the calcination process used to decompose our template particles, and finally, possibly the most important requirement at this stage, was that the material must not interfere with the decomposition of Prussian blue thereby preventing the formation of Fe_3C.

Both MgO and CaO fit most of these criteria. Both are thermally stable with melting points of 3250 °C[106] and 2531 °C[107] respectively. Both are soluble in dilute acid, providing a means for their removal post synthesis. Also of importance is their abundance, making them economically viable in industrially scalable processes. Thus, this section will examine their chemical compatibility with the Prussian blue decomposition process. Also examined is the unsuccessful use of $Mg(OH)_2$.

2.4.3.1 FURNACE DECOMPOSITION WITH $Mg(OH)_2$

Both soluble Prussian blue and $Mg(OH)_2$ can be peptized to give a stable colloidal dispersion in water. This gave rise to the idea that by combining colloidal sols of the two materials and drying, efficient mixing of template particles and cast particles to give a homogenous dispersion could be achieved. It was then hoped that by calcining this dried mixture the

Prussian blue particles would be physically inhibited from sintering. Thus, colloidal mixtures at various mass ratios of $Mg(OH)_2$: Prussian blue were prepared and analysed.

Unfortunately, the alkaline pH of the $Mg(OH)_2$ sol resulted in the chemical reaction of the Prussian blue particles, forming a brown solution, most likely iron hydroxide. Once dried, the mixtures were calcined at 800 °C then analysed by PXRD (Fig. 2.16). The resulting materials contained MgO; a product of the decomposition of $Mg(OH)_2$, and Fe_3O_4 rather than the desired Fe_3C. Considering that the process was performed under anaerobic conditions, it is possible that Fe_3O_4 was formed through the Schikorr reaction, shown in Eq. 2.3.

$$3Fe(OH)_2 \rightarrow Fe_3O_4 + H_2 + 2H_2O$$

Equation 2.3 The Schikorr reaction for the formation of magnetite from ferrous hydroxide[108].

Similar results, i.e. the formation of Fe_3O_4, were obtained when a dry mixture of Prussian blue and $Mg(OH)_2$ were ground in a mortar and pestle then calcined. In this case, it was thought that the formation of an oxide was caused by the release of water during the decomposition of $Mg(OH)_2$, occurring at approximately 330 °C. For these reasons $Mg(OH)_2$ was deemed incompatible with Fe_3C formation and its use was not examined any further.

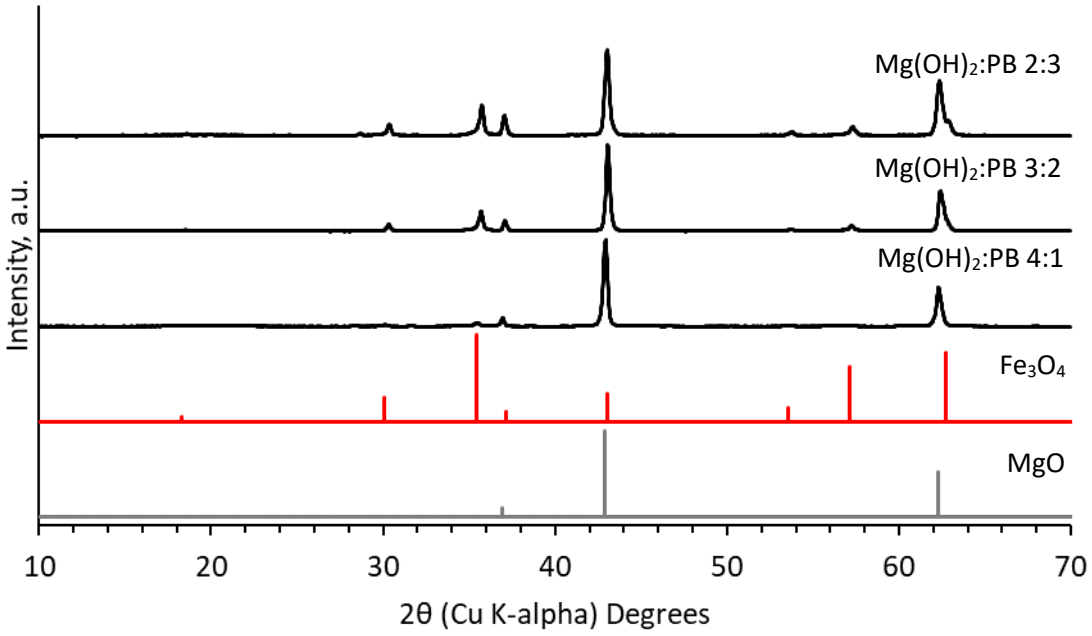

Figure 2.16 PXRD showing the decomposition products resulting from the calcination of dried mixtures of $Mg(OH)_2$: Prussian blue colloidal suspensions.

2.4.3.2 FURNACE DECOMPOSITION WITH MgO AND CaO

Following the issues experienced with $Mg(OH)_2$ it was decided that the more thermally stable oxides of magnesium and calcium would be examined. Samples of Prussian blue were mixed with MgO powder at a 1:1 mass ratio and ground in a mortar and pestle. They were then calcined at 100 °C intervals between 300 °C and 800 °C and analysed by PXRD, along with a non-calcined control sample for comparison, to ensure that Fe_3C could be synthesised. Fig. 2.17 shows the complete data set, with Fig. 2.18 showing the same data set between a 2θ range of 43.5 º - 46.5 º. This allows for a closer inspection of key peaks pertaining to Fe_3C, peaks which are hard to resolve in Fig. 2.17 due to the high relative intensity of the MgO diffraction peaks. These data show that Fe_3C formation begins at approximately 700 °C - 800

°C. This is a similar on-set point to that of Prussian blue in the absence of a cast material. This was a strong indication that the use of MgO was a possibility worth exploring.

A similar experiment was performed with CaO in place of MgO with analogous results. The full data set (Fig. 2.19) again shows the formation of Fe_3C at 700 °C - 800 °C, shown more clearly in Fig. 2.20, which shows the 43.5 ° - 46.5 ° 2θ range. However, an interesting feature of the full data set (Fig. 2.19) is the presence of a $CaCO_3$ phase, which can be seen more clearly in the diffraction pattern produced by the sample calcined at 600 °C shown in Fig. 2.21.

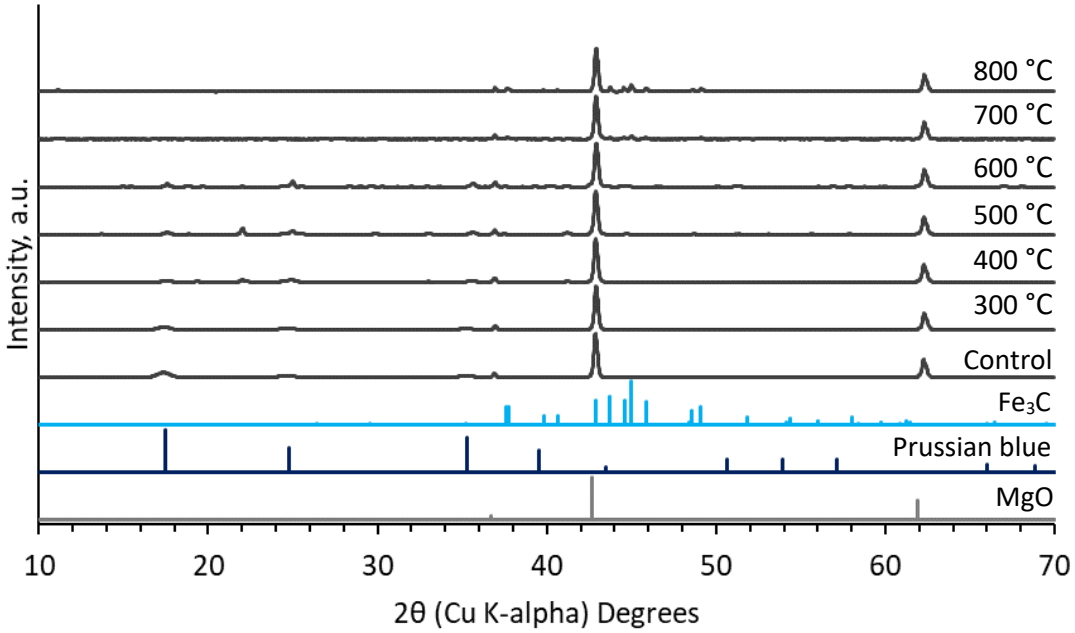

Figure 2.17 PXRD showing the decomposition of Prussian blue alongside magnesium oxide powder at 100 °C intervals.

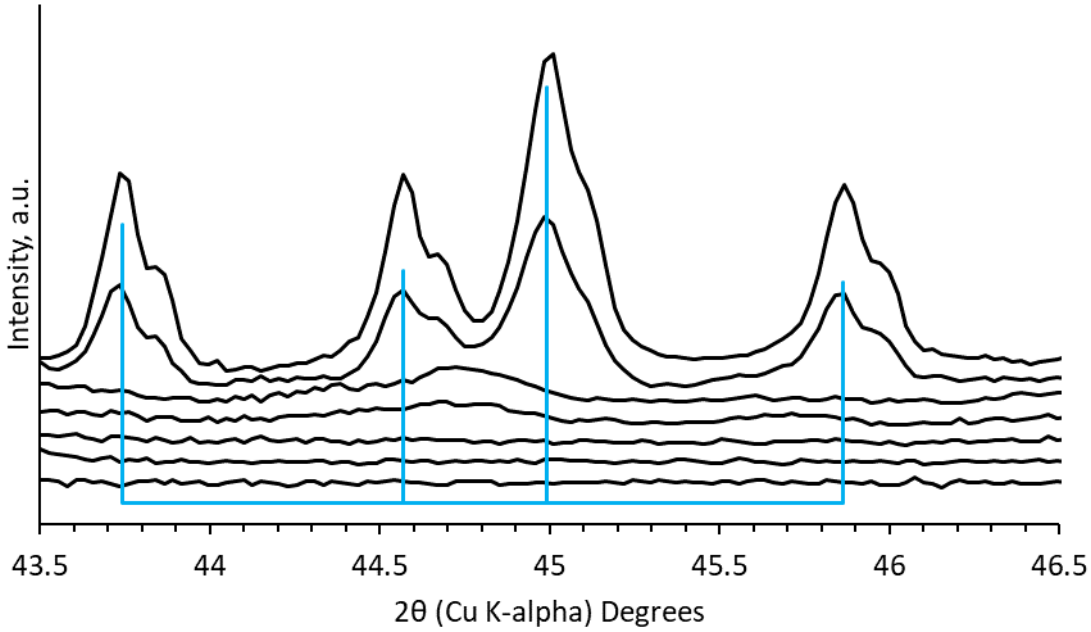

Figure 2.18 PXRD showing the decomposition of Prussian blue with magnesium oxide powder at 100 °C intervals. Top to Bottom – 800 °C, 700 °C, 600 °C, 500 °C, 400 °C, 300 °C, room temperature, Fe_3C

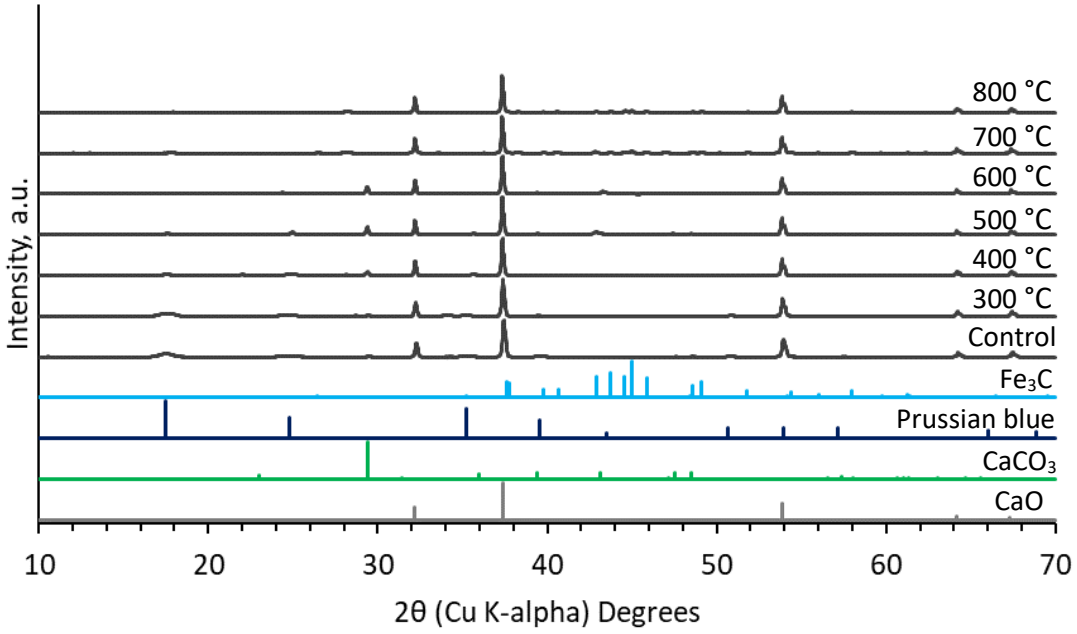

Figure 2.19 PXRD showing the decomposition of Prussian blue alongside calcium oxide powder at 100 °C intervals.

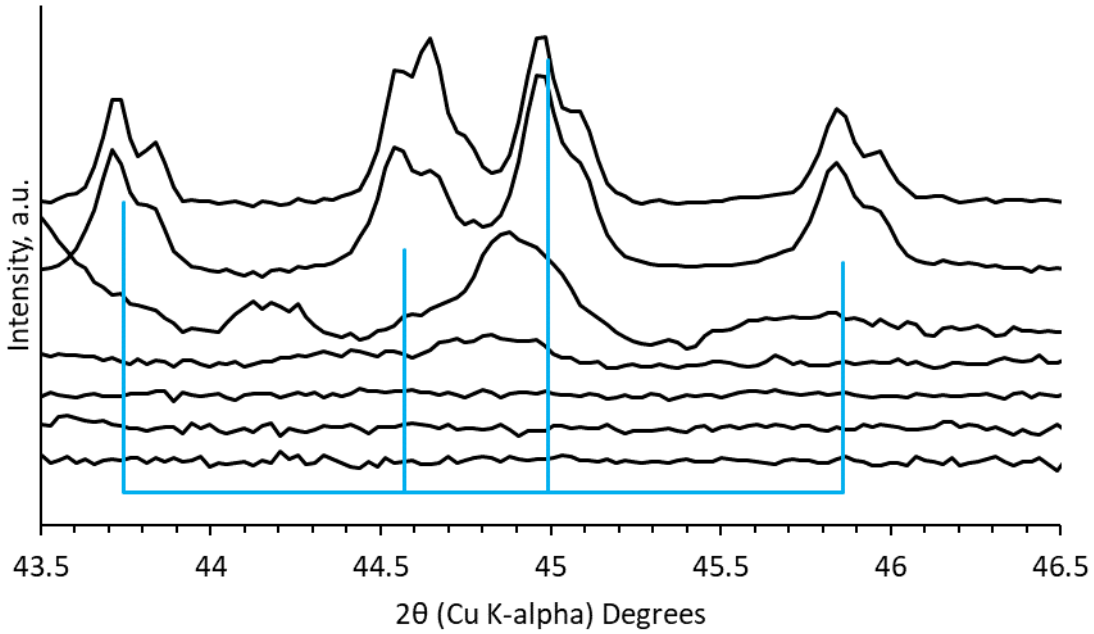

Figure 2.20 PXRD showing the decomposition of Prussian blue alongside calcium oxide powder at 100 °C intervals. Top to Bottom – 800 °C, 700 °C, 600 °C, 500 °C, 400 °C, 300 °C, room temperature, Fe_3C.

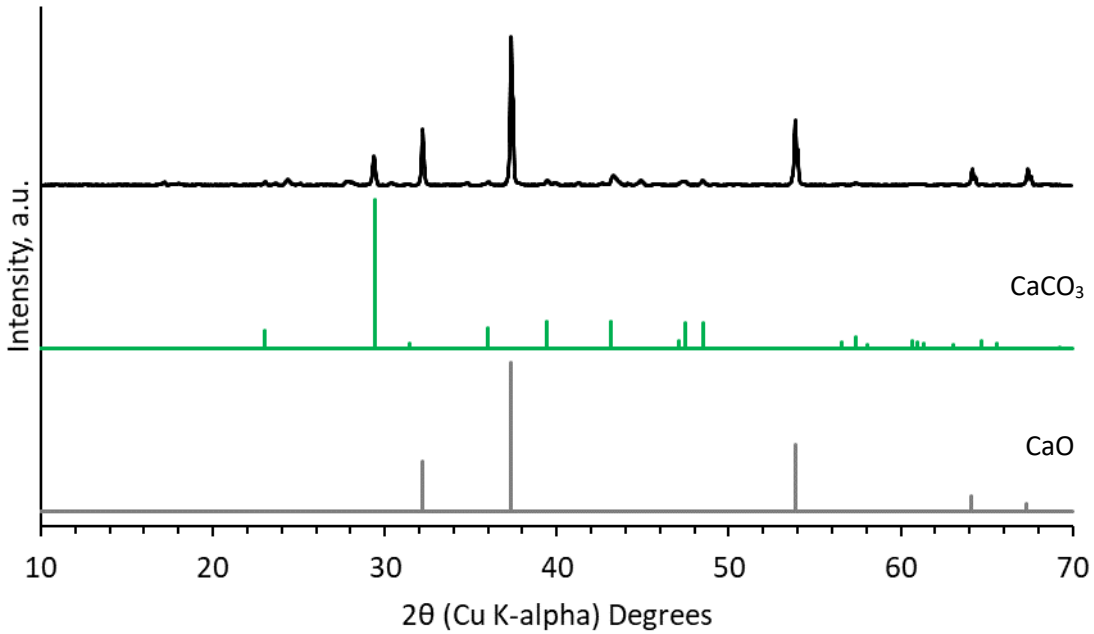

Figure 2.21 PXRD recorded for a 1:1 mass ratio of Prussian blue : CaO calcined at 600 °C.

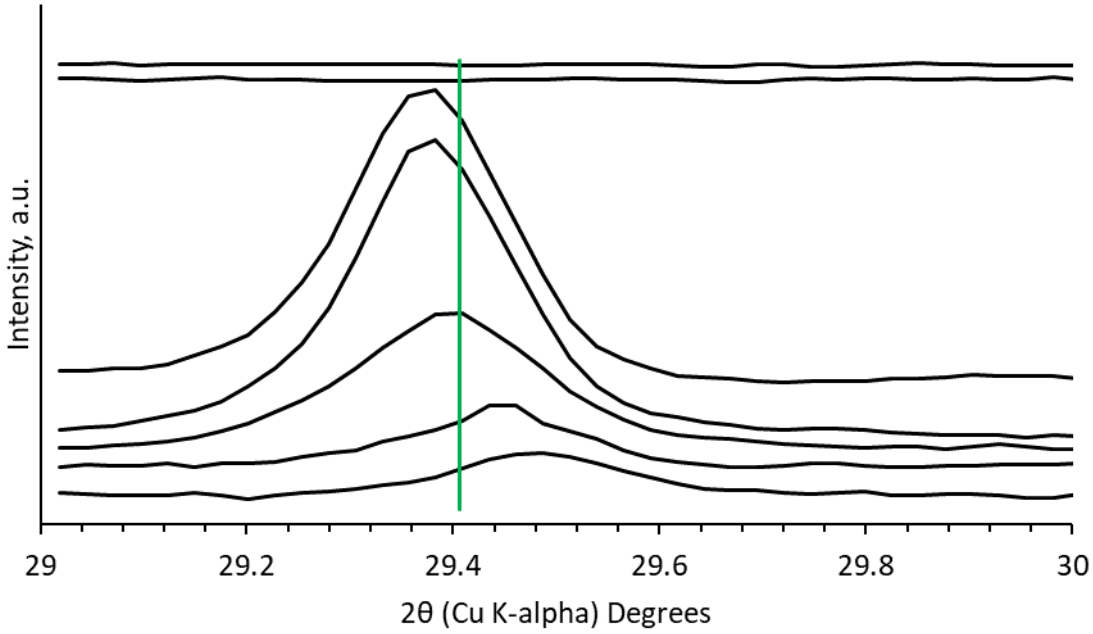

Figure 2.22 PXRD showing the decomposition of Prussian blue alongside calcium oxide powder at 100 °C intervals. Top to Bottom – 800 °C, 700 °C, 600 °C, 500 °C, 400 °C, 300 °C, room temperature, $CaCO_3$.

The $CaCO_3$ diffraction pattern is most notable for the peak at approximately 29 °. A closer inspection of this peak (Fig. 2.22) shows that it increases in intensity as the synthesis temperature increases, suggesting that the phase is forming alongside the decomposition of the Prussian blue particles. As an interesting aside, the phase is not present upon the formation of Fe_3C at 700 °C or later at 800 °C.

The formation of carbonate is an interesting occurrence as it could potentially be viewed as a method for the capture of carbon that would otherwise contribute to the carbon matrix surrounding the particles. This captured carbon could then be washed away during the cast removal step

2.4.3.3 MICROWAVE DECOMPOSITION WITH MgO AND CaO

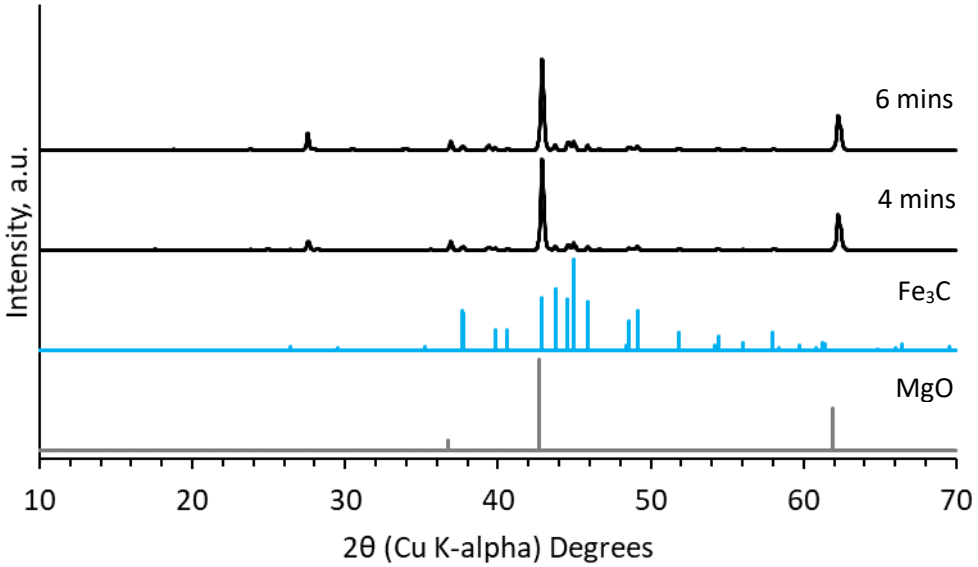

Figure 2.23 PXRD patterns recorded for Fe_3C produced by the decomposition of Prussian blue, alongside MgO Powder, in a microwave at 700 W.

Having shown the compatibility of both MgO and CaO in our furnace decomposition process it was then of interest to examine whether similar results could be obtained through the rapid heating conditions of our modified microwave oven. In this vein, an experiment was performed examining the behaviour of 1:1 mass ratio mixtures of Prussian blue : MgO and Prussian blue : CaO when heated for 4 minutes and 6 minutes with 700W of microwave power. Figs. 2.23 and 2.24 show the successful synthesis of Fe_3C alongside MgO. Likewise, Figs. 2.25 and 2.26 show the successful synthesis of Fe_3C alongside CaO.

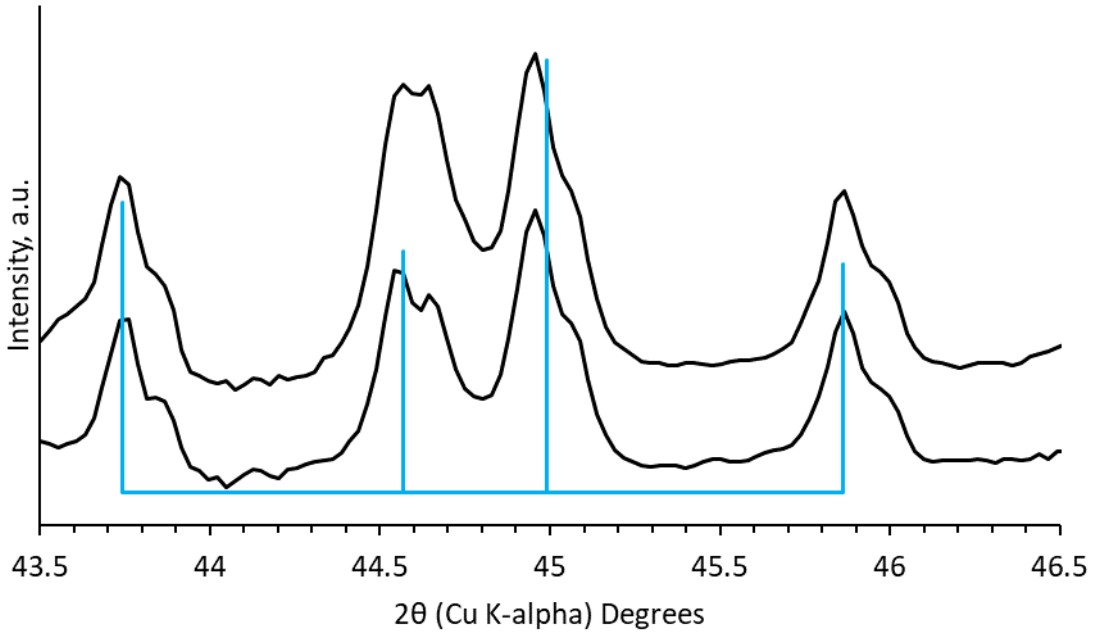

Figure 2.24 PXRD patterns for Fe_3C produced by the decomposition of Prussian blue, alongside MgO Powder, in a microwave at 700 W. Top to Bottom 6 mins, 4 mins, Fe_3C.

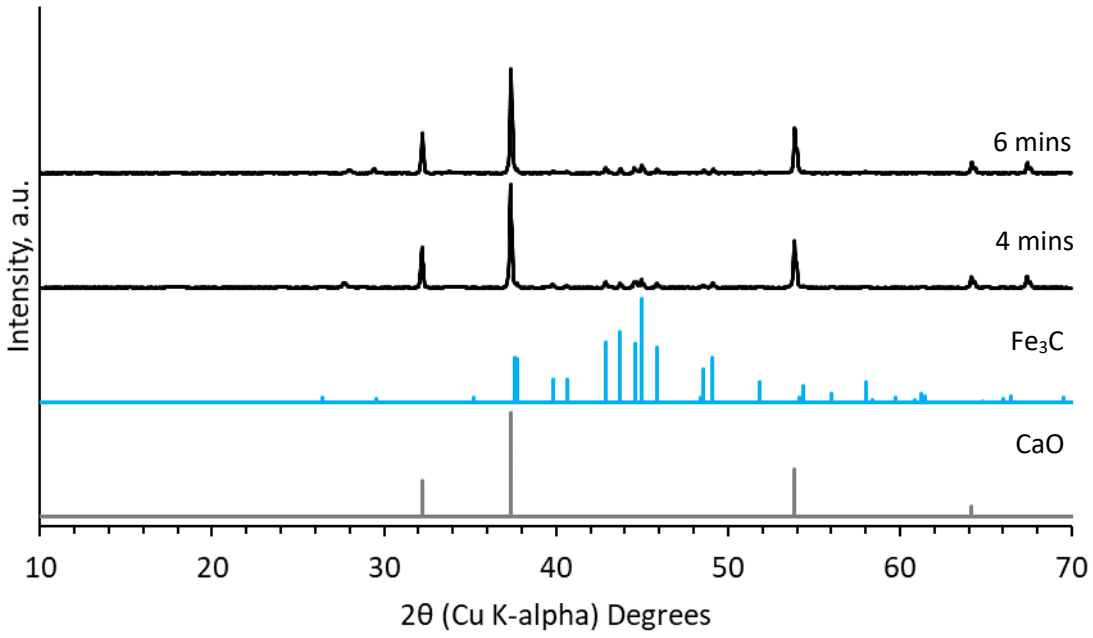

Figure 2.25 PXRD patterns for Fe_3C produced by the decomposition of Prussian blue, alongside CaO Powder, in a microwave at 700 W.

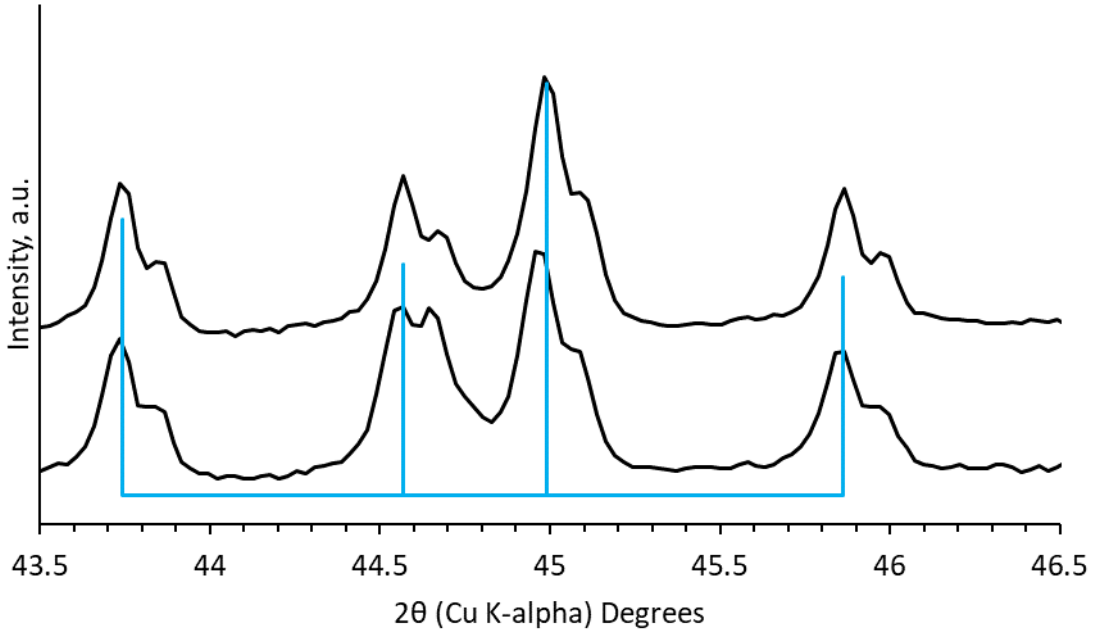

Figure 2.26 PXRD patterns for Fe_3C produced by the decomposition of Prussian blue, alongside CaO Powder, in a microwave at 700 W.

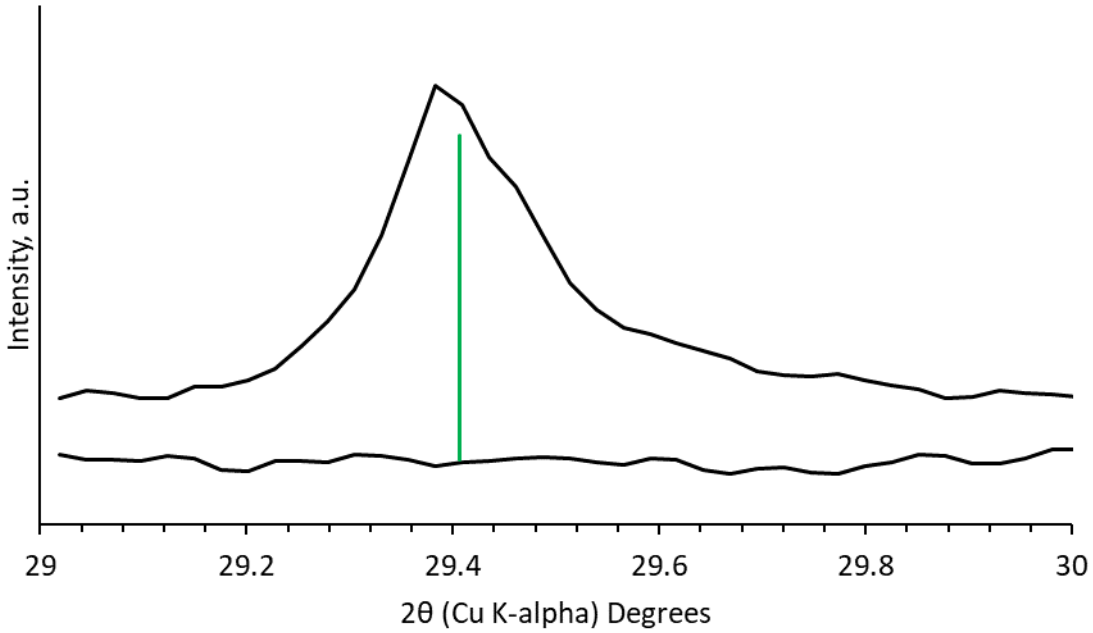

Figure 2.27 PXRD patterns for Fe_3C produced by the decomposition of Prussian blue, alongside CaO Powder, in a microwave at 700 W, examining showing the presence of $CaCO_3$.

Following on from the observations of $CaCO_3$ in the furnace Prussian blue/CaO decomposition, a closer examination of the region around the 2θ angle of 29° (Fig. 2.27) reveals a characteristic peak for $CaCO_3$ in the 6 minute preparation but not the 4 minute preparation. It appears therefore, that the 4 minute synthesis may simply have not been long enough to allow the formation of $CaCO_3$. The observation of $CaCO_3$ appearing alongside Fe_3C also runs counter to the observations made in the furnace decomposition analysis, in which $CaCO_3$ is not present in the diffraction patterns that also contain Fe_3C.

2.4.4 CAST REMOVAL

Analysis performed in the previous section has shown the chemical compatibility of both MgO and CaO powders in the decomposition of Prussian blue to give Fe_3C. However, as outlined previously, the ability to remove the cast is another important factor to consider. Thus, this section will explore the removal of the cast material by acid washing, with a focus on the use of MgO, starting with the use of hydrochloric acid, moving on to the use of ethylenediaminetetraacetic acid.

2.4.4.1 HYDROCHLORIC ACID (HCl) WASHING

MgO can be dissolved with hydrochloric acid to produce an aqueous solution of magnesium chloride. Thus, it was hoped that washing Fe_3C/MgO mixtures with HCl would provide a means for cast removal. The efficacy of the process would, however, be dependent on HCl preferentially reacting with MgO over Fe_3C. With the aforementioned in mind, attempts were

made to make the reaction conditions as mild as possible. Firstly, stirring was used in place of sonication to avoid the excess heat generated by sonication. Secondly, a 0.1 M concentration of HCl was used as a compromise between using as low of a concentration as possible, while being able to maintain a molar excess relative to MgO, at a sensible volume for working with. While finally, the solutions were monitored for any colour changes indicating the dissolution of iron containing phases. Fig. 2.28a-d shows PXRD patterns recorded for mixtures of Fe_3C and MgO produced via Prussian blue decomposition alongside MgO powder pre and post acid washing with 0.1M HCl. A discussion of which will now follow.

A sample of Fe_3C/MgO produced by calcining a 1:1 mass ratio mixture of Prussian blue and MgO was washed with a molar excess of 0.1 M HCl relative to MgO for approximately 24 hours, by which time the solution had begun to turn a deep orange indicating the dissolution of iron. The acid washed material was then rinsed with deionised water and EtOH and left to dry at room temperature. Unfortunately, PXRD shows that the resulting material contained a significant amount of residual $Mg(OH)_2$, while observations of the resulting material showed that a significant amount of Fe_3C had been visibly lost. Further acid washing of this material to remove the residual $Mg(OH)_2$ resulted in the total loss of Fe_3C.

Acid washing of a subsequent sample, in which Fe_3C had been prepared by calcining a 4:1 mass ratio mixture of Prussian blue : MgO was then attempted in the hope that dissolving a smaller amount of MgO may simplify the process. Again, a slight molar excess of 0.1 M HCl was used relative to MgO content. Yet, again, total loss of Fe_3C was observed, with only minor Fe containing phases such as Fe_3O_4 and Fe_7C_3 left behind, even with the acid washing performed over a significantly shorter duration.

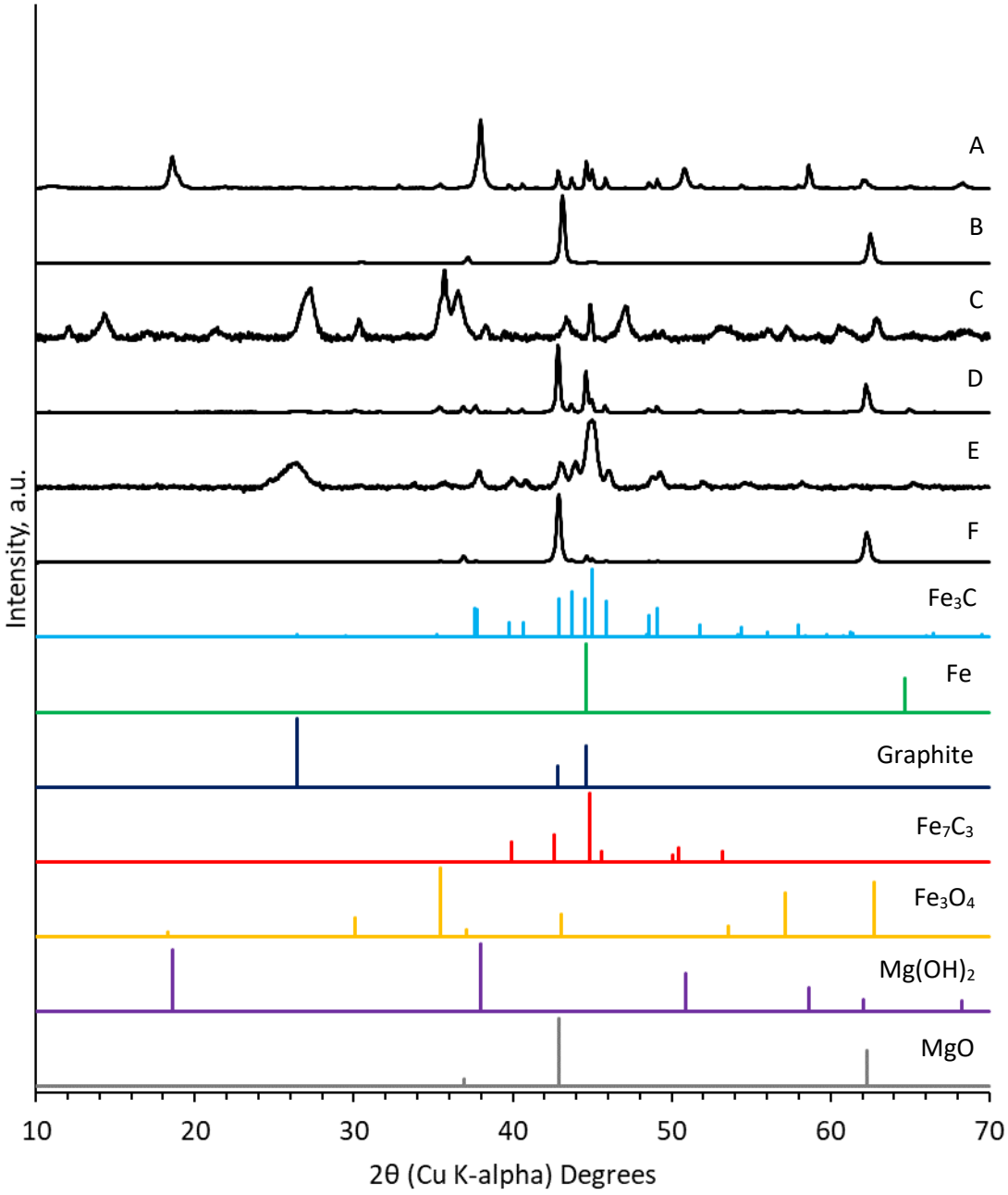

Figure 2.28 PXRD patterns recorded for HCl washed samples. Top to Bottom **A** - 1:1 Prussian blue : MgO 800 °C (washed), **B** - 1:1 Prussian blue : MgO 800 °C (unwashed), **C** - 4:1 Prussian blue : MgO 800 °C (washed), **D** - 4:1 Prussian blue : MgO 800 °C (unwashed), **E** - 1:1 PVP coated Prussian blue : MgO 800 °C (washed), **F** - 1:1 PVP coated Prussian blue : MgO 800 °C (unwashed).

These results suggested that Fe_3C was far too prone to dissolution in HCl for an acid wash of this type to be practical. However, one last experiment was performed. This time a surfactant protected Prussian blue, synthesised using a PVP : Fe^{2+} molar ratio of 20:1 was decomposed at a 1:1 mass ratio with MgO. The idea was that the excess carbon left over from the decomposition, performed in an anaerobic environment, might protect the Fe_3C particles from dissolution and to some extent this did prove to be the case. As can be seen in Fig. 2.28e,f, all crystalline Mg containing phases were removed with Fe_3C remaining alongside graphitised carbon. Yet while this was a positive result there were still fundamental issues remaining. One of which was the fact that a significant amount of Fe_3C was still lost during this process. Likewise, the amount of surfactant used was also likely to produce a massive excess of carbon, a significant issue when considering the goal of producing dispersible particles. Yet these results indicated that potentially the process could be tuned to allow for acid washing with HCl.

2.4.4.2 ETHYLENEDIAMINETETRAACETIC ACID (EDTA) WASHING

As an alternative to dissolving MgO with an HCl acid wash, EDTA was used to chelate Mg^{2+}, with subsequent washing steps performed with distilled water used to remove the bound Mg. An experiment was performed in which two samples Fe_3C/MgO were treated with 0.2 M EDTA. The first sample was treated with a 7% molar excess relative to Mg content, the second was treated with a 100% excess relative to Mg content. The samples were then washed with distilled water three times, with a sample of solid from each washing step kept for analysis by flame atomic absorption spectroscopy (FAAS), the results of which are displayed in Table 2.8.

Samples of pre- and post-EDTA washed material from each process were then analysed by PXRD (Fig. 2.29).

Analysis of the pre EDTA washed samples provides a control pattern showing the presence of both Fe_3C and MgO. After the EDTA washing process, evidence of crystalline Mg containing phases is absent from the diffraction patterns of both samples, suggesting the washing process has been a success. Interestingly, unlike the sample washed with a 7% molar excess of EDTA, a set of diffraction peaks belonging to graphite can also be seen for the sample washed with a 100% molar excess. It seems likely that this difference was caused by the partial dissolution of the Fe/Fe_3C phases, decreasing the relative intensity of their diffraction peaks relative to that of graphite. This is also supported by observation made during the washing process in which the 100% EDTA excess solution turned an orange/red colour – the colour of ferric EDTA.

Table 2.8 FAAS data for washings collected from EDTA washes using molar excess of 7% and 100% relative to initial MgO content.

Sample	**Mg (wt.%)**
7% Excess Washing 1	2.31
7% Excess Washing 2	2.69
7% Excess Washing 3	2.12
100% Excess Washing 1	0.09
100% Excess Washing 2	0.08
100% Excess Washing 3	0.11

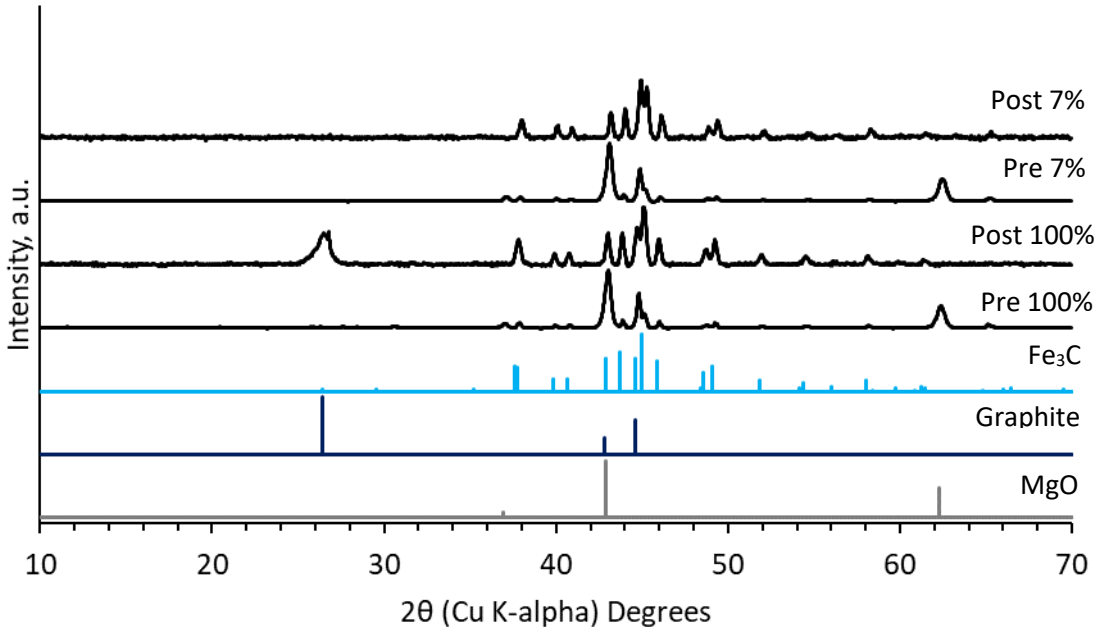

Figure 2.29 PXRD data showing patterns recorded for 1:1 Prussian blue : MgO mixtures calcined at 800 °C, pre and post EDTA washing.

While PXRD was used to detect any crystalline Mg containing phases, FAAS was used to detect any non-crystalline Mg containing residues. The technique was also used to assess whether the number of distilled water washes had a significant impact on the removal of the Mg(II)-EDTA.

The analysis (Table 2.8) showed that Mg was still present at approximately 2.5 wt.% in the sample washed with a 7% excess of EDTA, whereas the sample washed with a 100% excess had an Mg content of <0.2 wt.%. Thus, a significant improvement in Mg removal is possible if the EDTA molar excess is increased. However, while less destructive towards Fe_3C than the HCl washing process, a significant amount of Fe_3C is still visibly lost during the 100% excess EDTA wash. Taking these considerations into account, the improved Mg removal provided by

the 100% excess was not deemed advantageous enough to counter the loss of Fe containing phases. The data in Table 2.8 also shows that multiple distilled water washes seem to have little effect on residual Mg concentrations

Based on the strength of these results an EDTA wash was performed on a CaO/Fe_3C mixture, prepared by calcining a 1:1 mixture of CaO : Prussian blue. PXRD performed on the washed product (Fig. 2.30) shows the removal of CaO to leave Fe_3C, with the unassigned peaks belonging to a small amount of residual $Ca(OH)_2$. Again, this washing process shows great potential and with tuning is likely to result in total removal of Ca containing phases.

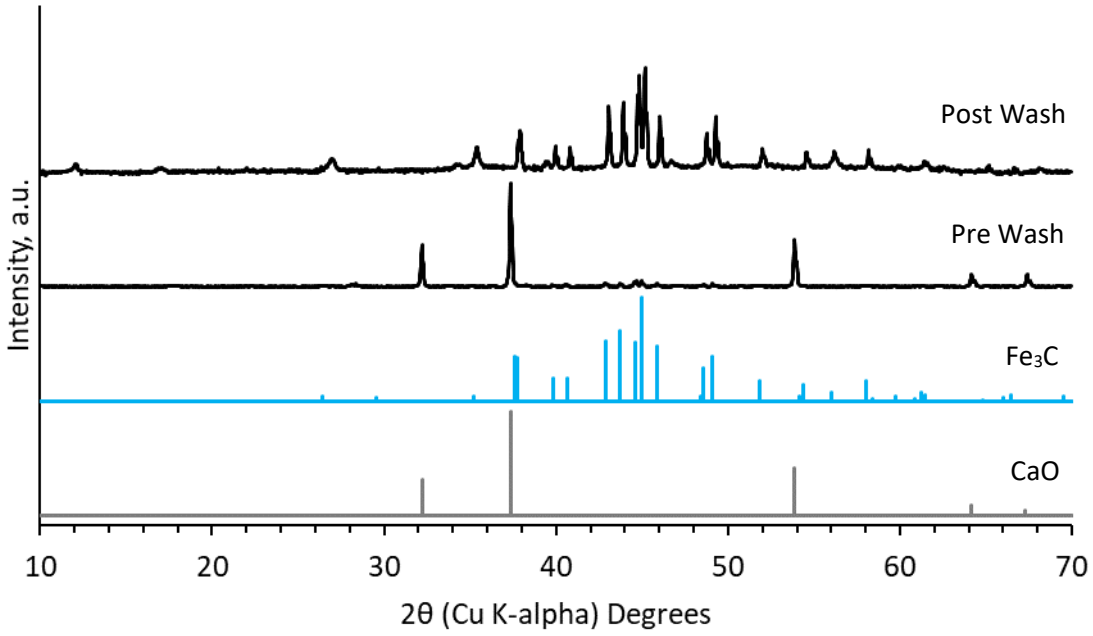

Figure 2.30 PXRD data showing patterns recorded for a 1:1 Prussian blue : CaO mixture calcined at 800 °C, pre and post EDTA washing.

2.5 CONCLUSIONS

This chapter has shown that soluble Prussian blue can be thermally decomposed in a reproducible manner to produce Fe_3C. PVP can then be incorporated into the synthesis without adverse effects on the phase composition of the product. However, the use of PVP in the synthesis of precursor particles with tuneable diameters has proven more difficult than first expected and requires further work. It must also be noted that the use of a carbon rich surfactant such as PVP introduces another significant source of carbon that can contribute to an unwanted amorphous carbon matrix.

The chapter then goes on to show that both MgO and CaO are chemically compatible with the Prussian blue decomposition process, with CaO demonstrating a possible carbon capture ability in via the formation of $CaCO_3$. Finally, EDTA has been shown to be effective at MgO and CaO cast removal, providing a means for isolating Fe_3C nanoparticles post synthesis.

CHAPTER 3

OPTIMISING MORPHOLOGY AND INVESTIGATING PROPERTIES OF IRON CARBIDE NANOPARTICLES

3.1 INTRODUCTION

Fe_3C nanoparticles have a wide range of potential uses, almost all of which are born of two key characteristics; the particles high magnetic susceptibilities and their impressive catalytic activity in a range of reactions[109, 110, 111, 112]. While these properties are characteristic of Fe_3C, controlling the morphology of the material can allow for the tuning of these properties. So, whereas chapter 2 had a focus almost purely relating to the synthesis of an Fe_3C phase, this chapter will now focus on the synthesis of Fe_3C nanoparticles and how the use of cast materials can affect nanoparticle morphology. This introduction will therefore focus on how iron carbide particle morphologies have been controlled in the literature and how such control can produce impressive magnetic and catalytic performances for a range of applications.

3.1.1 MAGNETISM

Fe_3C is a ferromagnetic material below its Curie temperature of approximately 480 K, above which it becomes paramagnetic[113]. Thus, the potential for the synthesis of superparamagnetic particles of Fe_3C exists. The literature contains many reports of superparamagnetic iron oxide nanoparticles (SPIONS) for use in applications such as chemotherapy[114] and magnetic resonance imaging[115]. Yet, despite the high Fe wt.% found in Fe_3C, reports of superparamagnetic Fe_3C appear to be less prevalent.

Ferromagnetic materials contain long range ordering of unpaired electron spins in a parallel fashion, in regions known as magnetic domains. Thus, within a domain there is a strong magnetic field, but the bulk materials in which these domains are randomly oriented has a net

zero field. An applied external magnetic field can then cause the alignment of these domains in the direction of the field, resulting in strong magnetic attraction[116].

With sufficiently small particles, with the exact diameter dependent on the composition of the material, materials that display spontaneous magnetisation can contain just one magnetic domain. Such a material is termed superparamagnetic and is highly susceptible to a magnetic field, making them ideal for use in ferrofluids and a range of biomedical applications such as hyperthermia treatment[117].

While superparamagnetic Fe_3C particles have been produced by industrially scalable techniques such as laser ablation[118], control over particle size and therefore the tunability of magnetic properties is still left wanting. Yet, the literature does contain instances of magnetic tunability through morphological control of Fe_3C in laboratory scale syntheses. Kolhatkar *et al.* have prepared an extensive review that covers a wide variety of methods for controlling the size and properties of magnetic nanoparticles in general[119]. However, this introduction will focus on control over Fe_3C particles specifically.

As far as the synthesis of a superparamagnetic nanopowder is concerned, Giordano *et al.*[120] were able to demonstrate an impressive synthesis capable of producing discrete superparamagnetic Fe_3C nanoparticles via a urea based sol gel like synthesis. The synthesis revolves around the calcination of polymeric urea-metal complexes. The synthesis itself is versatile in that by varying the precursor metal salt and the metal to urea molar ratio a range of transition metal carbides and nitrides can be synthesised including Mo, W, Cr and Ti carbides as well as Ti, V, Nb, Ga, Mo, W and Cr nitrides[121 122]. Yet, while impressive, the work does not address ways of tuning particle size.

Meffre *et al.*[117] on the other hand were able to tune the size and magnetic anisotropy of their superparamagnetic iron carbide nanoparticles to gain access to "unprecedented hyperthermia properties". The authors achieved this with a synthesis that involved the use of Fe^0 seed particles which were then heated alongside $Fe(CO)_5$ under Ar and H_2. Interestingly, the Ar synthesis gave a core shell $Fe^0/Fe_{2.2}C$ – Fe_5C_2 structure, whereas the H_2 synthesis resulted in the elimination of the Fe^0 core. Controlling the temperature and reaction time then allowed for the controlled incorporation of carbon to differing extents, leading to control over the magnetic properties of the particles.

Likewise, Gu *et al*.[123] were able to tune the magnetic properties of their Fe_3C particles, this time purely through the control of particle size. Their synthesis involved calcining a mixture of Fe_2O_3 and carbon produced by the combustion of iron nitrate, glycine and glucose. By systematically increasing the amount of glucose employed, the authors were able to reduce particle size, while simultaneously increasing the particles saturation magnetisation.

Also of interest is the ability to grow superparamagnetic grains of Fe_3C on a carbon film demonstrated by Lee *et al.*[118]. They were able to achieve this by employing magnetron sputtering, in which Fe cations in a plasma vapour were accelerated by an electric field towards a negatively charged target, namely graphite. The grains, which contained long range ordering of magnetic moments, could then be enlarged by post deposition annealing, thereby modifying their magnetic behaviour. The authors found that with increased annealing temperatures and therefore increased grain growth, magnetic susceptibility was increased, and superparamagnetic blocking temperatures were raised i.e. superparamagnetic behaviour became evident at higher temperatures.

3.1.2 CATALYSIS

Fe_3C has also shown impressive activities in the catalysis of various reactions. A particularly high impact example is the synthesis of a bifunctional oxygen reduction/oxygen evolution reaction catalyst, using a Prussian blue precursor, by Barmun *et al.*[124]. The formation of ORR active sites in this material was believed to be due to interactions between the Fe containing particles and the N-doped carbon support formed during the synthesis. In fact, this assumed synergy between Fe_3C and N-doped structures in ORR catalysis has been studied and shown not to be an isolated phenomena[78]. Yet with regards the work of Barmun *et al.*, even in such a high-profile example, their ability to tune particle size is limited, highlighting the need for techniques with this capability. Perhaps then the catalyst performance could be improved even further.

The role of Fe_3C in ORR catalysis has been supported by studies performed by Jiang *et al*. looking at graphite protected Fe_3C particles[78]. Removal of the graphitic layers by ball milling led to the dissolution of the Fe_3C particles in the acidic electrolyte used and therefore a loss of catalytic activity. This observation yields two important factors for consideration. The first is that the catalytic activity cannot be purely attributed to the graphitic carbon and thus even though the Fe_3C does not come into direct contact with the electrolyte, it is still playing an important role. The second is that for applications that use an acidic electrolyte, Fe_3C particles must be stabilised to prevent decomposition. The authors were also able to show that the graphitic layers could stabilise the particles in alkaline electrolytes. Similar recent studies also support the idea that Fe_3C particles can be stabilised by graphitic shells in acidic and basic

electrolytes[125]. These results suggest that graphite protected Fe_3C nanoparticles could be of use in both proton exchange membrane fuel cells and alkaline fuel cells.

The idea of protecting Fe_3C nanoparticles in graphite and N-doped graphite matrices has also been taken further, with more complex matrix morphologies having been explored. For example, the work by Barmun *et al.* which utilised a Prussian blue precursor to produce Fe_3C for ORR catalysis, found evidence of Fe_3C particles being encapsulated within N-doped carbon nanotubes. The resulting structures appeared to have a bamboo like morphology.

Similarly, Wu *et al*. were able to utilise carbon nanofibers for Fe_3C stabilisation[126]. Here, the N-doped mesoporous carbon nanofibers encapsulated the Fe_3C particles to produce reportedly high catalytic activity in the ORR when used in alkaline electrolytes. The carbon nanofibers were pre-prepared by hydrothermal carbonization, then mixed with pyrrole. The pyrrole was then polymerized through the addition of $FeCl_3$. Once dried this mixture was calcined under N_2 to produce the catalyst. Another point which makes this a particularly interesting piece of work is that it is highly likely that the presence of the carbon nanofibers during calcination also helped preserve the nanoscale dimensions of the Fe_3C particles.

In fact, this kind of work on the encapsulation of Fe_3C nanoparticles has been carried out with high rates of success several times in the literature. Encapsulation by single carbon shells[127] and even graphene nanoribbons[128] are two examples.

3.1.3 OTHER EXAMPLES OF MORPHOLOGICAL CONTROL

Wen *et al*. were able to produce Fe/Fe_3C-C nanorods composed of a Fe/Fe_3C nanorod core and a N-doped graphite shell, for catalysis of the oxygen reduction reaction[129]. In this case, an aqueous solution of $FeCl_3$ was mixed with cyanamide (NH_2CN) and dried. Once dried the powder was annealed at 750 °C. Upon decomposition during the annealing process, the cyanamide was found to produce various carbon nitride gases though to be key to producing the N doping believed by some to be necessary for high activity in the ORR. The overall result was to produce core shell Fe-Fe_3C N-doped carbon nanorods that the authors claim are have impressively high ORR activities when used in a neutral phosphate buffer solution. Interestingly, the nanorods were also shown to be effective catalysts for hydrogen evolution in microbial fuel cells.

3.1.4 CONCLUSIONS

While the literature contains many reports of the synthesis of iron carbide nanoparticles with exceptional magnetic and catalytic properties, there is a lack of examples of truly dispersible, discrete particles. Most reports involve the synthesis of iron carbide nanoparticles in a carbon matrix. The presence of such a matrix does not necessarily work to the detriment of the particles for the authors chosen applications, however the synthesis of discrete, stabilised particles in an industrially scalable synthesis could open up an array of new possibilities. A significant possibility being the dispersal of the particles over a range of different catalyst supports.

This chapter will take a closer look at the morphology of the Fe_3C particles produced using the cast concept established in chapter 2. An emphasis will be placed on the production of discrete, dispersible Fe_3C nanoparticles with desirable properties such as superparamagnetism and protective carbon shells.

3.2 EXPERIMENTAL

3.2.1 MATERIALS

Table 3.1 List of materials used in chapter 3.

Chemical	Supplier	CAS number
Iron (II) Chloride tetrahydrate ($FeCl_2.4H_2O$) - 98%	Sigma Aldrich	13478-10-9
Potassium ferricyanide ($K_3Fe(CN)_6$) >99%	Sigma Aldrich	13746-66-2
Polyvinylpyrrolidone $(C_6H_9NO)_n$ >99%	Sigma Aldrich	9003-39-8
Magnesium Oxide (MgO) >99%	Acros Organics	1309-48-4
Magnesium Oxide Nanopowder (MgO) >99%	Sigma Aldrich	1309-48-4
Magnesium nitrate hexahydrate ($Mg(NO_3)_2$) - >99%	Sigma Aldrich	233-826-7
Calcium Oxide (CaO) >99%	Acros Organics	1305-78-8
Ethylenediaminetetraacetic acid ($C_{10}H_{16}N_2O_8$) >99%	Sigma Aldrich	60-00-4
Agar $(C_{12}H_{18}O_9)_n$	Sigma Aldrich	9002-18-0
Soluble Prussian blue ($KFe(Fe(CN)_6$) >99%	Sigma Aldrich	12240-15-2
Methanol (CH_3OH) 99.8%	VWR	13446-18-9
Ethanol (CH_3CH_2OH) >99%	VWR	64-17-5
Acetone (CH_3COCH_3) >99%	VWR	67-64-1
Hydrogen Peroxide (H_2O_2) 30%	Sigma Aldrich	7722-84-1

3.2.2 PRUSSIAN BLUE/CAST METHANOL MIXING

$FeCl_2.4H_2O$ (0.6 g) and a given mole fraction of polyvinylpyrrolidone were added to distilled water (240 cm^3). $K_3[Fe(CN)_6]$ (0.99 g) was added to distilled water (60 cm^3). The $K_3[Fe(CN)_6]$ solution was then added to the $FeCl_2$ solution dropwise with vigorous stirring. The solution was then stirred for a further 30 mins. Acetone (300 cm^3) was then added to induce agglomeration of the Prussian blue particles. The particles were then washed three times with acetone via centrifugation. The solid was then transferred in MeOH (300 mL). The MeOH was then removed from the thoroughly mixed MeOH, Prussian blue, MgO mixture by rotary evaporation. The dried solid was then further dried for another 24 hours at 70 °C.

3.2.3 PREPARATION OF Fe_3C DISPERSIONS ON SILICA

3.2.3.1 PREPARATION WITHOUT CTAB

Fe_3C in distilled water was added to silica (0.1 g) then sonicated for 30 mins. The sample was then dried at room temperature for 24 hrs.

Coating Concentration (mg of Fe_3C per g of silica)	**Fe_3C stock Conc. (mg mL^{-1})**	**Volume of Fe_3C stock (µl)**	**Mass of Silica (g)**
1.5	0.5	300	0.1
3.0	1.0	300	0.1
30	1.0	1500	0.05

In the case of the 30 mg g^{-1} sample, excess water was decanted after the sample had been left to settle overnight. The solid was then left to dry at room temperature for 24 hrs.

3.2.3.2 PREPARATION WITH CTAB

CTAB (0.0429 g L^{-1}, 0.5 mL) was added to Fe_3C suspended in distilled water (1.0 mg mL^{-1}, 1.5 mL) and sonicated for 30 mins. Silica (0.05 g) was then added and sonicated for a further 30 mins. The sample was then left to settle overnight. The excess water was then decanted and the solid was left to dry for 24 hrs.

Surface area of 100 nm particle	$= 4\pi r^2$ $= 4\pi 50^2$ $= 34416\ nm^2$
CTAB molecules required to form a monolayer	= 34416/0.33 (effective CTAB cross section)

	= 95200 nm^3
Volume of 100 nm particle	= $4/3\pi r^3$
	= $4/3\pi 50^3$
	= 523600 nm^3
Mass of Fe_3C particle	= 523600 x 10^{-21} * 1.8 (Fe_3C Density)
	= 4.03 x 10^{-15}
Particles of Fe_3C per gram	= 1/4.03 x 10^{-15}
	= 2.48 x 10^{14}
Molecules of CTAB require per gram of Fe_3C	= 2.48 x 1014 x 95200
	= 2.36 x 10^{19}
Moles of CTAB required per gram of Fe_3C	= 2.36 x 10^{19} / 6.022 x 10^{23}
	= 3.92 x 10^{-5}
Mass of CTAB required per gram of Fe_3C	= 3.92 x 10^{-5} x 364.45
	= 0.0014 g

Equation 3.1 Approximate monolayer calculation.

3.2.4 H_2O_2 WASHING OF Fe_3C

Fe_3C was prepared using the MeOH mixing technique with a MgO nanopowder cast, at a 1:1 Prussian blue : MgO nanopowder mass ratio, followed by subsequent EDTA washing.

Fe_3C (0.075 g) was mixed with H_2O_2 (10%, 20 cm^3) and stirred for 2 hrs. The sample was then isolated by centrifugation and washed with distilled water then EtOH. The washed sample was then left to dry at room temperature for 24 hrs.

3.2.5 SCALE UP SYNTHESIS

Commercially sourced Prussian blue nanoparticles (5 g) were mixed with MgO nanoparticles at given mass ratios. The mixtures were then ground in a mortar and pestle until a homogeneous mixture was formed. The mixture was then calcined inside of a retort with a N_2

atmosphere and placed inside of a box furnace. Calcination was performed at 5 °C min^{-1} to 800 °C where it was held for 1 hour.

3.2.6 TRANSMISSION ELECTRON MICROSCOPY

Samples (≈ 100 mg) were dispersed in EtOH (≈ 1 mL) and sonicated for approximately 15 mins. One drop of the dispersed sample was then applied to a Cu TEM grid with a holey carbon coating. All CTEM images were recorded using a JEOL 2100 TEM with a tungsten filament and a charge coupled device (CCD) detector.

3.2.7 SCANNING ELECTRON MICROSCOPY

Samples were coated with a thin layer of iridium (2 nm) using a sputter coater Cressington 208HR in order to improve surface conductivity and avoid sample charging in the electron beam. Samples were then imaged using an FEI Nova NanoSEM 450 operating at 3 kV. Elemental analysis was made by EDAX (AMTEK) at 18 kV.

3.2.8 ENERGY DISPERSIVE X-RAY ANALYSIS/HIGH ANNULAR ANGLE DARK FIELD ANALYSIS

Samples (≈ 100 mg) were dispersed in EtOH (≈ 1 mL) and sonicated for approximately 15 mins. One drop of the dispersed sample was then applied to a Cu TEM grid with a holey carbon coating. 2D EDX maps were acquired using the Hitachi HD2700C Scanning Transmission Electron Microscope operating with a 200 kV accelerating voltage.

3.2.9 SCANNING TRANSMISSION ELECTRON MICROSCOPE TOMOGRAPHY

Samples (≈ 100 mg) were dispersed in EtOH (≈ 1 mL) and sonicated for approximately 15 mins. One drop of the dispersed sample was then applied to a Cu TEM grid with a holey carbon coating. 3D Tomography maps were acquired using the Hitachi HD2700C Scanning Transmission Electron Microscope operating a 200 kV accelerating voltage.

3.2.10 SUPERCONDUCTING QUANTUM INTERFERENCE DEVICE MEASUREMENTS (SQUID)

Samples were prepared using the MeOH mixing technique with a MgO nanopowder cast, at a 1:1 Prussian blue : MgO nanopowder mass ratio, followed by subsequent EDTA washing. SQUID data was collected using an MPMS XL, from Quantum Design used in DC mode. Hysteresis plots were obtained by increasing and subsequently decreasing the field strength between -5.01 and 5.01 Oe at 300 K and -1.20 and 1.00 Oe at 400 K.

3.2.11 POWDER X-RAY DIFFRACTION

Powder samples were prepared by first grinding them in a mortar and pestle to give homogeneous crystallite sizes and then either placing on a silicon wafer or sample holder sourced from Panalytical. In both cases, samples were flattened to give a uniform sample height.

All samples were analysed using a Panalytical Empyrean diffractometer in a flat plate reflection geometry. The diffractometer was not equipped with a monochromator, but a nickel filter was used to remove Kβ radiation. Thus, samples were analysed with Kα radiation.

A Pixcel-2D position sensitive detector was used to collect data between the 2θ angle range 10-70 °. The majority of this data was simply used for phase identification by comparison with the ICDD PDF-4+ database using the EVA software

3.3 CHAPTER SUMMARY

This chapter will take the information gleaned in chapter 2 on the compatibility of prospective cast materials with the Prussian blue decomposition process and apply it in such a way as to demonstrate an effect on Fe_3C nanoparticle morphology. To this end, a combination of electron microscopy, energy dispersive X-ray analysis and tomography will be used to demonstrate various anti-sintering effects on the way to creating Fe_3C nanopowders.

The ability to disperse an Fe_3C nanopowder over a catalyst support will then be demonstrated with a description of various attempts at optimisation. The aim of which is to highlight the potential for the use of Fe_3C nanoparticles with supports other than the commonly reported mesoporous carbons.

The magnetic properties of a Fe_3C nanopowder are then examined through superconducting quantum interference device (SQUID) measurements that provide evidence of superparamagnetism and a high saturation magnetisation value.

The chapter then ends with attempts to scale up the Fe_3C synthesis. The ultimate aim of the scale up will be to create a process that can produce gram scale quantities of Fe_3C nanopowder.

3.4 RESULTS AND DISCUSSION

3.4.1 PREPARATION OF PRUSSIAN BLUE/CAST MIXTURES

For a cast material to fulfil its function of inhibiting the sintering of template particles, the cast and template particles need to be efficiently mixed. A fundamental challenge in this pursuit is ensuring that the template Prussian blue particles do not form agglomerates prior to mixing. As discussed in the introduction to chapter 2, soluble Prussian blue can be peptised into a colloidal sol in water. Mixing a sol such as this with a cast material was thought, therefore, to be one approach to achieving efficient mixing. The initial problem with this approach was that our chosen cast materials, MgO and CaO, undergo hydrolysis on contact with water to give $Mg(OH)_2$ and $Ca(OH)_2$ respectively, with $Mg(OH)_2$ having been shown to be incompatible with the formation of Fe_3C in chapter 2. Thus, alternative solvents that could be used to create suspensions of soluble Prussian blue nanoparticles were sought after. This problem provided a challenge in and of itself, as it is not possible to disperse Prussian blue particles in organic solvents to the same degree as is possible in water. Fortunately, this is not the case if the particle surfaces are functionalised with PVP.

To find an appropriate solvent, a sample of Prussian blue with a PVP : Fe^{2+} molar ratio loading of 100:1 was prepared then dispersed in solvents including MeOH, EtOH, CH_3CN and CH_2Cl_2. After 12 hours, the MeOH suspension was the only one to display no signs of sedimentation. Further experimentation showed that the PVP : Fe^{2+} molar ratio could be reduced to 1:1 to give the same results in MeOH. TEM micrographs showing sub 100 nm particles in this sample can be seen in Fig. 3.1. For a control sample without a PVP loading on the other hand, even the initial redispersion was impossible. Methanol was therefore selected as a solvent for the

re-dispersal of PVP coated Prussian blue, and as a solvent for the mixing of the dispersed Prussian blue particles and the prospective cast materials.

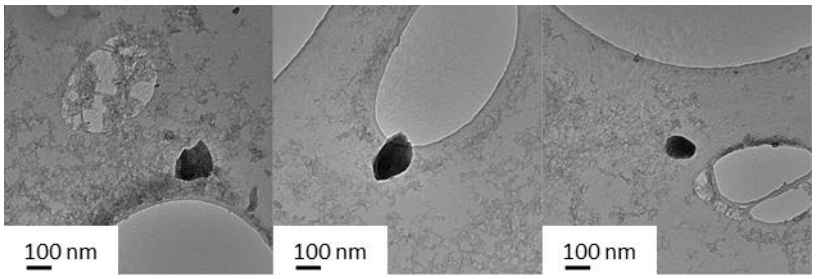

Figure 3.1 TEM micrographs of PVP coated Prussian blue particles that have been dispersed in MeOH.

Once the materials had been thoroughly mixed in MeOH, the MeOH was removed to give dry homogenous mixtures. A comparison of these mixtures, prepared using MgO and CaO (Fig. 3.2), show that while the phases present in the MgO/Prussian blue mixture remain unchanged, the original phases present in the CaO/Prussian blue mixture have decomposed. The majority of the CaO seems to have decomposed to give $Ca(OH)_2$, potentially due to a reaction with trace amounts of water in the MeOH. Whereas the Prussian blue seems to have decomposed to give a phase not identifiable using the international crystal structure database, likely due to the alkaline conditions created by the formation of $Ca(OH)_2$.

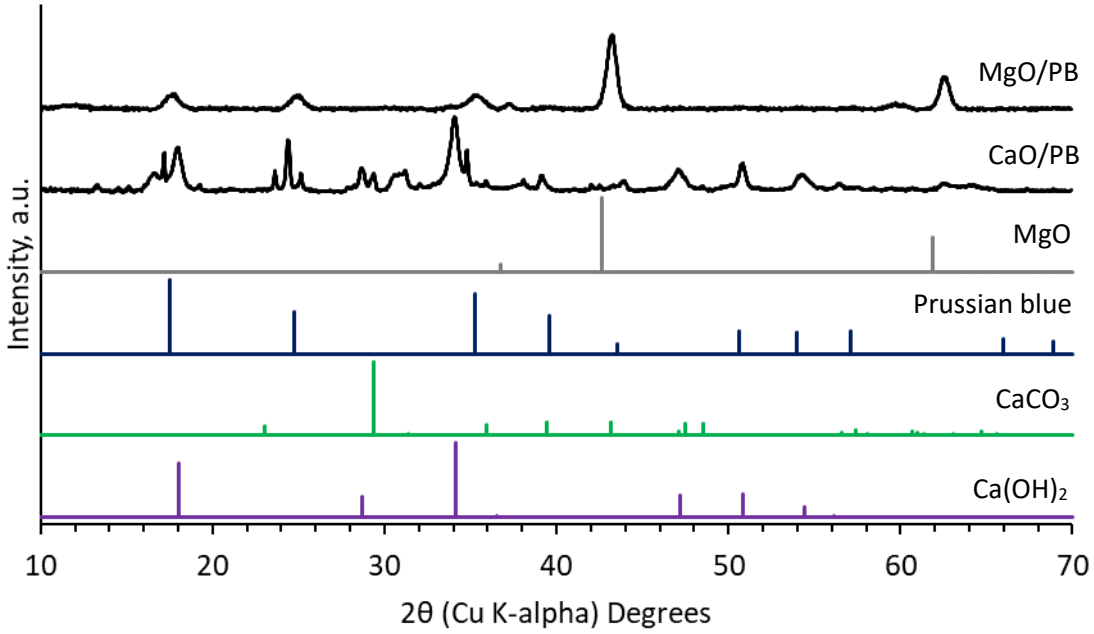

Figure 3.2 PXRD patterns recorded for 1:1 mass ratios of cast material to Prussian blue, dried from a MeOH mixture.

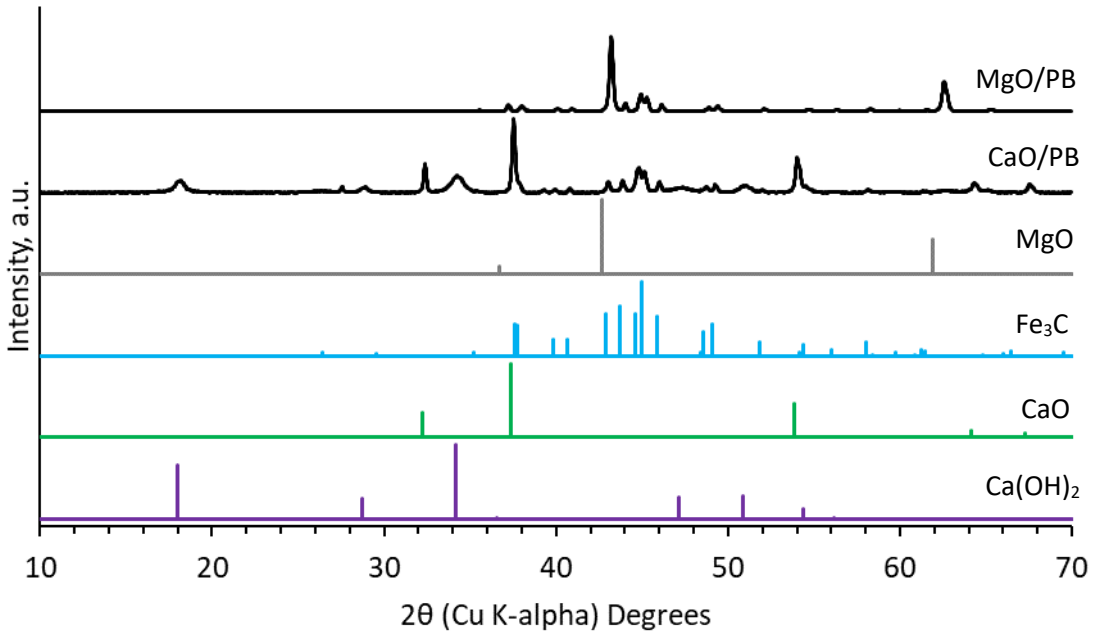

Figure 3.3 PXRD patterns recorded for Fig. 3.2 samples calcined at 800 °C.

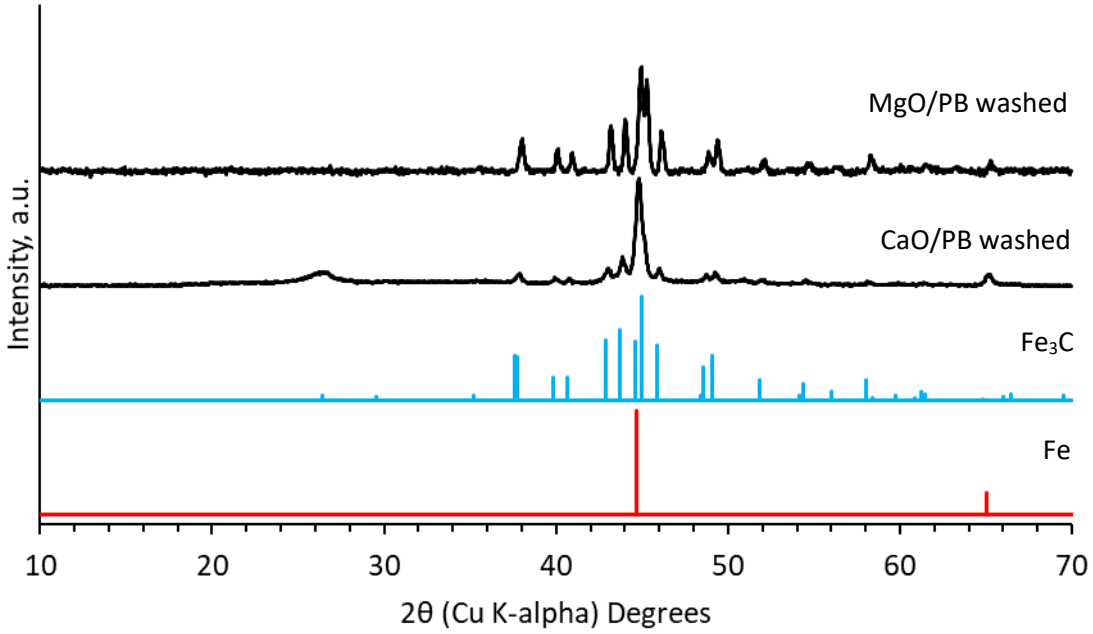

Figure 3.4 PXRD patterns recorded for Fig. 3.3 samples washed with EDTA solution.

Upon calcination, PXRD patterns recorded for both the MgO/Prussian blue and the CaO/Prussian blue samples show the presence of Fe_3C. The calcium containing sample also contains both $Ca(OH)_2$ and its decomposition product CaO (Fig. 3.3), which is to be expected given the $Ca(OH)_2$ decomposition temperature of approximately 510 °C and the calcination temperature of 800 °C. The formation of Fe_3C in the $Ca(OH)_2$ containing preparation is somewhat unexpected given the failure of $Mg(OH)_2$ as a cast material, making this an interesting observation. However, the decomposition of the Prussian blue particles means that our templates structural information will have been lost. As an aside, EDTA washing of the CaO preparation gave a sample with a diffraction pattern containing a significant amount of Fe^0. The EDTA washed MgO preparation on the other hand gave a diffraction pattern showing Fe_3C with a small amount of Fe^0 (Fig. 3.4).

Given the added chemical complexity of the CaO : Prussian blue mixture in MeOH, MgO was selected as a cast material for use in the MeOH mixing synthesis used in all of the sample preparations that follow in this chapter. Namely, the fact that the Prussian blue template particles appear to have been dissolved making them useless as a structural template, and the presence of large quantities of Fe^0 in the washed product.

3.4.2 INCORPORATION OF A MgO BULK POWDER CAST

Having shown that MgO is compatible with the thermal decomposition reaction of Prussian blue to give Fe_3C and that MgO can be removed post Fe_3C synthesis, the next hurdle was to examine how different morphologies of MgO performed with regards to preventing template particle sintering. The obvious first step was to examine the bulk MgO powder used in the compatibility tests discussed in chapter 2. As the material was likely to be composed of large particles and agglomerates, it was assumed that the material would not be able to efficiently pack around the template particles, thereby immobilising them. Thus, further analysis was performed to ascertain whether the material would be able to prevent sintering via another mechanism.

3.4.2.1 PXRD ANALYSIS

Although the bulk MgO powder has been shown to be compatible with our process, all analysis up to this point has involved 1:1 mass ratios of Prussian blue and MgO. However, it was deemed a reasonable assumption that increasing and decreasing the ratio may have had

significant effects on both the anti-sintering performance of the cast and the chemical compatibility of the two materials. For example, if water is adsorbed to the surface of the cast, would increasing the amount of cast material increase the amount of water in the system and thereby have a knock-on effect on the potential for oxidation of the product particles during calcination? To answer this question 1:1, 1:2, 1:3, 1:4 and 1:5 mass ratios mixtures of soluble Prussian blue and bulk MgO powder were prepared using the MeOH mixing technique, then calcined. The resulting materials were then analysed by PXRD (Fig. 3.5).

While the patterns displayed in Fig. 3.5 very clearly show the presence of MgO, due to the relative intensity of the two main phases, they only hint at the presence of Fe_3C. Closer analysis of the 43.5-46.5° 2θ region (Fig. 3.6) reveals clearly visible characteristic Fe_3C diffraction peaks in each sample, with the 1:2 ratio also showing the peak at approximately 44.8° having a slightly higher relative intensity compared to the Fe_3C peaks compared to the 1:1 pattern. This may indicate the presence of Fe^0. Reduction of iron cations to Fe^0 in this synthesis is something that is observed fairly regularly and is consequently not a surprise. It may be due to a temperature differential in the furnace, with slightly hotter spots causing the formation of Fe^0. It is also possible that the choice of crucible may lead to the favourable crystallisation of Fe^0. It is entirely possible then that this is not necessarily a reproducible result, in fact, given the diffraction patterns for the other samples this seems quite likely.

Regardless, the composition of this sample will be taken into account when discussing further of analysis by electron microscopy and care will be taken not to draw conclusions about the morphology of this sample.

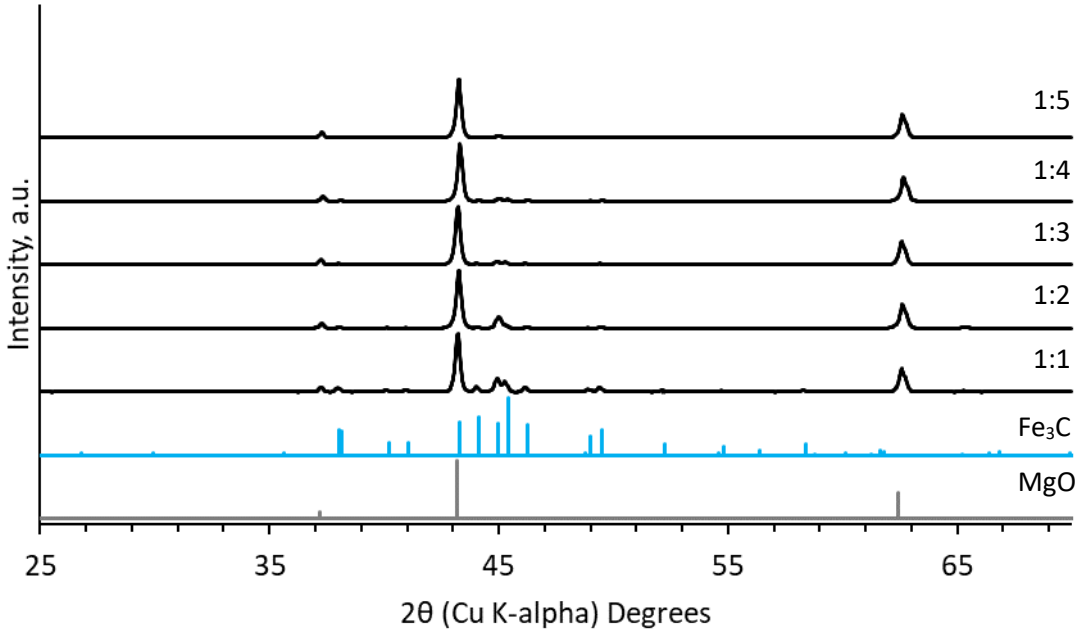

Figure 3.5 PXRD data recorded for various mass ratio mixtures of Prussian blue : MgO, calcined at 800 °C for 1 hour.

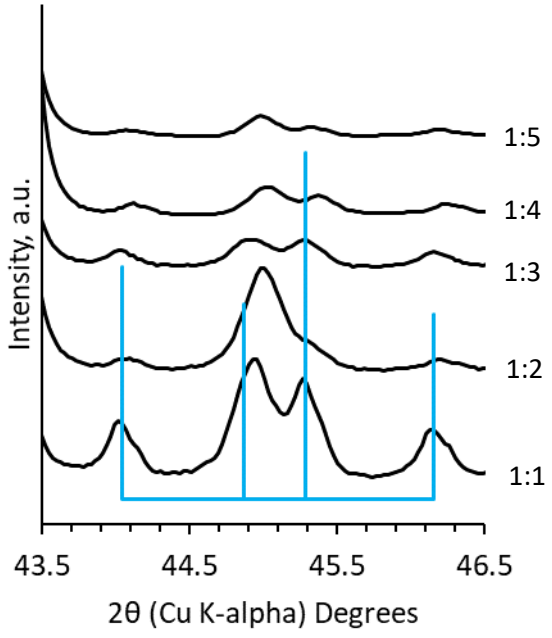

Figure 3.6 PXRD data recorded for various mass ratio mixtures of Prussian blue : MgO, calcined at 800 °C for 1 hour. Top to bottom - 1:5, 1:4, 1:3, 1:2 1:1, Fe_3C.

3.4.2.2 CTEM ANALYSIS

Fig. 3.7 shows conventional transmission electron microscopy (CTEM) micrographs recorded for each of the samples analysed by PXRD. Fig. 3.7A, which shows a sample of the bulk MgO powder that has been calcined at 800 °C for 1 hour, will be used as a control sample for comparison. In doing so, it is possible to identify several features of interest.

When Fig. 3.7B, a mixture of Fe_3C and MgO, synthesised using a 1:1 mass ratio of Prussian blue to MgO, is compared to the control sample (Fig. 3.7A), it is possible to discern small particles, with a mean particle size of approximately 31 nm, bound to the surface of the surrounding MgO matrix. Based on the presence of Fe_3C in the corresponding PXRD (Fig. 3.6) pattern it can be tentatively inferred that these particles are composed of Fe_3C. As the relative amount of MgO cast material is increased, small particles that differ in morphology to the particles in the control sample can be seen. However, unlike those seen in Fig. 3.7B, the majority of the particles do not appear to be bound directly to the MgO matrix material. Instead, these particles appear to be bound to a third phase. Based on the limited evidence provided by these micrographs, it is possible that this third phase is composed of smaller particles of MgO. However, it is also possible that this material is amorphous carbon produced by the reduction of the carbon contained within Prussian blue and PVP. The particles bound in this third phase also appear to differ significantly in size from those seen in Fig. 3.7B. With the exception of Fig. 3.7C, which was shown by PXRD to contain a significant amount of Fe^0, the results shown in subsequent samples infer that this third phase behaves differently with regards to the inhibiting sintering of our Fe_3C particles.

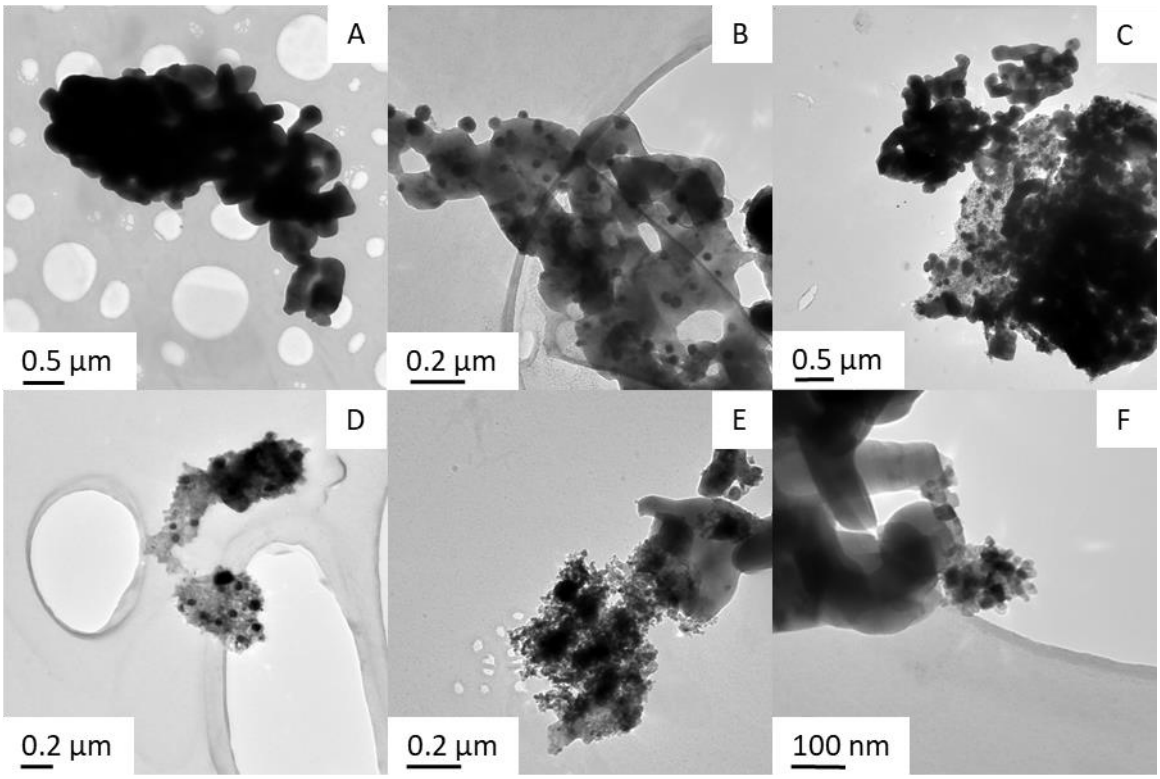

Figure 3.7 CTEM micrographs of Fe_3C/ MgO Mixtures synthesised by calcining of various mass ratio mixtures of Prussian blue : MgO, at 800 ˚C for 1 hour. **A** - MgO control, **B** - 1:1, **C** - 1:2, **D -** 1:3, **E** - 1:4, **F** - 1:5

3.4.2.3 EDX ANALYSIS

As a proof of concept, the CTEM images, along with the PXRD results, help show the promise of this process. Yet up to this point, it is hard to conclusively match the observed morphologies to specific phases. With this problem in mind, the next step was to investigate the samples with energy dispersive X-ray analysis (EDX) using the scanning transmission electron microscopy technique (STEM). This technique allowed the elemental composition of each phase to be inferred with more certainty.

Fig. 3.8 shows 2D EDX maps recorded for the sample of Fe_3C/MgO synthesised from a 1:1 mass ratio of Prussian blue : MgO. It is now possible to clearly discern each phase and its elemental composition. All samples were deposited onto holey carbon TEM grids. Thus, the web like carbon structures visible in green in the images are a contribution of this TEM grid carbon coating. Fig. 3.8A shows a cluster of <100 nm iron and carbon containing particles that while in close proximity, appear to be discrete. Fig. 3.8B on the other hand appears to show much smaller iron and carbon containing particles that appear to correspond to the small particles observed in Fig. 3.7B. The image also contains several other interesting features. Firstly, there is clear evidence of a carbon shell surrounding an iron containing particle. This observation may be of importance when considering potential applications such as catalysis in acid and basic electrolytes, as a carbon shell may help stabilise the particles when subjected to a wider pH range. A second interesting feature is the way in which the particles appears to be interacting with the MgO matrix. Rather than being dispersed throughout the matrix, the particles in Fig. 3.8B seem to be embedded into the surface of the MgO. This suggests that packing small cast particles around our template particles may not be the only mechanism available for inhibiting sintering. Exploiting interfacial interactions between the two phases may be possible.

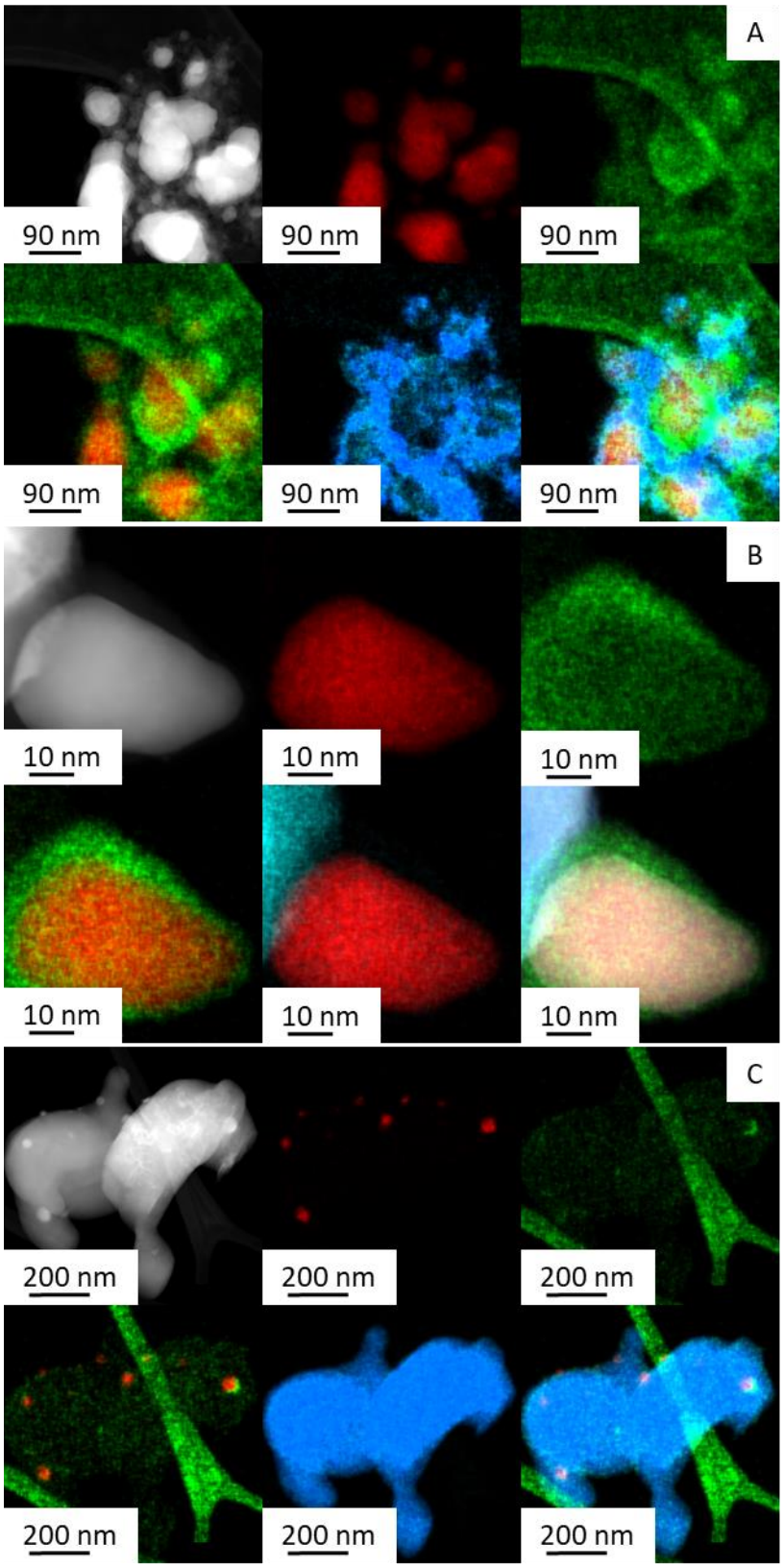

Figure 3.8A – C 2D EDX and HAADF maps recorded at various magnifications, for a Fe_3C/MgO mixture synthesised by calcining a **1:1** mass ratio of Prussian blue : MgO Bulk Powder. HAADF, Fe, C, O, Mg.

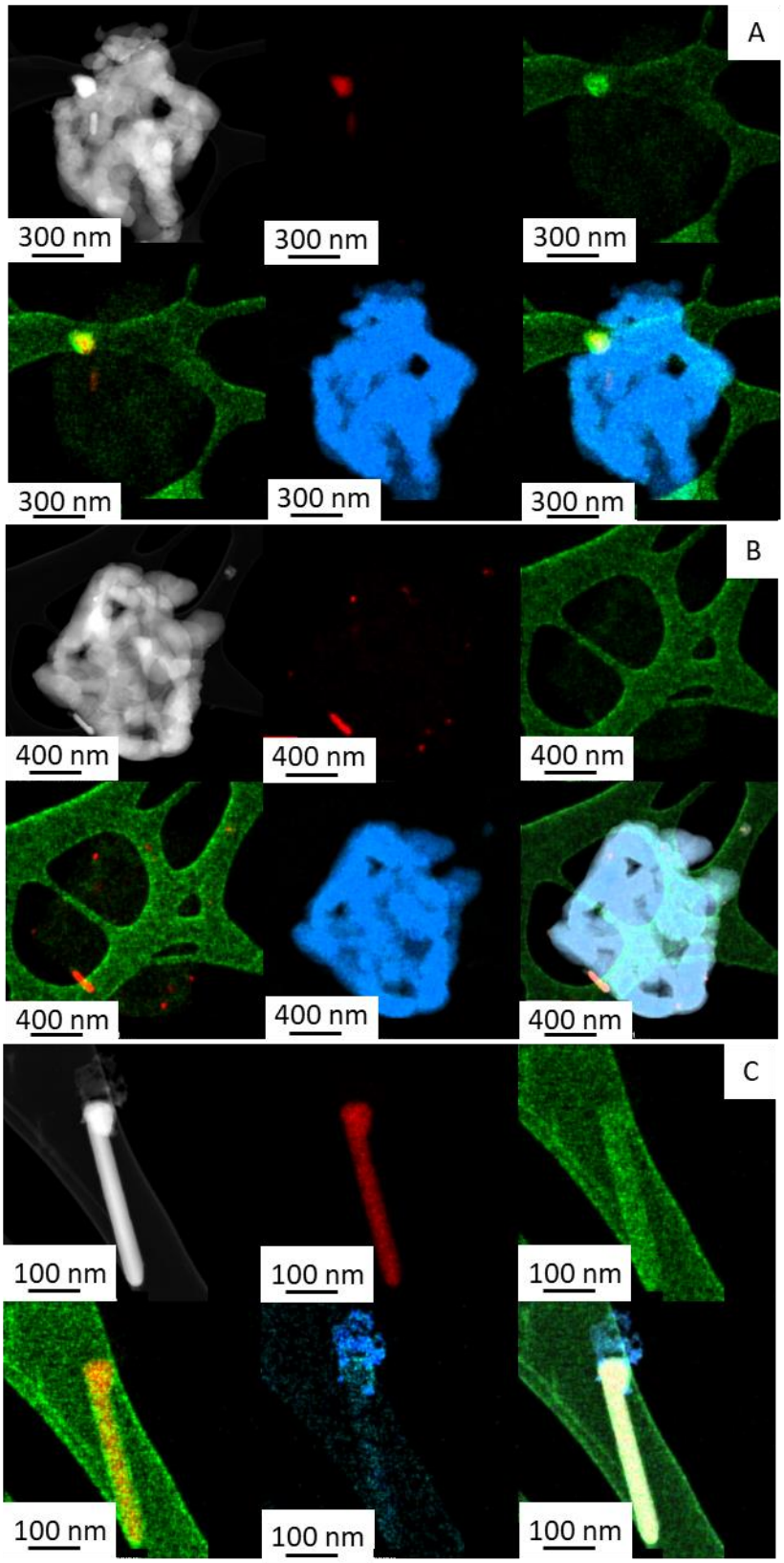

Figure 3.9A-C 2D EDX and HAADF maps recorded at various magnifications, for a Fe_3C/MgO mixture synthesised by calcining a **1:3** mass ratio of Prussian blue : MgO Bulk Powder. HAADF, Fe, C, O, Mg.

This point ties in nicely to observations made on the EDX maps recorded for the sample synthesised from a 3:1 mix of Prussian blue : MgO (Fig. 3.9). In this sample there are multiple examples of iron and carbon containing rods, one of which can be seen in Fig. 3.9b and one of which can be seen in Fig. 3.9c. These are observations that are unique to this sample. It is possible that an interaction between the precursor particles and the cast during calcination is causing this unique morphology. Fig. 3.9C for example, appears to show MgO clustered around an iron and carbon containing particle situated at the end of a rod. It is possible that the MgO has somehow aided in the transport of the iron/carbon particle, seeding a nanorod in the process.

3.4.2.4 TOMOGRAPHY ANALYSIS

Following on from the CTEM and EDX observations that suggest the Fe_3C particles in this system are bound to the surface of the MgO matrix, tomography performed using STEM was used to provide further evidence.

Tomography was performed on the sample used to create the 2D EDX maps, that is, the sample synthesised using a 1:1 mass ratio of Prussian blue to MgO. Fig. 3.10 shows a set of high annular angle dark field (HAADF) images in which heavier elements have a higher scattering factor and therefore appear brighter. Unfortunately, the contrast between elements is not substantial in these images, but when compared to Fig. 3.11, in which Fe and Mg can be differentiated by EDX analysis, the images appear to show iron containing particles bound to the surface of a larger Mg containing piece of material. Although these images are

at the resolution limit for this technique, coupled with the CTEM and EDX data, the results seem to corroborate one another.

To summarise, this system appears to be capable of producing Fe_3C particles with diameters well below 100 nm with the particles, in some cases, appearing to be embedded in the MgO surface. In other cases, iron carbide nanorods appear to have been seeded. However, care must be taken when attempting to make a conclusive judgement on this matter as the EDX maps collected cannot provide crystallographic information. For a more conclusive judgement about the nature of the crystalline phases present in these nanorods selected area electron diffraction (SAED) may be of use. This would allow for the observation of lattice planes in a localised area, allowing for the acquisition of the crystallographic information required to identify Fe_3C.

The presence of nanorods and unexpected small nanoparticles may also suggest that a more complicated decomposition process may be occurring than first thought. It may be the case for the small embedded nanoparticles, that iron is dissolving into the MgO and then precipitating back out to form Fe_3C. In addition to this, in the case of the observed nanorods, the MgO crystal surfaces may be acting as a seed, potentially through a form of heteroepitaxial growth in which a crystallographic plane of one phase can act as a seed for a second phase. Fe_3C is orthorhombic with a=5.09 Å, b=6.74 Å and c= 4.53 Å lattice parameters (PDF-00-034-001), whereas MgO is cubic with a=4.326 Å (PDF-00-004-0829). Thus, there would be a significant amount of strain which while not disproving the idea, does not necessarily support the idea either. Although these possibilities are not explored in this thesis, they are worth mentioning as they may warrant further research.

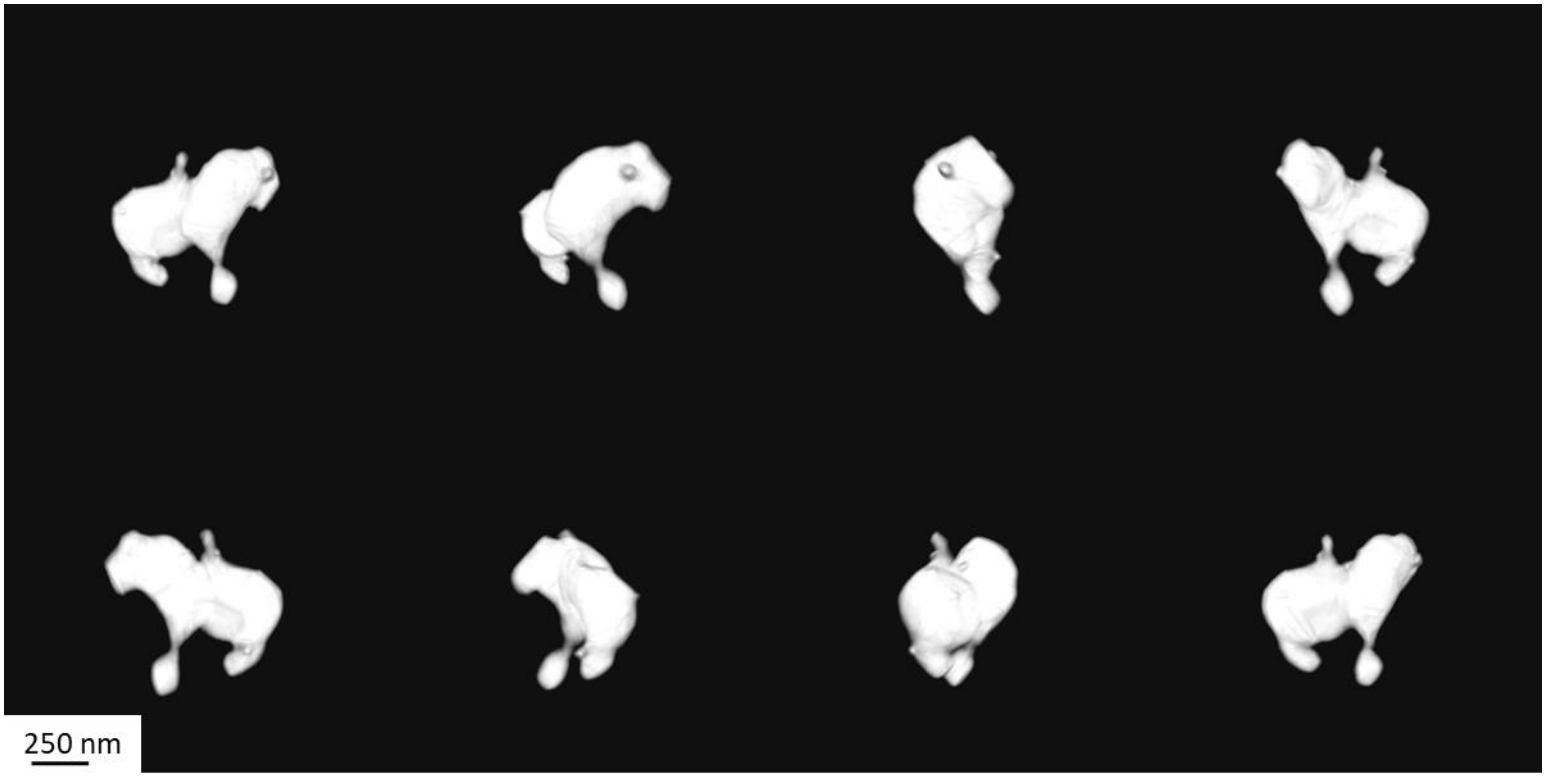

Figure 3.10 3D High Annular Angle Dark Field (HAADF) Tomography performed by STEM, recorded for a Fe_3C/MgO mixture synthesised by calcining a 1:1 mass ratio of Prussian blue : MgO bulk powder

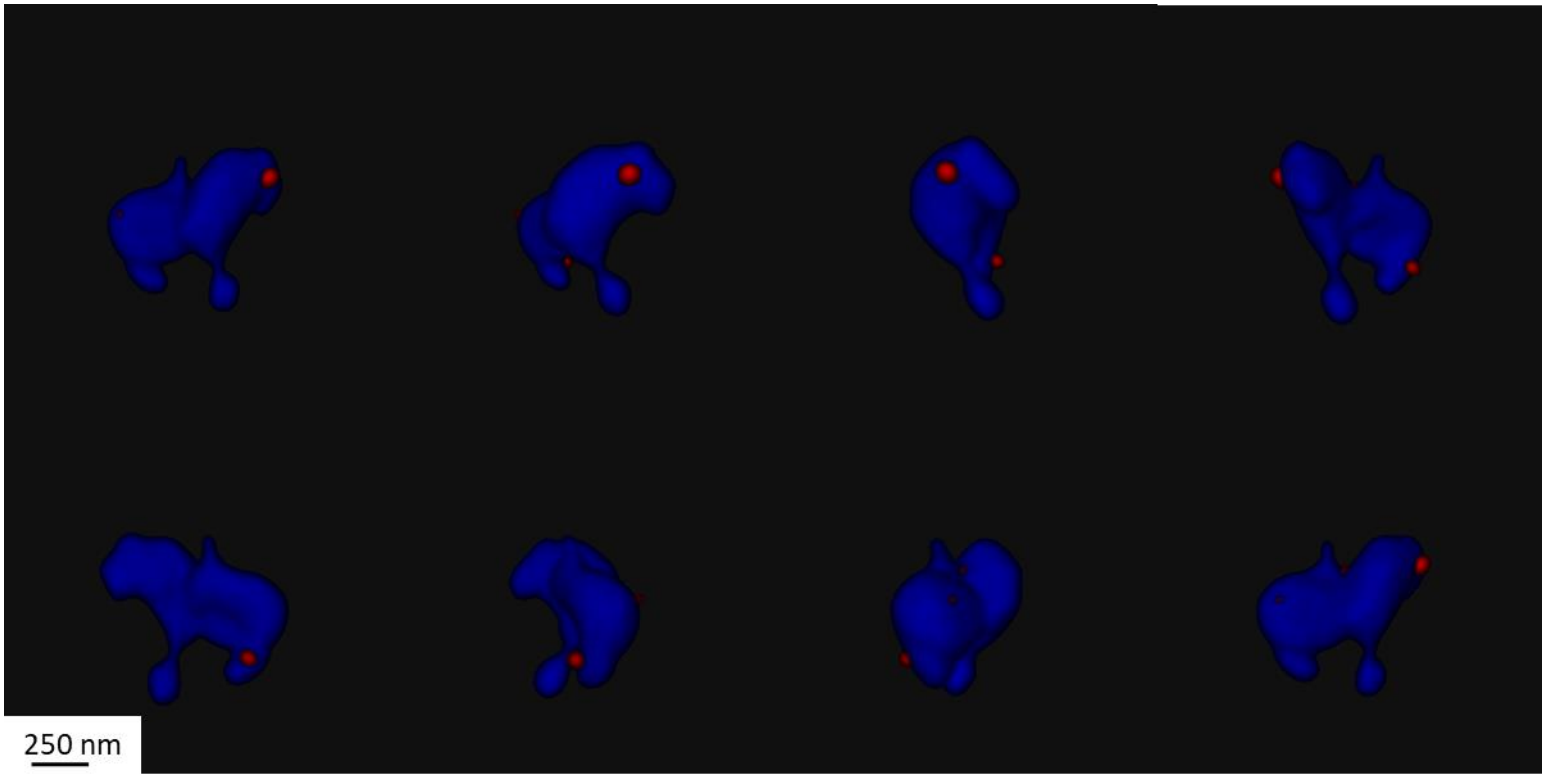

Figure 3.11 3D EDX Tomography performed by STEM, recorded for a Fe_3C/MgO mixture synthesised by calcining a 1:1 mass ratio of Prussian blue : MgO bulk powder, Fe, Mg

3.4.3 INCORPORATION OF AN MgO NANOPOWDER CAST

The previous section has shown how bulk MgO powder can affect the morphology of our templated Fe_3C nanoparticles in interesting ways. However, in closer keeping with the original concept of packing cast particles closely around our template particles, the use of an MgO nanopowder was examined next.

3.4.3.1 PXRD ANALYSIS

Having demonstrated the use of a bulk MgO nanopowder as a chemically compatible cast material, the effects of increasing the MgO surface area was next to be examined. The increased number of surface hydroxyl groups, other dangling bonds and adsorbed water for example, could potentially have unforeseen consequences on the Prussian blue decomposition process. An experiment analogous to the one performed on the bulk powder was therefore performed, in which 1:1, 1:2, 1:3, 1:4 and 1:5 mass ratios of soluble Prussian blue : MgO nanopowder were calcined and then examined by PXRD (Fig. 3.12).

Examination of the 43.5°-46.5° 2θ range (Fig. 3.13) shows that for this cast material, Fe_3C has only been successfully formed in the 1:1, 1:2 and 1:3 mixtures, with a small peak corresponding to Fe^0 seen in the 1:5 mixture. Thus, it appears that changing the morphology of the cast does have a knock-on effect on the composition of the product in this process, particularly as the amount of cast material relative to Prussian blue is increased. Yet at lower ratios the process is still successful.

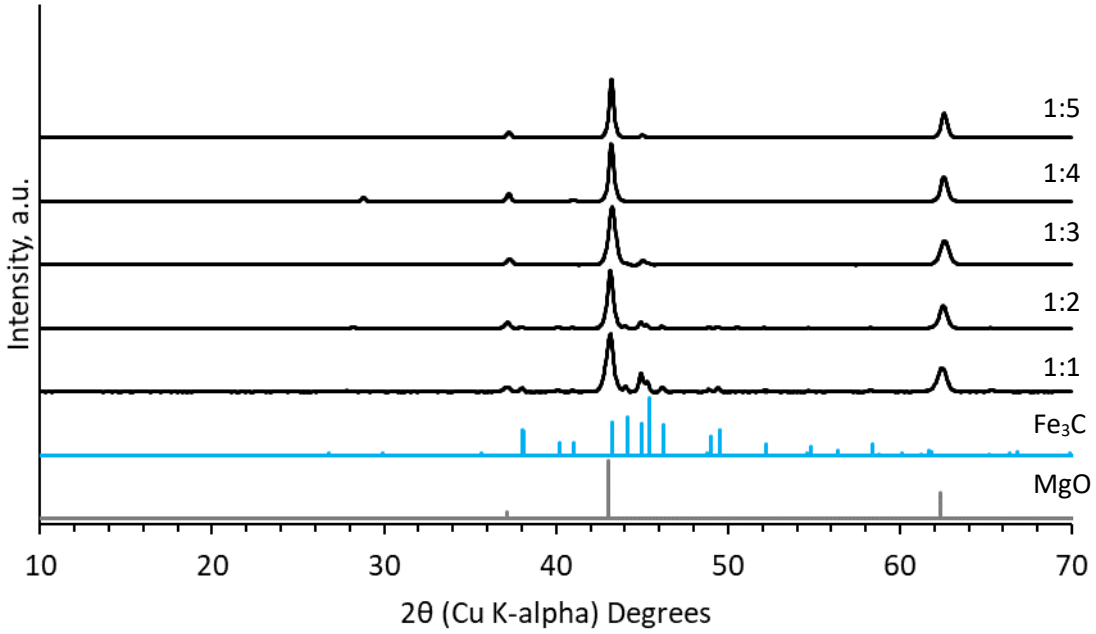

Figure 3.12 PXRD data recorded for various mass ratio mixtures of Prussian blue : MgO nanopowder, calcined at 800 °C for 1 hour.

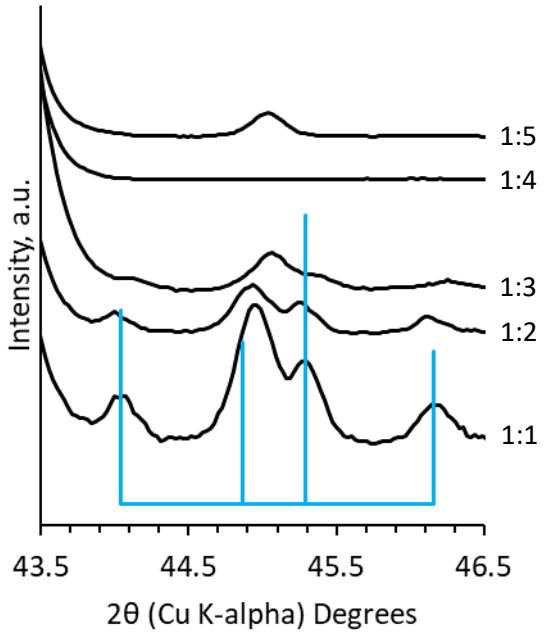

Figure 3.13 PXRD data recorded for various mass ratio mixtures of Prussian blue : MgO nanopowder, calcined at 800 °C for 1 hour. Top to bottom - 1:5, 1:4, 1:3, 1:2, 1:1, Fe_3C.

3.4.3.2 CTEM ANALYSIS

The next stage was to examine how the nanopowder affected the morphology of the Fe_3C particles and if, as hoped, the MgO particles were able to pack themselves around the Fe_3C particles.

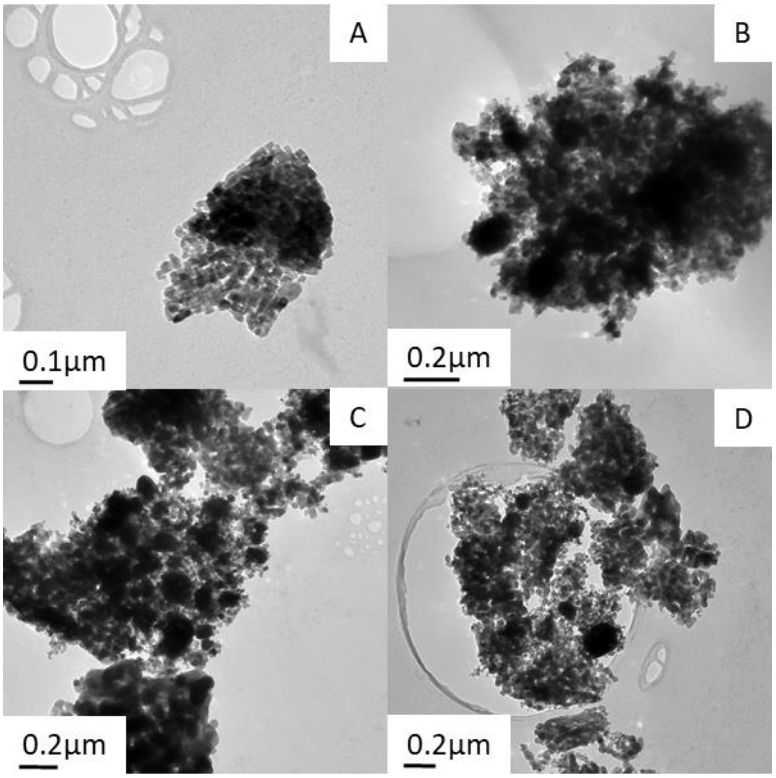

Figure 3.14 CTEM micrographs of Fe_3C : MgO mixtures synthesised by calcination of various mass ratio mixtures of Prussian blue : MgO nanopowder, at 800 °C for 1 hour. **A** - MgO control, **B** - 1:1, **C** - 1:2, **D** - 1:3, E - 1:4, F - 1:5

CTEM was performed on a control sample of MgO nanopowder calcined at 800 °C (Fig. 3.14A), as well as the samples synthesised from 1:1, 1:2 and 1:3 mass ratios of Prussian blue : MgO, in which Fe_3C had been successfully formed. The first key observations relate to the control sample. Whereas the bulk powder control sample (Fig. 3.8A) was composed of large agglomerates of MgO >1 μm in diameter, the nanopowder control sample (Fig. 3.14A) is composed of much smaller <100 nm diameter particles as hoped.

Moving on to Figs. 3.14A-C, darker spots can be seen, which while possibly just corresponding to thicker parts of the sample, in some cases appear to be particles of a separate phase, potentially Fe_3C. The initial results were promising as many of the suspected Fe_3C particles were close to 100 nm in diameter and importantly, they appear to be discrete.

3.4.3.3 EDX ANALYSIS

As the CTEM results were promising, yet somewhat ambiguous, EDX analysis was performed on each of the three samples in which Fe_3C had been successfully formed. Figs. 3.15 to 3.17 show 2D maps recorded for the successful samples examined in the previous two sections, which help clarify which features belong to which phases. The maps appear to confirm that the darker regions seen in the CTEM micrographs are indeed iron and carbon containing particles.

Fig. 3.15 shows that for a Prussian blue : MgO mass ratio of 1:1 the resulting calcined product contains discrete particles that are significantly larger than those seen for the bulk MgO powder cast, although even the larger particles seem to remain below 500 nm in diameter. As alluded to, it is also important to note the iron carbide particles are polydisperse, so while

promising, further tuning of Prussian blue particle size and anti-sintering performance would be desirable. There also seems to be little difference in sintering inhibition as the relative amount of cast is increased, when comparing Figs. 3.15 – 3.17.

The iron carbide particles also seem to be dispersed throughout the MgO nanopowder rather than embedded into the surface of larger agglomerates as they were in the bulk powder samples, suggesting the cast is inhibiting the sintering of our template particles in a manner closer to that which was initially expected. A closer inspection of the iron carbide particles shown in Fig. 3.15B also reveals the presence of carbon rich shells, which again, is another desirable property for applications in which the particles need to be stabilised in acid/basic media such as oxygen reduction reaction catalysis.

Another interesting observation which becomes particularly noticeable as the Prussian blue : MgO ratio is decreased, is that the iron concentration seems to spread out beyond the boundaries of the discrete particles (Fig. 3.16 and 3.17). That is to say, it appears that a significant amount of Fe may have dissolved into the MgO cast. Given the fact that both MgO (PDF-00-004-0829) and FeO (PDF-01-089-0687) have cubic crystal structures with the *Fm*-3*m* space group, and reported lattice parameters of 4.213 Å and 4.307 Å respectively, this kind of doping seems entirely possible.

There is also evidence of a significant amount of C spread beyond the boundaries of the particles. While it is an interesting possibility that very small Fe_3C particles may be forming as Fe precipitates out of the Fe doped MgO cast, it is also likely that this carbon is simply residual amorphous carbon left over from the reduction of the polymer surfactant in the anaerobic conditions used during calcination.

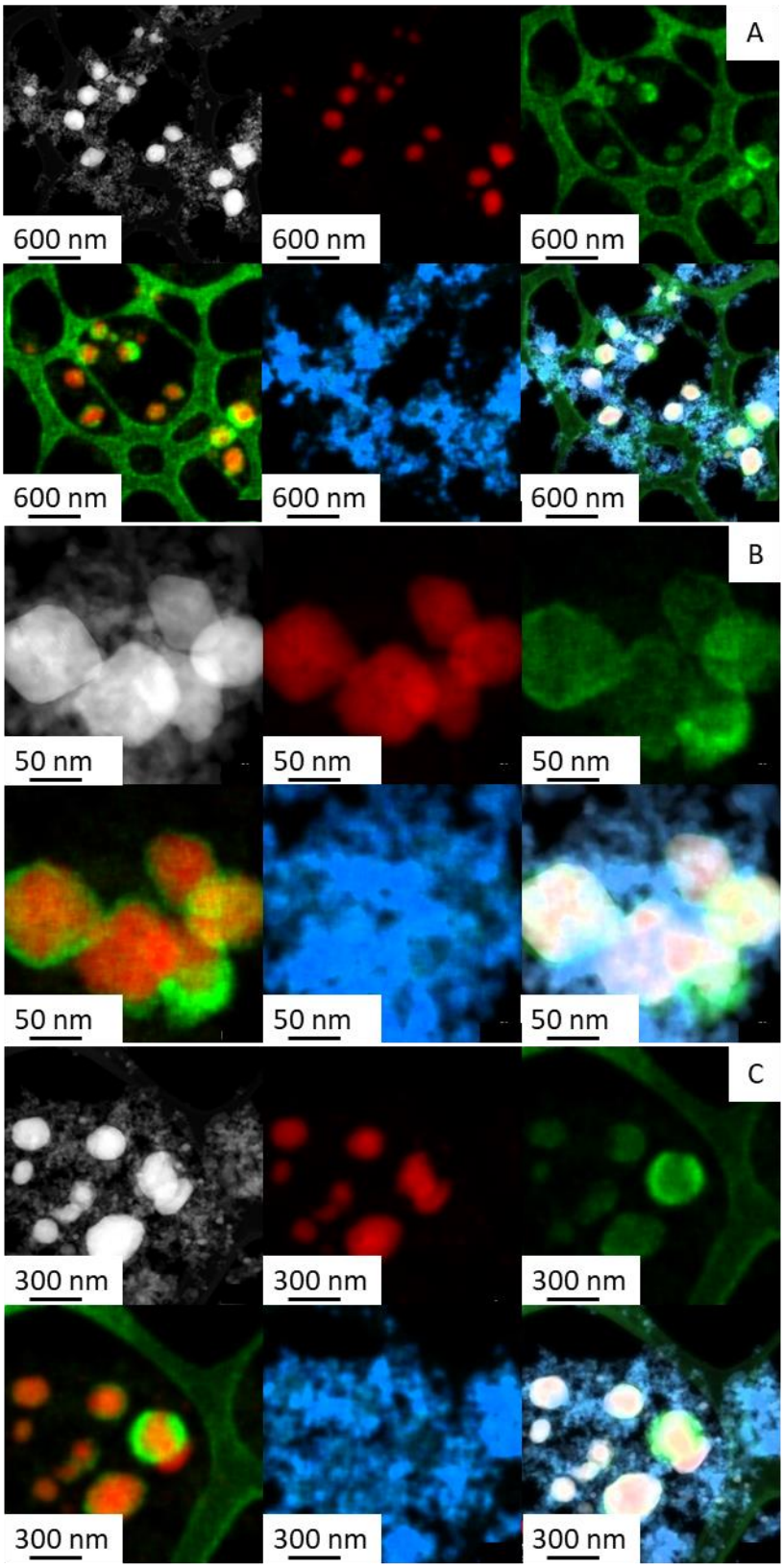

Figure 3.15A-C 2D EDX and HAADF maps recorded at various magnifications, for a Fe_3C/MgO mixture synthesised by calcining a **1:1** mass ratio of Prussian blue : MgO nanopowder. HAADF, Fe, C, O, Mg.

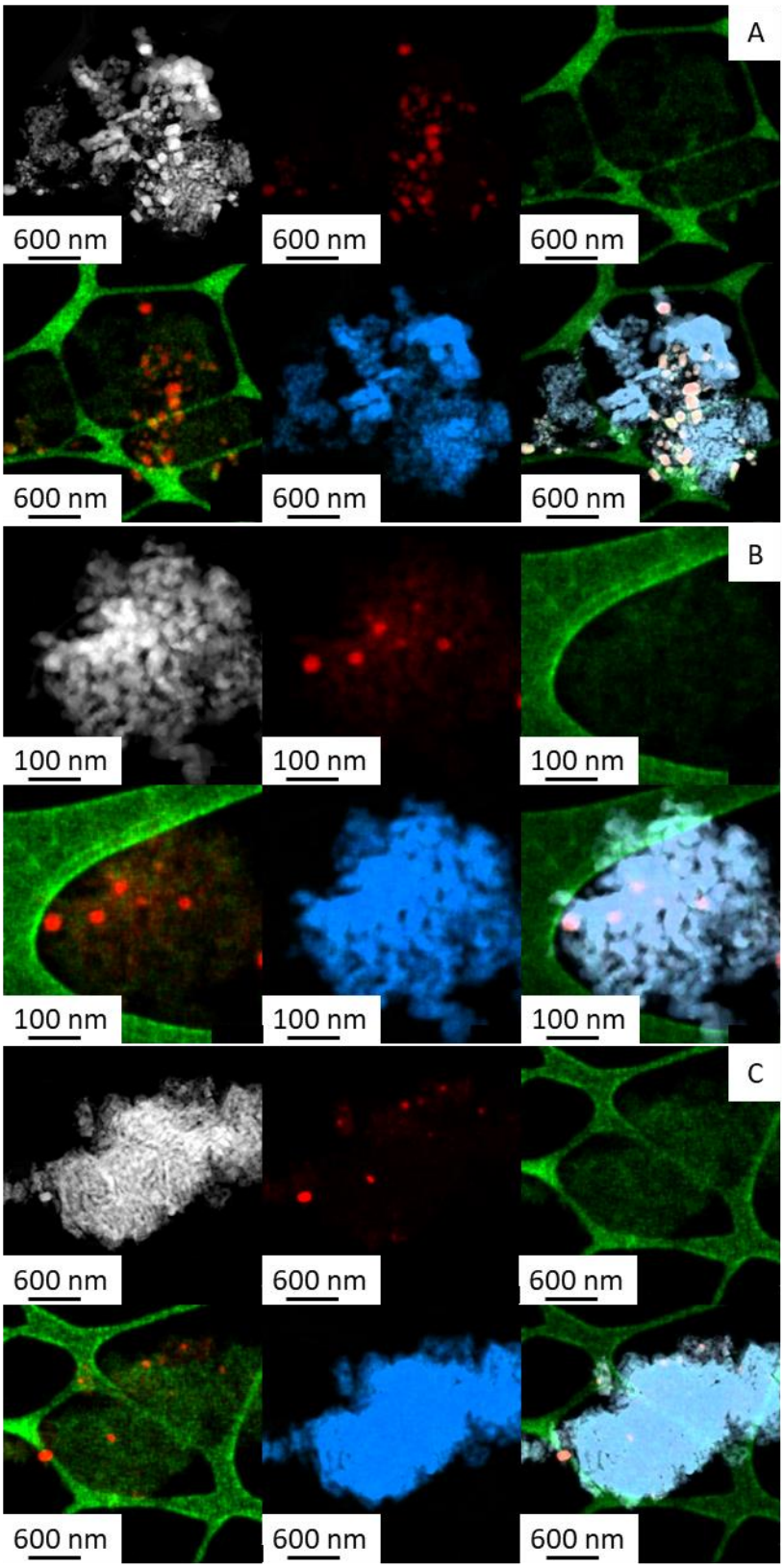

Figure 3.16A-C 2D EDX and HAADF maps recorded at various magnifications, for a Fe_3C/MgO mixture synthesised by calcining a **1:2** mass ratio of Prussian blue : MgO nanopowder. HAADF, Fe, C, O, Mg.

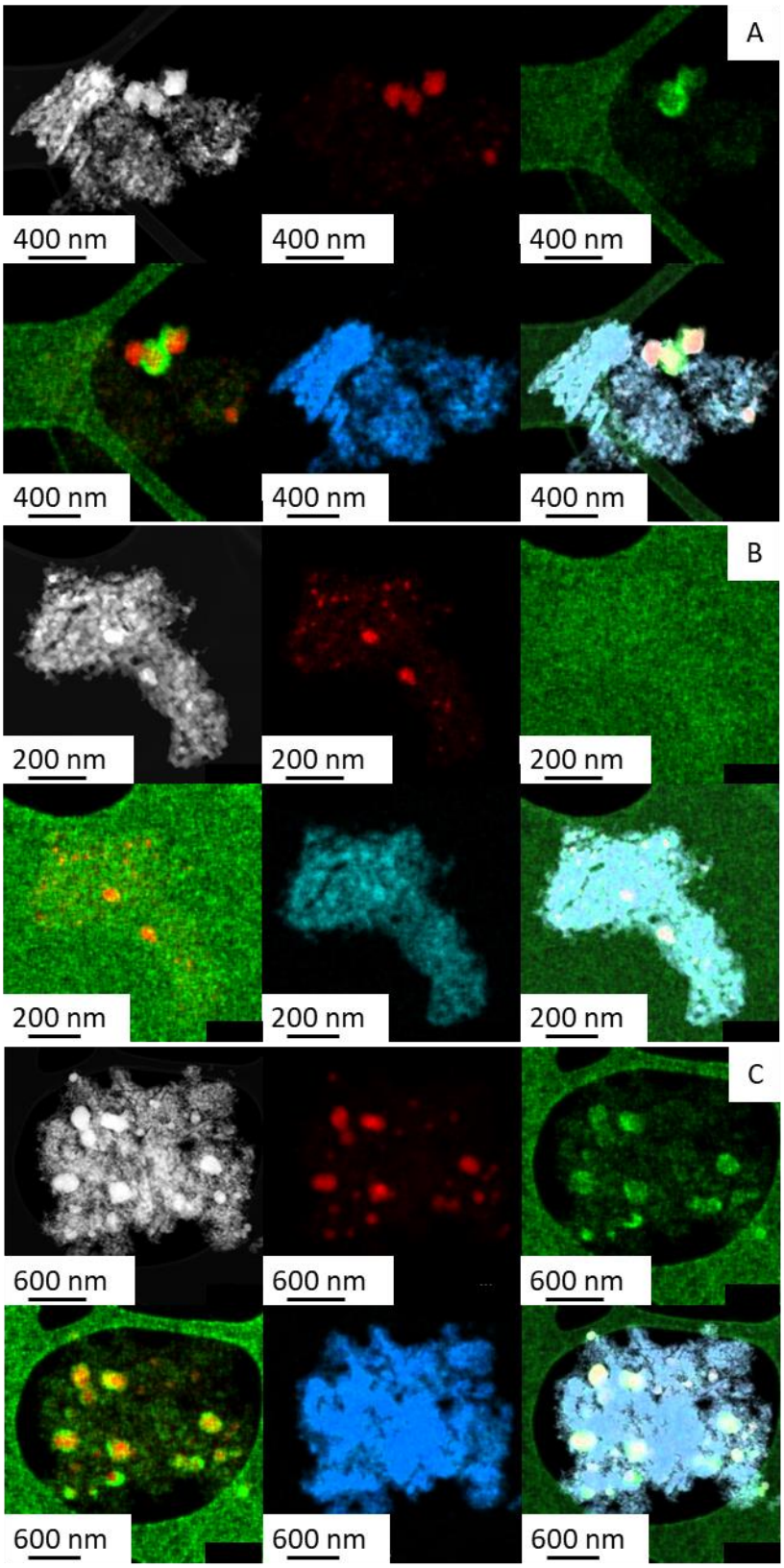

Figure 3.17A-C 2D EDX and HAADF maps recorded at various magnifications, for a Fe_3C/MgO mixture synthesised by calcining a **1:3** mass ratio of Prussian blue : MgO nanopowder. HAADF, Fe, C, O, Mg.

3.4.3.4 TOMOGRAPHY ANALYSIS

To gain a better insight into the manner in which the Fe_3C particles are mixed in with the cast particles, tomography was performed on the sample synthesised from a 1:1 Prussian blue : MgO nanopowder mass ratio. It is possible to identify two distinct phases containing elements of significantly different atomic mass in the HAADF images in Fig. 3.18. The brighter areas are likely to correspond to the Fe rich Fe_3C particles and the dimmer surrounding areas are likely to correspond to the MgO cast. This is corroborated by the EDX tomography shown in Fig. 3.19 in which the two phases can be clearly differentiated as Fe containing and Mg containing, but at a slightly lower resolution. Unfortunately, the limited resolution of this technique also means that it is not possible to detect the Fe/C concentrations seen beyond the larger particle boundaries in the 2D EDX maps.

The images in both Figs. 3.18 and 3.19 also seem to support the idea that the Fe_3C particles are mixed into the powder in a more homogeneous fashion than the Fe_3C particles observed in the bulk MgO powder cast. This lends weight to the argument that the two cast morphologies inhibit sintering in their own distinct ways.

In summary, the use of a MgO nanopowder cast appears to inhibit sintering by a mechanism closer to the original aim. The cast particles seem to pack around the precursor template particles, physically preventing them from sintering during the calcination process. The product Fe_3C particles are polydisperse yet still appear to have diameters of no more than a few hundred nanometres.

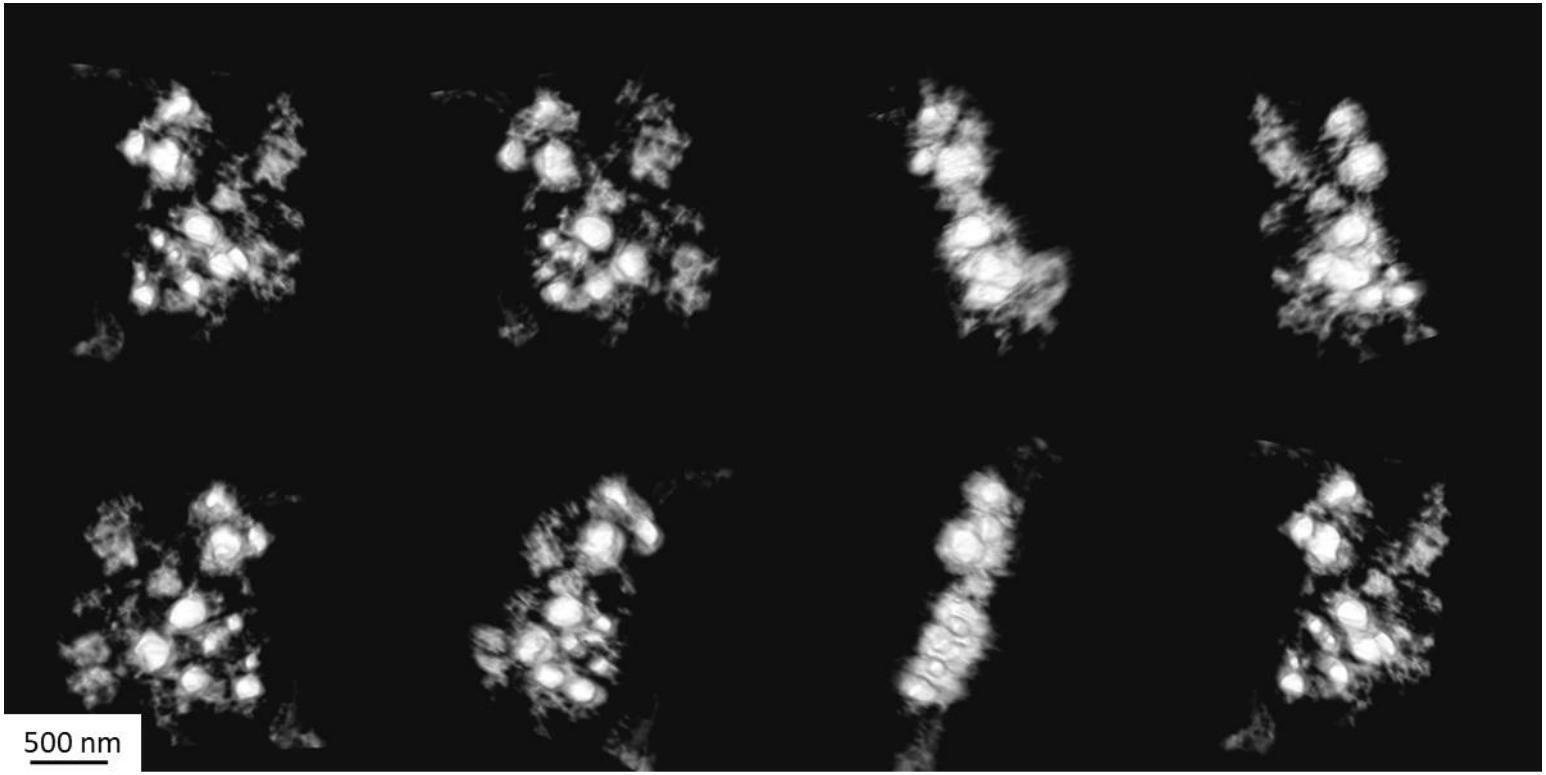

Figure 3.18 3D High Annular Angle Dark Field (HAADF) Tomography performed by STEM, recorded for a Fe_3C/MgO mixture synthesised by calcining a 1:1 mass ratio of Prussian blue : MgO nanopowder

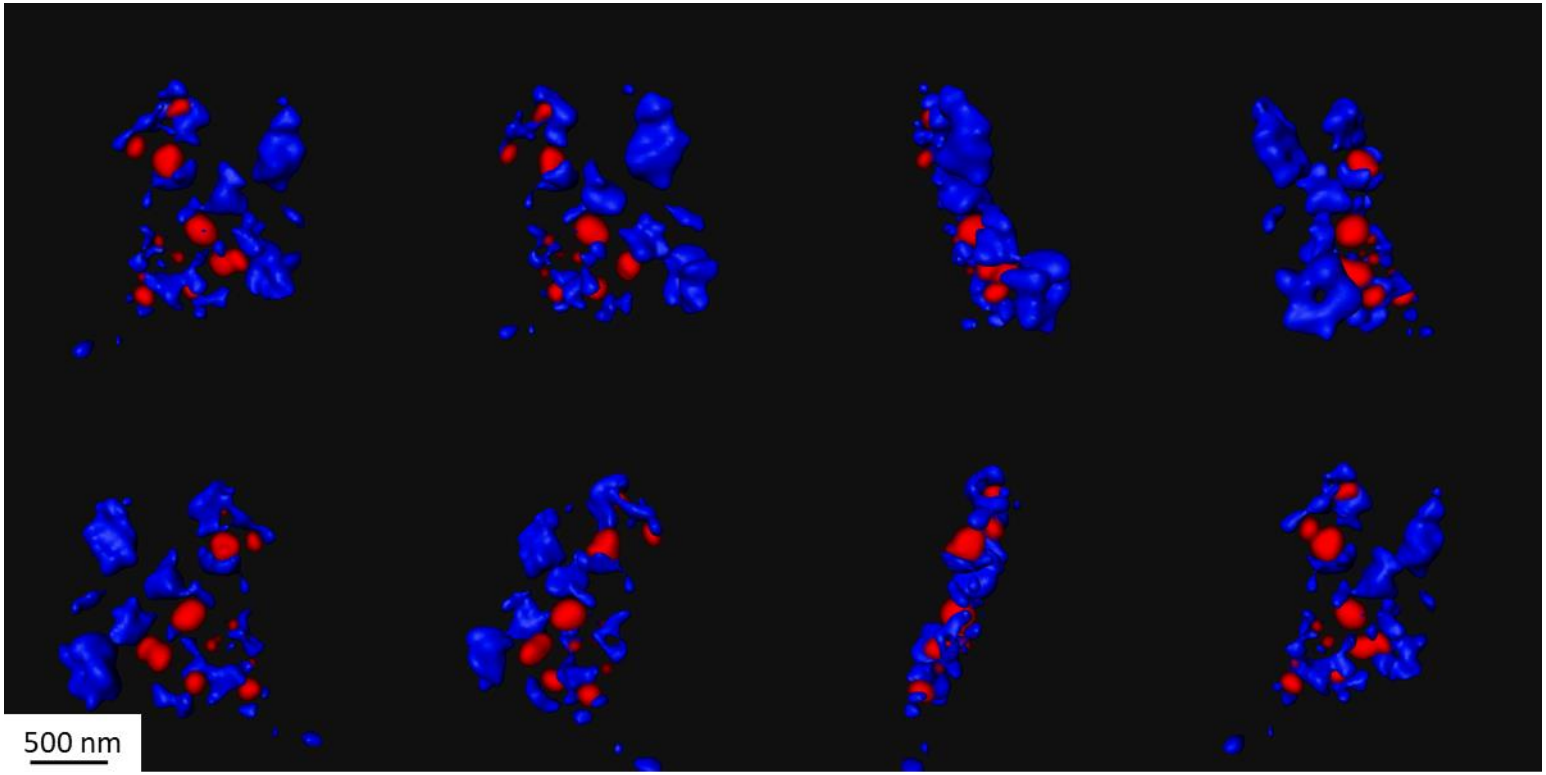

Figure 3.19 3D EDX Tomography performed by STEM, recorded for a Fe_3C/MgO mixture synthesised by calcining a 1:1 mass ratio of Prussian blue : MgO nanopowder, Fe, Mg

3.4.4 INCORPORATION OF A MgO MONOLITH CAST

Using the synthesis of CeO_2/Au nanocomposites by Schnepp *et al.*[130] (Fig. 3.20) as inspiration, a sponge like network of MgO nanoparticles was synthesised for use as a cast material. The biopolymer Agar was used to help aid in the controlled formation of the network, resulting in a material with hierarchical porosity. It was hoped that the mesopores seen in Figs. 3.21A and 3.21B might trap the Prussian blue template particles, immobilising them during calcination and that the macroporosity seen in Figs. 3.21C would allow for the flow of a colloidal sol of Prussian blue deep into the porous network.

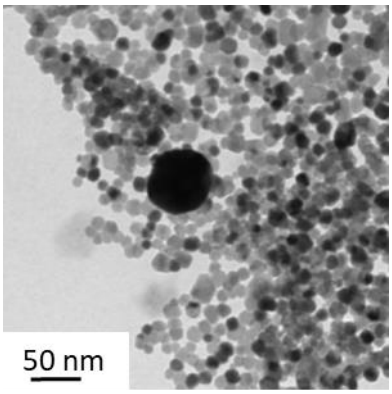

Figure 3.20 CTEM micrograph of an Au nanoparticle forming a nanocomposite with a CeO_2 nanostructure[130].

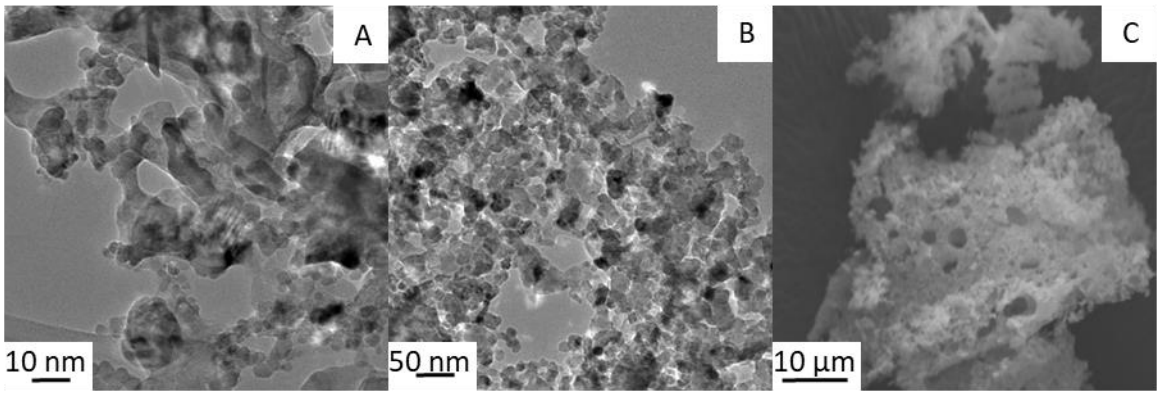

Figure 3.21 A and **B** – CTEM micrographs showing the mesoporosity found in our MgO monolith, C - SEM image showing the sponge like macroporosity found in our MgO monolith.

3.4.4.1 PXRD ANALYSIS

As was the case for the two previously examined MgO cast morphologies, the first step in the analysis of this new material was to characterise samples synthesised by calcining 1:1, 1:2, 1:3, 1:4 and 1:5 mass ratios of Prussian blue to cast material. PXRD analysis shows that for the first three mass ratios Fe_3C has been successfully formed. Whereas the 1:4 ratio gives diffraction peaks that correspond to FeN and Fe^0 and the 1:5 ratio simply gives Fe^0. Thus, the 1:4 and 1:5 mass ratios were not examined further for the purposes of this work. The full PXRD data set for this analysis can be seen in Fig. 3.22, with a closer examination of the 43.5° – 46.5° 2θ range given in Fig. 3.23.

It is possible that the larger surface area of this cast material means that at higher cast concentrations surface chemistry becomes far more important. Moisture adsorbed onto the surface of the cast may be playing a role for example.

Another interesting point to note about this cast material is that if the calcination is performed at 700 °C and held for just 1 minute, rather than 800 °C, for a 1:1 mass ratio, it is possible to reproducibly synthesise Fe_3N rather than Fe_3C. In order to test just how reproducible this result was, mixtures of MgO monolith and Prussian blue were stored overnight in a humid environment, a conventional oven (70 °C) and a vacuum oven in order to investigate moisture content as a causative factor. The samples were then calcined at 700 °C and 800 °C, with all synthesis performed in duplicate. In each case the observation held true, with X-ray diffraction patterns containing peaks corresponding to $Fe_3N_{0.97}$ and MgO produced for each sample calcined at 700 °C (Fig. 3.24).

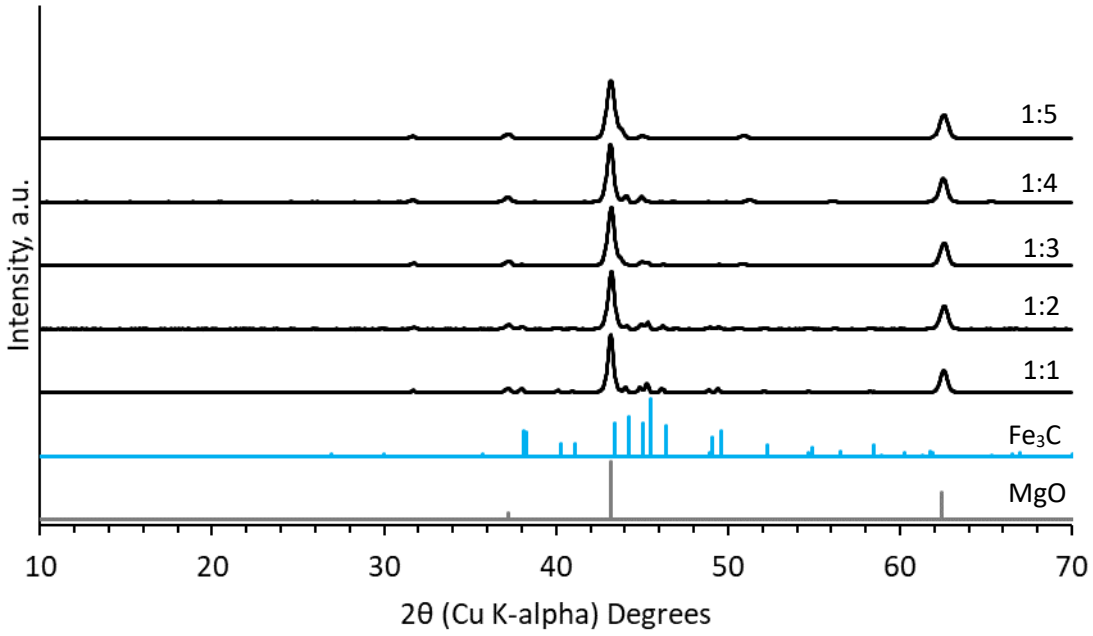

Figure 3.22 PXRD data recorded for various mass ratio mixtures of Prussian blue : MgO monolith, calcined at 800 °C for 1 hour.

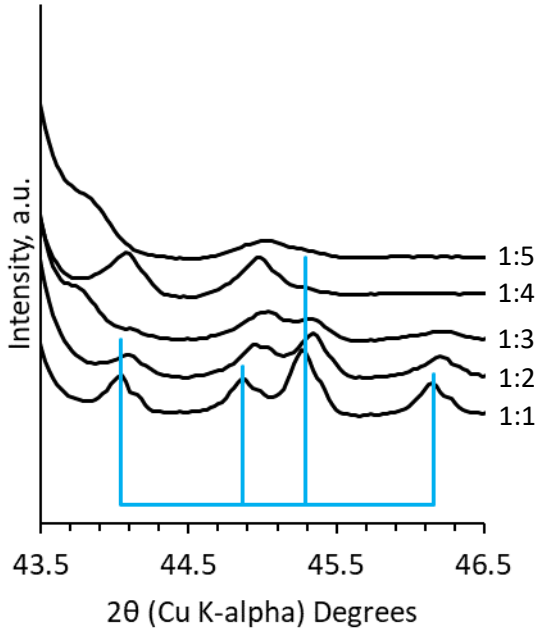

Figure 3.23 PXRD recorded for various mass ratio mixtures of Prussian blue : MgO monolith, calcined at 800 ˚C for 1 hour. Top to bottom - 1:5, 1:4, 1:3, 1:2 1:1, Fe_3C.

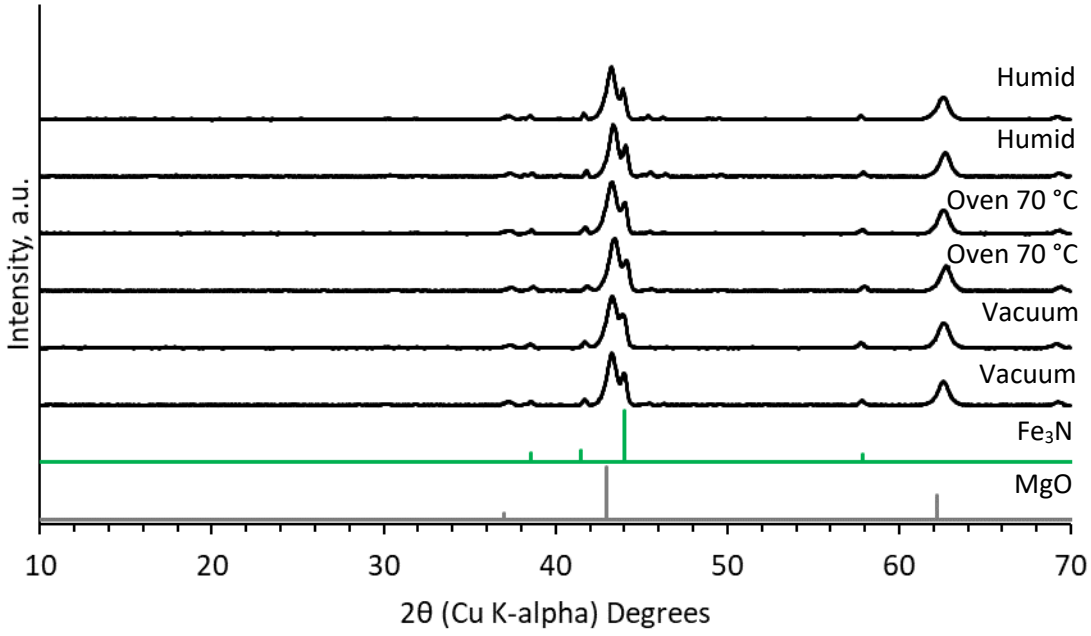

Figure 3.24 PXRD data recorded for Fe_3N/MgO mixtures formed by calcining 1:1 mixtures of Prussian blue : MgO monolith, at 700 ˚C for 1 min. Top to bottom – Stored in a humid environment x2, dried in a conventional oven x2, dried under vacuum x2, Fe_3N, MgO

Although this result is not examined further in this thesis, ε-iron nitride is an industrially useful material due to its high magnetic susceptibility. Thus, the result is worth mentioning here for the purposes of any potential future work.

3.4.4.2 CTEM ANALYSIS

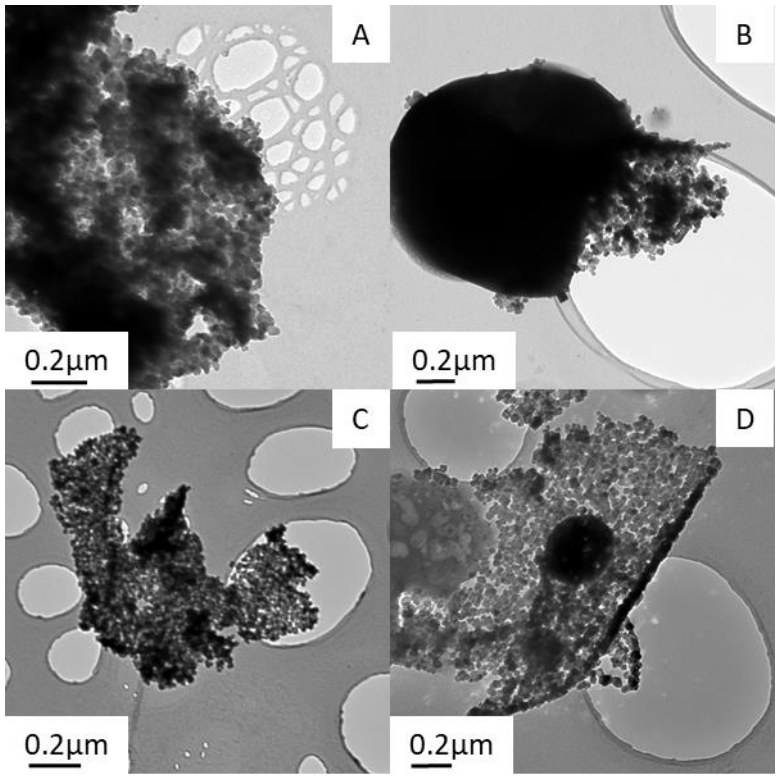

Figure 3.25 CTEM micrographs of Fe_3C/ MgO mixtures synthesised by calcining of various mass ratio mixtures of Prussian blue : MgO monolith, at 800 ˚C for 1 hour. **A** – MgO control, **B** - 1:1, **C** – 1:2, **D** – 1:3

Initial screening of the samples in which Fe_3C had been formed proved more difficult here than for the samples synthesised with the previous two cast materials. When examining the

control sample, calcined at 800 °C (Fig. 3.25A) the material seemed to be less uniform in thickness making it a challenge to discern which parts of Figs. 3.25B and 3.25C are separate phases and which parts are simply thicker pieces of cast. Fig. 3.25D on the other hand quite clearly shows a particle of a separate phase, approximately 200 nm in diameter. Likewise, Fig. 3.25D shows a very large agglomerate over 0.5 μm in diameter that appears to be a separate phase, yet these were not particularly representative of the sample at large meaning any assumptions about the sample had to be made with extra care.

Thus, despite the promising PXRD data produced for the samples synthesised at lower cast concentrations, it was difficult to determine the effectiveness of the cast at this stage, based solely on these micrographs.

3.4.4.3 EDX ANALYSIS

Fortunately, further analysis of the 1:1 and 1:2 samples by EDX was much more productive than the CTEM analysis. Again, as with the previous cast morphologies, the EDX maps (Figs. 3.26 and 3.27) show discrete iron and carbon containing particles, yet there are some key differences compared to the other casts. One of the most noticeable differences is that unlike the MgO nanopowder cast, there does not seem to be any evidence of Fe doping into the MgO monolith cast. Conversely, there does appear to be a significant amount of excess carbon. As was postulated for the nanopowder samples, this is likely to be amorphous carbon resulting from the calcination of the polymer surfactant that coats the Prussian blue template particles.

There also seems to be a much lower density of Fe_3C particles in the MgO monolith samples. This is a particularly encouraging observation given the aim of this work is to inhibit sintering

by physically separating the template particles during calcination. It is also not an unexpected result as the cast has a high surface area, resulting from its hierarchical porosity.

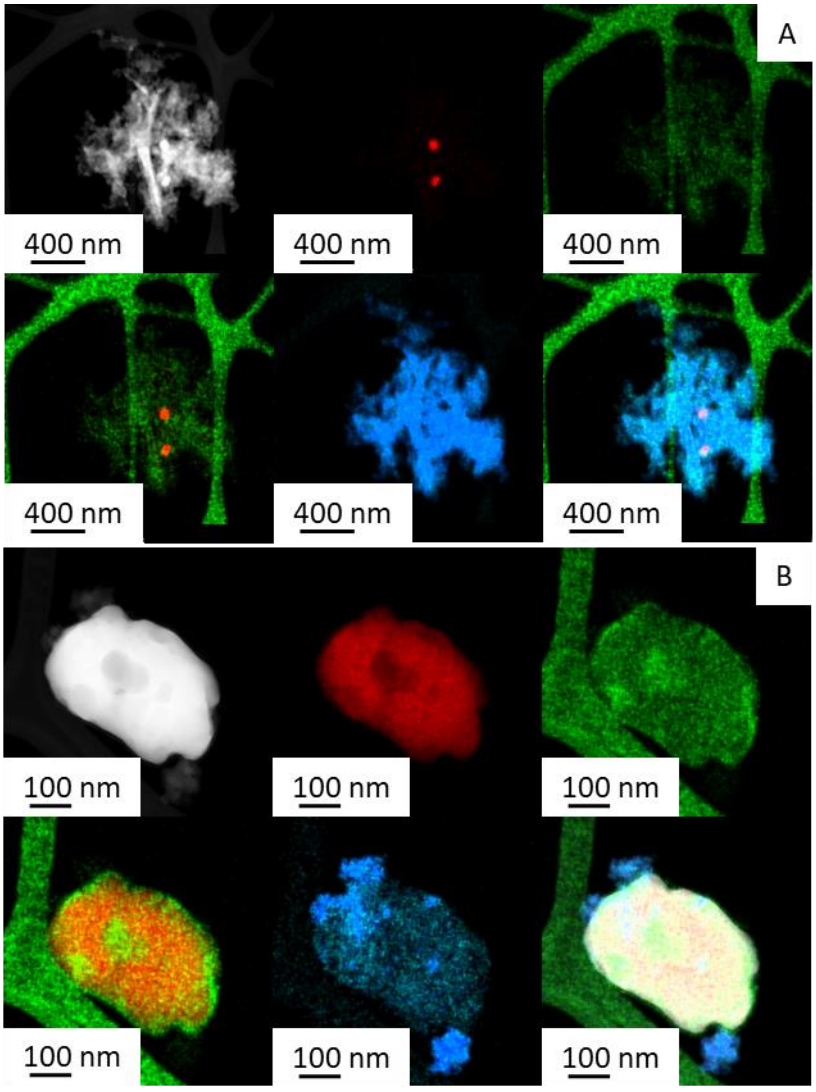

Figure 3.26A-C 2D EDX and HAADF maps recorded, at various magnifications, for a Fe_3C/MgO mixture synthesised by calcining a **1:1** mass ratio of Prussian blue : MgO monolith cast. HAADF, Fe, C, O, Mg.

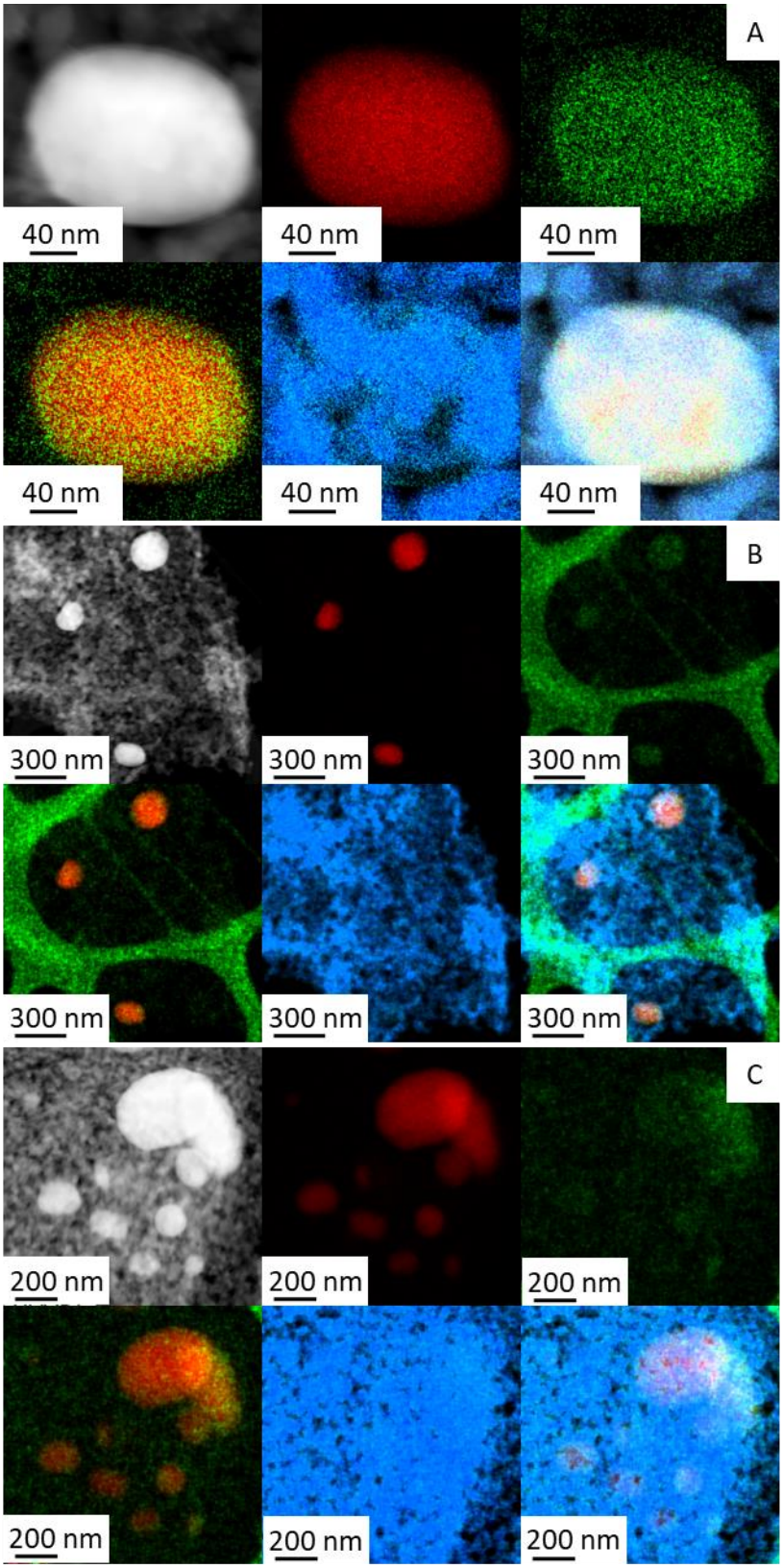

Figure 3.27A-C 2D EDX and HAADF maps recorded at various magnifications, for a Fe_3C/MgO mixture synthesised by calcining a **1:2** mass ratio of Prussian blue : MgO monolith cast. HAADF, Fe, C, O, Mg.

As for the morphology of the product Fe_3C nanoparticles, like the MgO nanopowder cast samples, there is far less evidence of a high population of <100 nm Fe_3C. It could be argued that this result suggests that the mechanism by which sintering is inhibited in these samples is closer to the nanopowder than the bulk powder i.e. the cast surrounds the particles thereby immobilising them. However, as with the other microscopy results discussed within this thesis, it is important to consider the fact that techniques such as TEM are limited by the size of the area observed. In order to add weight to some of these ideas future work in which bulk analysis is carried out would be very advantageous. Small angle X-ray scattering (SAXS) would be one such useful technique.

3.4.4.4 TOMOGRAPHY ANALYSIS

Tomography performed on the sample synthesised from a 1:2 mass ratio of cast to Prussian blue appears to support the view of a homogenous mixture formed between the product Fe_3C nanoparticles and the MgO monolith cast.

The darkfield tomography seen in Fig. 3.28 shows the heavier iron containing particles as the brighter spots with the dimmer more diffuse cast material enveloping them. The EDX tomography (Fig. 3.29) corroborates the key elemental compositions of these phases, albeit at a lower resolution.

Based on these tomography results this cast may give the most homogenous mixing of three cast morphologies examined.

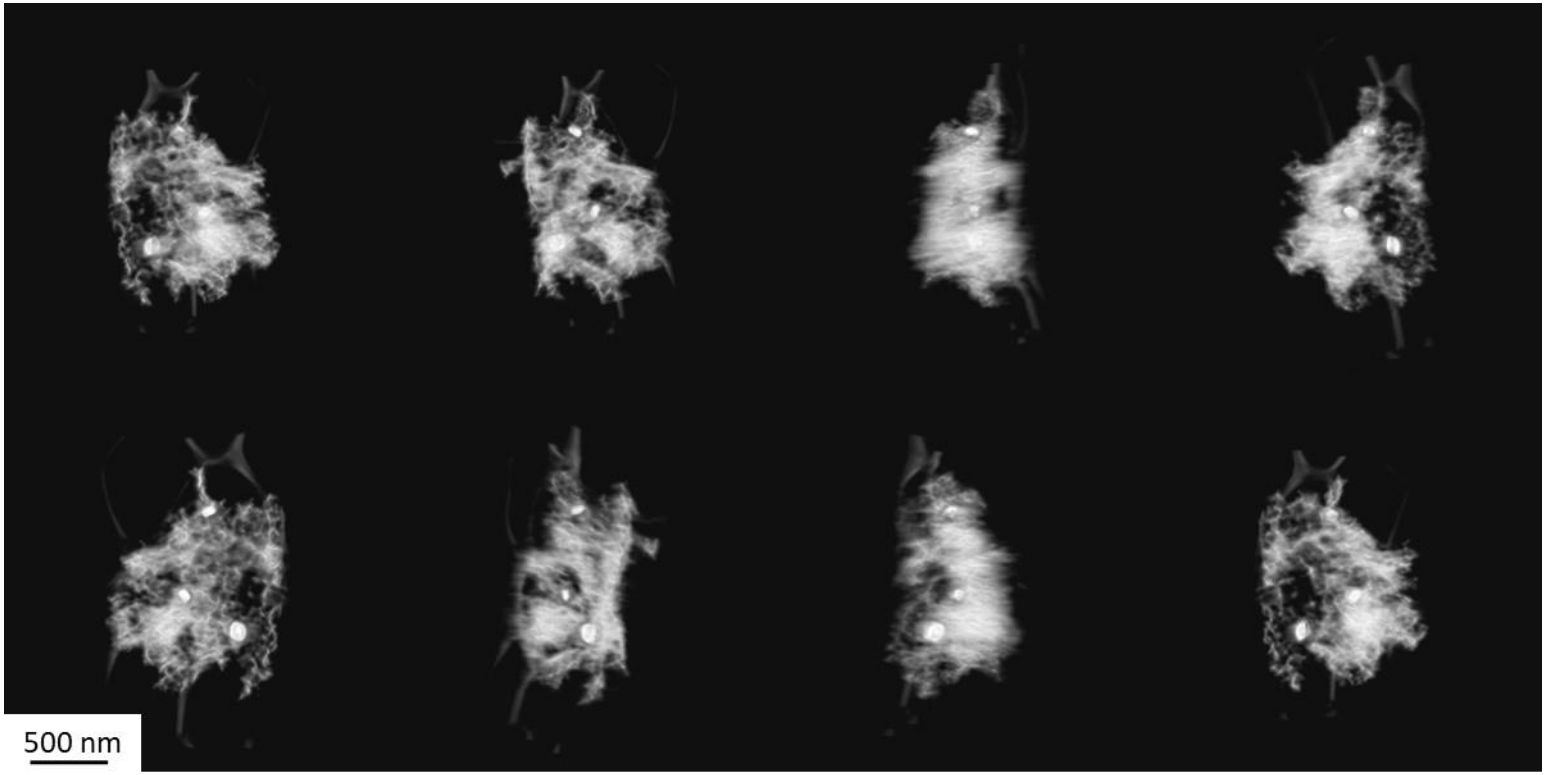

Figure 3.28 3D High Annular Angle Dark Field (HAADF) Tomography performed by STEM, recorded for a Fe_3C/MgO mixture synthesised by calcining a 1:2 mass ratio of Prussian blue : MgO monolith.

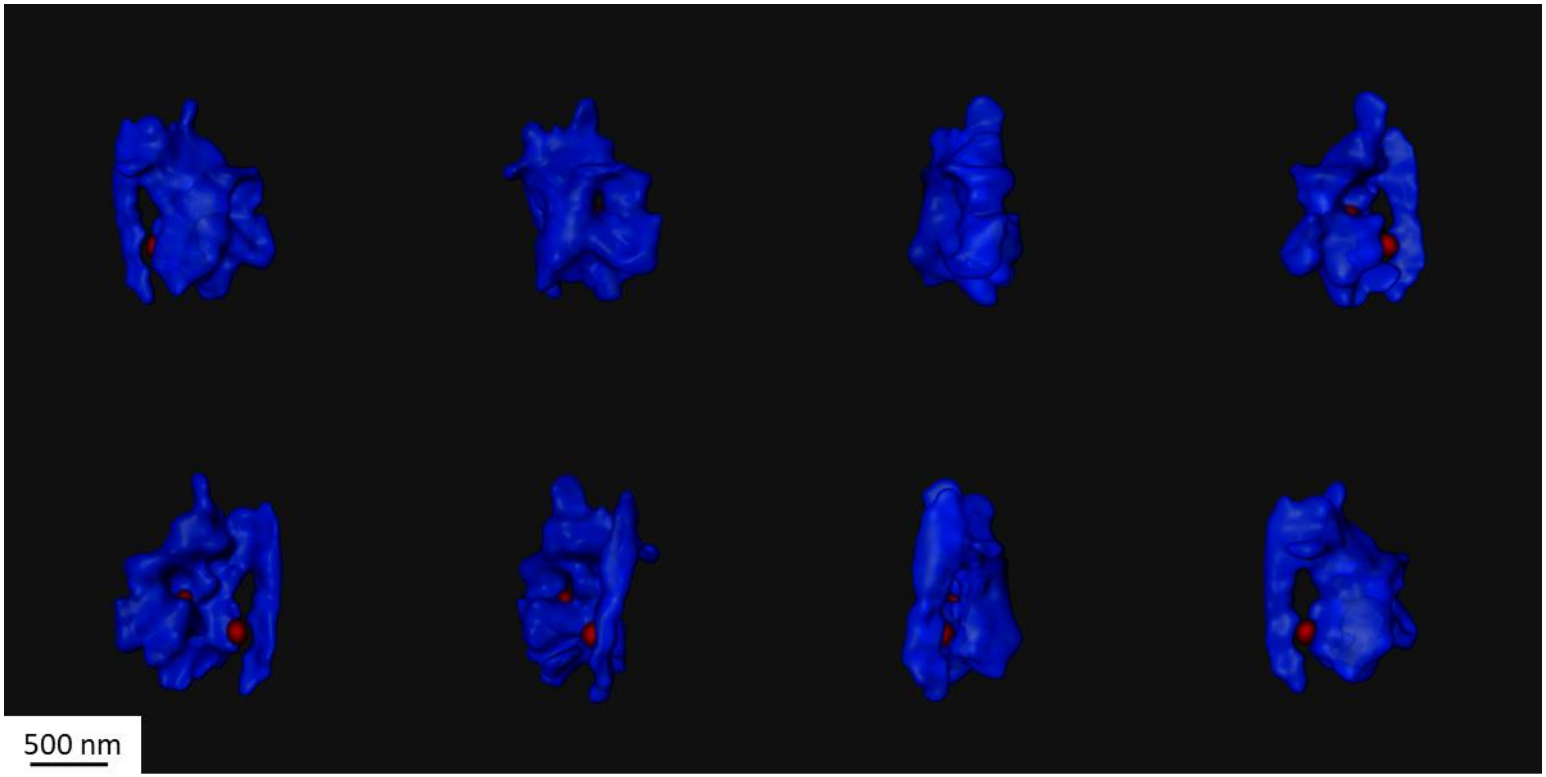

Figure 3.29 3D EDX Tomography performed by STEM, recorded for a Fe_3C/MgO mixture synthesised by calcining a 1:2 mass ratio of Prussian blue :

MgO monolith, Fe, Mg

3.4.5 COATING A SUPPORT WITH Fe_3C NANOPARTICLES

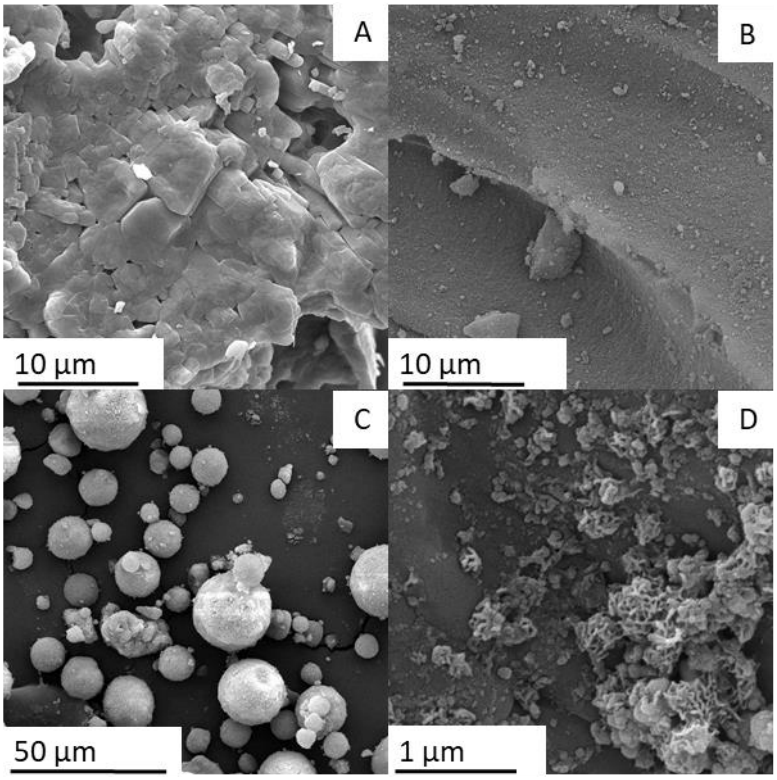

Figure 3.30 SEM micrographs of various catalyst supports: **A** - Cordierite, **B** - Silica, **C** - Alumina, **D** - Fe_3C on cordierite with a Pt coating

One of the foremost advantages to having a material composed of discrete nanoparticles rather than particles that have formed agglomerates, or are bound to a matrix material, is that they can be dispersed over various supports for applications such as catalysis. In this section, the prospect of dispersing Fe_3C nanoparticles over various supports will be examined. In each case, the Fe_3C nanoparticles will have been synthesised through our MgO nanopowder cast synthesis at a 1:1 Prussian blue to cast mass ratio.

The first stage in this process was to identify a suitable support material. Cordierite, silica and alumina were examined by SEM (Fig. 3.30) with silica ultimately selected as our potential support. Cordierite (Fig. 3.30A), whilst providing a suitable surface for coating with Fe_3C, contains Fe. It would therefore be difficult to differentiate between the particle coating and cordierite support surface by EDX. The alumina sample (Fig. 3.30C) on the other hand, had spherical morphology, making it more difficult to coat and image. The alumina sample also had more of a propensity for charging in the electron beam meaning a conductive coating would be required for detailed imaging. When a Pt coating was used to image Fe_3C on silica, the Pt coating significantly obscured detail on the nanoscale, (Fig. 3.30D) making the ability to image a material without a conductive coating advantageous. The silica sample (Fig. 3.30B) seemed to provide a good compromise. It had a suitable surface for coating, gave minimal charging in an electron beam and does not containing Fe, making it suitable for EDX analysis.

3.4.5.1 FINDING A SUITABLE Fe_3C CONCENTRATION

Having identified a suitable support material, an appropriate method for making up samples was required, as well as a suitable Fe_3C concentration for coating the silica support.

The initial step was to identify a minimum amount of water required to wet the silica. To achieve this, distilled water was added to 0.1 g of silica in 100 µl increments. At 300 µl the distilled water was judged by eye to have wetted the whole sample. The next step was to find a suitable Fe_3C dilution. Fe_3C, which when suspended in water gives the water a black coloration, was diluted to a point at which the colouration was barely visible (0.5 mg mL^{-1}). This was determined to be a suitable starting concentration. So, in order to make up the initial

sample, 300 µl of 0.5 mg mL^{-1} Fe_3C in distilled water was added to silica (0.1 g) and mixed by sonication, to give a sample with an Fe_3C/silica concentration of 1.5 mg g^{-1}. The sample was then dried at room temperature for 24 hours prior to analysis.

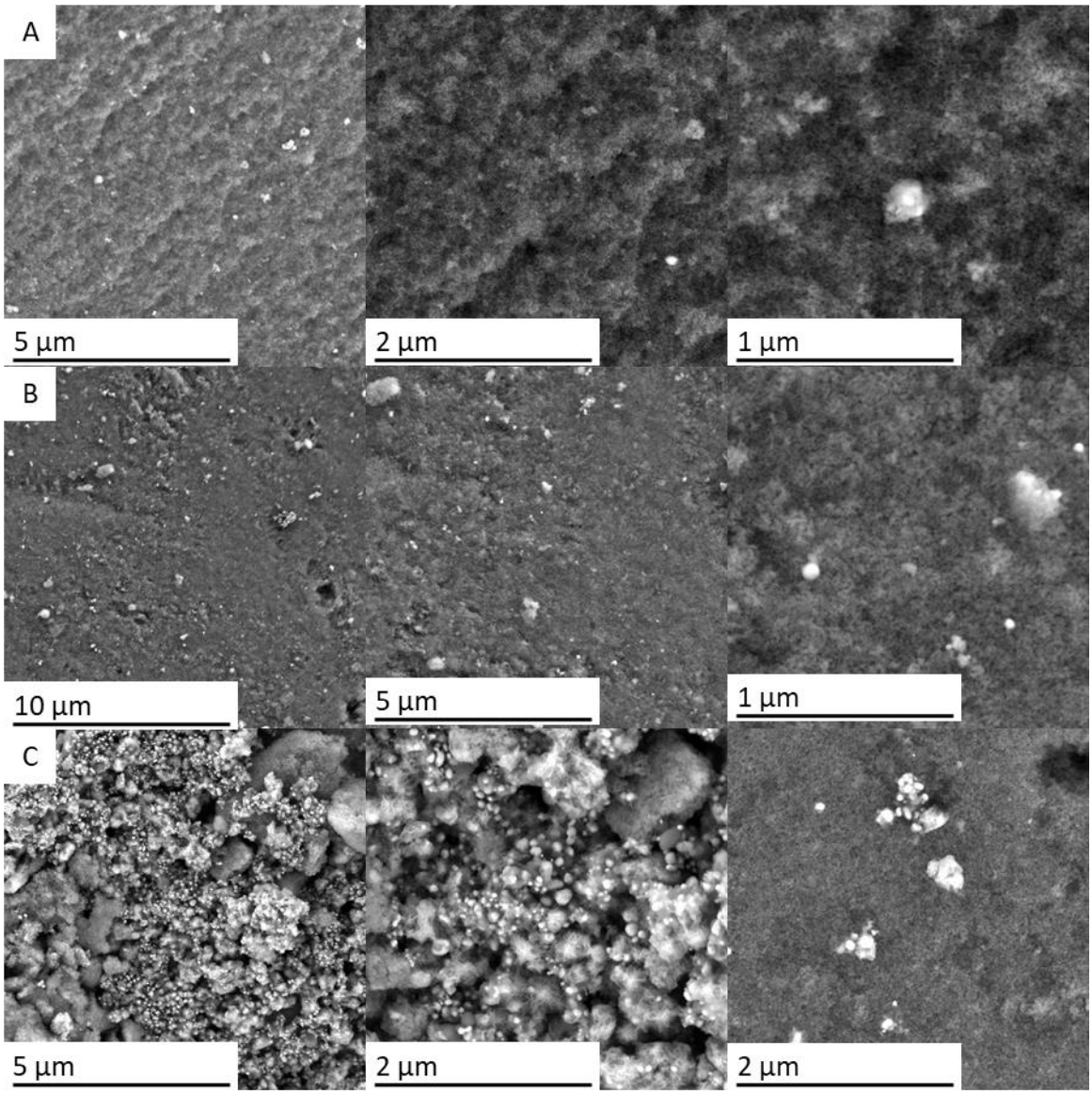

Figure 3.31 A – SEM micrographs of Fe_3C on Silica: Fe_3C on Silica 1.5 mg g^{-1}, **B** - SEM: Fe_3C on Silica 3.0 mg g^{-1}, **C** - SEM: Fe_3C on Silica 30 mg g^{-1}.

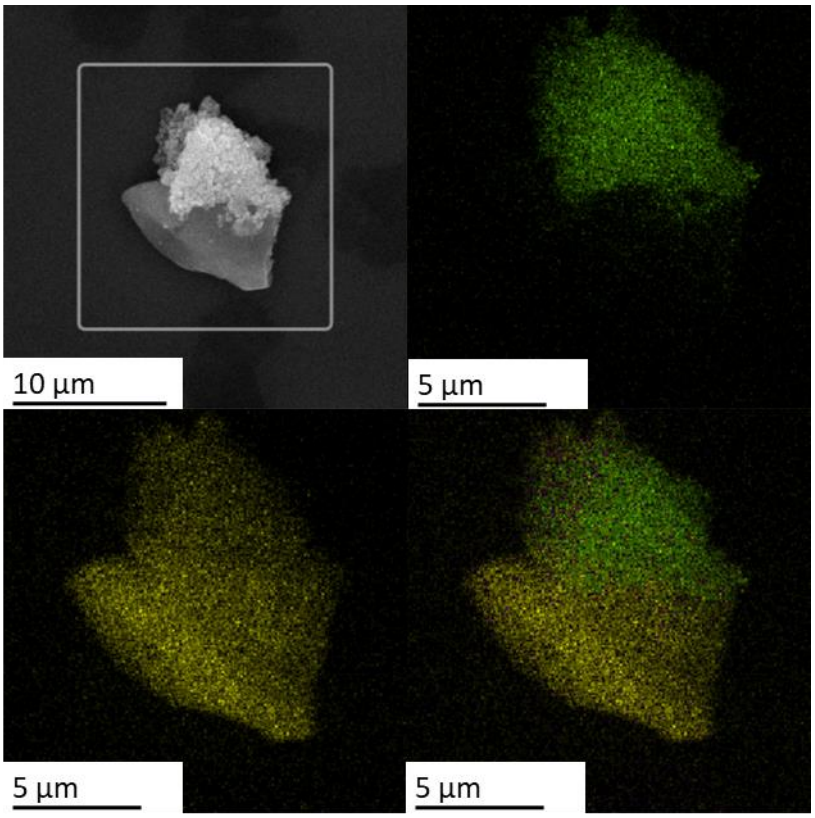

Figure 3.32 EDX micrographs recorded by SEM for Fe_3C on silica: Fe_3C on Silica 1.5 mg g^{-1} EDX Maps Fe, O.

In order to give contrast between phases with different elemental compositions, the sample was then analysed by SEM using a back-scattered electron detector. The Fe_3C particles were expected to be the brightest features in the images, with Fe being a heavier atom than Si, C and O.

At this concentration the back-scattered electron detector was able to resolve bright spots appearing to correspond to Fe_3C particles at the silica surface (Fig. 3.31A). However, the resolution of the EDX technique is not sufficient to confirm this observation for particles with

such small diameters that are so sparsely distributed. Thus, a second sample was prepared at an Fe_3C/Silica concentration of 3.0 mg g^{-1}.

SEM analysis of the 3.0 mg g^{-1} sample using a back-scattered electron detector once more appeared to show sparsely distributed Fe_3C particles at the silica surface (Fig. 3.31B), but again it was not possible to confirm this by EDX due to the detection limit of the technique. So finally, a third sample with an Fe_3C/silica concentration of 30 mg g^{-1} was prepared.

In order to prepare the 30 mg g^{-1} sample the volume of stock solution used was increased from 300 µl to 1.5 mL and the mass of silica used was decreased from 0.1 g to 0.05 g. The ratio of water to silica was therefore greatly increased meaning a modification to the drying process was required. To dry this sample, it was left to settle overnight then decanted. The solid was then left to dry at room temperature for a further 24 hours. Analysis of the 30 mg g^{-1} sample gave mixed results (Fig. 3.31C). While the sample contains higher density regions of what appears to be Fe_3C, there is also a significant amount of agglomeration between Fe_3C particles. Once more, EDX is not able to resolve Fe in the individual nanoparticles of this sample, but the technique is able to identify a high average concentration of Fe in the micron scale densely packed regions at the silica surface (Fig. 3.32). This observation lends evidence to the proposition that the large agglomerates are composed of an iron containing material, suggesting that the smaller bright spots are indeed Fe_3C nanoparticles. It seemed evident therefore that although Fe_3C can be dispersed over a silica support, extra steps maybe require in order to achieve a more homogeneous coating.

3.4.5.2 IMPROVING HOMOGENEITY

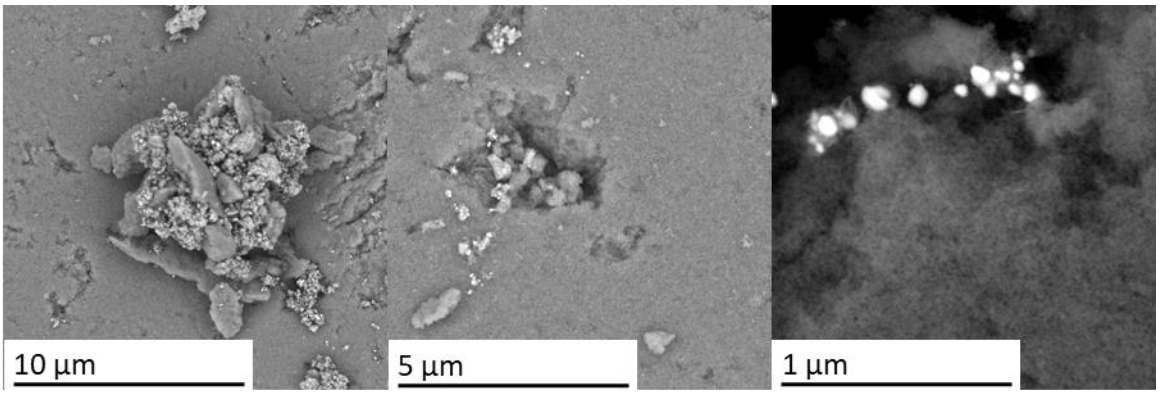

Figure 3.33 SEM micrographs of Fe_3C on silica: Fe_3C on Silica 30 mg g^{-1} with a CTAB monolayer coating.

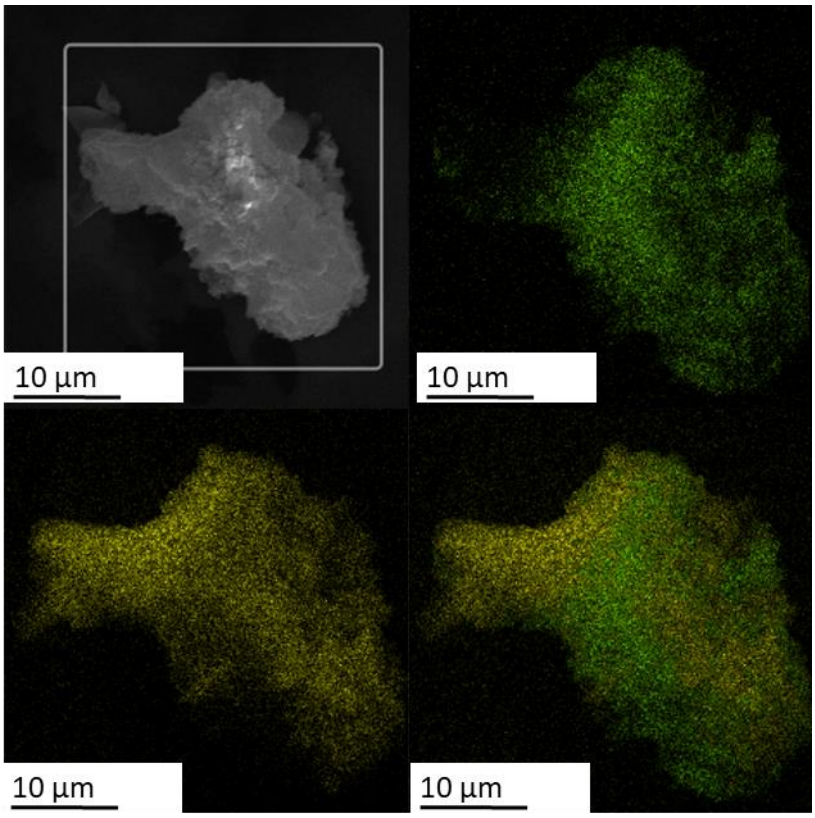

Figure 3.34 EDX maps recorded by SEM for Fe_3C on Silica: Fe_3C on Silica 30 mg g^{-1} with a CTAB monolayer coating - EDX Maps Fe, O.

The first step in attempting to improve the homogeneity of the Fe_3C particle coating was to coat the particles in the surfactant cetyltrimethylammonium bromide (CTAB). An approximate calculation was performed in order to estimate an amount of CTAB required for a monolayer coating. Once coated, the particles were dispersed over silica using the same method as before. Analysis of this sample by back-scattered electron SEM (Fig. 3.33), while showing examples of discretely distributed Fe_3C particles, was not able to demonstrate any definitive improvements gained through the use of CTAB. The sample still appeared to contain densely packed regions of Fe_3C which could again be identified as Fe containing by EDX (Fig. 3.34).

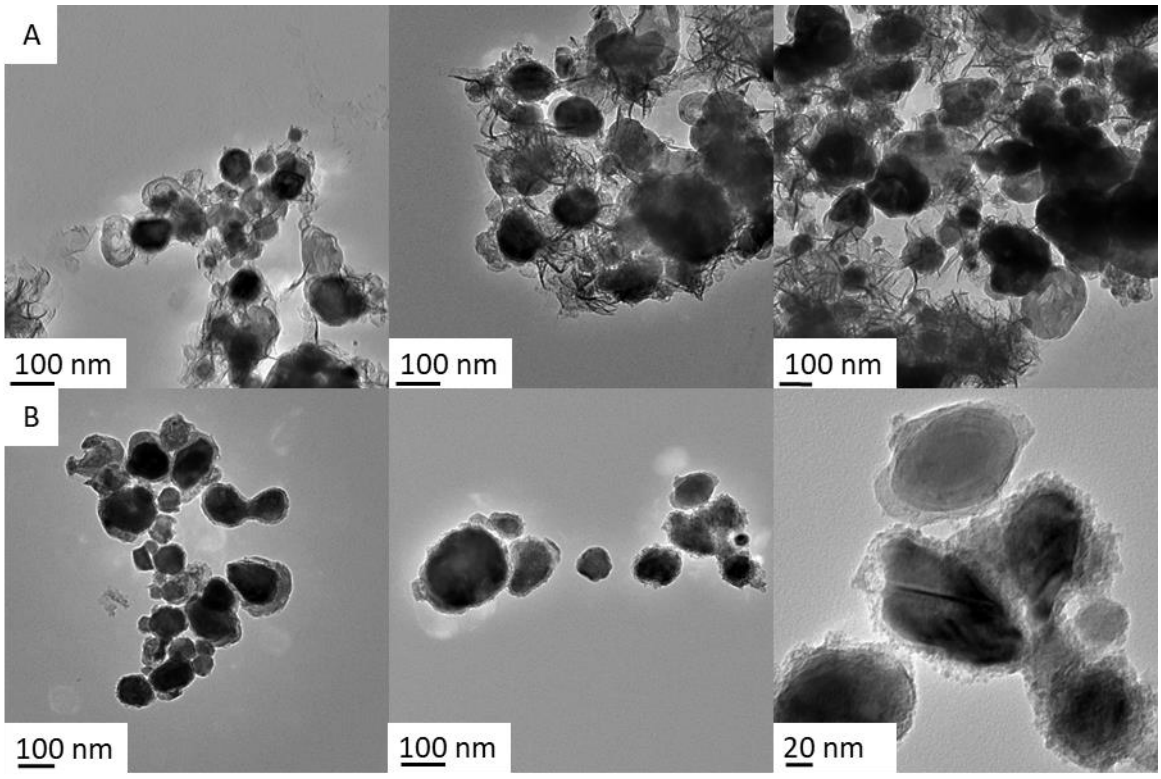

Figure 3.35 A - CTEM micrographs recorded for an Fe_3C Control sample, **B** - CTEM micrographs recorded for an Fe_3C control sample washed with H_2O_2.

It was at this point that residual carbon was considered as a cause of agglomeration. When examining a control sample of Fe_3C by TEM, regions of the sample were found to contain large agglomerates of Fe_3C bound by a less dense second phase (Fig. 3.35A). In order to remove this second phase, thought to be composed of carbon, the sample was washed with H_2O_2, an idea inspired by the work of Schliehe *et al*.[93]. TEM performed on the H_2O_2 washed sample shows a reduction in the quantity of the carbon phase present, exemplified by Fig. 3.35B. The much thinner layers of carbon surrounding some of the particles appears to have been attacked by the H_2O_2.

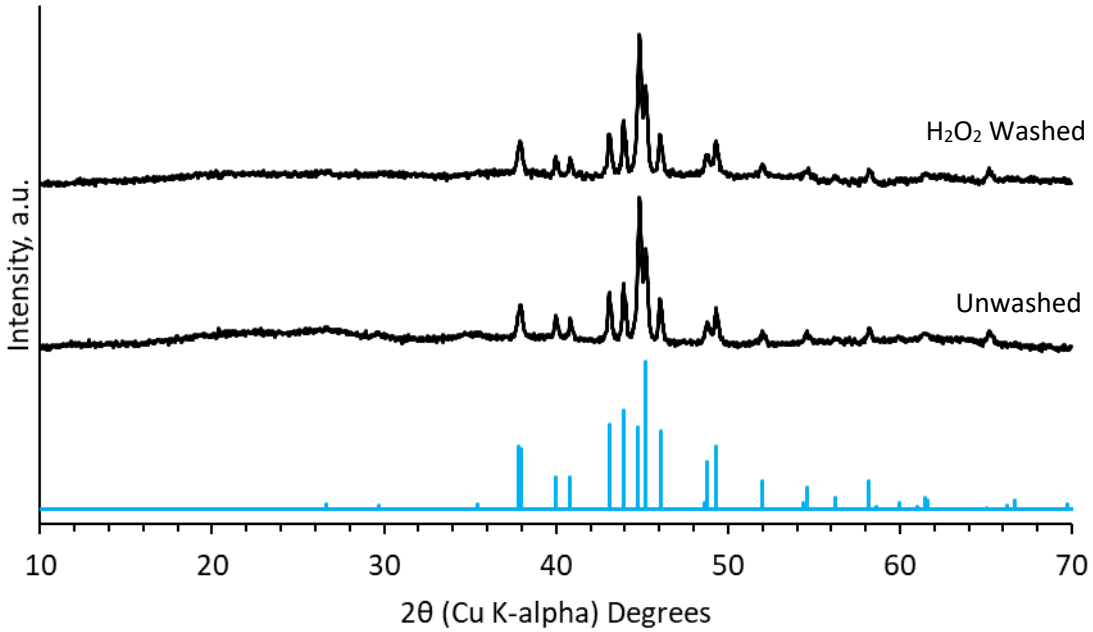

Figure 3.36. PXRD data recorded for H_2O_2 washed and unwashed Fe_3C.

PXRD was also performed on the H_2O_2 washed sample. As H_2O_2 is a strong oxidising agent the formation of an iron oxide phase was a concern. However, the resulting diffraction pattern

showed no evidence of this having happened (Fig. 3.36). Thus, this material was then dispersed over silica, both on its own and with an approximate CTAB monolayer. When analysed by SEM with a backscattered electron detector there appeared to be significantly less agglomeration throughout both samples as a whole (Fig. 3.37A and 3.37B). EDX performed on the more densely packed areas of the silica surface again shows a material with a high Fe content (Fig. 3.38).

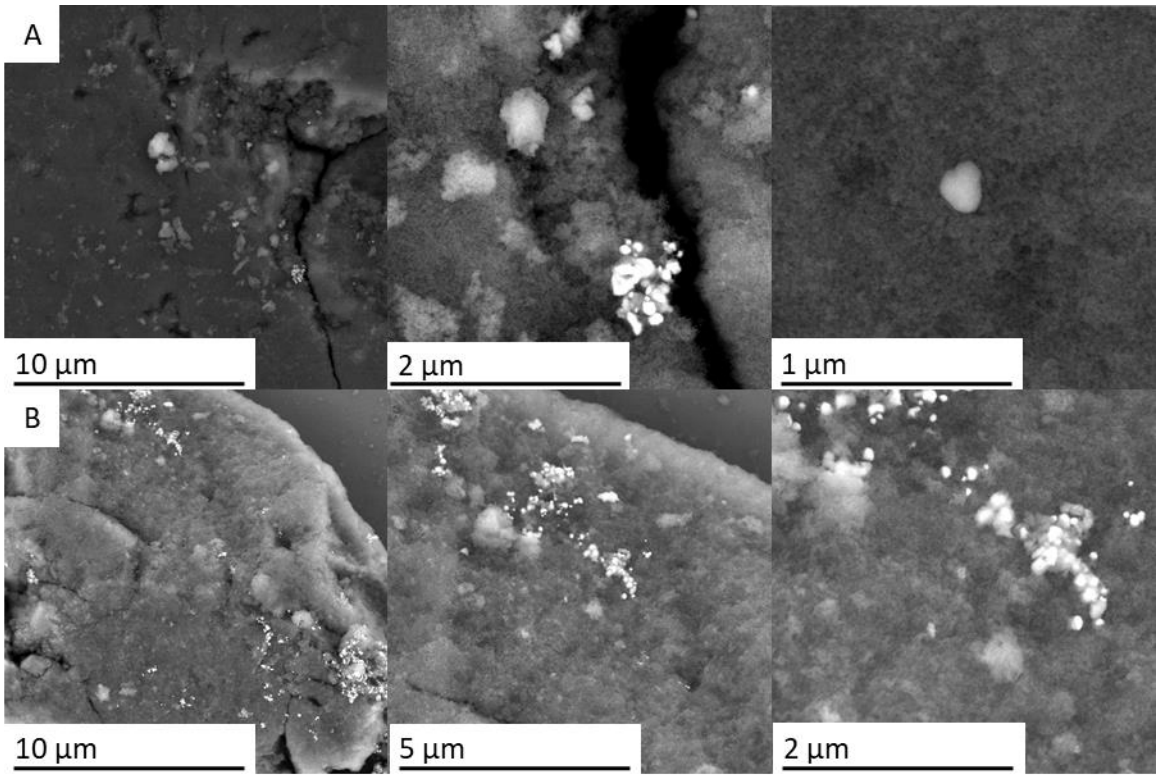

Figure 3.37 SEM micrographs of **A** - H_2O_2 washed Fe_3C on Silica 30 mg g^{-1}, **B** - H_2O_2 washed Fe_3C with a CTAB monolayer on Silica 30 mg g^{-1}.

Based on the progression of these results it seems that the levels of amorphous carbon remaining in the Fe_3C samples is significantly hindering the dispersal of the particles. However,

it appears that improvements can be gained when this carbon is removed through washing with H_2O_2. This also provides another motivation for reducing carbon content in this synthesis.

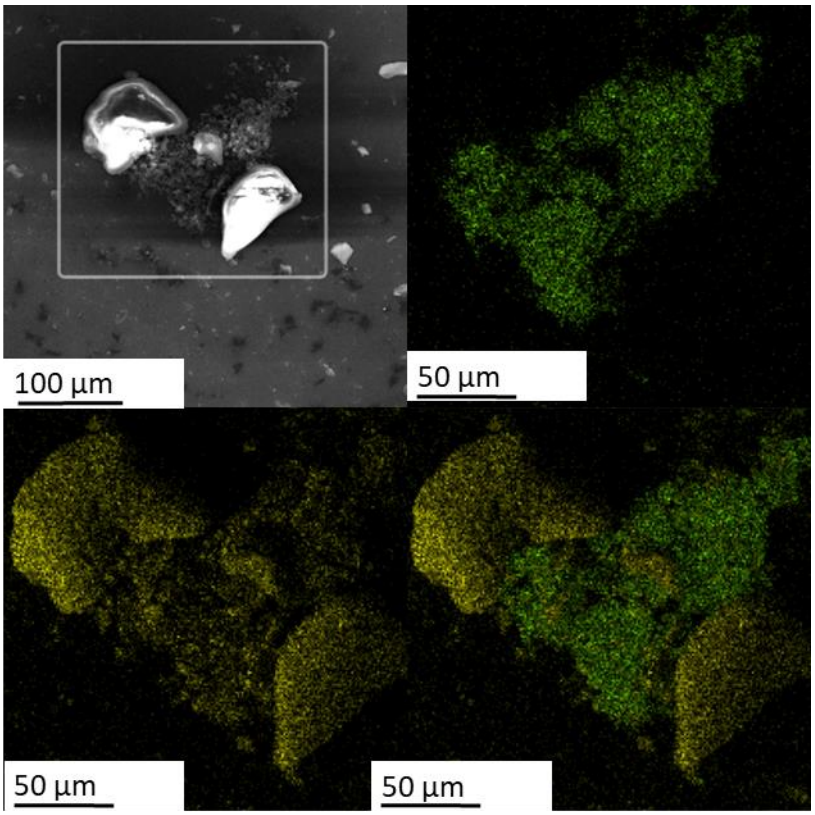

Figure 3.38 EDX maps recorded by SEM for H_2O_2 washed Fe_3C with a CTAB monolayer on silica 30 mg g^{-1} - EDX Maps Fe, O.

3.4.6 SQUID MEASUREMENTS

At sufficiently small particles sizes, with the exact diameters dependent on the composition of the material, materials that display spontaneous magnetisation can become superparamagnetic. The effect is caused by the fact that each particle is small enough that it contains just one magnetic domain. A highly sensitive magnetometer known as

superconducting quantum interference device (SQUID) can be used to take measurements that can identify superparamagnetism in materials.

As nanoparticles are often composed of single crystals the single domains that make up each discrete particle have only two stable orientations, antiparallel to one another. The direction of magnetisation will flip between these two stable orientations at a temperature dependent rate, resulting in a net zero magnetisation in the absence of an external field. The time interval between the flipping of these two states, which should increase with temperature due to disruption of the states by thermal motion, is known as the Néel relaxation time. Thus, when measurements are taken at a set field strength/frequency and scanned across a temperature range, the superparamagnetic effect can be seen when the Néel relaxation time becomes shorter than the magnetization measurement time used[119, 131].

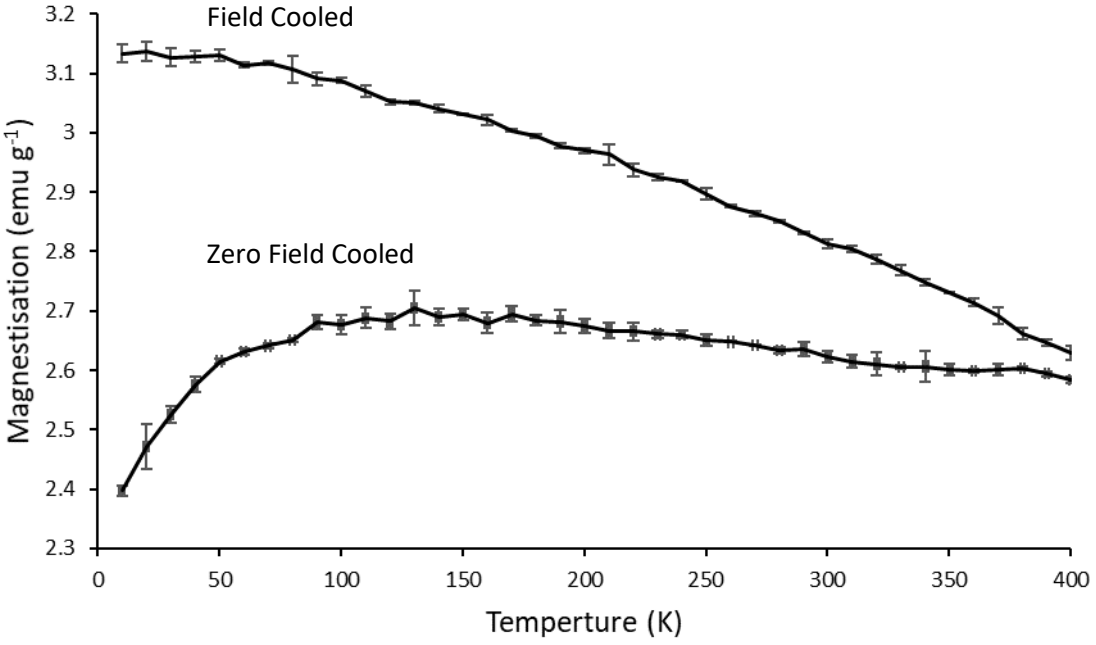

Figure 3.39 SQUID measurements showing the temperature dependent magnetic susceptibilities of 100 Oe field cooled and zero field cooled samples of Fe_3C prepared by calcining a 1:1 mixture of Prussian blue : MgO nanopowder, followed by subsequent EDTA washing.

In an attempt to observe these properties SQUID measurements were performed on a sample of Fe_3C nanopowder prepared by calcining a 1:1 mixture of Prussian blue and MgO nanopowder, followed by subsequent EDTA washing. Fig. 3.39 shows the zero-field cooled and the 100 Oe field cooled temperature dependent magnetic susceptibility of the sample. The characteristic drop in magnetisation for the zero-field cooled sample indicates that the particles in this sample are indeed superparamagnetic.

The temperature at which the Néel relaxation time is equal to the measurement time and thus fluctuations in the direction of magnetisation cannot be observed, is termed the blocking temperature. Fig. 3.39 indicates that the blocking temperature for this sample is slightly above 400 K in a 100 Oe applied field. Unfortunately, 400 K was the maximum analysis temperature attainable with the instrument used to record these measurements[119].

To measure the saturation magnetisation of the material an AC field can be applied, that is, the applied field strength is varied with time to the point at which the material is fully magnetized. This measurement can also give an indication of the kind of magnetism displayed by the sample. For example, paramagnetic and diamagnetic materials show linear attraction and repulsion respectively. Ferromagnetic materials will display a sigmoidal shape that contains hysteresis due to remanence, meaning the material remains in a magnetised state for a given period after external field is removed. Superparamagnetic materials on the other hand produce a sigmoidal curve with no hysteresis. The lack of hysteresis shows that the particles have a coercivity value close to zero, meaning it takes a negligible reverse field to reverse any remanence effects after becoming saturated[119, 132].

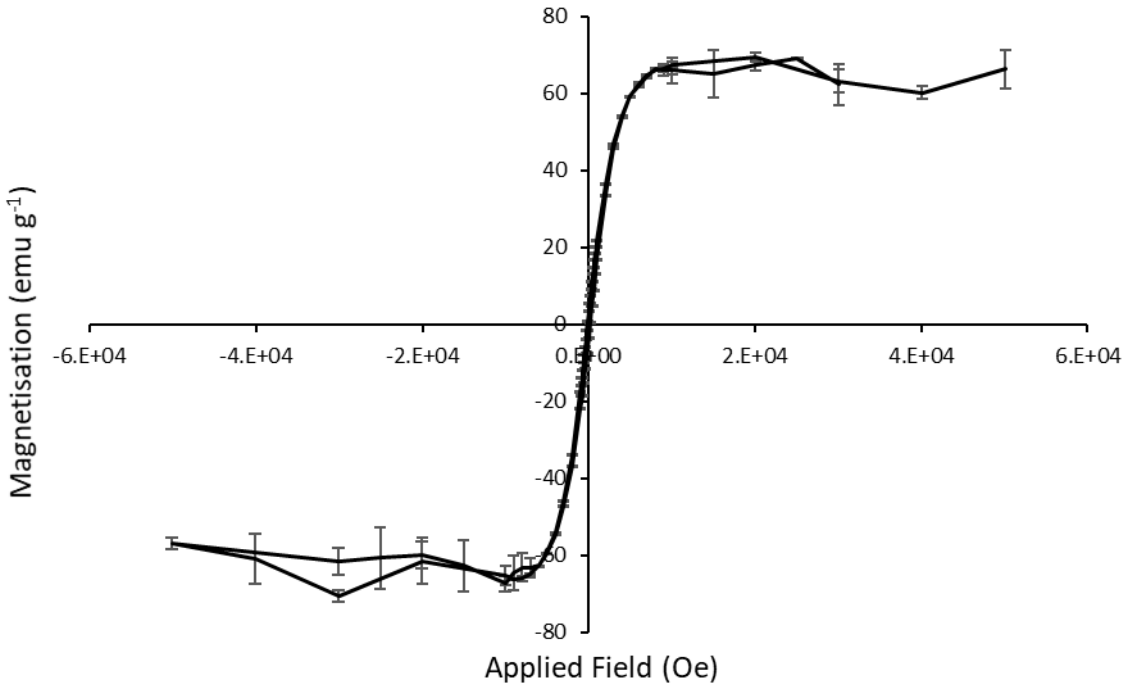

Figure 3.40 SQUID measurement showing the dependence between applied magnetic field (-5.01 x10^4 – 5.01 x 10^4 Oe) and induced magnetization at 300 K, for a sample of Fe_3C prepared by calcining a 1:1 mixture of Prussian blue : MgO nanopowder, followed by subsequent EDTA washing.

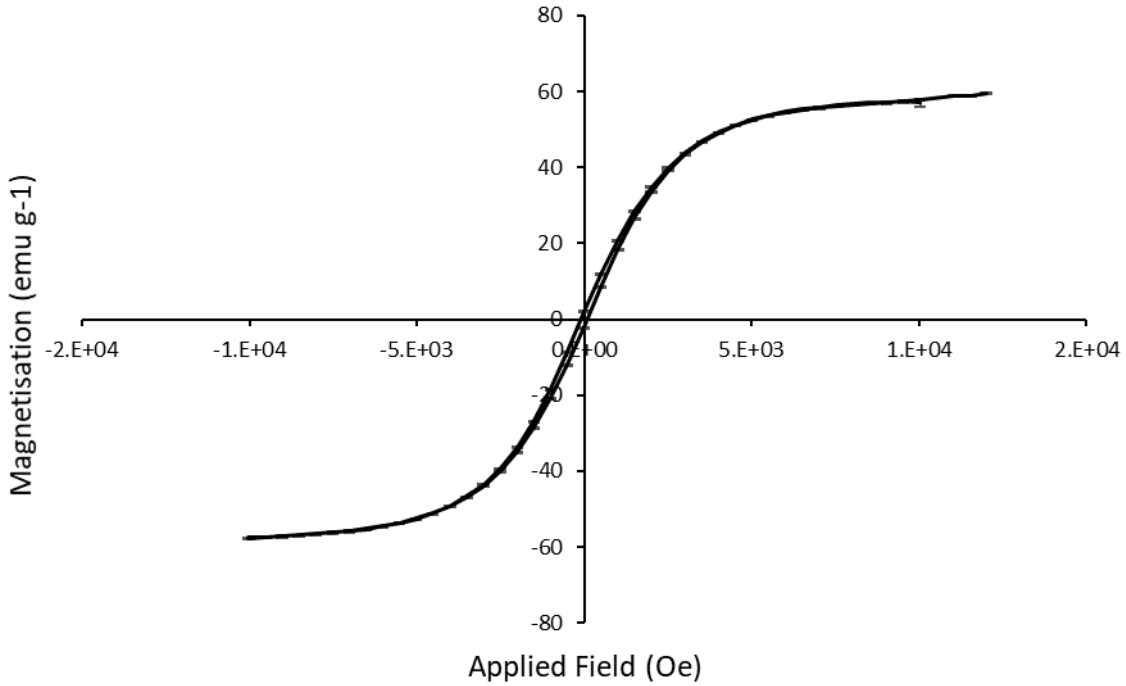

Figure 3.41 SQUID measurement showing the dependence between applied magnetic field (-1.00 x10^4 – 1.20 x 10^4 Oe) and induced magnetization at 400 K.

The plot shown in Fig. 3.40 shows the characteristic sigmoidal curve associated with superparamagnetic particles, recorded for our Fe_3C nanopowder at 300 K. The data set does, however, appear to contain significant error at high field strengths, because of this apparent error, a second data set was recorded at 400 K (Fig. 3.41). Again, at 400 K we see the characteristic sigmoidal curve, this time with very low error margins. At both 300 and 400 K the saturation magnetization value for the sample appears to be approximately 60 emu g^{-1}. Comparison of this value with the data reported in table 3.2 shows that it is comparable to Fe_3O_4 particles measuring approximately 10 nm in diameter[133]. While the value is significantly lower than the bulk value for Fe_3C[134] as well as Fe_3C particles measuring 100 nm in diameter[135] it is important to note that a drop in saturation magnetisation for a nanoparticulate material relative to the bulk material is to be expected. The reason for this is the high fraction of atoms located at the surface of a nanoparticle. Surface atoms find themselves in a different coordination to their bulk counterparts which can lead to a misalignment of spins. Thus, a nanoparticle can have a shell of atoms that do not contribute to the magnetic saturation value[135]. It is therefore also expected that the saturation magnetisation value will decrease as particle size and therefore volume to surface ratio decreases.

Table 3.2 Reported saturation magnetisation values for magnetic iron containing phases.

Material (Particle diameter)	**Measurement Temperature (K)**	**Saturation Magnetisation (emu g^{-1})**
Fe – (Bulk) [136]	293	218
Fe – (5 nm) [137]	300	170
Fe_3O_4 – (Bulk) [133]	300	80
Fe_3O_4 – (10 nm) [133]	353	57
Fe_3C – (Bulk) [134]	307	132
Fe_3C – (100 nm) [135]	300	75

3.4.7 SCALE UP SYNTHESIS

To produce larger sample quantities for analysis, attempts were made to scale up the MeOH mixing synthesis. To make this feasible, rather than synthesising the Soluble Prussian blue template particles in the lab, commercially available particles were purchased. These commercially available particles were used in order to demonstrate that the synthesis could be performed with readily available commercial materials on a slightly larger scale, in order to produce gram scale quantities of Fe_3C nanopowder.

The first stage was to screen the Commercial Prussian blue (CPB) particles to ensure that they were comparable to the laboratory synthesised particles. CTEM was used to confirm that the externally sourced Prussian blue particles were sub 100 nm in diameter (Fig. 3.42A) and that they could be coated with PVP for dispersal in MeOH, without significantly altering their morphology (Fig. 3.42B).

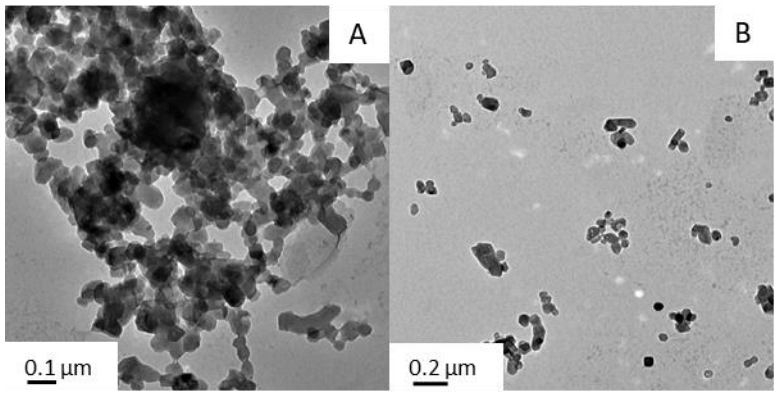

Figure 3.42 TEM micrographs of: **A** – Soluble Prussian blue sourced from Sigma Aldrich, **B** – Soluble Prussian blue sourced from Sigma Aldrich, coated with PVP.

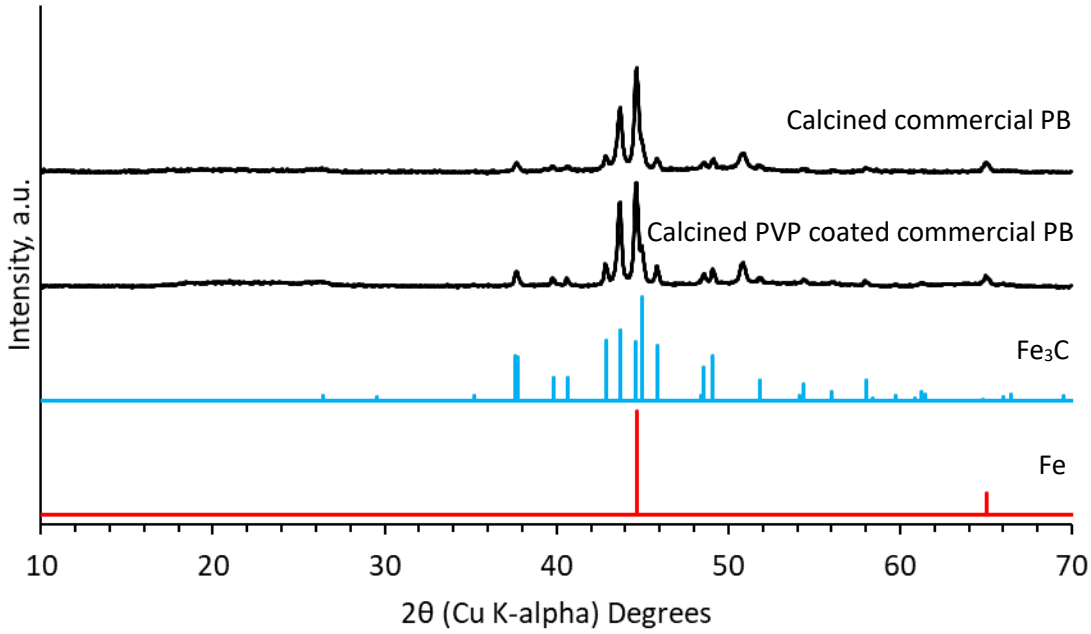

Figure 3.43 PXRD data recorded for calcined CPB: Top to bottom – CPB calcined at 800 °C under N_2, CPB coated with PVP calcined at 800 °C, Fe_3C, Fe^0.

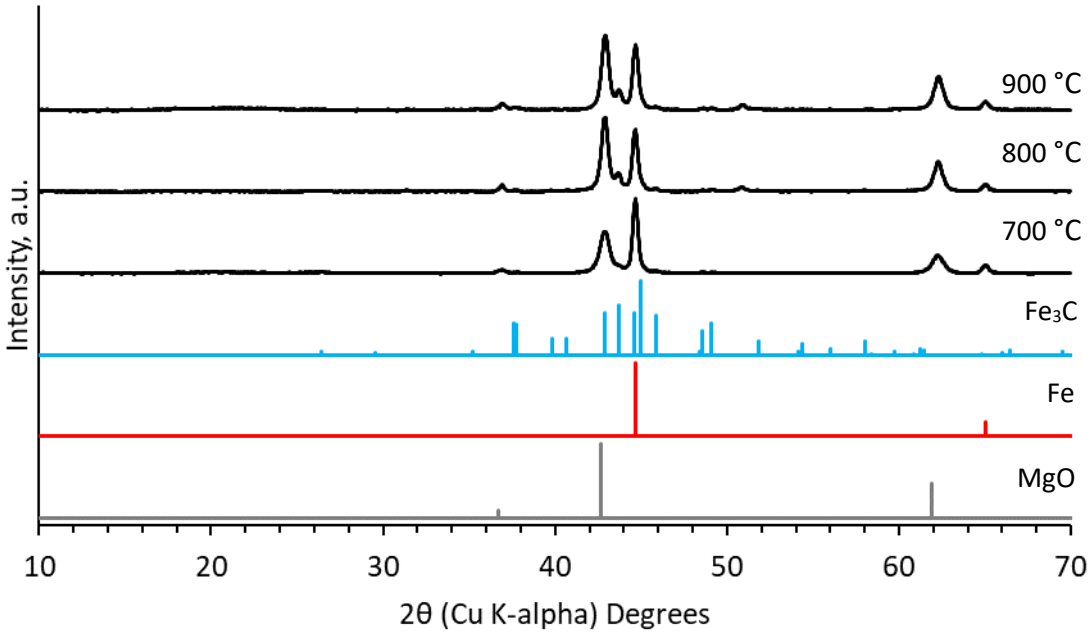

Figure 3.44 PXRD data recorded for calcined Commercial Prussian blue calcined at 100 °C intervals: 1:1 CPB : MgO nanopowder mixtures calcined at various temperatures under N_2.

The commercial particles, both PVP coated and uncoated, were then calcined at 800 °C and analysed by PXRD to ensure that Fe_3C could be produced (Fig. 3.43). The diffraction patterns confirm the formation of Fe_3C, yet they also appear to contain Fe^0 in relatively small amounts. Unfortunately, Fe^0 content becomes a major issue when the particles are mixed with the MgO nanoparticles in our MeOH mixing synthesis. Fig. 3.44 displays PXRD patterns recorded for 1:1 ratios of PVP coated commercial Prussian blue : MgO nanopowder calcined at 700, 800 and 900 °C. At each temperature the dominant Fe containing phase is Fe^0. This observation remains true if the sample is decomposed under Ar rather than N_2 and if the MeOH mixed product is ground in a mortar and pestle or left unground prior to calcination.

These results suggested that the MeOH mixing strategy employed up to this point was in some way incompatible with the formation of phase pure Fe_3C from our CPB and MgO cast. Thus, the MeOH mixing strategy was dropped in favour of a return to the solvent free mortar and pestle grinding strategy used in chapter 2.

Fig. 3.45 shows a selection of PXRD patterns recorded for CPB calcined alongside cast materials having been mixed simply by grinding together in a mortar and pestle at various ratios. Fig. 3.46 shows the corresponding normalised patterns cut off between 2θ values of 43.5 ° - 46.5 °, showing more clearly the presence of Fe_3C. Fig. 3.47 displays the diffraction patterns for corresponding EDTA washed samples. The data indicates that a tenfold increase in the relative amount of MgO nanopowder used, from a 2:1 CPB : MgO nanopowder ratio to 1:5 does not seem to inhibit Fe_3C formation.

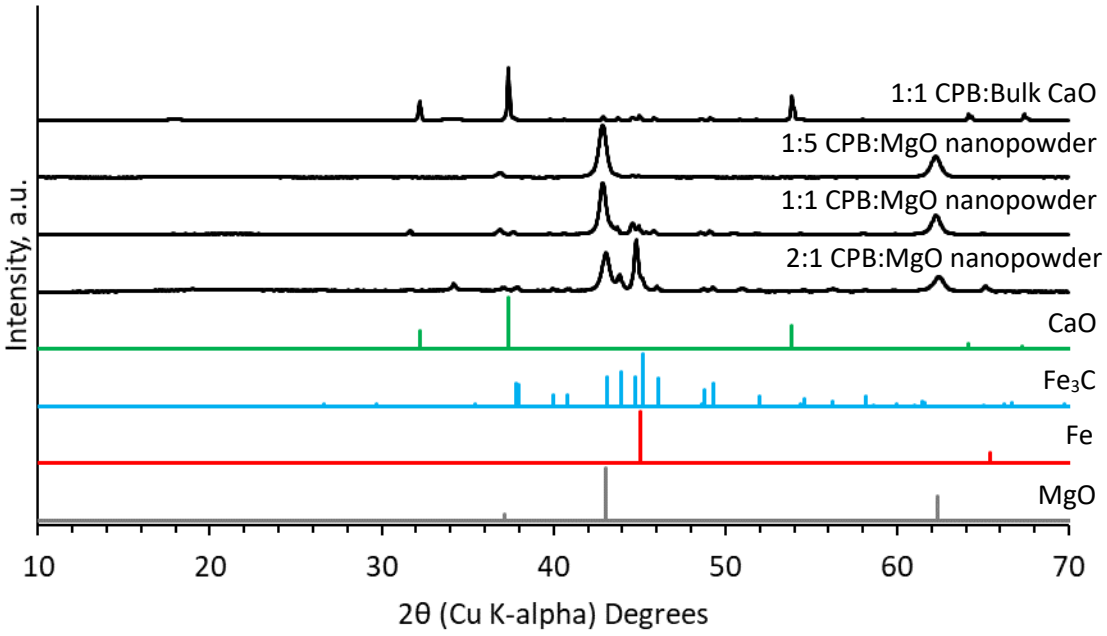

Figure 3.45 PXRD data recorded for various CPB : cast mixtures calcined at 800 °C under N_2.

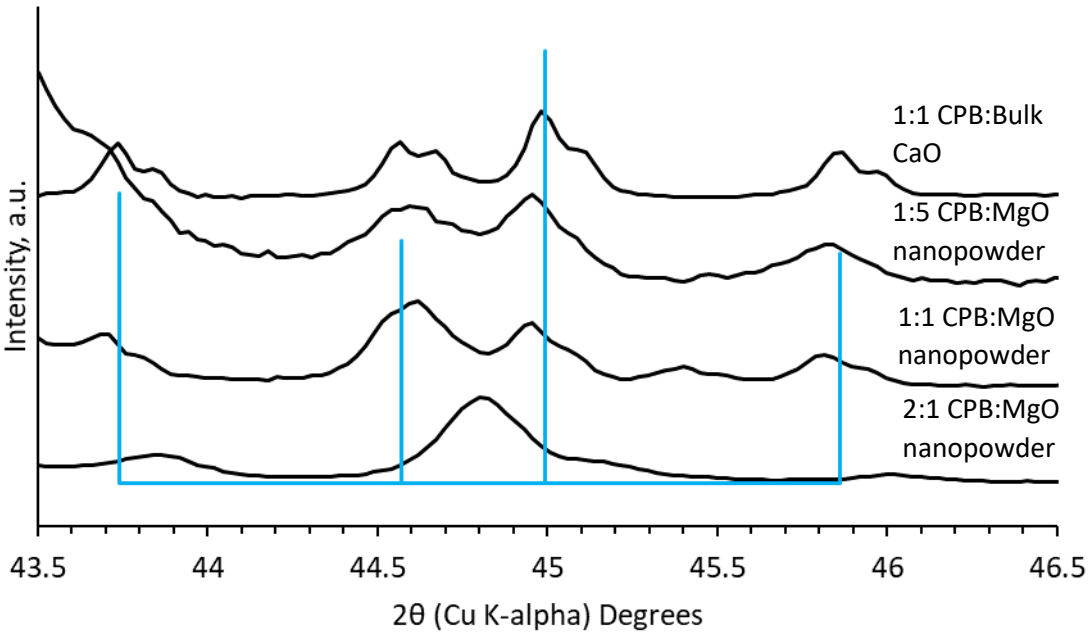

Figure 3.46 PXRD data recorded for various CPB : cast mixtures calcined at 800 °C under N_2, giving an expanded view of the 43.5-46.5 2θ range, Fe_3C.

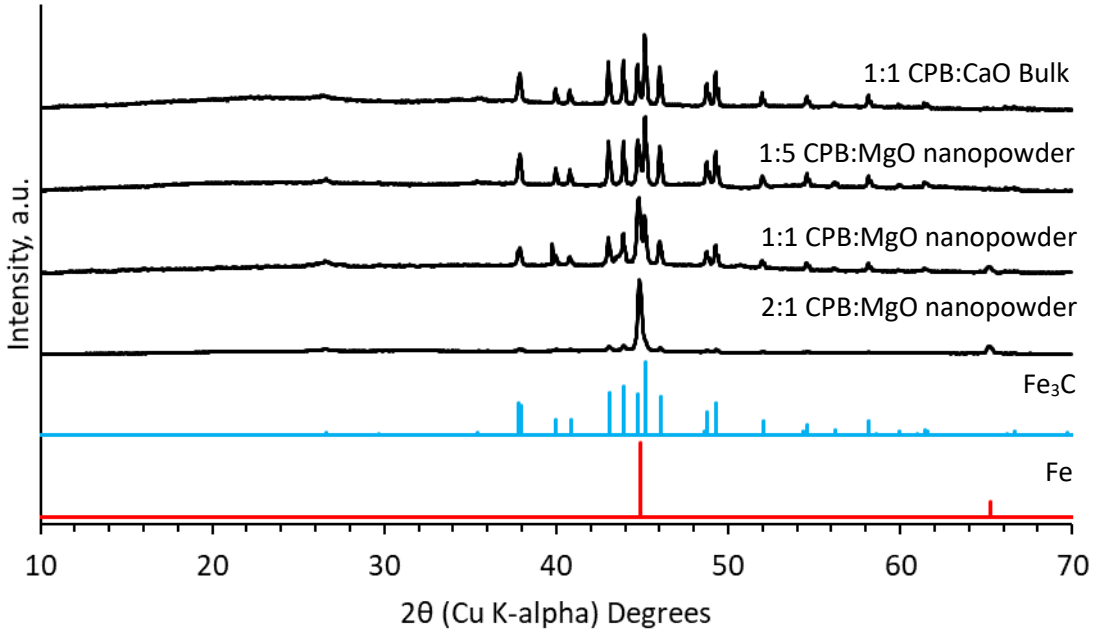

Figure 3.47 PXRD data recorded for various CPB : cast mixtures calcined at 800 °C under N_2, washed with EDTA.

In fact, it could be said that the amount of Fe^0 relative to Fe_3C seems to be reducing as the relative amount of MgO is increased, based on the data in Fig. 3.47. However, given the frequency with which Fe^0 appears alongside Fe_3C in many syntheses it is difficult to rule out other external factors. Crucible size and shape, which can affect the rate with which gases escape, has been shown to have a profound effect on the synthesis of mesoporous metal oxides, for example[138]. It is also worth mentioning at this point that a concurrent project looking at this system, though yet unpublished, has shown a strong dependence between crucible position within the furnace and final Fe^0 content.

Examination of these samples pre and post EDTA washing by CTEM reveals further insights. In the case of all three pre-washed MgO containing samples (Fig. 3.48A-C, 3.49A-C, 3.50A-B) the

TEM micrographs show evidence of the mixing of the Fe_3C and MgO phases. Likewise, EDTA washing of these samples (Fig. 3.48D-F, 3.49D-F, 3.50C-E) appears to have removed the MgO phase to leave particles with what appear to be carbon shells in many cases,

The EDTA washing process also seems to have had unforeseen consequences. Figs. 3.49D-F show evidence of empty carbon shells. It seems probable that these shells are the result of the EDTA washing process dissolving some of the Fe_3C particles, potentially the smaller ones. This fits with experimental observations in which an orange/red solution, the colour expected for a solution of ferric EDTA, was formed while EDTA washing the material. While it is unadvisable to suggest a trend based on the small sample size observed in a TEM experiment it seems possible that this may prove to be a greater issue as the relative amount of cast material is increased and thus a greater amount of EDTA is required.

CaO is also shown to be compatible with commercial Prussian blue when using this dry grinding technique, both at the pre and post EDTA washing stage. PXRD analysis (Fig. 3.46 and 3.47) and CTEM micrographs (Fig. 3.51A-F) support this claim.

Thus, it appears that in hindsight this synthesis would be much simpler if commercially available soluble Prussian blue were used and if the materials were mixed together mechanically rather than as a colloidal mixture. The initial MeOH mixing strategy main remain valid in some cases and may be of particular use if lab based Prussian blue sysnthesis were used to tune particle size.

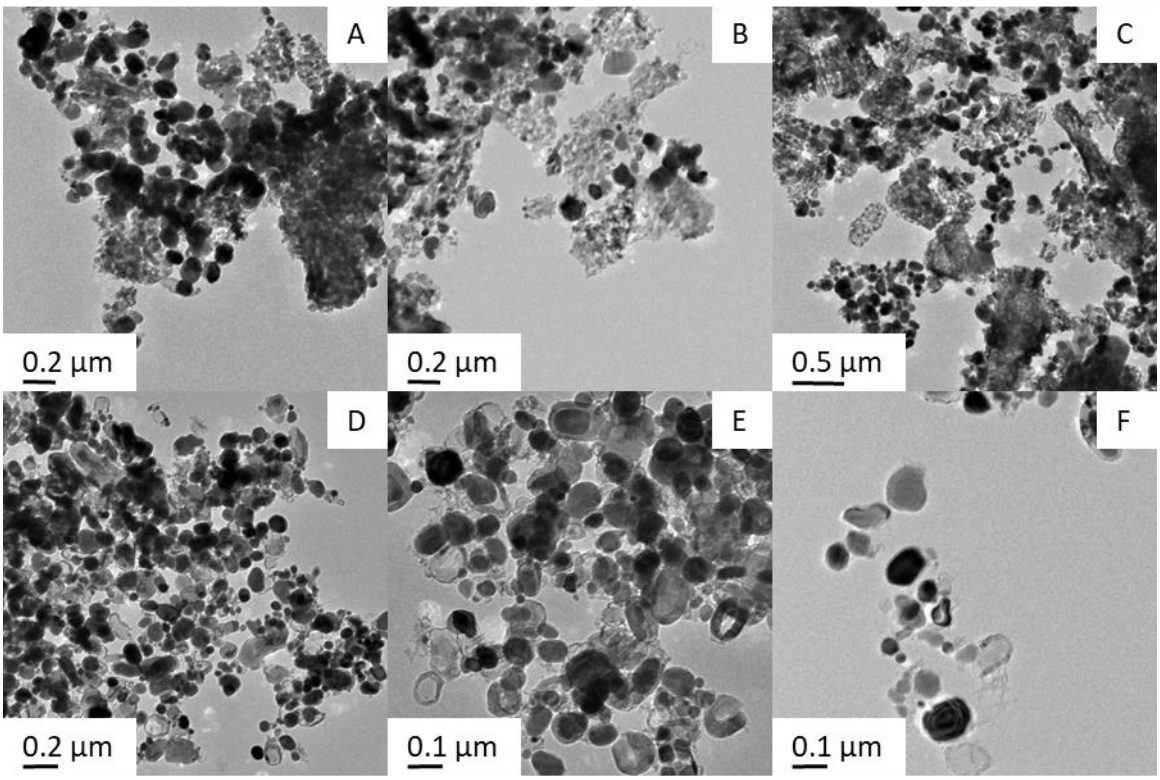

Figure 3.48 TEM micrographs of - 2:1 CPB : MgO, **A – C** Pre EDTA wash, **D – F** Post EDTA wash.

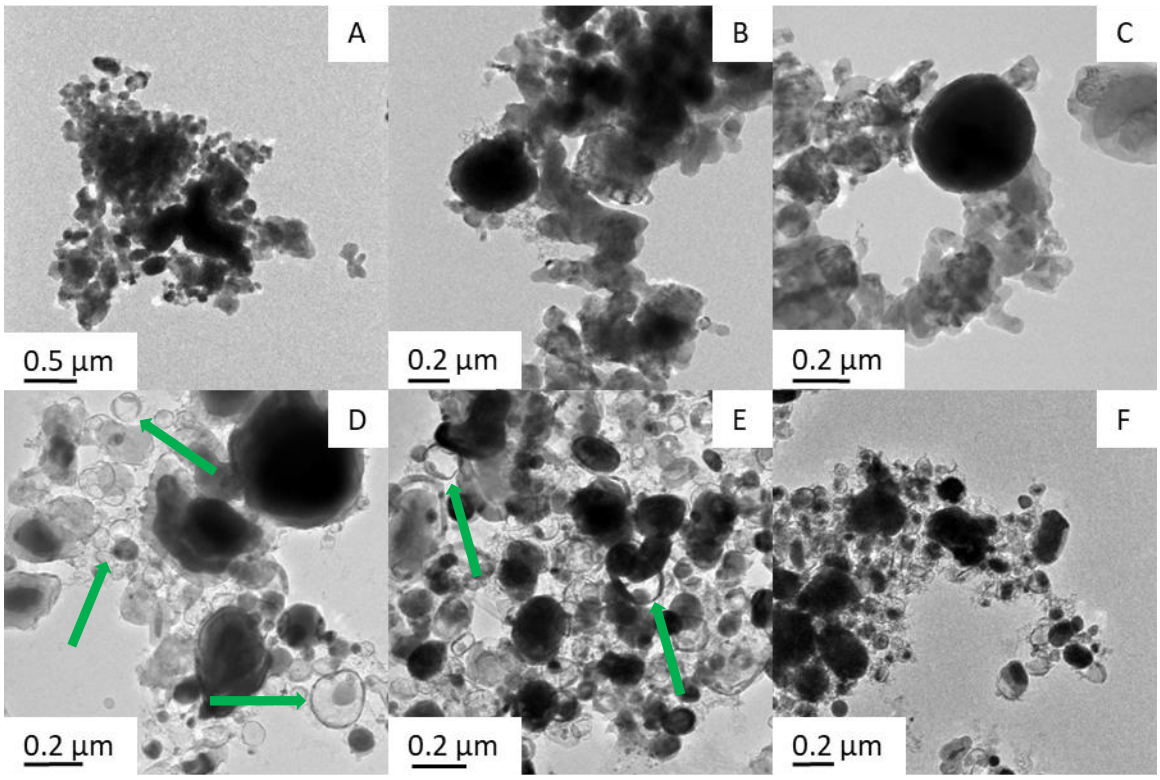

Figure 3.49 TEM micrographs of - 1:1 CPB : MgO, **A – C** Pre EDTA wash, **D – F** Post EDTA wash.

Examples of empty carbon shells are marked with green arrows.

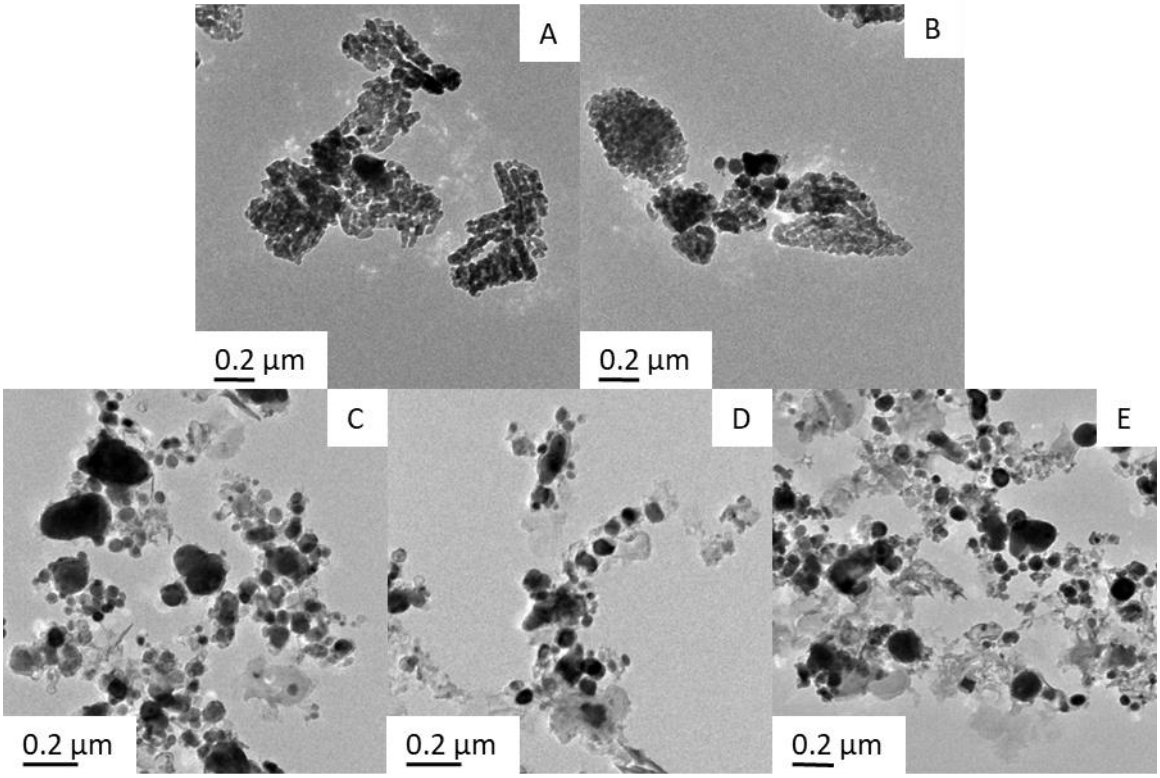

Figure 3.50 TEM micrographs of - 1:5 CPB : MgO, **A – B** Pre EDTA wash, **C – E** Post EDTA wash.

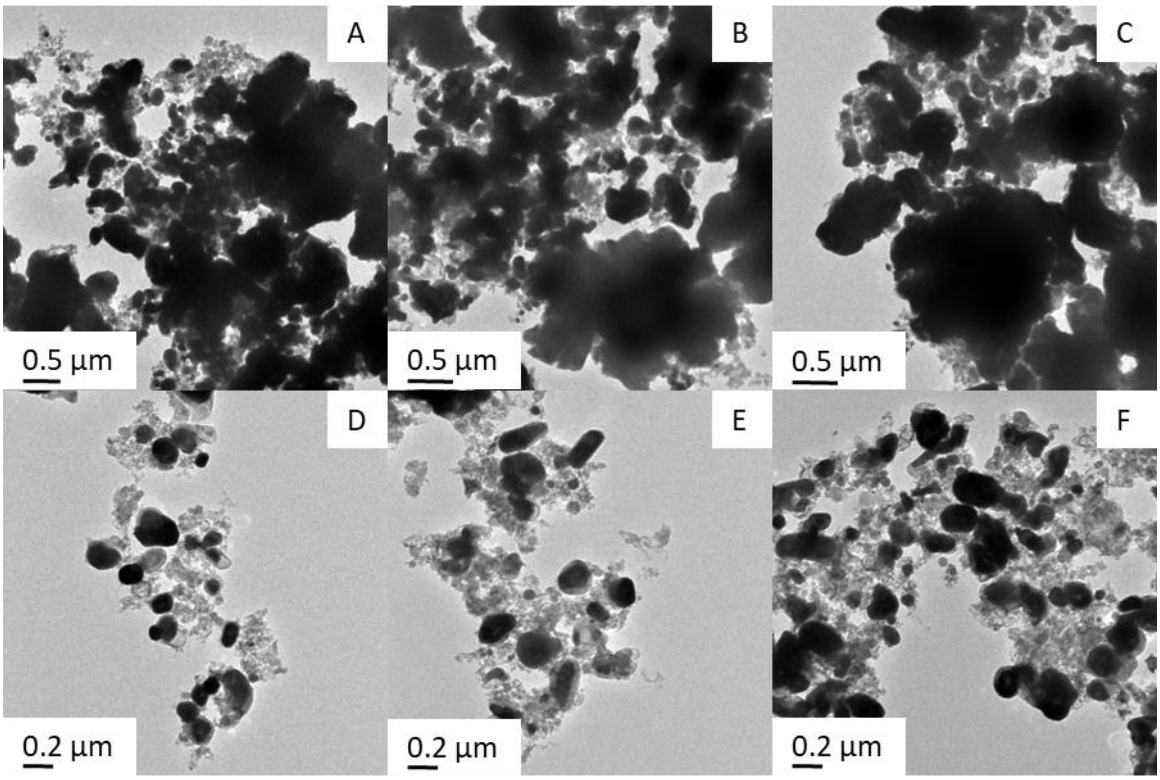

Figure 3.51 TEM micrographs of – 1:1 CPB : CaO, **A – C** Pre EDTA wash, **D – F** Post EDTA wash.

3.5 CONCLUSIONS

This chapter has shown that the templated synthesis of an Fe_3C nanopowder can be achieved using soluble Prussian blue nanoparticles as templates and three distinct MgO morphologies as anti-sintering agents. EDX mapping has shown that discrete Fe_3C and MgO phases are retained post calcination and that the morphology of the MgO cast material has a direct effect on the morphology of the resulting Fe_3C nanopowder.

Table 3.3 Average Fe_3C particle diameters calculated from TEM micrographs for samples produced using 1:1 Prussian blue : MgO cast mixtures.

Cast Material	**Average Fe_3C Particle Diameter – TEM (nm)**
Bulk MgO	42
MgO Nanopowder	108
MgO Monolith	192

Table 3.3 shows average Fe_3C particles size data for 1:1 mass ratios of Prussian blue template material to MgO cast material, calculated using EDX STEM data. The data suggest differing anti sintering performances for the three studied cast morphologies. The bulk powder appears to have produced the smallest particles, giving an average particle diameter of 42 nm. However, it is important to note that this synthesis method appeared to produce a bimodal dispersion, containing two distinct particles sizes. Through centrifugation and potentially, magnetic separation, it may be possible to isolate the two distinct particle types. This may be an area for further investigation.

The porous MgO monolith, on the other hand, appears to have produced larger particle diameters, with an average diameter of 192 nm. Though, the figure for this sample has been calculated with limited data. In any case, the absence of smaller particles and the added complexity of synthesising the cast itself does not reflect favourably on this potential cast material. When considering the initial motivation for the use of the porous monolith, the cast material also seems to have failed on a second count. It was hoped that the pores within the structure might be able to trap and thereby immobilise the Prussian blue particles, providing a mechanism for the inhibition of sintering. Unfortunately, the cast does not appear to have been successful in this regard either. Thus, the porous MgO monolith appears to be the least appealing option out of the three studied cast morphologies.

Finally, the MgO nanopowder seems to have produced particles with an intermediate average particle diameter relative to the other casts, measuring approximately 108 nm. While the average particle diameter is larger than that of the bulk MgO powder the resultant Fe_3C nanoparticles appear more monodisperse in size. The cast also offers the simplicity of being commercially available, unlike the porous monolith, avoiding the need for laboratory synthesis. For these reasons the MgO nanopowder was deemed to be the most promising cast material for the continuation of this work.

Electron tomography has also been used to demonstrate the different ways in which MgO cast morphology can affect the physical nature in which the Prussian blue nanoparticles and the MgO cast mix with one another. Perhaps most interestingly, unlike the MgO nanopowder and porous MgO monolith, the smaller Fe_3C nanoparticles in the bulk MgO mixture appear to have become attached to the surface of the MgO, rather than having been dispersed throughout

the cast in a more homogeneous fashion. This may be a significant contributory factor in the formation of the bimodal particle system produced by the bulk MgO synthesis strategy.

Once washed with EDTA solution, in order to remove the MgO phase, the ability to disperse the Fe_3C nanopowder over a silica support has also been demonstrated. It is hoped that this may lead the way to further testing of the material in catalysis applications. While it is not claimed that this will necessarily make Fe_3C a more active catalyst for specific reactions, it provides another alternative to a mesoporous carbon support and in doing so opens the way to the testing of the material in new and interesting ways.

The magnetic properties of the material have also been examined, showing the material to be superparamagnetic. This property is desirable in wide range of applications, again opening the way for this material to find potential uses outside of the research setting. In a similar vein, a simplified synthesis has also been demonstrated which could lend itself to an industrial production process, utilising a mechanical mixing process such as ball milling.

CHAPTER 4

EXTENSION OF THE CAST CONCEPT INTO THE BIOTEMPLATING OF CARBONISED MICROCOILS

4.1 INTRODUCTION

Biotemplates, in theory, can be derived from any part of a living organism. In general, however, the physical and chemical procedures involved in biotemplating require some degree of robustness and so selected biotemplates often have a significant structural role in the parent organism. Nature is renowned for its ability to create strong materials from organic building blocks, sometimes incorporating an inorganic (mineral) component to increase hardness. Fortunately, properties such as these also lend themselves well to many biotemplating processes. The organic component of biomass for example, can allow for the efficient binding of metals[139, 140, 141] to the template surface, whereas the robustness of the inorganic component, on the other, hand can lend the structural stability[142] sometimes required by harsher biotemplating syntheses.

Chapter 4 of this thesis will focus on the use of the microalgae species spirulina as a biotemplate for the production of carbonised microcoils through calcination processes. The process of biotemplating itself, is introduced in chapter 1 of this thesis.

4.1.1 MICROALGAE

With walls composed mainly of polysaccharides[143, 144] such as cellulose[145], the surface of microalgae cells provide possibilities for metal binding and therefore coating, as well as providing a carbon source for the reduction of metals. This, coupled with their widespread abundance in nature and the relative ease with which many species can be grown and harvested[146], means that microalgae are an extremely useful resource in biotemplating research.

The number of microalgae species in existence is a hotly debated topic in the world of taxonomy. Estimates range from tens of thousands to millions depending on how people interpret the definition of algae. In 2012, the AlgaeBase and Irish Seaweed Research Group settled on a number in region of 72500[147]. Within this number is a vast range of structural variety, but it is the spiral structure of spirulina that is of interest in this chapter.

4.1.2 CELLULOSE

As the most abundant organic molecule in the biosphere, cellulose is a key component in the cell walls of microalgae, as well as higher plants and many fungi, bacteria, protozoans and animals (tunicates)[148]. It is therefore worth examining some of its properties.

Cellulose consists of linear chains of anhydroglucose units joined via β-1,4-glycoside linkages (Fig. 4.1). Due to the abundance of hydroxyl groups bound to these glucose units, cellulose is subject to extensive hydrogen bonding and is thus known to form crystalline structures through chain aggregation.

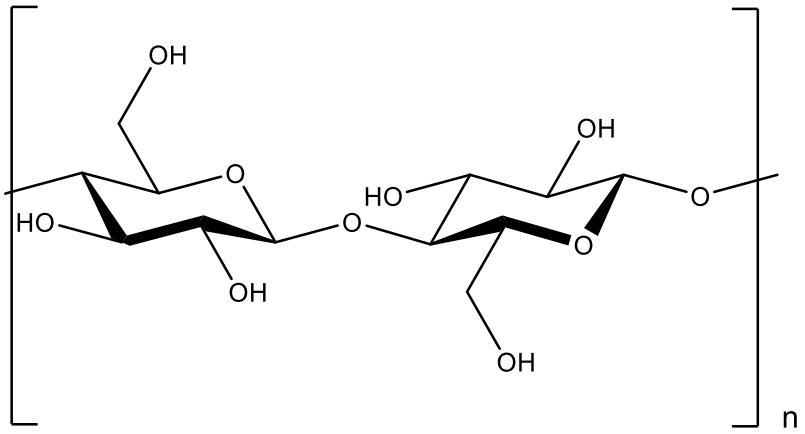

Figure 4.1 Skeletal formula of cellulose.

The crystalline regions of cellulose in biomass, often referred to as 'fibrils', are connected by regions of significantly more soluble, poorly crystalline or amorphous cellulose. By removing the amorphous component, it is possible to isolate the individual cellulose crystallites, known as cellulose 'nanowhiskers'[149], 'nanofibers'[150] or 'nanocrystals'[151]. This is normally achieved by first disrupting the hydrogen bonding by acid hydrolysis or TEMPO-mediated oxidation[152], followed by physical or mechanical processes such as sonication to break up the structure.

Cellulose nanocrystals can be extracted from a variety of sources, such as cotton fibres[153] and wood pulp[154]. A comprehensive review of this process has been prepared by A. Isogai *et al.*[155], illustrating the potential of TEMPO oxidised cellulose nano-fibrils as bio-based nanomaterials. Interestingly, cellulose nanocrystals themselves have found uses in biotemplating processes[156, 157, 158]. Nano-fibrillated cellulose (NFC) can form nematic liquid crystalline phases[159]. Moreover, due to the natural screw symmetry found in crystalline cellulose superstructures, the aforementioned nematic phases display chirality[159]. Understandably then, these phases have shown potential as chiral biotemplates. In 2003 Dujardin *et al*.[160] were able to demonstrate this potential by injecting droplets of NFC with pre-hydrolysed silane, in an attempt to synthesise chiral mesoporous silica. Unfortunately, during this step, in which the concentration of the droplet was shifted, the nematic structure was destabilised. Following an evaporation step the structure was re-established, however, although some localised helical structure could be observed by TEM in the resulting mesoporous silica, it was not possible to prove the template contained any chirality.

In work published shortly after this, Thomas *et al*.[161] went on to show that hydroxypropyl cellulose (HPC) nematic phases were less sensitive to slight changes in concentration.

Following their silica nanocasting process, they were able to create a mesoporous silica cast with local pore structure very closely matching the cellulose template strands. However, some of the finer HPC details were not replicated. The pitch of the silica cast's channels, for example, had shortened slightly compared to the template strands.

Following on from the above-mentioned work, in 2010 Shopsowitz *et al*.[162] were able to demonstrate an important development. By controlling the pH of the aqueous NFC suspension, keeping it at a constant value of 2.4 prior to the addition of their silica precursor, they were able to hydrolyse the precursor without disrupting the chiral nematic NFC phase. The importance of this method should not be underestimated. The team were able to show that their mesoporous silica films contained an accurate replica of the chiral nematic organisation found in the template, which resulted in chiral reflectance that can be tuned across the entire visible and near infra-red spectrum. Furthermore, the films were produced with a simple method, utilising a renewable template, making the technique economical with a view to bulk production.

4.1.3 EXAMPLES OF THE USE OF SPIRULINA IN BIOTEMPLATING PROCESSES

The incorporation of metal microstructures into polymeric composites has been touted as a potential electromagnetic shielding solution for modern electronics[163]. Electroless plating of spirulina is a popular method for producing metal microcoils. To this end Lan *et al.* have shown that the electroless deposition of a Ni-Fe-P alloy coating onto spirulina can give favourable electromagnetic absorption properties[164]. Their synthesis, like many electroless plating procedures, required structural fixation of the spirulina with glutaraldehyde and a Pd

nanoparticle coating to catalyse coating growth. The spirulina was then exposed to an electroless plating bath containing $NiSO_4$ and $FeSO_4$ along with NaH_2PO_2 which acts as the reducing agent. Variation of the Fe : Ni ratio gave varying coating uniformity with a 4 : 1 ratio shown to give the best quality coating by electron microscopy. Significantly, coating uniformity could be improved using a 400 °C heat treatment under an N_2 atmosphere. Any sintering effects suffered during a process such as this could potentially be mediated using our cast technique.

Similar procedures can be used to produce Cu coated coils[165], and Ag coated coils. In the case of the Ag coils, they have been shown to have electrical resistivity that is dependent on the volume content of the coils in an insulating matrix[166]. Furthermore, they have also been shown to have structural flexibility, being stretchable like a spring when embedded in a polymer matrix[167]. The authors tout these properties as desirable in flexibility circuitry. It has also been shown that metal microcoils templated by spirulina can be aligned into continuous microcoil lines in a polydimethylsiloxane composite, using an electric field[168]. By using low microcoil weight fractions the authors managed to create single lines with unique end to end microcoil connections, significantly improving conductivity. These results again seem to move these kind of spirulina templated microcoils slightly closer to potential usage in integrated circuits.

Spirulina can also be used as a template for the fabrication of silicon microcoils[169]. The spirulina is first used to create silica microcoils by immersing them in tetramethyl orthosilicate and ammonium hydroxide. These can then be reduced using magnesiothermal reduction to give silicon. The authors hope that the production of silicon microstructures such as these may

provide alternatives to the energy intensive lithography and chemically harsh etching techniques currently used to pattern and impart structure onto silicon substrates.

Recently spirulina has also been used in the synthesis of $LiMn_2O_4$/C hierarchical structures for use as battery cathode materials[170]. However, this work exploits the material more as a renewable source of carbon rich biomass over which new architectures can be formed, rather than a microcoil template. By introducing hierarchical structure such as this it is thought that the stability and cycling performance of a cathode can be improved. To perform the synthesis, MnO_2 nanoparticles were first deposited onto the spirulina by immersion in $KMnO_4$ and Na_2SO_4. $LiOH.H_2O$ was then introduced under hydrothermal conditions to give $LiMn_2O_4$. A calcination step was then performed to improve crystallinity. Finally, the composites were coated with carbon using sucrose as a carbon source.

4.1.4 CONCLUSIONS

While there are already examples of the use of spirulina as a biotemplate in the literature, there are a lack of examples in which the carbon template has been removed by simple means such as calcination. High temperature treatments in general are problematic when preserving the spiral structure of the template, again due to sintering effects. To this end, the anti-sintering cast concept developed in chapters 2 and 3 will be applied in attempts to produce discrete microcoil replicas, which have been carbonised at high temperatures. While there are no immediate uses for such structures, the aim of the work is to expand the scope of the cast concept and show its utility in applications other than those demonstrated so far.

4.2 CHAPTER SUMMARY

In this chapter, the microalgae spirulina will be used as a biotemplate in the synthesis of discrete carbonised microcoils. In doing so, the cast concept laid out in chapters 2 and 3 will be utilised as a means of preventing sintering. The work is broken up into 3 sections. The first section will lay out how a suitable spirulina source was selected in order to provide high purity and template uniformity. The second section will then look at ways of optimising these templates so that structural information is preserved when performing various chemical and thermal processes. Finally, high temperature syntheses will be performed in which the spirulina biotemplates are converted into carbonised microcoil replicas.

4.3 EXPERIMENTAL

4.3.1 MATERIALS

Table 4.1 List of materials used in chapter 4.

Chemical	Supplier	CAS number
Sodium phosphate monobasic dihydrate ($NaH_2PO_4.2H_2O$) >99%	Sigma Aldrich	13472-35-0
Sodium phosphate dibasic (Na_2HPO_4) >99%	Sigma Aldrich	231-448-7
Glutaraldehyde ($OCHC(CH_2)_3CHO$) 25%	Sigma Aldrich	111-30-8
Magnesium oxide nanopowder (MgO) >99%	Sigma Aldrich	1309-48-4
Iron nitrate nonahydrate ($Fe(NO_3)_3.9H_2O$) >99%	Sigma Aldrich	7782-61-8
Iron (II) acetate ($Fe(CO_2CH_3)_2$) 95%	Sigma Aldrich	3094-87-9
Ethylenediaminetetraacetic acid ($C_{10}H_{16}N_2O_8$) >99%	Sigma Aldrich	60-00-4
Sodium carbonate (Na_2CO_3) >99%	Sigma Aldrich	497-19-8
Sodium bicarbonate ($NaHCO_3$) >99%	Sigma Aldrich	144-55-8
Potassium phosphate dibasic (K_2HPO_4) >98%	Fluka	7785-11-4
Ethanol (CH_3CH_2OH) >99%	VWR	64-17-5

4.3.2 GLUTARALDEHYDE FIXATION

A pH 7.0 phosphate buffer (0.2 M) was prepared by creating two solutions: solution A – $NaH_2PO_4.2H_2O$ (3.12 g) dissolved in distilled water (100 cm^3), solution B – Na_2HPO_4 (2.84 g) dissolved in distilled water (100 cm^3). Solution A (39 cm^3) was then added to solution B (61 cm^3). A 4% glutaraldehyde solution was then prepared by adding 25% glutaraldehyde stock solution (16 g) to distilled water (50 cm^3) which was then made up to 100 cm^3 with phosphate

buffer solution. Likewise, an 8% glutaraldehyde solution was prepared using 25% glutaraldehyde stock solution (32 g).

Spirulina in culture medium (100 cm^3) was isolated by centrifugation. The spirulina was then added to the prepared glutaraldehyde solution (100 cm^3) and left to stir overnight. The sample was then isolated by centrifugation and washed several times with distilled water.

4.3.3 FREEZE DRYING

Samples of spirulina were isolated from culture medium by centrifugation and washed several times with water. If glutaraldehyde fixation was performed the procedure was followed as described above. The samples were then frozen with liquid nitrogen and then dried under a 1 mbar vacuum for 48 hours.

4.3.4 CARBONISATION

Freeze dried spirulina (0.05 g) was mixed with MgO nanopowder (0.50 g). The sample was then mechanically mixed with a lab dancer to improve homogeneity. The samples were then calcined in a tube furnace under a N_2 atmosphere at 5 °C min^{-1} to 500/600 °C. EDTA washing was performed using a 7% molar excess of EDTA solution (0.2 M), relative to MgO content.

4.3.5 CARBONISATION WITH METAL SALTS

Spirulina medium (25 cm^3) with a spirulina content of approximately 2 mg cm^{-3} was washed with distilled water, with the spirulina isolated by centrifugation to give approximately 0.05 g of spirulina. By assuming the spirulina was approximately 75% water by mass and that the resulting mass was composed primarily of cellulose ($C_6H_{10}O_5$), which itself is composed of 44.45% carbon by mass, it was assumed that the sample contained approximately 0.006 g of carbon and thus 4.63 x 10^{-4} mol. In order to fully convert the material to Fe_3C, 1.4 x 10^{-3} mol of Fe is therefore required.

1%w/v and 0.5%w/v solution of $Fe(C_2H_3O_2)_2$ were prepared by dissolution in distilled water. According to the above approximate calculation the mass of iron acetate require for full conversion is equal to 1.4 x 10^{-3} x 173.93 = 0.224 g. Thus, the isolated biomass was mixed with 25 cm^3 of 1%w/v and 25 cm^3 of 0.5%w/v iron acetate solution. The mixtures were then freeze dried, with the freeze-dried product mixed with ten times its mass of MgO nanopowder. The samples were then calcined in a tube furnace under a N_2 atmosphere at 5 °C min^{-1} to 800 °C and held for 1 min. EDTA washing of the calcined samples was performed using a 7% molar excess of EDTA solution (0.2 M), relative to MgO content.

4.3.6 POWDER X-RAY DIFFRACTION

Powder samples were prepared by first grinding them in a mortar and pestle to give homogeneous crystallite sizes and then either placing on a silicon wafer or sample holder sourced from Panalytical. In both cases, samples were flattened to give a uniform sample height.

All samples were analysed using a Panalytical Empyrean diffractometer in a flat plate reflection geometry. The diffractometer was not equipped with a monochromator, but a nickel filter was used to remove Kβ radiation. Thus, samples were analysed with Kα radiation. A Pixcel-2D position sensitive detector was used to collect data between the 2θ angle range 10-70 °. The majority of this data was simply used for phase identification by comparison with the ICDD PDF-4+ database using the EVA software.

4.3.7 OPTICAL MICROSCOPY

All optical microscopy was performed us an Imager .A1m microscope by Karl Zeiss, equipped with an Axio Cam MRc digital camera.

4.4 RESULTS AND DISCUSSION

Spirulina was selected as a biotemplate in the hope that its innate left handed microcoil structure could be preserved after thermal conversion, potentially forming graphitised microcoils. If possible, this would then be extended to the formation of transition metal carbide replicas. To aid in this goal, the anti-sintering cast concept developed in chapters 2 and 3 of this thesis was applied in the hope that the microcoil replicas remained discrete. It was also hoped that this work would help illustrate a possible extension of the cast concept, proving its utility beyond the nanoscale and into other size regimes.

4.4.1 SOURCING SPIRULINA

The first step in this process was to select a suitable source of spirulina. As with many biotemplating procedures, a primary early stage concern was template uniformity. Factors such as sample purity, for example, are a major consideration. Take the growth conditions employed by the manufacturer for example. Depending on the level of caution taken in their growth and harvesting procedures, contamination by other strains of algae is always a possibility. Equally, sample preparation and storage have to be serious considerations.

Many commercially available spirulina products have been dried prior to sale, usually either through conventional drying or freeze drying. These processes could have a significant effect on the fidelity of the algae's microcoil structure. The integrity of the company manufacturing the product is even an important factor, with the product advertised not always guaranteed to match reality.

Taking all of these factors into account, a selection of commercially available spirulina products were sourced and examined by microscopy, with none found to be suitable. Most were found to have very low levels of purity with a negligible number of intact spirulina microcoils present. As a result, the decision was taken to culture spirulina samples in the lab. A spirulina culture was started using a commercially available algae culturing kit purchased from algaeresearchsupply.com.

Information contained in said kit suggested that the life cycle of spirulina involves an initial lag period of 1-10 days in which very little growth is observed. This is then followed by a period of exponential growth that eventually plateaus into a stationary phase at which a limiting factor such as food or CO_2 availability is reached. If the algae is not harvested and nutrients are not replaced at this stage, then a decline will be observed as the algae population starts to die off. Following this cycle, harvesting 50% of the growth media near the end of the exponential growth period and replacing it with an equal volume of fresh growth media, a 5 litre spirulina stockpile with a good degree of purity was eventually produced. This stockpile was harvested on a weekly basis, with the growth medium providing a biomass concentration of approximately 2 mg mL^{-1}.

To produce a good quality spirulina sample several steps were taken to provide hospitable growth conditions. The growth medium itself was based on a recipe created by Aiba *et al.*[171] which includes a mixture of trace metals and salts dissolved in unchlorinated water. The salt mixture, composed of sodium carbonate, sodium bicarbonate and potassium phosphate dibasic, provided both a carbon source to sustain the algae and helped maintain a pH of approximately 10. An alkaline pH provided a favourable environment for spirulina growth,

whilst creating conditions hostile towards many other strains of algae, thereby improving selectivity to give a high purity product. Another important consideration was CO_2 availability. To ensure an adequate CO_2 concentration, a pump was used to periodically aerate the growth medium, replenishing the dissolved CO_2 over time. Light levels were also controlled for the first few weeks, with the culture exposed to 8 hours of light from a fluorescent bulb per day. The culture was then left in natural light to follow a natural day night cycle. Once harvested, optical light microscopy performed on samples of the spirulina exhibited the high quality microcoil structures desirable in a template (Fig. 4.2).

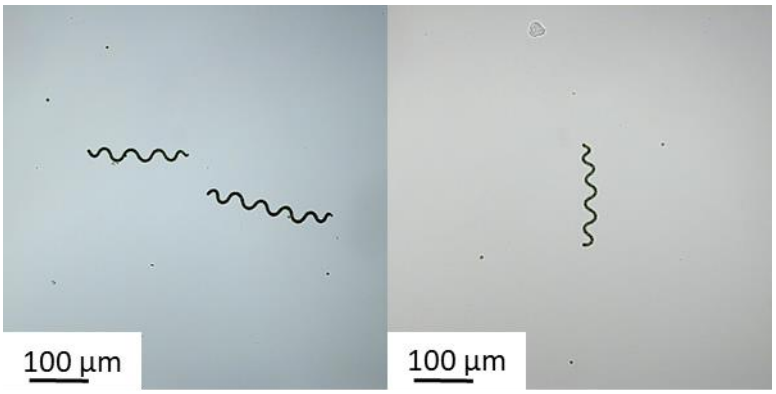

Figure 4.2 Optical microscopy performed on harvested spirulina.

4.4.2 OPTIMISATION OF SPIRULINA

Although many biotemplates have structural properties that are desirable in functional materials, the template itself may require of optimization in order for it to become useful in a chemical process. In this work, spirulina was mixed with a magnesium oxide nanopowder and calcined at high temperatures. This raised two key issues that needed to be addressed early

on. The first was that if the spirulina was to be mixed with an ethanolic MgO slurry the spirulina templates would need to be resistant to EtOH. Ordinarily, when biomass such as algae is exposed to a solvent like EtOH, lipids in the algal cell membranes are dissolved resulting in the breakdown of cells and the dissolution of their contents. This was likely to lead to the loss of the desired microcoil structure.

The second issue was that spirulina, like many other biological materials, has a high water content. If a biological structure with a high water content is subjected to high temperatures the water will evaporate and in many cases the capillary forces that result from water leaving will deform the template. Calcination of spirulina was likely to be no different.

4.4.2.1 GLUTARALDEHYDE TREATMENT

Glutaraldehyde is a commonly used fixative agent used for fixing biological structures, particularly for use in scanning electron microscopy experiments[172, 173] in which the sample is exposed to a vacuum. The reagent works by forming a bridge between amine groups found in amino acids, thereby crosslinking proteins together. The result is a much more robust structure. For this reason, a glutaraldehyde treatment was applied to spirulina samples, firstly to help fix the structures for the carbonisation process, but secondly to help provide a greater resistance to solvents such as EtOH. Due to glutaraldehyde's propensity for undergoing an aldol condensation reaction in alkaline conditions, all glutaraldehyde treatments were performed using a pH 7 phosphate buffer.

Figs. 4.3A and B show optical microscopy images of spirulina microcoils that have been centrifuged to separate them from the growth medium, then redispersed in water and EtOH

respectively. The contrast between these two images is quite stark. Whilst the spirulina microcoils can be redispersed in water without a great amount of structural damage, redispersal in EtOH completely distorts the coiled structure. These results do at least indicate that centrifugation does not lead to significant damage and is thus an appropriate method for the extraction of the algae from the growth medium.

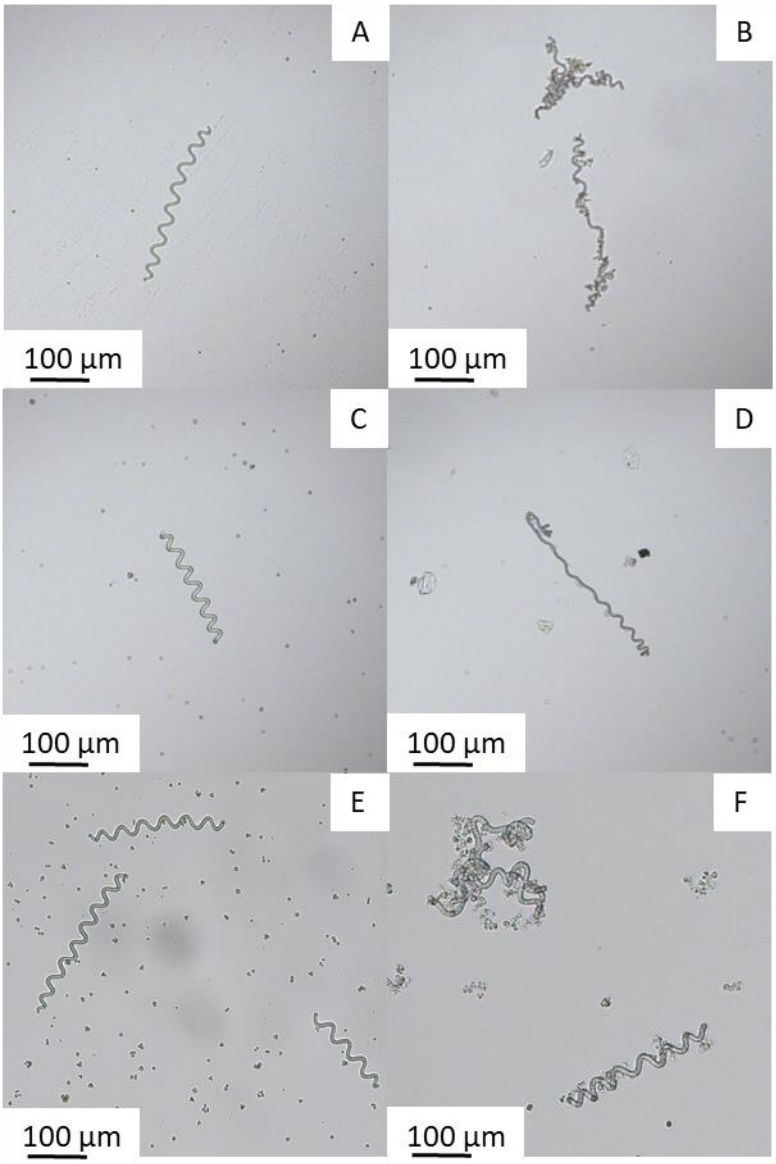

Figure 4.3 Optical microscopy performed on - Untreated algae, centrifuged and redispersed in: **A** – Water, **B** – EtOH, 4% glutaraldehyde treated algae, centrifuged and redispersed in: **C** – Water, **D** – EtOH,8 % Glutaraldehyde treated algae, centrifuged and redispersed in: **E** – Water, **F** – EtOH

Figs. 4.3C and D follow up to show that when treated with a 4% glutaraldehyde solution in a pH 7 phosphate buffer solution, similar results are obtained. When redispersed in water the coil structure remained intact, however, when redispersed in EtOH, while not as badly distorted as the untreated algae, the microcoils were still significantly distorted. Finally, the algae were treated with an 8% glutaraldehyde solution in a pH 7 phosphate buffer solution. The optical microscopy images shown in Figs. 4.3 E and F show the resulting samples. While the algae could, again, be redispersed in water, significant distortion is still visible for the EtOH dispersed sample. This sample does however contain examples of intact microcoils, providing an improvement over the untreated and 4% glutaraldehyde treated samples. Unfortunately, these improvements were not yet great enough for a high fidelity biotemplating process.

4.4.2.2 FREEZE DRYING

While the glutaraldehyde treatment was aimed at fixing the structure of the microcoils, it did not address the issue of water content. Conventional drying of a biotemplate involves the heating of liquid water and therefore subjects the template to capillary forces. Freeze drying, on the other hand, involves the sublimation of frozen water, avoiding the issue of damage from capillary forces. A follow-up experiment was therefore performed in which glutaraldehyde treated spirulina was freeze dried.

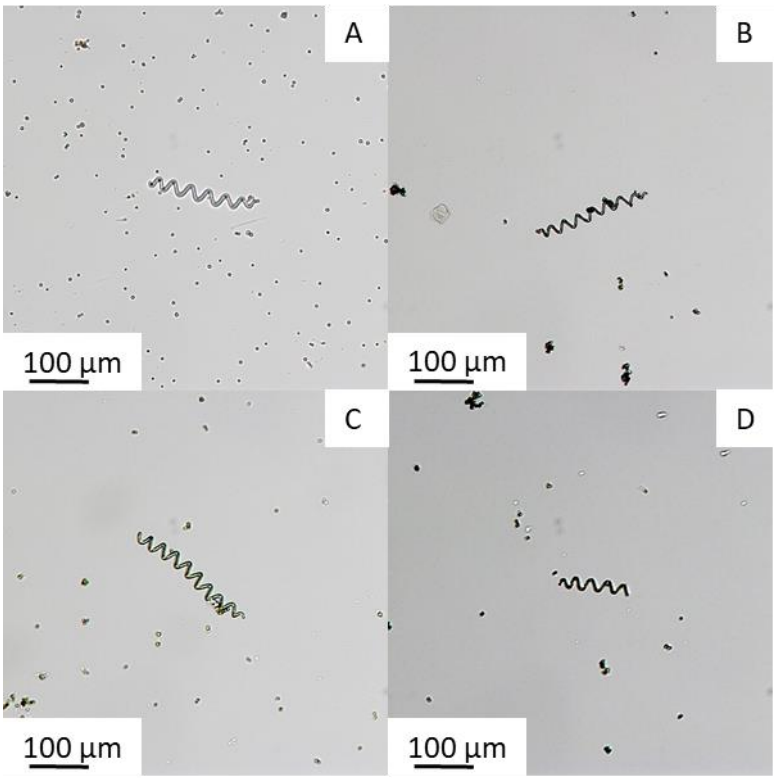

Figure 4.4 Optical microscopy performed on - Freeze dried, 4% Glutaraldehyde treated algae, centrifuged and redispersed: **A** – Water, **B** – EtOH, Freeze dried, 8% Glutaraldehyde treated algae, centrifuged and redispersed: **C** – Water, **D** – EtOH

The optical microscopy images in Figs. 4.4A and 4.4C show that freeze drying both the 4% and 8% glutaraldehyde treated spirulina gives results similar to the non-freeze dried sample when redispersing in water. However, there is a definite observable improvement when redispersing both in EtOH (Figs. 4.4B and 4.4D). In both cases the sample contained a large population of intact microcoils.

4.4.2.3 OPTIMISATION CONCLUSIONS

When it comes to optimising spirulina for various simple chemical processes, this initial vetting process gives some basic indications. It appears that for the addition of spirulina to aqueous solutions, a weak glutaraldehyde treatment may be sufficient to fix the structures. In some cases, even this may not be necessary. When it comes to drying the templates, freeze drying seems to be a perfectly adequate approach. Then finally, for dispersal of the algae in solvents such as ethanol, a glutaraldehyde treatment followed by freeze drying may prove to be a useful optimisation strategy. These findings will form the basis of template optimisation throughout this chapter.

4.4.3 THERMAL CONVERSION

Thermal conversion is a common technique utilised in biotemplating[174, 175]. One of the simplest forms of thermal conversion is carbonisation performed by heating the sample in anaerobic conditions[176]. In some cases, this approach can be used to induce graphitisation. An enhancement on this can be the addition of metal salts to form metal nanoparticles that catalyse graphitisation[88 89]. Metals such as Ni, Co and Fe are particularly effective at this. The formation of metal carbides is also a possibility, with the biomass itself acting as a carbon source.

4.4.3.1 CARBONISATION

To help prove the utility of the cast concept in a biotemplating process, this section will look at simply carbonising spirulina biotemplates alongside a MgO nanopowder cast, by following a process analogous to that set out in Fig. 4.5.

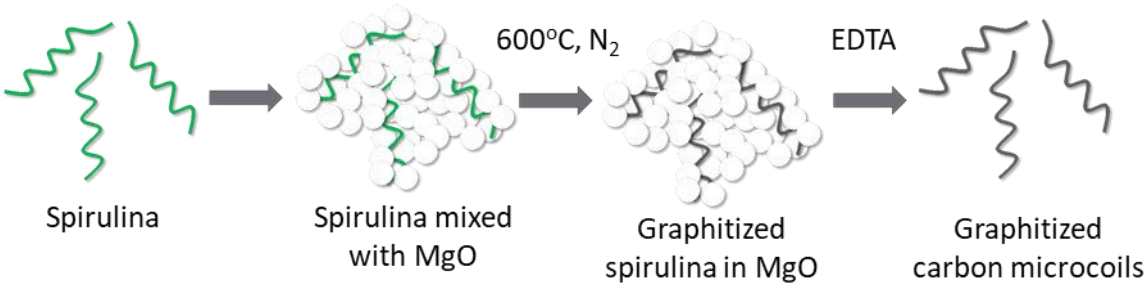

Figure 4.5 Scheme for the graphitisation of spirulina alongside a MgO nanopowder cast.

A sample containing freeze dried spirulina that had been calcined at 500 °C was prepared for use as a control sample. Examination of this sample by optical microscopy revealed a large amount of agglomeration, to the extent at which it was difficult to identify individual coils (Fig. 4.6A). In contrast to this, by mixing spirulina with 10 times its mass of MgO nanopowder (Fig. 4.6B), then calcining it a 500 °C, individual microcoils could be resolved by optical microscopy (Fig. 4.6C). Again, intact coils could be seen when repeating this process at 600 °C (Fig. 4.6E). By EDTA washing the material a large portion of the MgO appears to have been removed (Fig. 4.6D and F). However, it is at this stage of the process that significant difficulties arise. Carbonisation of the coils appears to have resulted in much more brittle mechanical properties and thus, centrifugation of the EDTA washed sample tended to result in the destruction of the microcoils. Small fragments resulting from the destruction of the coils can

be seen in the form of particles in Fig. 4.6D and F. So, to summarise, while as an anti-sintering measure the addition of MgO nanopowder appears to have served a purpose, the final washing process requires further optimisation.

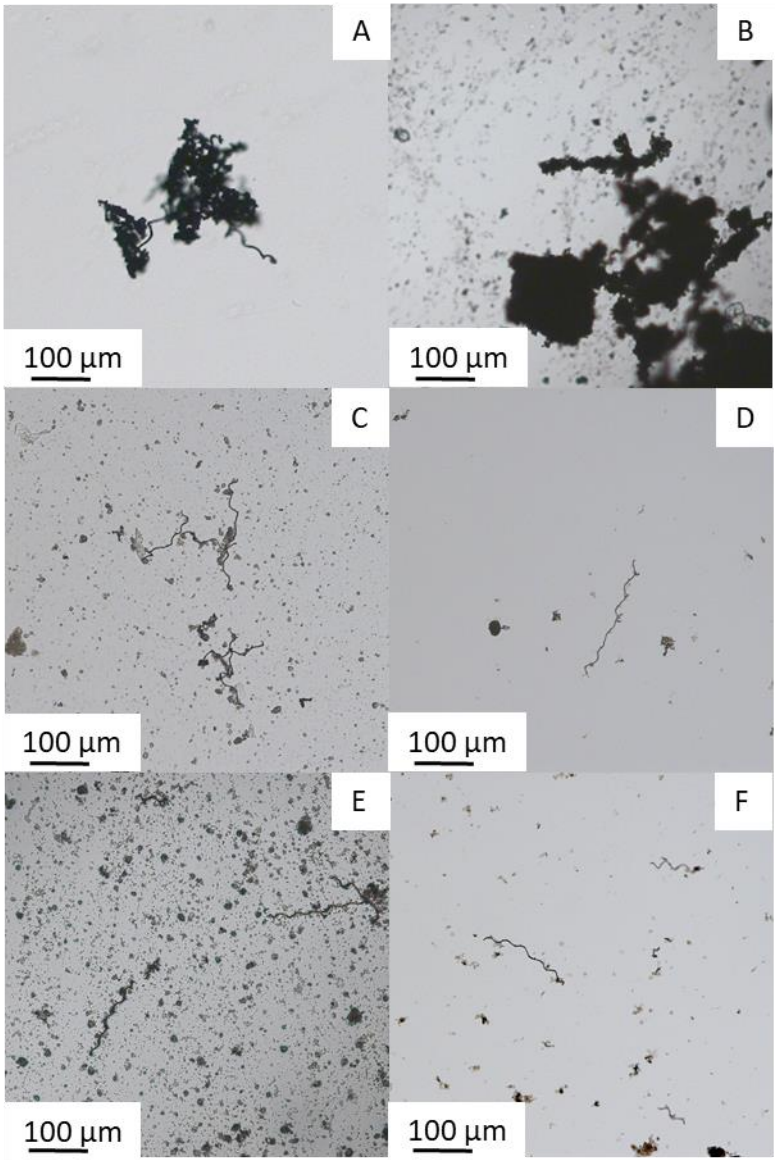

Figure 4.6 Optical Microscopy performed on - **A** – Freeze dried algae, calcined at 500 ˚C, no cast, **B** – Freeze dried algae : MgO 1:10, pre-calcination, **C** - Freeze dried algae : MgO 1:10, post-calcination (500 ˚C), **D** - Freeze dried algae : MgO 1:10, post-calcination (500 ˚C), EDTA washed, **E** - Freeze dried algae

: MgO 1:10, post-calcination (600 °C), **F** - Freeze dried algae : MgO 1:10, post-calcination (600 °C), EDTA washed.

4.4.3.2 CARBONISATION WITH IRON SALTS

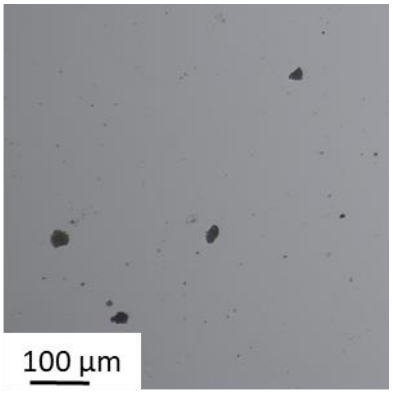

Figure 4.7 Optical microscopy performed on a representative sample, showing the lack of spirulina microcoils that result from treatment with $Fe(NO_3)_2$.

Taking the idea of thermally converting spirulina a step further, the addition of Fe salts was examined in the hope that iron carbide might form using the biomass itself as a carbon source. An experimental approach was designed in which spirulina was mixed with a solution of aqueous iron salts then freeze dried. The freeze dried material was then mechanically mixed with dry MgO nanopowder using a lab dancer shaker, then calcined at 800 °C under N_2. Initial experiments conducted using various concentrations of $Fe(NO_3)_3$ found that the treatment was too harsh, resulting in total destruction of the spirulina templates (Fig. 4.7). In all likelihood this was due to the oxidising nature of the NO_3^- anion. Milder, less oxidising

conditions were achieved by performing experiments with $Fe(C_2H_3O_2)_2$. These experiments proved more fruitful.

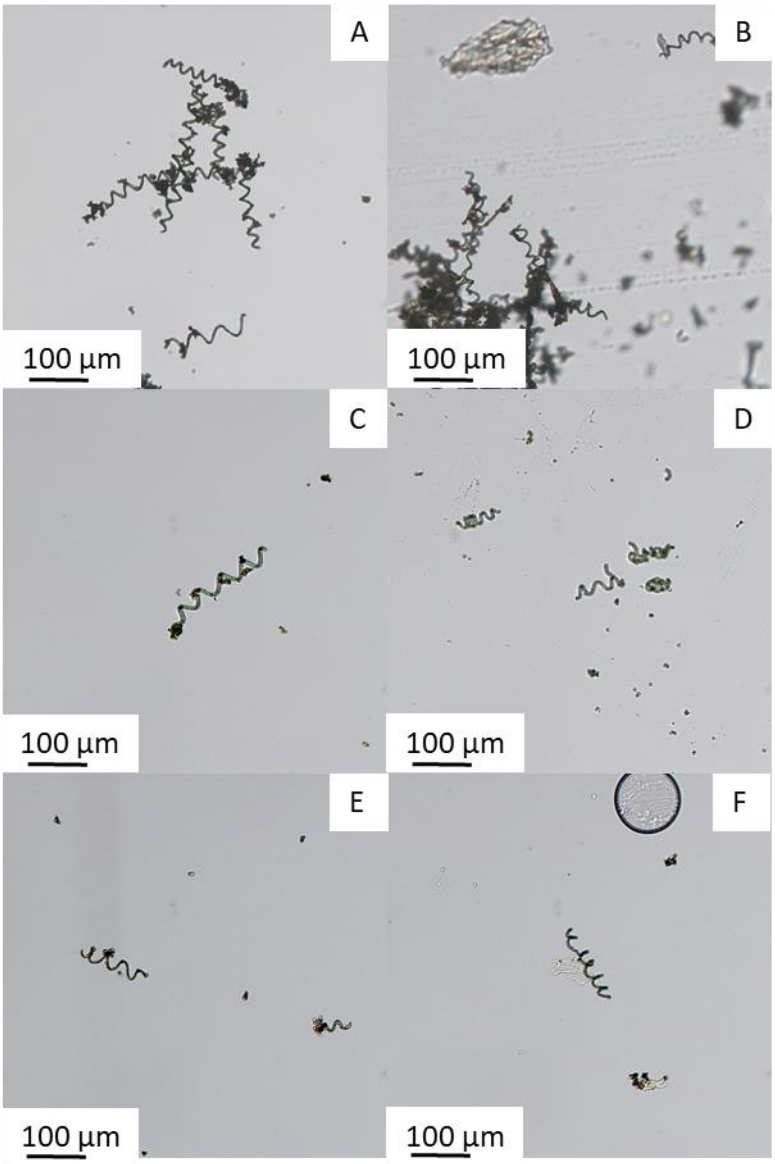

Figure 4.8 Optical microscopy performed on - **A** - Iron acetate (0.5%w/v) soaked algae, freeze dried, **B** - Iron acetate (1%w/v) soaked algae, freeze dried, **C** - Iron acetate (0.5%w/v) soaked algae, freeze dried, dispersed in water, **D** - Iron acetate (1%w/v) soaked algae, freeze dried, dispersed in water, **E** - Iron acetate (0.5%w/v) soaked algae, freeze dried, dispersed in EtOH, **F** - Iron acetate (1%w/v) soaked algae, freeze dried, dispersed in EtOH.

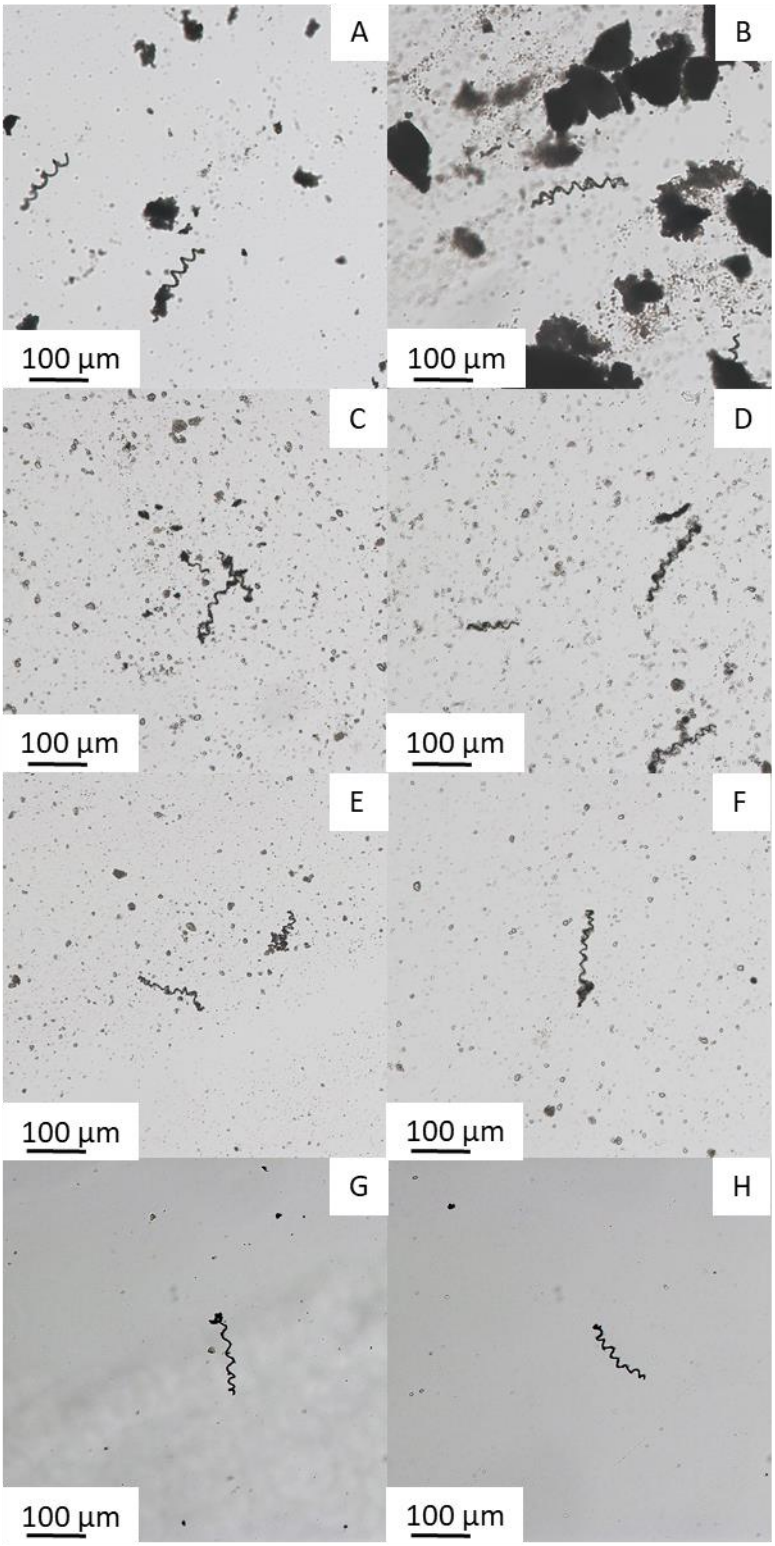

Figure 4.9 Optical microscopy performed on **-** All algae samples prepared at a 1:10 algae : MgO mass ratios: **A** - Iron acetate (0.5%w/v) soaked algae, freeze dried, **B** - Iron acetate (1%w/v) soaked algae, freeze dried, **C** - Iron acetate (0.5%w/v) soaked algae, freeze dried, calcined (800 °C), dispersed in

water, **D** - Iron acetate (1%w/v) soaked algae, freeze dried, calcined (800 ˚C) dispersed in water, **E** - Iron acetate (0.5%w/v) soaked algae, freeze dried, calcined (800 ˚C), dispersed in EtOH, **F** - Iron acetate (1%w/v) soaked algae, freeze dried, calcined (800 ˚C), dispersed in EtOH. **G** - Iron acetate (0.5%w/v) soaked algae, freeze dried, calcined (800 ˚C), EDTA washed, **H** - Iron acetate (1.0%w/v) soaked algae, freeze dried, calcined (800 ˚C), EDTA washed.

Figs. 4.8 A, C and E show $Fe(C_2H_3O_2)_2$ coated freeze dried spirulina, prepared using a 0.5%w/v solution of $Fe(C_2H_3O_2)_2$. Whereas Figs. 4.8 B, D and F were prepared using a 1.0%w/v solution. At this early coating stage, it appears that the spirulina templates remain relatively, structurally unharmed. Upon mechanical mixing of these coated templates, with 10 times their mass of MgO nanopowder, (Fig. 4.9 A and B) intact microcoils are still visible. These Fe coated samples were then calcined under N_2 at 800 °C in the hope of forming Fe_3C replicas. Figs. 4.9 C and D, and E and F show optical microscopy images of the calcined products redispersed in water and EtOH. Water was used as it was less likely to harm the microcoil, yet its drawback was that it would convert the MgO cast to $Mg(OH)_2$. EtOH was then also used for contrast, as it would not dissolve the cast particles. As it turned out, both sets of images appear similar, showing microcoil replicas surrounded by cast particles. Finally, Figs. 4.9 G and H show the EDTA washed coils. Unfortunately, washing of these samples to remove the EDTA bound magnesium again resulted in destruction of the coils.

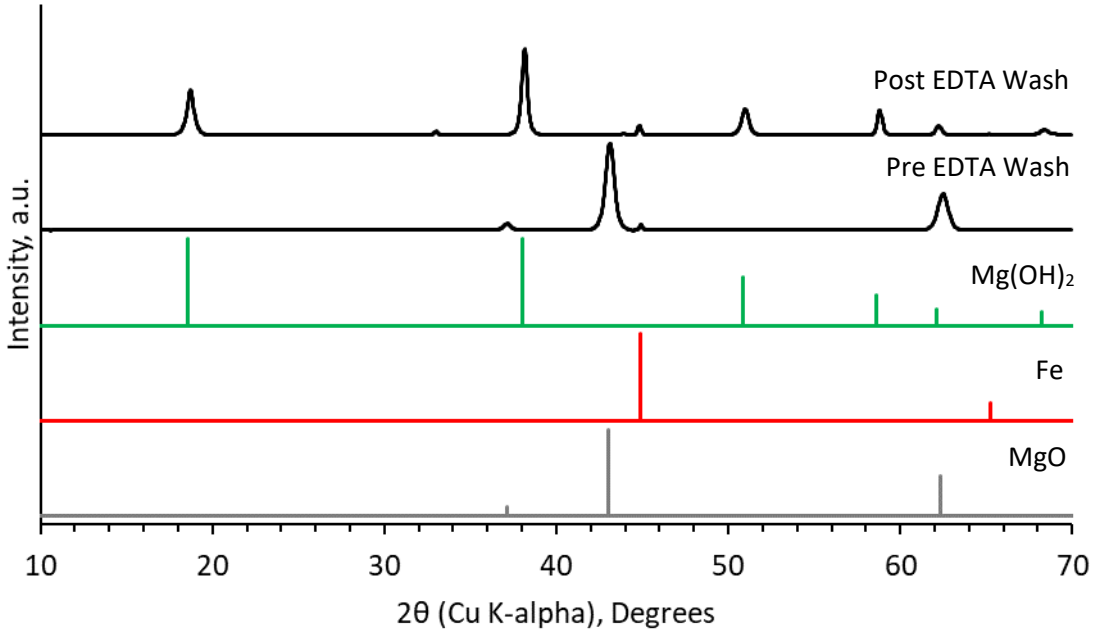

Figure 4.10 PXRD data recorded for iron acetate (0.5%w/v) soaked algae : MgO 1:10, freeze dried, calcined at 800 °C:

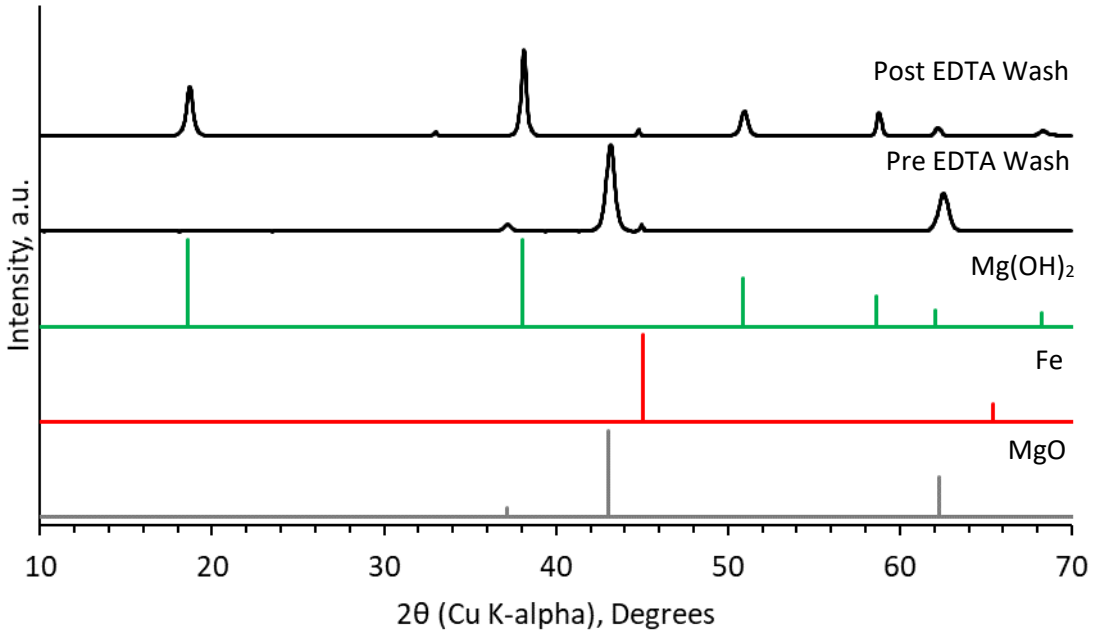

Figure 4.11 PXRD recorded for iron acetate (1.0%w/v) soaked algae : MgO 1:10, freeze dried, calcined at 800 °C:

PXRD performed on both the pre and post EDTA washed samples (Fig. 4.10 and 4.11) show Fe^0 to be the primary Fe phase. However, it is difficult to say how much of the replica coils are simply carbon and how much is actually Fe^0. In all likelihood, rather than producing Fe^0 replicas, Fe^0 nanoparticles have been formed, which then act to catalyse graphitisation in the carbonised replicas, potentially in the form of a network of carbon nanotubes. This may also help explain why the microscopy images appear to suggest slightly improved mechanical stability for the Fe treated samples (Figs 4.9 G and H) relative to the non-treated samples (Fig. 4.6 C-F). Precedent for the catalysis of a nanotube network like this in biomass can be seen in the work of Schnepp *et al.*[89] In this work the authors were able to convert sawdust into a nanostructured material through a very similar process. Thus, further analysis of these materials by TEM may prove insightful

The washed samples also appear to contain a large amount of $Mg(OH)_2$ indicating that the washing process has not been particularly successful. Further work to tune the washing process is therefore required.

4.5 CONCLUSIONS

By combining the anti-sintering cast concept with this biotemplating process the scope of the concept has been extended to a significantly larger size regime. Yet even though the anti-sintering properties have been tentatively demonstrated, there are still significant hurdles to be overcome. The EDTA washing process represents one such challenge. At present, residual $Mg(OH)_2$ is still an issue, as is removing the EDTA bound magnesium without destroying the microcoil replicas. Further optimisation of reaction conditions is also required if the hope of

forming iron carbide replicas is to be realised. At present there is only evidence of the formation of an Fe^0 phase.

Unfortunately, this work was severely hampered by issues related to culturing spirulina as the project progressed. It became difficult to selectively produce spirulina with the problem progressing to the point at which the population of spirulina microcoils in the growth medium became zero. It is possible that this was due to temperature and natural light cycle changes as the year progressed. It also seems that contamination by a secondary species may have been an issue.

CHAPTER 5

CONCLUDING REMARKS

5.1 INTRODUCTION

This thesis set out to find and explore new routes to the synthesis of dispersible metal carbide nanostructures. The work has focussed on combining high temperature templating processes with a variation on “nanocasting”, in which a secondary material, namely MgO, in a variety of morphologies, has been used as a “cast” to physically separate templates during heat treatments. This chapter will now set out to draw some final conclusions from this work, as well as some potential avenues for future work.

This chapter will also draw attention to work carried out during the course of this project not covered in the main body of this thesis. It is hoped that some of this work may provide useful information for future research.

5.2 TEMPLATE SELECTION

5.2.1 NANOPARTICLE TEMPLATES

The metal carbide of choice in this thesis was cementite (Fe_3C). However, it is hoped the strategies described within this thesis may be able to be applied to the synthesis of other metal carbides in the future. For example, in regard to nanoparticle synthesis, this work has used Prussian blue nanoparticles as templates due to the ease with which nanoscale particles can be synthesised and a high Fe and C content. However, by utilising new template materials and combining them with the described casting strategies, the synthesis of a variety of additional metal carbide nanoparticles may be possible. Take Prussian blue ($KFe[Fe(CN)_6]$) for example, the coprecipitation reaction used to synthesise Prussian blue involves the addition

of $FeCl_2$ to $K_3[Fe(CN)_6]$. However, the Fe^{2+} salt can be replaced with other divalent transition metal salts such as $CoCl_2$, $CuCl_2$ or $NiCl_2$ to form the nanoparticulate Prussian blue analogues ($KFe[Co(CN)_6]$), ($KFe[Cu(CN)_6]$) and ($KFe[Ni(CN)_6]$)[104]. While these materials contain both Fe and a second transition metal, rather than just one transition metal, it may provide an interesting avenue to explore.

Taking this idea further, it is possible to synthesise Prussian blue analogue nanoparticles that do not contain iron if both salts are varied during synthesis. For example, $K_3[Co(CN)_6]$ can be combined with $Co(CH_3COO)_2$ to produce $Co_3[Co(CN)_6]_2$ nanoparticles[177]. $K_3[Co(CN)_6]$ can also be combined with other divalent transition metal salts, in a similar way to the previously described Prussian blue analogues, to give mixed metal, metal organic frameworks[177]. Again, these particles may provide interesting options as new template materials.

5.2.2 BIOTEMPLATES

Chapter 4 of this thesis is aimed at demonstrating the extension of the anti-sintering casting concept to larger size regimes, through the inclusion of a cast material into a biotemplating process. The chosen biotemplate, the microalgae spirulina, measures on the micron scale rather than the nano, giving contrast against the Fe_3C nanoparticle templating work described in chapters 2 and 3. While the initial aim of forming Fe_3C microcoils from the spirulina templates was not fulfilled, the work still serves as a demonstration of the anti-sintering effects of the “cast concept” at a new size regime.

During the course of this project a variety of other biotemplating strategies have been explored. One notable result was the replication of the chitionous nanostructures found on a

blue Morpho butterfly wing. This was achieved without the use of a cast material. The process involved first treating the butterfly wings with NaOH then HCl in a process known to help reduce the hydrophobicity of the wing surface[178]. The treated wings were then alternately dipped in ethanol and $Fe(NO_3)_3$ and then calcined at 800°C under an argon atmosphere. Before and after images of the wings can been seen in Fig 5.1. The images show that after calcination (Fig 5.1B) the carbonised wings appear to have undergone slight deformation of their nanostructure compared to the image of the pre-treated wing (Fig 5.1A), yet the overall fidelity seems good. The post calcination image also appears to show a selection of particles dispersed over the wing surface. PXRD performed on the sample (Fig 5.2) gives a diffraction pattern containing peaks that correspond to Fe_2O_3 and Fe_3O_4, the likely composition of the particles in Fig 5.1B. The wings were also observed to be magnetic, an observation expected from Fe_3O_4.

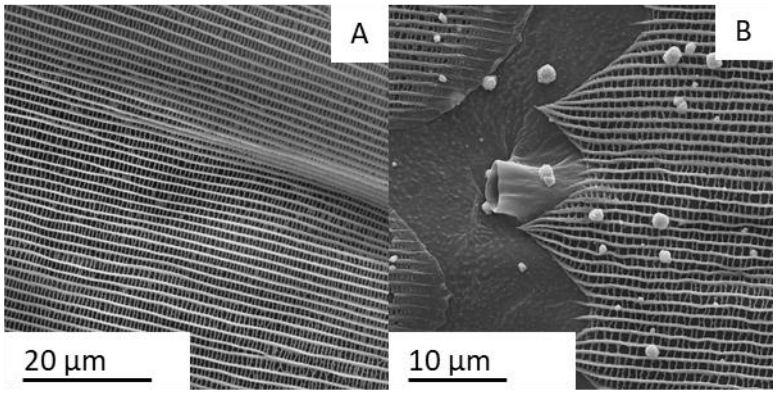

Figure 5.1 SEM images showing a blue morpho butterfly wing: **A** - before treatment and calcination, **B** – the carbonised wing produced after calcination.

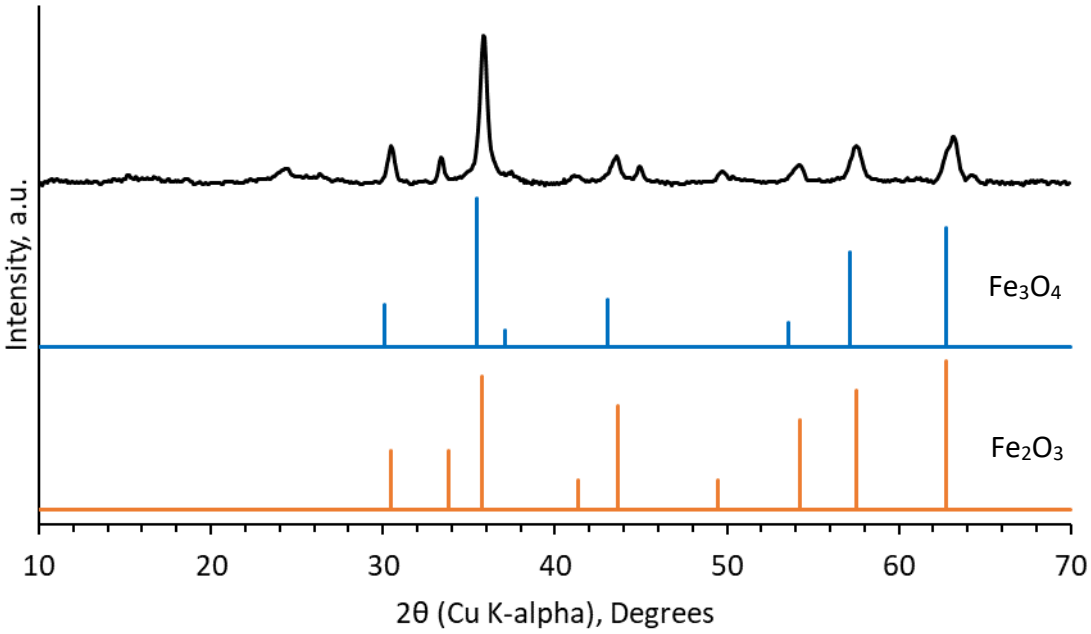

Figure 5.2 PXRD of the carbonised butterfly wing.

A significant amount of time in this project was also spent examining the use of pollen grains as a template for ceramic microspheres. The primary difficulty in this work related to the hydrophobic surface of pollen grains, which made infiltration of the pollen templates with aqueous metal salt solutions very difficult. Various pre-treatments were examined to help alleviate this problem. A key strategy explored was the use of hydrothermal treatments that employed various iron salts such as $FeCl_2$ and $Fe(CH_3COO)_2$ to seed a layer of iron oxide onto the surface of the grains. It was hoped that this iron oxide layer could then be reduced in a second heat treatment to give Fe_3C, using the grain itself as a carbon source. Unfortunately, it was not possible to form a homogeneous coating without damaging the structure of the pollen grains.

This work did, however, yield one interesting result. It was found that hydrothermal treatment of the pollen grains in water at 180°C for 6 hours yielded hollow shells which appeared slightly less hydrophobic. Work using these hollow shells as templates yielded little success, but may provide useful templates for hollow microspheres in future work. Fig 5.3A shows a selection of hollow microspheres with openings through which the contents of the pollen grains have escaped. Fig. 5.3B shows the fine level of detail that remains after the hydrothermal treatment process.

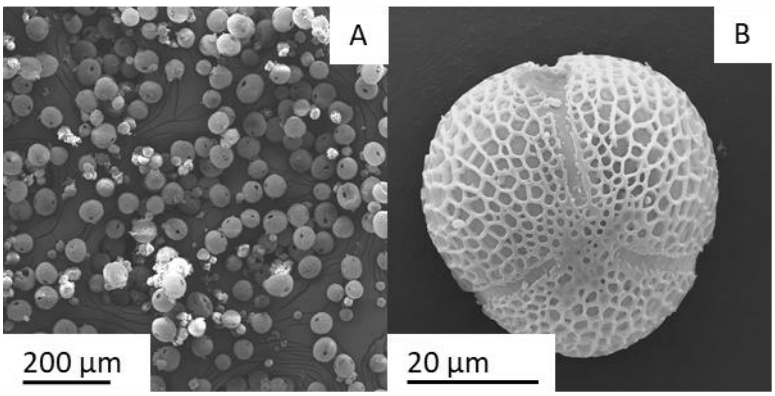

Figure 5.3 SEM images showing hollow microspheres yielded by the hydrothermal treatment of pollen grains.

5.3 CAST SELECTION

This thesis has examined 3 distinct morphologies of MgO for use as an anti-sintering nanocast; a bulk MgO powder; a MgO nanopowder; and a porous MgO monolith produced by a biopolymer based sol gel reaction. Each cast was used to inhibit the sintering of Prussian blue

particles with crystalline domain sizes of approximately 10 nm, that were shown to form agglomerates measuring up 100 nm by DLS.

The MgO bulk powder produced the smallest average Fe_3C particle diameters from the Prussian blue template particles, as measured by TEM (Table 5.1). However, there appeared to be two distinct particles sizes, the small sub 40 nm particles that were found attached to the surface of the MgO cast, an observation supported by electron tomography data, and the much larger particles dispersed throughout the cast. Thus, if the aim is to produce the smallest possible particles this method is the most useful, on the condition that the small particles can be separated from the large particles via centrifugation or magnetic separation. Were work on separating these particles to be carried out in the future, it could vastly increase the utility of this technique.

The MgO monolith on the other hand produced the largest particles as measured by TEM, with average diameters of 192 nm (Table 5.1). The principle behind the use of this cast material was the hope that the porous network would be able to trap Prussian blue template particles, providing a mechanism for their immobilisation during calcination and therefore the prevention of sintering. Unfortunately, the material failed on this count and appears to have acted in way not totally dissimilar to the MgO nanopowder. Given the added complexity of the laboratory based sol gel synthesis of this material, it was not deemed a particularly useful cast option.

Finally, the MgO nanopowder, produced larger average diameters than the bulk MgO powder. Measuring an average of 108 nm in diameter, based on TEM measurements (Table 5.1), these particles also appeared much more monodisperse in size. The cast also appears to have

behaved in a way that matches the initial principle goal of packing small cast particles around the template Prussian blue particles thereby producing a secondary template of sorts, that help prevent the sintering of the template particles. Thus, this cast material seems to be the best option for making a uniform sample in which 100 nm particles can be produced. The magnetic properties of the Fe_3C particles produced by this method have even led to a continuation of the work within our research group in which an undergraduate student has functionalised the particles with oleic acid and then dispersed them in kerosene to produce a ferrofluid (Fig 5.4).

Table 5.1 Average Fe_3C particle diameters calculated from TEM micrographs for samples produced using 1:1 Prussian blue : MgO cast mixtures.

Cast Material	**Average Fe_3C Particle Diameter – TEM (nm)**
Bulk MgO	42
MgO Nanopowder	108
MgO Monolith	192

Figure 5.4 A ferrofluid containing Fe_3C nanoparticles synthesised using the MgO nanopowder cast, under the influence of an applied magnetic field.

The MgO nanopowder is also readily available from commercial chemical suppliers such as Sigma Aldrich avoiding the need for laboratory synthesis. For these reasons, this cast material was chosen as the cast material in the scale up synthesis and as the cast used in the chapter 4 biotemplating work.

Removal of the MgO nanopowder post synthesis has been demonstrated via an EDTA washing process in the case of the Prussian blue templated Fe_3C nanoparticle synthesis. However, in the biotemplated microcoil work it has been shown to be less successful. The use of centrifugation during this process appears to have led to the break up of many of the templated structures. Improving this washing process would be a particularly fruitful area for future work as the preservation of the microcoils leading up to the final centrifugation step ,in which the EDTA bound Mg is removed, seems good.

The overall promise shown by the Fe_3C nanoparticle synthesis using an MgO nanopower has been expanded on through a scale up of the Prussian blue templated Fe_3C nanoparticle synthesis, using commercially available soluble Prussian blue nanoparticles. While this approach does not offer the opportunity for template size control and therefore the tuning of Fe_3C particles size for specific applications, it does provide a potential launching point for an industrially scalable process. One could imagine a set up in which a continuous stream of Prussian blue/MgO mixture is fed through high temperature N_2 atmosphere and then collected in a hopper in a relatively simple process. Again, this may provide a chemical engineering challenge for future work.

5.4 OTHER WORK

5.4.1 NANO-POPCORN

Finally of note, is work that was carried out on the synthesis of “nano-popcorn”. The aim of this work was to produce $Fe(NO_3)_3$ containing biopolymer beads with a robust outer shell. The hope was that when exposed to microwaves the contents of the beads would couple to the microwaves generating heat and therefore autogenerating pressure, to the point at which the contents of the bead would rupture the outer shell. Under inert conditions the biopolymer/$Fe(NO_3)_3$ gel could then undergo a one pot sol gel reaction to produce Fe_3C nanoparticles embedded in a porous carbon support, as per the work of Schnepp *et al*.[179] The simple bead synthesis involved the addition of a warm $Fe(NO_3)_3$/starch gel to a stirring solution of sodium alginate. The beads where then removed from the sodium alginate solution and treated with a glutaraldehyde solution (1%) for 5 mins, in order to form a robust outer shell.

Fig 5.5A shows the beads pre microwave treatment. Fig. 5.5B and C then show the beads after 30 seconds and 1 minute of heating in a 700 W microwave. Fig 5.5C clearly shows the remnants of the outer shell and both Fig. 5.5B and C show the foaming of the bead contents. At the time of this work it was not possible to access a microwave that could heat samples under inert conditions. Thus, Fe_3C formation was not an option at the time. However, continuation of this work using a microwave reactor like the one described in chapter 2 of this thesis may allow for the completion this work.

Figure 5.5 "nanopopcorn" beads containing $Fe(NO_3)_3$ and starch **A** - pre microwave, **B** - 30 second in 700W microwave, **C** - 1 min in 700W microwave.

CHAPTER 6

APPENDICES

6.1 CRYSTALLOGRAPHY

Atoms within a crystalline solid are arranged in a lattice composed of repeating units that contain each type of symmetry present in the crystal as a whole. This unit is known as the "unit cell". Through the use of translational symmetry, the unit cell can be used to generate the entire crystal lattice. The lattice points in a unit cell can be described by a set of lattice parameters; *a*, *b* and *c* being the lengths of the unit cell edges and *α*, *β* and *γ* being the angles at which these edges intersect. The various possible values of these lattice parameters produce 7 primitive (P) lattice types. When centring is introduced a total 14 lattice types are possible. Possible centring arrangements include; face centring (F), body centring (I) or base centring (C). Full descriptions of the 14 Bravais lattice types can be seen in Table 6.1. By introducing atomic positions into these lattice types, the total possible of symmetry operations give rise to 230 space groups.

Planes within a lattice are described by values equal to the reciprocal of the intercepts along the unit cell edges *a*, *b* and *c* by the notation "(hkl)". These values are known as "Miller Indices". The symmetry of the unit cell can give rise to equivalent miller indices. For example, a cubic system can give rise to (100), (010) and (001) planes with the complete set denoted {hkl}. The number of equivalent planes is known as the multiplicity and will have a direct effect on the peak intensities observed in an X-ray diffraction pattern. Each equivalent plane in a crystal lattice is separated by a distance (d_{hkl}).

Table 6.1 Description of the 14 Bravais Lattices

Crystal System	**Unit Cell Lengths**	**Unit Cell Angles**	**Essential Symmetry**	**Allowed Lattices**
Triclinic	$a \neq b \neq c$	$\alpha \neq \beta \neq \gamma \neq 90°$	None	P
Monoclinic	$a \neq b \neq c$	$\alpha = \gamma = 90°, \beta \neq 90°$	One twofold axes	P, C
Rhombohedral	$a = b = c$	$\alpha = \beta = \gamma \neq 90°$	One threefold axes	R
Hexagonal	$a = b \neq c$	$\alpha = \beta = 90°$ $\gamma = 120°$	One sixfold axes	P
Orthorhombic	$a \neq b \neq c$	$\alpha = \beta = \gamma = 90°$	Three perpendicular twofold axes	P, I, F, C
Tetragonal	$a = b \neq c$	$\alpha = \beta = \gamma = 90°$	One fourfold axis	P, I
Cubic	$a = b = c$	$\alpha = \beta = \gamma = 90°$	Four Threefold axes in tetrahedral arrangement	P, I, F

6.2 X-RAY DIFFRACTION

X-rays can be scattered by electron clouds, thus each plane within a crystal is capable of X-ray scattering. If two consecutive planes scatter two in phase monochromatic X-rays, one X-ray will have to travel a greater distance than the other resulting in the waves becoming phase shifted. The superposition of two phases shifted waves is subject to destructive interference. The waves will start moving back in phase as the difference in path length becomes equal to a multiple of the incident X-ray wavelength. The superposition of the two waves will then be subject to constructive interference. The incident angle at which the difference in path length is equal to nλ, and thus diffracted intensity is observed, can be calculated using the bragg equation (Fig. 6.1). However, this is only strictly true for a crystal with an infinite number of lattice planes. When fewer diffraction planes are present there is less destructive interference either side of the bragg angle. Thus, there is a relationship between crystallite size and the full width at half maximum of given peak in an X-ray diffraction experiment. In reality the X-ray

diffraction instrument, thermal motion and strain also contribute to peak width. However, if these factors are accounted for, the crystallite size is directly proportional to peak width and can be calculated using the Scherrer equation (Eq. 6.1).

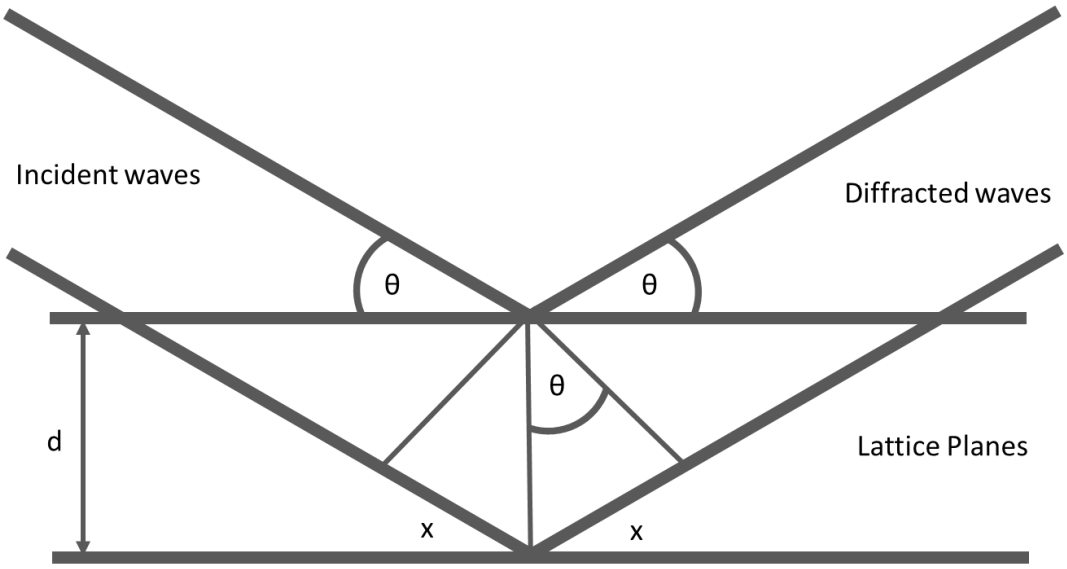

$2x = n\lambda$

$\sin\theta$ = opposite / hypotenuse

Opposite = $\sin\theta$ * hypotenuse

X = $\sin\theta$ * d

$2x = 2d\sin\theta$

$n\lambda = 2d\sin\theta$

Figure 6.1 Schematic illustrating the derivation of the Bragg equation with accompanying mathematical expressions.

$\tau = K\lambda/\beta\cos\theta$

τ = Mean crystalline domain size

K = Shape factor

λ = X-ray wavelength

β = Line broadening at the full width at half maximum after subtracting instrumental broadening in radians

θ = The Bragg angle

Equation 6.1 The Scherrer equation

Whereas a single crystal X-ray diffraction experiment results in the elucidation of a complete reciprocal lattice, a powder experiment in which crystals are randomly oriented results in the smearing of equivalent reciprocal lattice points. The result is that planes with the same d spacings produce diffraction rings. Thus, a large amount of structural information relating to symmetry is lost.

As diffraction data is taken from a section of the ring an averaged intensity around the ring is assumed, however this is only true if the crystallites are truly randomly oriented. Preferred orientation of crystallites is therefore an issue. Peak intensity is also affected by atomic positions, thermal motions and the multiplicity of the lattice planes. Absolute intensity is also affected by the wavelength and intensity of the incident X-rays, the data collection time and efficiency of the detector, as well as the ability of the sample itself to scatter X-rays.

6.3 TEM

A transmission electron microscope operates under many of the same principles as a conventional light microscope with the added benefit of using electrons rather than visible light. Electrons have a typical de Broglie wave length in the range of 1 nm, approximately 100 times smaller than a photon of equivalent energy. Thus, the limiting resolution in TEM is much smaller. As electrons are easily scattered by gas molecules, transmission electron microscopy must be performed under a vacuum. Thermionic emission is the usual mechanism used for generating the electrons. A current, usually ranging anywhere from 100 to 300 kV, is passed through a filament ordinarily made of tungsten. At the point at which enough heat is generated, electrons possessing enough kinetic energy are ejected from the surface of the filament. An anode is then given a positive charge, creating an accelerating voltage, attracting ejected electrons. A negatively charged component known as a Wehnelt cap is positioned between the filament and the anode to act as a focussing lens, helping form a beam. This lens also helps remove spherical aberration caused by the electrons passing through the centre of the Wehnelt cap being refracted less than ones passing through the periphery. Further focussing of the beam is performed using convex electromagnetic lenses formed of coils of copper wire through which an electric current is passed.

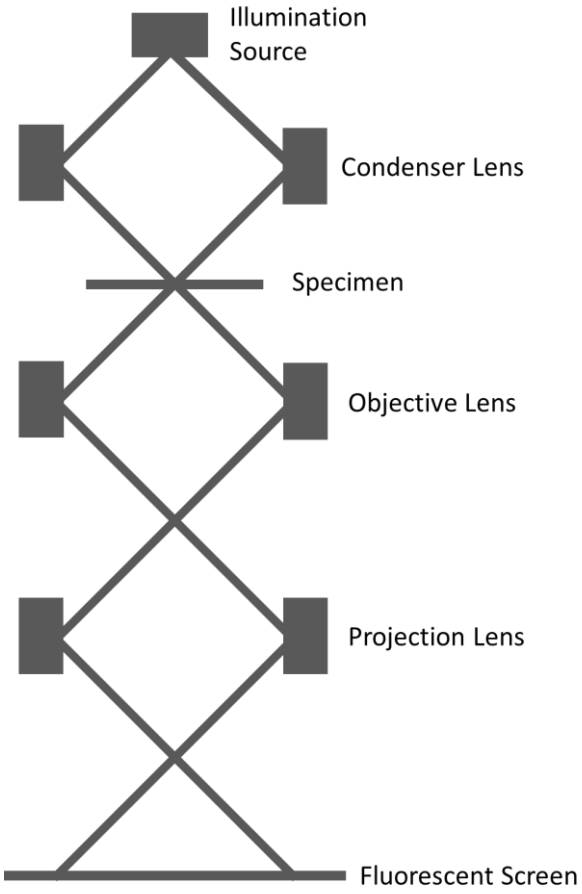

Figure 6.2 Schematic representation of a TEM.

The schematic shown in Fig. 6.2 shows the general set up. The condenser lens serves to focus electrons onto the specimen area of interest. Electrons passing through the sample are then subjected to the objective lens which helps focus and magnify the image. A liquid N_2 cooled cold finger is also present at this stage to help condense and remove contaminants. Finally, the projector lens helps further magnify the image, creating a projection on a phosphorescent screen. A charge coupled device (CCD) camera can then be used to capture a digital image.

Key issues that must be overcome by the operator in a TEM experiment include chromatic aberration caused by electrons with differing energies converging at different focal planes.

Chromatic aberration is usually remedied by increasing the accelerating voltage, checking the quality of the vacuum and potentially using a thinner sample. Astigmatisms are another issue. These are cause by the focussed beam having a higher intensity in one plane relative to the other. Stigmators in the objective lens are used to try and remove this effect.

6.4 SEM

The electron beam used in an SEM experiment is generated in much the same way as the beam used in a TEM experiment, using a tungsten/LaB_6 filament, albeit with a much smaller accelerating voltage of <40kV. Common issues associated with TEM also apply to SEM. Examples include; chromatic aberration caused by the generation of electrons of varying energies, and diffraction caused by out of phase electrons passing through a lens. Both problems can be bypassed by ensuring electron are monochromatic and in phase. Again, spherical aberration must also be considered as well as astigmatism.

Fig. 6.3 shows a schematic representation of an SEM. The condenser lenses act to demagnify the beam. The lens aperture is very important, with smaller apertures giving better resolution, depth of field and less sample charging, but also a lower intensity beam. Depth of field, or the distance over the z axis in which the sample remains in focus can also be improved by increasing the working distance - the distance between the sample and the final lens while the sample is in focus. The final lens contains the raster coils which act to raster (scan) the beam over sample. By telling the coils to scan a shorter distance across the sample, magnification can be increased.

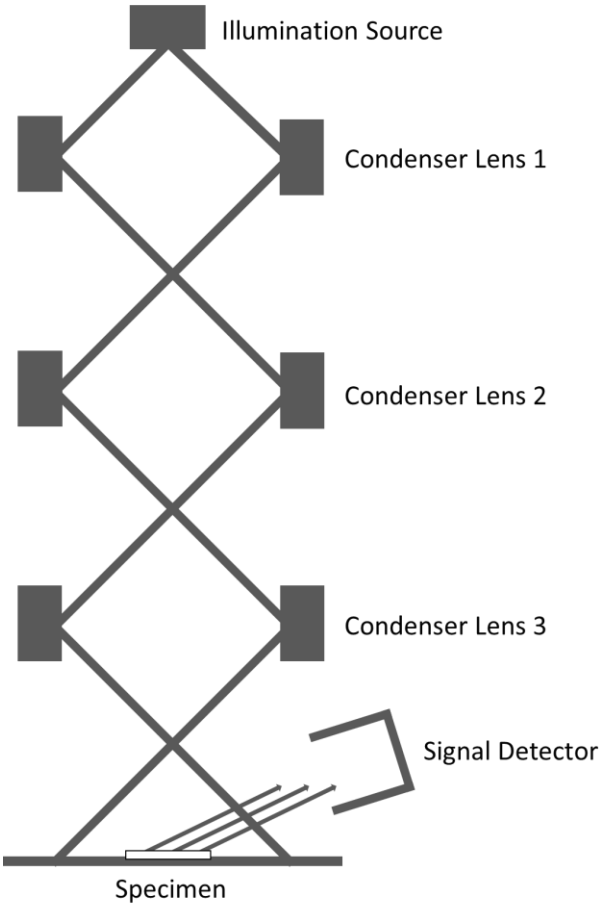

Figure 6.3 Schematic representation of an SEM.

Fig. 6.4 demonstrates the various ways in which the beam can interact with the sample. Backscattered electrons are an example of elastic scattering. Primary electrons, i.e. electrons in the incident beam, that come close to atomic nuclei near the surface of the sample are scattered at angles of up to 180 °. The number of electrons scattered is therefore proportional to the mass of the nuclei it is interacting with, with heavier nuclei giving a higher "backscattered coefficient". The intensity of backscattered electrons can therefore be used to infer a contrast in atomic weight.

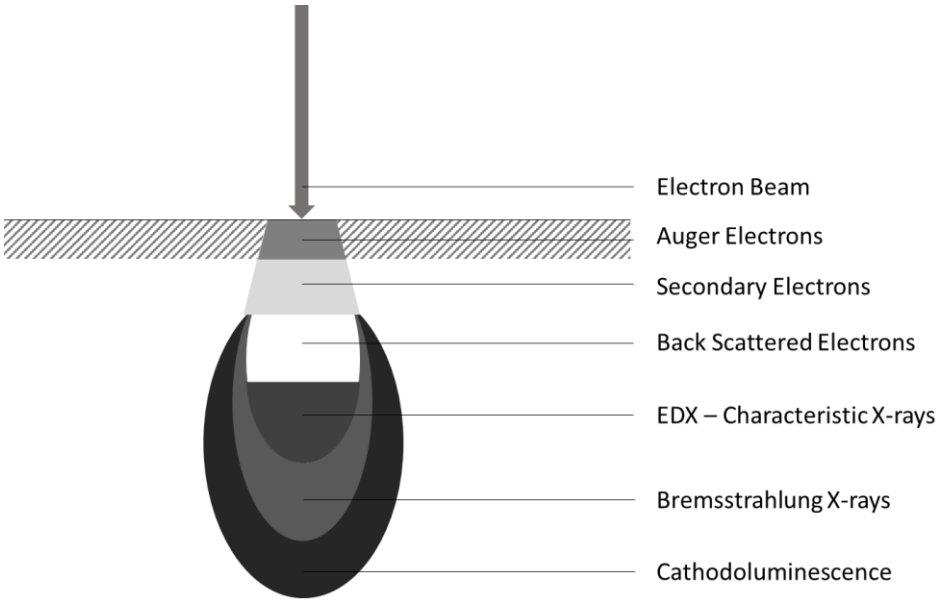

Figure 6.4 Diagram illustrating the possible signals emitted by a sample in an SEM experiment.

The remaining types of information displayed in Fig. 6.4 are a caused by inelastic events. Secondary electrons are used to produce high resolution images. These are electrons knocked out of their parent atoms by primary electrons. The short mean free path of electrons mean that these electrons are only generated very close to the sample surface. The increased surface area seen at sample edges mean more secondary electrons can escape resulting in edges appearing brighter in many images.

Moving deeper beneath the sample surface, characteristic X-rays are emitted. This is caused by high energy electrons dropping into orbitals left vacant by electrons that have been ejected by collisions with primary electrons. Slightly deeper and bremsstrahlung radiation is emitted by the deceleration of primary electrons. Beyond this point cathodoluminescence can be observed i.e. the emission of visible light. Additionally, very close to the surface of the sample,

Auger electrons can be observed. When an electron relaxes into an orbital left vacant by a core electron that has been ejected by a primary electron, it is possible that the emitted photon may excite a second electron causing it to be ejected. This electron is known as an Auger electron.

6.5 DYNAMIC LIGHT SCATTERING

The bombardment of particles by surrounding solvent molecules causes random particle motion known as Brownian motion. By measuring the speed of the Brownian motion of particles in a suspension, dynamic light scattering measurements can be used to calculate particles size. This follows from the fact that larger particles will need a larger transfer of kinetic energy to move at a greater speed than smaller particles. Or in other words, larger particles experience slower Brownian motion.

The speed of Brownian motion is measured by measuring the speed with which the intensity of incident light fluctuates as it passes through a sample. These fluctuations are caused by the constant phase shifting of the in phase, monochromatic, incident light as it is scattered by particles that are in constant motion resulting in a constant fluctuation in constructive and destructive interference. As has already been alluded to, larger particles move at a slower pace and therefore cause less frequent light fluctuations.

These signal fluctuations are measured using a correlator. In effect this compares a signal at a time (t) with a signal at a short time later, potentially a few nanoseconds later, ($t+\delta t$). This signal will correlate strongly with the original signal for slower fluctuations. Thus, as particle

size decreases and signal fluctuation increases the correlation will start to rapidly decay from t to t+δt to t+2δt etc. Put simply, signal correlation will last longer for larger particles.

There are several limitations to dynamic light scattering measurements. The first is that it is actually measuring hydrodynamic diameters rather than particle diameters, thus anything bound to the surface of the particles will be included in the overall diameter value. Substances bound to the surface that affect the diffusion speed of the particles through a solvent will also introduce error into the calculated diameter value.

The second limitation is that a single diameter value can only be used to describe a spherical particle. Non-spherical particles may also diffuse through a solvent at a different rate compared to a spherical particle. Polydispersity can also introduce significant error.

CHAPTER 7

BIBLIOGRAPHY

1 M. E. Vance, T. Kuiken, E. P. Vejerano, S. P. McGinnis, M. F. Hochella and D. R. Hull, *Beilstein J. Nanotechnol.*, 2015, **6**, 1769–1780.

2 J. Sun and S. L. Simon, *Thermochim. Acta*, 2007, **463**, 32–40.

3 G. L. Allen, R. A. Bayles, W. W. Gile and W. A. Jesser, *Thin Solid Films*, 1986, **144**, 297–308.

4 Wahajuddin and S. Arora, *Int. J. Nanomedicine*, 2012, **7**, 3445–3471.

5 D. Bimberg and U. W. Pohl, *Mater. Today*, 2011, **14**, 388–397.

6 S. Abe, J. J. Joos, L. I. D. J. Martin, Z. Hens and P. F. Smet, *Light Sci. Appl.*, 2017, **6**, 1–9.

7 B. L. Cushing, V. L. Kolesnichenko and C. J. O. Connor, *Chem. Rev.*, 2004, **104**, 3893–3946.

8 Y. Yin and D. Talapin, *Chem. Soc. Rev.*, 2013, **42**, 2484–2487.

9 Y.-H. Chen, Z.-H. Huang, M.-M. Lu, W.-Q. Cao, J. Yuan, D.-Q. Zhang and M.-S. Cao, *J. Mater. Chem. A*, 2015, **3**, 12621–12625.

10 S. Rajput, C. U. Pittman and D. Mohan, *J. Colloid Interface Sci.*, 2016, **468**, 334–346.

11 M. Z. Kassaee, E. Motamedi and M. Majdi, *Chem. Eng. J.*, 2011, **172**, 540–549.

12 A. K. Rathi, M. B. Gawande, J. Pechousek, J. Tucek, C. Aparicio, M. Petr, O. Tomanec, R. Krikavova, Z. Travnicek, R. S. Varma and R. Zboril, *Green Chem.*, 2016, **1581**, 1577–1581.

13 K. Cai, X. He, Z. Song, Q. Yin, Y. Zhang, F. M. Uckun, C. Jiang and J. Cheng, *J. Am. Chem. Soc.*, 2015, **137**, 3458–3461.

14 J. D. Mackenzie and E. P. Bescher, *Acc. Chem. Res.*, 2007, **40**, 810–818.

15 A. E. Danks, S. R. Hall and Z. Schnepp, *Mater. Horizons*, 2016, **3**, 91–112.

16 US Patent, 3330697A, 1967, 434, 117–215.

17 Z. Schnepp, *Angew. Chemie - Int. Ed.*, 2013, **52**, 1096–1108.

18 Z. Schnepp, S. C. Wimbush, M. Antonietti and C. Giordano, *Chem. Mater.*, 2010, **22**, 5340–5344.

19 Z. Schnepp, M. Thomas, S. Glatzel, K. Schlichte, R. Palkovits and C. Giordano, *J. Mater. Chem.*, 2011, **21**, 17760–17764.

20 X. Feng, H. Guo, K. Patel, H. Zhou and X. Lou, *Chem. Eng. J.*, 2014, **244**, 327–334.

21 D. J. McClements, *Soft Matter*, 2012, **8**, 1719–1729.

22 I. Capek, *Adv. Colloid Interface Sci.*, 2004, **110**, 49–74.

23 C. T. Seip and C. J. O'Connor, *Nanostructured Mater.*, 1999, **12**, 183–186.

24 J. F. Rivadulla, M. C. Vergara, M. C. Blanco, J. Rivas and M. A. Lo, *J. Phys. Chem. B*,

1997, **101**, 8997–9004.

25 Y. Ikeda, T. Imae, J. Hao and M. Iida, *Langmuir*, 2000, **16**, 7618–7623.

26 K. K. K. Hamada, K. Hatanaka, T. Kawai, *Shikizai Kyokaishi*, 2000, **73**, 385-389.

27 H. Hayashi and Y. Hakuta, *Materials (Basel).*, 2010, **3**, 3794–3817.

28 T. N. J. I. Edison, R. Atchudan, J. J. Shim, S. Kalimuthu, B. C. Ahn and Y. R. Lee, *J. Photochem. Photobiol. B Biol.*, 2016, **158**, 235–242.

29 T. Wu, Y. Liu, X. Zeng, T. Cui, Y. Zhao, Y. Li and G. Tong, *ACS Appl. Mater. Interfaces*, 2016, **8**, 7370–7380.

30 Y. Hakuta, H. Hayashi and K. Arai, *J. Mater. Sci.*, 2004, **39**, 4977–4980.

31 P. Colombo, *Philos. Trans. A. Math. Phys. Eng. Sci.*, 2006, **364**, 109–24.

32 A. R. Studart, U. T. Gonzenbach, E. Tervoort and L. J. Gauckler, *J. Am. Ceram. Soc.*, 2006, **89**, 1771–1789.

33 H. Il Won, N. Hayk, C. W. Won and H. H. Lee, *J. Mater. Sci.*, 2011, **46**, 6000–6006.

34 P. V. Prabhakaran, K. J. Sreejith, B. Swaminathan, S. Packirisamy and K. N. Ninan, *J. Mater. Sci.*, 2009, **44**, 528–533.

35 W. Wang, Z. H. Jin, T. Xue, G. Bin Yang and G. J. Qiao, *J. Mater. Sci.*, 2007, **42**, 6439–6445.

36 Y. Hua, L. Zhang, L. Cheng, Z. Li and J. Du, *J. Mater. Sci.*, 2010, **45**, 392–398.

37 T. Nardin, J. Cambedouzou, J. Ravaux, C. Rey, D. Meyer and O. Diat, *RSC Adv.*, 2015, **5**, 86156–86162.

38 L. Toth, *Transition Metal Carbides and Nitrides.*, 1st edn., 1971.

39 L. Chuenchom, R. Kraehnert and B. M. Smarsly, *Soft Matter*, 2012, **8**, 10801–10812.

40 P. Rani, R. Srivastava and B. Satpati, *Cryst. Growth Des.*, 2016, **16**, 3323–3333.

41 P. Behrens, *Solid State Ionics*, 1997, **101**–**103**, 229–234.

42 M. Froba and O. Muth, *Adv. Mater.*, 1999, **11**, 564–567.

43 A. Stein, F. Li and N. R. Denny, *Chem. Mater.*, 2008, **20**, 649–666.

44 M. Schwickardi, T. Johann, W. Schmidt and F. Schüth, *Chem. Mater.*, 2002, **14**, 3913–3919.

45 Z. B. Zhang, D. Gekhtman, M. S. Dresselhaus and J. Y. Ying, *Chem. Mater.*, 1999, **11**, 1659–1665.

46 D. Ugarte, a. Chatelain and W. a. de Heer, *Science (80-.).*, 1996, **274**, 1897–1899.

47 S. Sotiropoulou, Y. Sierra-Sastre, S. S. Mark and C. A. Batt, *Chem. Mater.*, 2008, **20**, 821–834.

48 X. Tao, R. Wu, Y. Xia, H. Huang, W. Chai, T. Feng, Y. Gan and W. Zhang, *ACS Appl. Mater. Interfaces*, 2014, **6**, 3696–3702.

49 Y. Xia, W. Zhang, H. Huang, Y. Gan, Z. Xiao, L. Qian and X. Tao, *J. Mater. Chem.*, 2011, **21**, 6498–6501.

50 K. Kamata, Z. Piao, S. Suzuki, T. Fujimori, W. Tajiri, K. Nagai, T. Iyoda, A. Yamada, T. Hayakawa, M. Ishiwara, S. Horaguchi, A. Belay, T. Tanaka, K. Takano and M. Hangyo, *Sci. Rep.*, 2014, **4**, 4919–4926.

51 G. Kostovski, D. J. White, A. Mitchell, M. W. Austin and P. R. Stoddart, *Biosens. Bioelectron.*, 2009, **24**, 1531–1535.

52 M. Sun, C. Luo, L. Xu, H. Ji, Q. Ouyang, D. Yu and Y. Chen, *Langmuir*, 2005, **21**, 8978–8981.

53 A. H. Lu and F. Schüth, *Adv. Mater.*, 2006, **18**, 1793–1805.

54 V. Hornok and I. Dékány, *J. Colloid Interface Sci.*, 2007, **309**, 176–182.

55 N. Pinna, J.-F. Hochepied, M. Niederberger and M. Gregg, *Phys. Chem. Chem. Phys.*, 2009, **11**, 3607–3614.

56 E. Gallegos-Suárez, A. F. Pérez-Cadenas, F. J. Maldonado-Hódar and F. Carrasco-Marín, *Chem. Eng. J.*, 2012, **181**–**182**, 851–855.

57 Y. Shin, J. Liu, J. H. Chang, Z. Nie and G. J. Exarhos, *Adv. Mater.*, 2001, **13**, 728–732.

58 J. C. Zhou, C. M. Soto, M.-S. Chen, M. a Bruckman, M. H. Moore, E. Barry, B. R. Ratna, P. E. Pehrsson, B. R. Spies and T. S. Confer, *J. Nanobiotechnology*, 2012, **10**, 18–30.

59 K. Kamata, S. Suzuki, M. Ohtsuka, M. Nakagawa, T. Iyoda and A. Yamada, *Adv. Mater.*, 2011, **23**, 5509–5513.

60 Q. Xu, Y. Tang, L. Zhai, Q. Chen and D. Jiang, *Chem. Commun.*, 2017, **53**, 11690–11693.

61 E. Senoz, R. P. Wool, C. W. J. McChalicher and C. K. Hong, *Polym. Degrad. Stab.*, 2012, **97**, 297–307.

62 M. Adam, M. Oschatz, W. Nickel and S. Kaskel, *Microporous Mesoporous Mater.*, 2015, **210**, 26–31.

63 Z. Schnepp, W. Yang, M. Antonietti and C. Giordano, *Angew. Chemie - Int. Ed.*, 2010, **49**, 6564–6566.

64 A. K. Suri, C. Subramanian, J. K. Sonber and T. S. R. C. Murthy, *Int. Mater. Rev.*, 2010, **55**, 4–40.

65 V. A. Rozenenkova, *Glas. Ceram.*, 2013, **70**, 26–28.

66 M. M. Vopson, *Crit. Rev. Solid State Mater. Sci.*, 2015, **40**, 223–250.

67 Y. Zhong, X. Xia, F. Shi, J. Zhan, J. Tu and H. J. Fan, *Adv. Sci.*, 2016, **3**, 1–28.

68 Y. Xie, M. Naguib, V. N. Mochalin, M. W. Barsoum, Y. Gogotsi, X. Yu, K. W. Nam, X. Q. Yang, A. I. Kolesnikov and P. R. C. Kent, *J. Am. Chem. Soc.*, 2014, **136**, 6385–6394.

69 D. J. Ham and J. S. Lee, *Energies*, 2009, **2**, 873–899.

70 W.-F. Chen, J. T. Muckerman and E. Fujita, *Chem. Commun.*, 2013, **49**, 8896–8909.

71 N. De Leon, X. X. Yu, H. Yu, C. R. Weinberger and G. B. Thompson, *Phys. Rev. Lett.*, 2015, **114**, 1–5.

72 D. H. Jack and K. H. Jack, *Mater. Sci. Eng.*, 1973, **11**, 1–27.

73 G. J. Long and H. P. Leighty, *J. Chem. Educ.*, 1982, **59**, 948–953.

74 B. K. Kumbhar, S. R. Patil and S. M. Sawant, *Eng. Sci. Technol. an Int. J.*, 2015, **18**, 432–438.

75 I. K. Herrmann, B. Beck-Schimmer, C. M. Schumacher, S. Gschwind, A. Kaech, U. Ziegler, P.-A. Clavien, D. Günther, W. J. Stark, R. Graf and A. A. Schlegel, *Nanomedicine*, 2016, **11**, 783–796.

76 J. Yu, F. Chen, W. Gao, Y. Ju, X. Chu, S. Che, F. Sheng and Y. Hou, *Nanoscale Horiz.*, 2017, **2**, 81–88.

77 G. Huang, J. Hu, H. Zhang, Z. Zhou, X. Chi and J. Gao, *Nanoscale*, 2014, **6**, 726–730.

78 W. J. Jiang, L. Gu, L. Li, Y. Zhang, X. Zhang, L. J. Zhang, J. Q. Wang, J. S. Hu, Z. Wei and L. J. Wan, *J. Am. Chem. Soc.*, 2016, **138**, 3570–3578.

79 H. Jiang, Y. Yao, Y. Zhu, Y. Liu, Y. Su, X. Yang and C. Li, *ACS Appl. Mater. Interfaces*, 2015, **7**, 21511–21520.

80 K. Xu, B. Sun, J. Lin, W. Wen, Y. Pei, S. Yan, M. Qiao, X. Zhang and B. Zong, *Nat. Commun.*, 2014, **5**, 1–8.

81 X. W. Liu, Z. Cao, S. Zhao, R. Gao, Y. Meng, J. X. Zhu, C. Rogers, C. F. Huo, Y. Yang, Y. W. Li and X. D. Wen, *J. Phys. Chem. C*, 2017, **121**, 21390–21396.

82 A. K. Das, S. V. Bhoraskar, M. Kakati and S. Karmakar, *AIP Conf. Proc.*, 2008, **1063**, 159–176.

83 V. I. Podgornyi, B. Z. Belashev, R. N. Osaulenko and a. N. Ternovoi, *Tech. Phys.*, 2013, **58**, 1007–1010.

84 V. Amendola, P. Riello and M. Meneghetti, *J. Phys. Chem. C*, 2011, **115**, 5140–5146.

85 C. L. Sajti, R. Sattari, B. N. Chichkov and S. Barcikowski, *J. Phys. Chem. C*, 2010, **114**, 2421–2427.

86 X. Wang and G. Yushin, *Energy Environ. Sci.*, 2015, **8**, 1889–1904.

87 D. W. Lee, J. H. Yu, B. K. Kim and T. S. Jang, *J. Alloys Compd.*, 2008, **449**, 60–64.

88 S. Esconjauregui, C. M. Whelan and K. Maex, *Carbon N. Y.*, 2009, **47**, 659–669.

89 E. Thompson, A. E. Danks, L. Bourgeois and Z. Schnepp, *Green Chem.*, 2014, **17**, 551–556.

90 H. Yoshida, S. Takeda, T. Uchiyama, H. Kohno and Y. Homma, *Nano Lett.*, 2008, **8**, 2082–2086.

91 C. F. Poole, *J. Chromatogr. A*, 2004, **1037**, 49–82.

92 L. Lartigue, J. Long, X. Dumail, S. I. Nikitenko, C. Cau, Y. Guari, L. Stievano, M. T. Sougrati, C. Guérin, C. Sangregorio and J. Larionova, *J. Nanoparticle Res.*, 2013, **15**, 1490–1503.

93 C. Schliehe, J. Yuan, S. Glatzel, K. Siemensmeyer, K. Kiefer and C. Giordano, *Chem. Mater.*, 2012, **24**, 2716–2721.

94 C. Aparicio, L. Machala and Z. Marusak, *J. Therm. Anal. Calorim.*, 2012, **110**, 661–669.

95 M. B. Zakaria, *RSC Adv.*, 2016, **6**, 10341–10351.

96 C. Aparicio, J. Filip and L. Machala, *Powder Diffr.*, 2017, **32**, S207–S212.

97 J. Agrisuelas, J. J. García-Jareño, D. Gimenez-Romero and F. Vicente, *J. Electrochem. Soc.*, 2009, **156**, 149–156.

98 R. Zboril, L. Machala, M. Mashlan and V. Sharma, *Cryst. Growth Des.*, 2004, **4**, 1317–1325.

99 Z. Schnepp, A. E. Danks, M. J. Hollamby, B. R. Pauw, C. A. Murray and C. C. Tang, *Chem. Mater.*, 2015, **27**, 5094–5099.

100 N. Tapia-Ruiz, J. V Laveda, R. I. Smith, S. A. Corr and D. H. Gregory, *Inorg. Chem. Front.*, 2015, **2**, 1045–1050.

101 A. E. Danks, University of Birmingham, 2017.

102 A. Gutiérrez-Becerra, M. Barcena-Soto, V. Soto, J. Arellano-Ceja, N. Casillas, S. Prévost, L. Noirez, M. Gradzielski and J. I. Escalante, *Nanoscale Res. Lett.*, 2012, **7**, 83–95.

103 T. Uemura and S. Kitagawa, *J. Am. Chem. Soc.*, 2003, **125**, 7814–7815.

104 Q. Kong, X. G. Chen, J. L. Yao and D. S. Xue, *Nanotechnology*, 2005, **16**, 164–168.

105 J. K. Armstrong, R. B. Wenby, H. J. Meiselman and T. C. Fisher, *Biophys. J.*, 2004, **87**, 4259–4270.

106 C. Ronchi and M. Sheindlin, *J. Appl. Phys.*, 2001, **90**, 3325–3331.

107 E. Schumacher, *J. Am. Chem. Soc.*, 1926, **48**, 396–405.

108 M. Ma, Y. Zhang, Z. R. Guo and N. Gu, *Nanoscale Res. Lett.*, 2013, **8**, 1–7.

109 A. V. Syugaev, S. F. Lomaeva and S. M. Reshetnikov, *Prot. Met. Phys. Chem. Surfaces*, 2010, **46**, 82–89.

110 P. H. Matter, E. Wang, J. M. M. Millet and U. S. Ozkan, *J. Phys. Chem. C*, 2007, **111**,

1444–1450.

111 T. Wu, H. Zhang, X. Zhang, Y. Zhang, H. Zhao and G. Wang, *Phys. Chem. Chem. Phys.*, 2015, **17**, 27527–27533.

112 S. Mazzucco, Y. Wang, M. Tanase, M. Picher, K. Li, Z. Wu, S. Irle and R. Sharma, *J. Catal.*, 2014, **319**, 54–60.

113 D. V. Wilson, *Nature*, 1951, **167**, 899–900.

114 M. Mahmoudi, S. Sant, B. Wang, S. Laurent and T. Sen, *Adv. Drug Deliv. Rev.*, 2011, **63**, 24–46.

115 R. Qiao, C. Yang and M. Gao, *J. Mater. Chem.*, 2009, **19**, 6274–6293.

116 G. BL, P. AJ, S. J, S. GM, Wi. H and B L Gyorffy and A J Pindor and J Staunton and G M Stocks and H Winter, *J. Phys. F Met. Phys.*, 1985, **15**, 1337–1386.

117 A. Meffre, B. Mehdaoui, V. Kelsen, P. F. Fazzini, J. Carrey, S. Lachaize, M. Respaud and B. Chaudret, *Nano Lett.*, 2012, **12**, 4722–4728.

118 Y. Lee and T. Han, *Jpn. J. Appl. Phys.*, 2004, **43**, 7477–7482.

119 A. G. Kolhatkar, A. C. Jamison, D. Litvinov, R. C. Willson and T. R. Lee, *Int. J. Mol. Sci.*, 2013, **14**, 15977–16009.

120 C. Giordano, A. Kraupner, S. C. Wimbush and M. Antonietti, *Small*, 2010, **6**, 1859–1862.

121 C. Giordano, C. Erpen, W. Yao and M. Antonietti, *Nano Lett.*, 2008, **8**, 4659–4663.

122 C. Giordano, C. Erpen, W. Yao, B. Milke and M. Antonietti, *Chem. Mater.*, 2009, **21**, 5136–5144.

123 Y. Gu, M. Qin, Z. Cao, B. Jia, X. Wang and X. Qu, *J. Am. Ceram. Soc.*, 2016, **99**, 1443–1448.

124 B. K. Barman and K. K. Nanda, *Green Chem.*, 2016, **18**, 427–432.

125 M. Xiao, J. Zhu, L. Feng, C. Liu and W. Xing, *Adv. Mater.*, 2015, **27**, 2521–2527.

126 Z. Y. Wu, X. X. Xu, B. C. Hu, H. W. Liang, Y. Lin, L. F. Chen and S. H. Yu, *Angew. Chemie - Int. Ed.*, 2015, **54**, 8179–8183A.

127 M. Tavakkoli, T. Kallio, O. Reynaud, A. G. Nasibulin, C. Johans, J. Sainio, H. Jiang, E. I. Kauppinen and K. Laasonen, *Angew. Chemie - Int. Ed.*, 2015, **54**, 4535–4538.

128 X. Fan, Z. Peng, R. Ye, H. Zhou and X. Guo, *ACS Nano*, 2015, **9**, 7407–7418.

129 Z. Wen, S. Ci, F. Zhang, X. Feng, S. Cui, S. Mao, S. Luo, Z. He and J. Chen, *Adv. Mater.*, 2012, **24**, 1399–1404.

130 Z. Schnepp, S. R. Hall, M. J. Hollamby and S. Mann, *Green Chem.*, 2011, **13**, 272–275.

131 N. Steigenberger, *Phys. Stat. Sol*, 1972, **133**, 133–139.

132 M. Muhammed, 2001, **44**, 1713–1717.

133 W. Szczerba, J. Żukrowski, M. Przybylski, M. Sikora, O. Safonova, A. Shmeliov, V. Nicolosi, M. Schneider, T. Granath, M. Oppmann, M. Straßer and K. Mandel, *Phys. Chem. Chem. Phys.*, 2016, **18**, 25221–25229.

134 L. J. E. Hofer and E. M. Cohn, *J. Am. Chem. Soc.*, 1959, **81**, 1576–1582.

135 K. Lipert, J. Kazmierczak, I. Pelech, U. Narkiewicz, a Slawska-Waniewska and H. K. Lachowicz, *Mater. Sci.*, 2007, **25**, 399–404.

136 R. Society, 2018, **202**, 224–243.

137 D. Zhang, K. Klabunde, C. Sorensen and G. Hadjipanayis, *Phys. Rev. B - Condens. Matter Mater. Phys.*, 1998, **58**, 14167–14170.

138 X. Sun, Y. Shi, P. Zhang, C. Zheng, X. Zheng, F. Zhang, Y. Zhang, N. Guan, D. Zhao and G. D. Stucky, *J. Am. Chem. Soc.*, 2011, **133**, 14542–14545.

139 X.-X. Li, R.-M. Wang, Y.-F. He, F. Pei and T.-T. Zhao, *J. Control. Release*, 2013, **172**, e136–e137.

140 J. L. Geddie and I. W. Sutherland, *J. Appl. Bacteriol.*, 1993, **74**, 467–472.

141 N. C. Braier and R. A. Jishi, *J.Mol.Struct.THEOCHEM*, 2000, **499**, 51–55.

142 J. T. Chao, M. J. Biggs and A. S. Pandit, *Expert Opin. Drug Deliv.*, 2014, **11**, 1687–1695.

143 B. Wang, Q. Liu, Y. Huang, Y. Yuan, Q. Ma, M. Du, T. Cai and Y. Cai, *Evidence-Based Complement. Altern. Med.*, 2018, **2018**, 1–8.

144 O. Pignolet, S. Jubeau, C. Vaca-Garcia and P. Michaud, *J. Ind. Microbiol. Biotechnol.*, 2013, **40**, 781–796.

145 A. M. Aguirre and A. Bassi, *Biotechnol. Bioeng.*, 2013, **110**, 2114–2122.

146 C. P. Bravo-Fritz, C. A. Sáez-Navarrete, L. A. Herrera Zeppelin and R. Ginocchio Cea, *Algal Res.*, 2015, **11**, 343–349.

147 M. D. Guiry, *J. Phycol.*, 2012, **48**, 1057–1063.

148 J. Wertz, J, Bédué, O, Mercier, *Cellulose Science and Technology*, Taylor and Francis Group, Boca Raton, USA, 1st edn., 2010.

149 S. J. Eichhorn, *Soft Matter*, 2011, **7**, 303–315.

150 S. J. Eichhorn, A. Dufresne, M. Aranguren, N. E. Marcovich, J. R. Capadona, S. J. Rowan, C. Weder, W. Thielemans, M. Roman, S. Renneckar, W. Gindl, S. Veigel, J. Keckes, H. Yano, K. Abe, M. Nogi, A. N. Nakagaito, A. Mangalam, J. Simonsen, A. S. Benight, A. Bismarck, L. A. Berglund and T. Peijs, *J. Mater. Sci.*, 2010, **45**, 1–33.

151 Y. Habibi, L. A. Lucia and O. J. Rojas, 2010, **d**, 3479–3500.

152 T. Saito, S. Kimura, Y. Nishiyama and A. Isogai, *Biomacromolecules*, 2007, **8**, 2485–

2491.

153 Y. Yue, C. Zhou, A. D. French, G. Xia, G. Han, Q. Wang and Q. Wu, *Cellulose*, 2012, **19**, 1173–1187.

154 A. Habibi, Yousseff, Goffin, Anne-Lise, Schiltz, Nancy, Duquesne, Emmanuel, Dubois, Philippe, Dufresne, *J. Mater. Chem.*, 2008, **18**, 5002–2010.

155 A. Isogai, T. Saito and H. Fukuzumi, *Nanoscale*, 2011, **3**, 71–85.

156 A. Ivanova, D. Fattakhova-Rohlfing, B. E. Kayaalp, J. Rathouský and T. Bein, *J. Am. Chem. Soc.*, 2014, **136**, 5930–5937.

157 L. Kong, C. Zhang, J. Wang, D. Long, W. Qiao and L. Ling, *Mater. Chem. Phys.*, 2015, **149**, 495–504.

158 D. Van Opdenbosch and C. Zollfrank, *Adv. Eng. Mater.*, 2014, **16**, 699–712.

159 J. A. Kelly, M. Giese, K. E. Shopsowitz, W. Y. Hamad and M. J. MacLachlan, *Acc. Chem. Res.*, 2014, **47**, 1088–1096.

160 E. Dujardin, M. Blaseby and S. Mann, *J. Mater. Chem.*, 2003, **13**, 696–699.

161 A. Thomas and M. Antonietti, *Adv. Funct. Mater.*, 2003, **13**, 763–766.

162 K. E. Shopsowitz, H. Qi, W. Y. Hamad and M. J. Maclachlan, *Nature*, 2010, **468**, 422–425.

163 M. Jalali, S. Dauterstedt, A. Michaud and R. Wuthrich, *Compos. Part B Eng.*, 2011, **42**, 1420–1426.

164 M. Lan, J. Cai, L. Yuan, Y. Xu and D. Zhang, *Surf. Coatings Technol.*, 2013, **216**, 152–157.

165 J. Liu, X. Zhang, S. Li and M. Yu, *Mater. Lett.*, 2012, **77**, 51–53.

166 J. Cai, M. Lan, D. Zhang and W. Zhang, *Appl. Surf. Sci.*, 2012, **258**, 8769–8774.

167 J. Cai, Y. Shi, X. Li and D. Zhang, *J. Bionic Eng.*, 2017, **14**, 631–639.

168 X. Li, J. Cai, Y. Shi, Y. Yue and D. Zhang, *ACS Appl. Mater. Interfaces*, 2017, **9**, 1593–1601.

169 N. M. Dorval Courchesne, S. A. Steiner, V. J. Cantú, P. T. Hammond and A. M. Belcher, *Chem. Mater.*, 2015, **27**, 5361–5370.

170 J. Wang, W. Liu, S. Liu, J. Chen, H. Wang and S. Zhao, *Electrochim. Acta*, 2016, **188**, 645–652.

171 S. Aiba and T. Ogawa, *J. Gen. Microbiol.*, 1977, **102**, 179–182.

172 K. Ratnayake, D. C. Joyce and R. I. Webb, *Sci. Hortic. (Amsterdam).*, 2012, **140**, 12–18.

173 M. Wiegemann and F. Lehmann, *J. Mater. Sci.*, 2009, **44**, 3813–3818.

174 J. Cao, C. R. Rambo and H. Sieber, *Ceram. Int.*, 2004, **30**, 1967–1970.

175 C. Zollfrank, R. Kladny, H. Sieber and P. Greil, *J. Eur. Ceram. Soc.*, 2004, **24**, 479–487.

176 M. Krzesińska, B. Pilawa, S. Pusz and J. Ng, *Biomass and Bioenergy*, 2006, **30**, 166–176.

177 P. Nie, L. Shen, H. Luo, B. Ding, G. Xu, J. Wang and X. Zhang, *J. Mater. Chem. A*, 2014, **2**, 5852–5857.

178 Z. He, W. Zhang, W. Wang, M. Tassin, J. Gu, Q. Liu, S. Zhu, H. Su, C. Feng and D. Zhang, *J. Mater. Chem. B*, 2013, **1**, 1673–1677.

179 Z. Schnepp, M. J. Hollamby, M. Tanaka, Y. Matsushita, Y. Xu and Y. Sakka, *Chem. Commun.*, 2014, **50**, 5364–5366.